CONTENTS

DE GRUYTER
OPEN

DOI 10.1515/ama-2016-0025

acta mechanica et automatica, vol.10 no.3 (2016)

ELECTRICAL INTERFACE FOR A SELF-POWERED MR DAMPER-BASED VIBRATION REDUCTION SYSTEM

Łukasz JASTRZĘBSKI*, Bogdan SAPIŃSKI*

*Mechanical Engineering and Robotics, Department of Process Control, University of Science and Technology, al. Mickiewicza 30, 30-059 Kraków, Poland

lukasz.jastrzebski83@gmail.com, deep@agh.edu.pl

received 31 March 2016, revised 8 July 2016, accepted 11 July 2016

Abstract: The study investigates the behaviour of an electrical interface incorporated in a MR damper-based vibration reduction system powered with energy recovered from vibration. The interface, comprising the R, L and C elements, is connected in between the coil in an electromagnetic electric generator and the control coil in the MR damper and its function is to convert the output voltage from the generator. The interface model was formulated and computer simulations were performed to find out how the parameters of the interface should influence the frequency responses of the vibration reduction system.

Key words: vibration, electrical interface, MR damper, energy harvesting

1. INTRODUCTION

In recent years mechanical systems with energy recovery capability have received a great deal of researchers' attention. Vibration energy is converted into electric energy mostly by the electromagnetic, electrostatic, piezoelectric or magnetostrictive mechanisms. Major developments in the field of energy recovery from mechanical systems to be used for power supply include alternative or conventional low-power energy sources to power the sensors. When the energy receivers are electric-controlled actuators, the generators are needed with significantly larger power outputs.

Typically, power outputs required for supplying (control) of MR dampers in semi-active vibration reduction systems in the automotive industry range from the tenths of watt to several watts. Nearly twenty years before first efforts were made to engineer vibration reduction systems equipped with MR dampers supplied with regenerated energy. Those systems make use of the electromagnetic method of energy conversion based on the Faraday's law. These issues are addressed in more detail in the works of Cho et al. 2005, 2007a, 2007b), Choi and Werely (2009), Wang et al. (2009), Sapiński (2008, 2011), Snamina and Sapiński (2011). Results reported in those papers indicate that energy recovered from vibration is sufficient to power MR dampers and ensure vibration reduction in the neighbourhood of the resonance frequency. This advantage of such systems comes at the cost of increased vibration amplitudes at frequencies above the resonance frequency. To prevent that happening, purpose-built electrical interfaces are incorporated in the system, connected between the generator coil and the control coil in the MR damper (Rosół et al., 2010; Sapiński, 2014; Sapiński et al., 2016).

The model was developed and computer simulations were performed of a semi-active vibration reduction system equipped with a MR damper supplied with energy regenerated from vibration and incorporating an electrical interface made of: R – resistor, C – capacitor, L – inductor elements, whose operation is based on electric resonance of voltages. The study was undertaken to investigate how the parameters of an electrical circuit formed by the interconnected generator coil, a MR damper coil and a electrical interface should affect the frequency responses of the 1 DOF vibration reduction system, shown schematically in Fig. 1. The source of vibration is a shaker, the vibration reduction system comprises a generator, a spring and a MR damper and the body to be vibro-isolated.

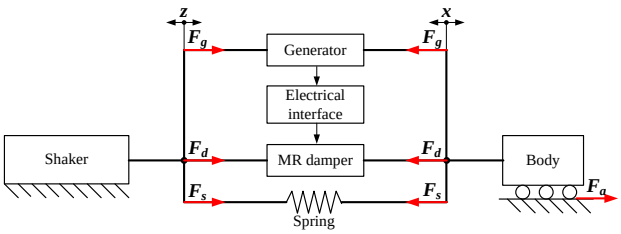

Fig. 1. Semi-active MR damper-based vibration reduction system

2. MODELLING

The model of an electrical circuit, comprising a generator coil, an electrical interface and a MR damper control coil, is assumed to be linear. The diagram of an equivalent circuit is shown in Fig. 2.

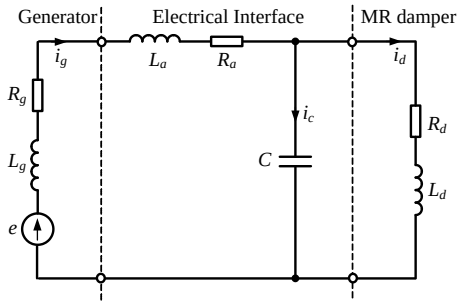

Fig. 2. Equivalent electric circuit

DOI 10.1515/ama-2016-0025

The input applied is the electromotive force e induced in the generator coil windings with resistance R_g and inductance L_g. The response will be current in the MR damper control coil i_d. The electrical interface also incorporates an additional coil with resistance R_a and inductance L_a, and a capacitor with capacity C. As the generator coil and the interface coil are connected in series, the equivalent resistance of those coils is introduced: $R=R_g+R_a$ as well as equivalent inductance $L=L_g+L_a$.

The equation of the circuit shown in Fig. 2 is given as:

$$CL_dL\frac{d^3i_d}{dt^3}+[C(L_dR+R_dL)]\frac{d^2i_d}{dt^2}+(CR_dR+L+L_d)\frac{di_d}{dt}+(R+R_d)i_d=e. \quad (1)$$

Assuming the relative displacement $y=x-z$, the MR damper force can be expressed by the formula (Guo et al., 2006, Kwok et al., 2006):

$$F_d=F_0\tanh\left[\beta\left(\frac{dy}{dt}+p_1y\right)\right]+C_1\left(\frac{dy}{dt}+p_2y\right). \quad (2)$$

It is assumed that parameters F_0 and C_1 are dependent on current i_d, in accordance with Eq (3) and (4) whilst the parameters β, ρ_1, ρ_2 are not related to current i_d.

$$F_0=b_1\cdot i_d^2+b_2\cdot i_d+b_3, \quad (3)$$

$$C_1=b_4\cdot i_d^2+b_5\cdot i_d+b_6. \quad (4)$$

The equation describing the circuit in Fig 1 is written as:

$$\frac{d^2x}{dt^2}=-\frac{1}{m}\left(F_s+F_d+F_g+F_a\right), \quad (5)$$

where: $F_a=b\cdot dy/dt$ is resistance force in kinematic pairs, $F_s=k\cdot y$ is elasticity force, $F_g=\kappa\cdot i_g$ is magnetic force in the generator. It is assumed that electromotive force e and current i_d in the generator coil are expressed by respective formulas:

$$e=\kappa\frac{dy}{dt}, \quad (6)$$

$$i_g=i_d+CR_d\frac{di_d}{dt}+CL_d\frac{d^2i_d}{dt^2}, \quad (7)$$

3. SIMULATION

Simulations were performed in the MATLAB/Simulink environment. The values of the MR damper model parameters were quoted from the work by (Sapiński et al., 2011): β=50 N·s/m, ρ_1= 4 1/s, ρ_2= 0.2 1/s, b_1=3415.7 N/A^2, b_2=93.32 N/A, b_3=74.487 N, b_4=2534.1 N·s/A^2·m, b_5= 19.55 N·s/A·m, b_6= 643.1 N·s/m. The remaining parameters were: body mass m=103 kg, stiffness coefficient k=90000 N/m, damping ratio b_r=50 N·s/m, electric constant of the generator κ=18.6 V·s/m, inductance of a MR damper control coil L_d=100 mH, MR damper coil resistance R_d=5Ω, equivalent inductance L=30 mH, equivalent resistance R=0.4 Ω, capacitor capacity C=47 mF. The simulation procedure involved three stages, the frequency characteristics were obtained for the equivalent system shown in Fig. 2 and for the vibration reduction system shown in Fig. 1, with and without the electrical interface.

3.1. Electrical interface

Fig. 3 shows how the variations of resistance R, capacitance C, inductance L and resonance frequency f_r of the electric circuit affect the frequency characteristics of the magnitude frequency response $|G_{ei}(j2\pi f)|=|I_d(j2\pi f)/E(j2\pi f)|$.

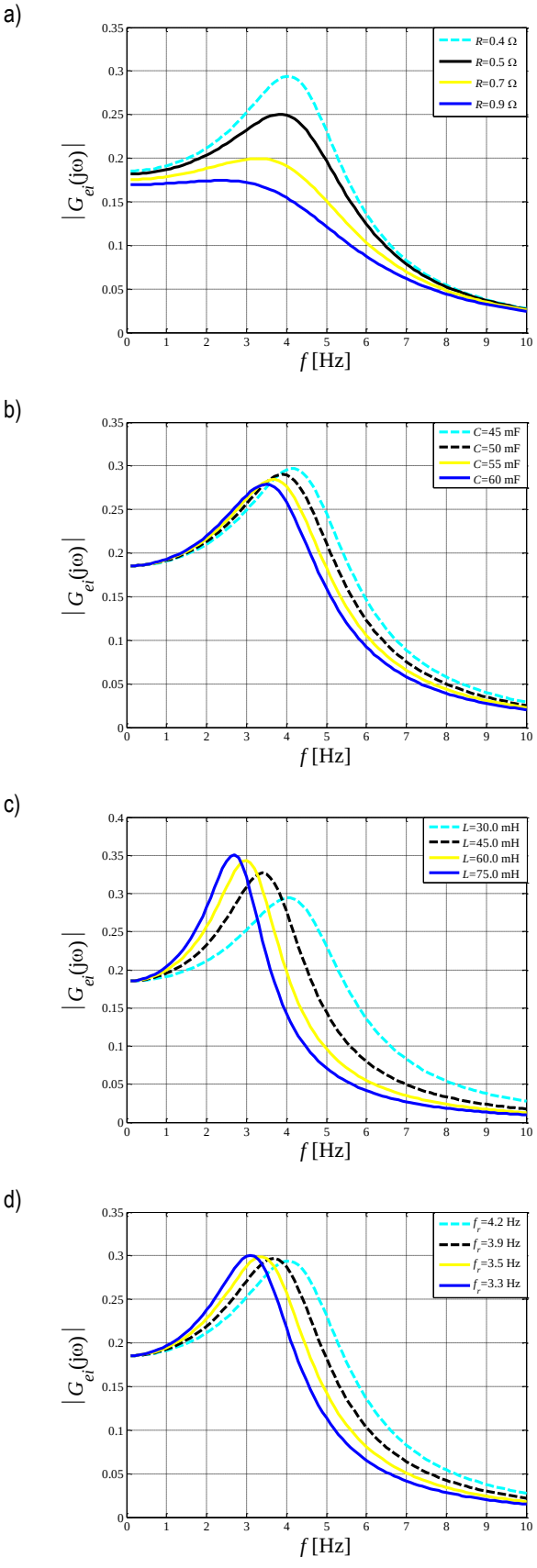

Fig. 3. Frequency response $|G_{ei}(j2\pi f)|$: a) R_g=var, b) C=var, c) L=var, d) f_r=var

DOI 10.1515/ama-2016-0025

It is apparent that:

- increase of resistance R and capacitor capacity C causes the resonance frequency f_r to be reduced and the maximum value of $|G_{ei}(j2\pi f)|$ to be lowered (Fig. 3a, b);
- for resistance R>0.9 Ω, the plot $|G_{ei}(j2\pi f)|$ does not have a maximum for the frequency f_r (Fig. 3a);
- increasing the inductance L results in reduction of resonance frequency f_r, at the same time the maximum value of $|G_{ei}(j2\pi f)|$ will increase (Fig. 3c);
- simultaneous increase of the values of C and L leads to the reduction of frequency f_r whilst the maximum value of $|G_{ei}(j2\pi f)|$ remains unchanged (Fig. 3d);
- simultaneous increase of inductance L and reduction of capacity C should result in an increase of the maximum value $|G_{ei}(j2\pi f)|$ whilst the frequency f_r remains constant.

The change of frequency f_r whilst the maximal value $|G_{ei}(j2\pi f)|$ remain constant allows this frequency to be tuned to the resonance frequency f_{rm} of the system shown in Fig. 1. The value of $|G_{ei}(j2\pi f)|$ for the frequency f_r is associated with the quality factor of the circuit $Q=\sigma/R$, which is proportional to wave impedance $\sigma=\sqrt{L/C}$. With decreasing σ, the characteristics tend to change, like with increasing resistance R (Fig. 3a).

3.2. Vibration reduction system without an electrical interface

Computer simulations were performed to investigate the behaviour of the system shown in Fig. 1 configured such that the MR damper control coil was directly supplied from the generator. The kinematic input excitation z was applied, with the amplitude A=3.5 mm and frequency from the range (0.1, 10) Hz. The purpose of the simulation procedure was to find the displacement transmissibility T_{xz} given by the formula (8), rms values of electromotive force E_{rms} and current level in the control coil I_{rms}, as well as the rms value of the damper force F_d.

$$T_{xz} = \frac{X_{rms}}{Z_{rms}} = \frac{\frac{1}{t}\sqrt{\int_0^t x(t)^2 dt}}{\frac{1}{t}\sqrt{\int_0^t z(t)^2 dt}} \tag{8}$$

Simulation data are compiled in Figs 4-7, plotting the frequency characteristics. Comparison was made between two cases: when the control coil was not supplied (P-passive system) and when the control coil was supplied directly from the generator (SP-self powered system).

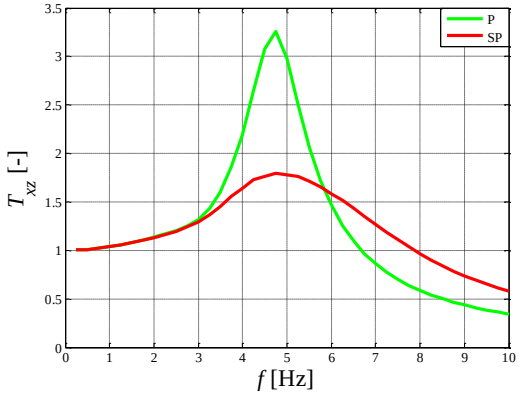

Fig. 4. Transmissibility vs frequency

Coefficients T_{xz} (see Fig. 4) for the systems P and SP reach the maximal value at the resonance frequency f_{rm}=4.75 Hz and are equal to T_{xz}=3.26 and T_{xz}=1.8, respectively. In the system SP the value of T_{xz} decreases in the range (3, 5.75) in relation to the system P and increases when f>5.75 Hz. E_{rms} in the system SP increases with frequency, whilst in the system P it reaches its maximum value for f=5 Hz (Fig. 5). Decreased value of I_{rms} for frequency f>8 Hz is attributed to the increase of the control coil's impedance (Fig. 6). The force F_d reaches its maximum value at frequency f=5 Hz in the system P and at f=9 Hz in the system SP (Fig. 7).

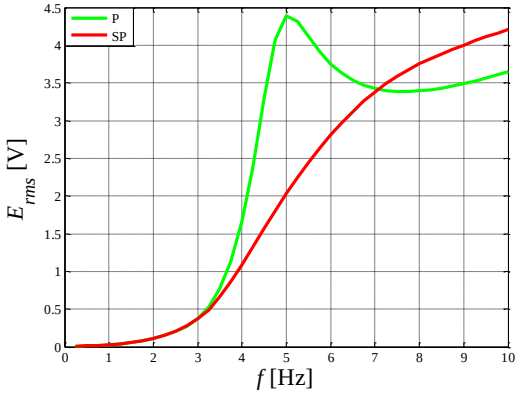

Fig. 5. Electromotive force vs frequency

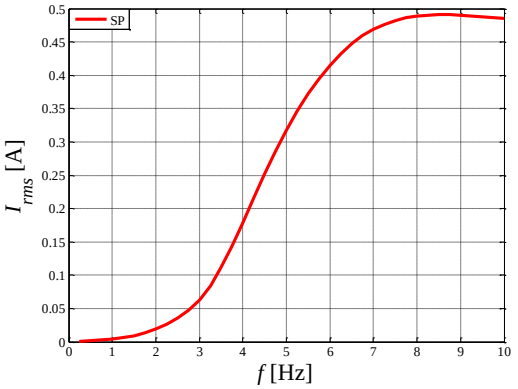

Fig. 6. Current vs frequency

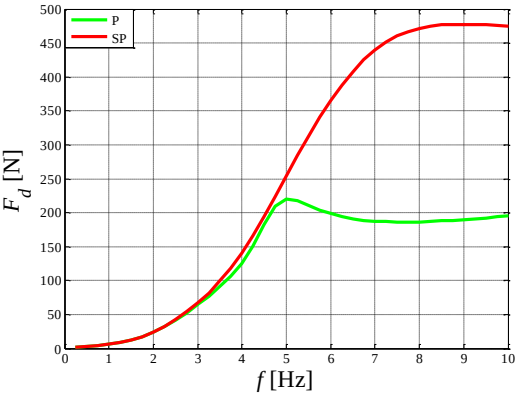

Fig. 7. Force vs frequency

DOI 10.1515/ama-2016-0025

3.3. Vibration reduction system incorporating an electrical interface

Simulations were performed to investigate the behaviour of the system shown in Fig. 1, configured such that an electrical interface is connected between the generator coil and the MR damper control coil (system SPI). The receiver's parameters considered in the simulation procedure were constant (R_d, L_d), and the parameters of the applied input were those given in section 3.2. The main objective was to establish how the parameters R, L, C, the generator's electric constant κ and resonance frequency f_r should influence the frequency characteristics of the system. Simulation data are summarised in Figs 8–27.

The analysis of plots shown in Figs 8–11 reveals that increasing the generator's electric constant κ leads to:

– decrease of T_{xz} in the neighbourhood of resonance frequency (Fig. 8);
– increase of electromotive force value E_{rms} and current I_{rms} (Figs 9, 10);
– increase of the force value F_d in the interval (4, 10) Hz (Fig. 11).

For the maximum value of the electric constant considered in the simulation procedure κ=20 V·s/m, we observe:

– the anti-resonance effect at the same frequency (f_a=4.75 Hz) at which the mechanical resonance f_{rm} is registered in the systems P and SP;
– nearly 3-fold reduction of the value of T_{xz} at frequency f_a in relation to that registered for system P and 1.5-fold reduction of T_{xz} in relation to SP;
– increased the T_{xz} value in the frequency range (6, 8) Hz, in relation to that registered in the system P.

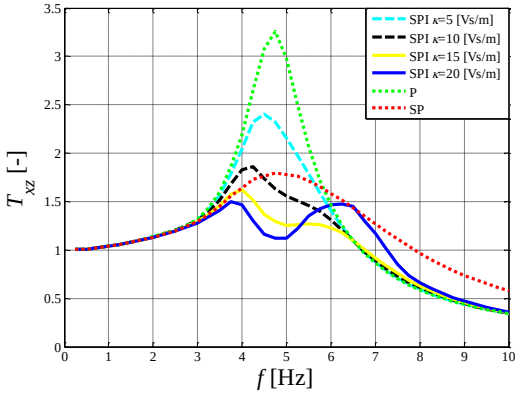

Fig. 8. Transmissibility vs frequency

The lowest value of T_{xz} in the investigated frequency range is registered for the system SPI, its electric constant being κ=15 V·s/m. At the same time the value of T_{xz} tends to decrease in the neighbourhood of resonance frequency and remains on the level similar to that registered for the system P at f>6.25 Hz. A capacitor with capacity C incorporated in the electrical interface lowers its impedance with increasing input frequency f, causing the current level I_{rms} to decrease in a control coil connected in parallel to the condenser at f>f_{rm} (Fig. 10). In the system SPI the value of T_{xz} is reduced at frequencies in excess of f_{rm}, when compared to SP.

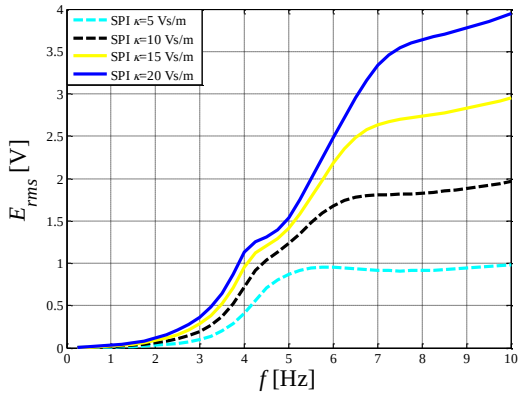

Fig. 9. Electromotive force vs frequency

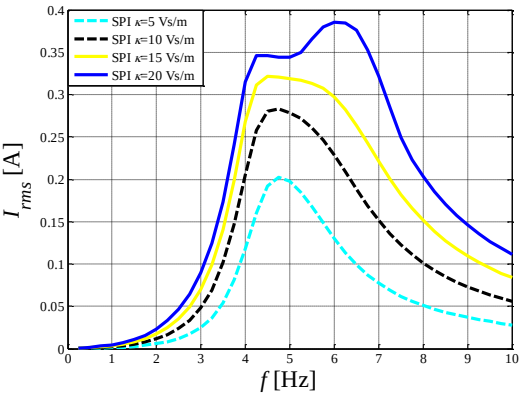

Fig. 10. Current vs frequency

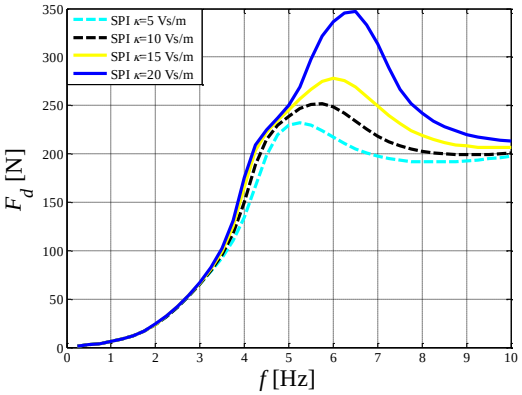

Fig. 11. Force vs frequency

The analysis of plots shown in Fig 12-15 reveals that decreasing the resistance R will lead to:

– lowering the value of T_{xz} in the neighbourhood of resonance frequency (Fig. 12);
– lowering the value of E_{rms} in the frequency range (4,7) Hz (Fig. 13);
– increasing the value of I_{rms} and force F_d at f>4 Hz (Figs 14, 15);

DOI 10.1515/ama-2016-0025

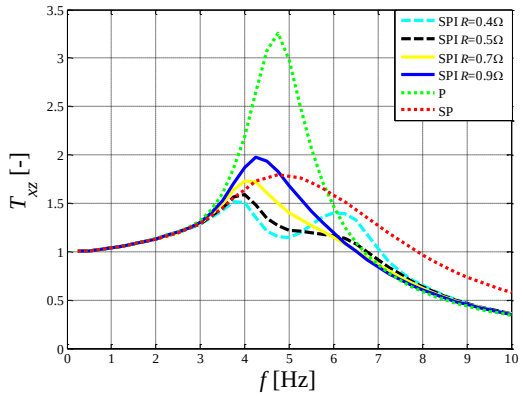

Fig. 12. Transmissibility vs frequency

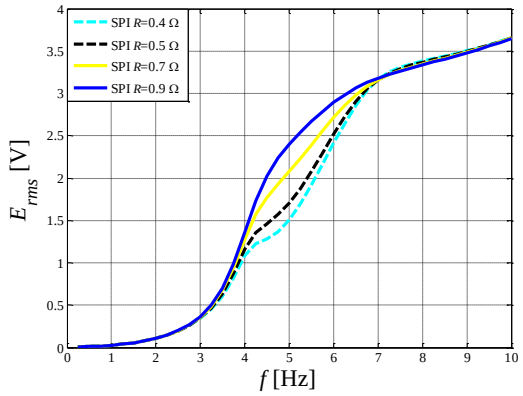

Fig. 13. Electromotive force vs frequency

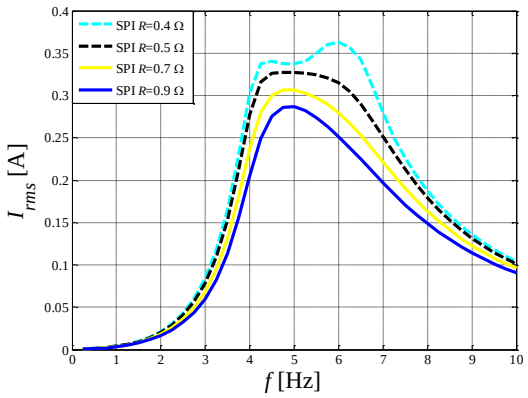

Fig. 14. Current vs frequency

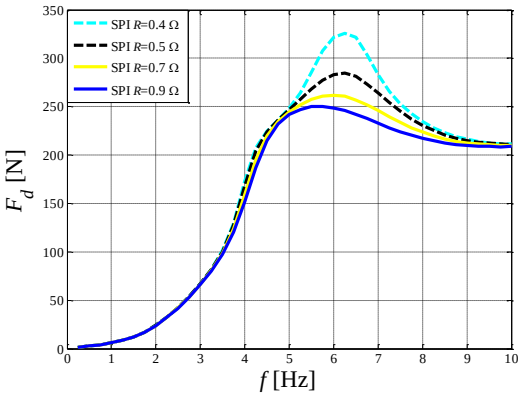

Fig. 15. Force vs frequency

When resistance R= 0.4 Ω, the anti-resonance effect will arise (f_a=4.75 Hz), at the same time the value of T_{xz} registered in the frequency range (6,8) Hz is higher than in the circuit P. In the investigated frequency range and at resistance R=0.5 Ω the value of T_{xz} in the circuit SPI is lower in relation to the values registered for P and SP.

The analysis of plots in Figs 16-19 reveals that reducing the condenser capacity C results in:

- decrease of the value of T_{xz} (Fig 16) at the anti-resonance frequency f_a, at the same time this frequency will increase;
- decrease of the E_{rms} value (Fig 17) in the frequency range (4, 8) Hz;
- increase of the I_{rms} value (Fig. 18) and of force F_d (Fig. 19) in the frequency range (4, 10) Hz.

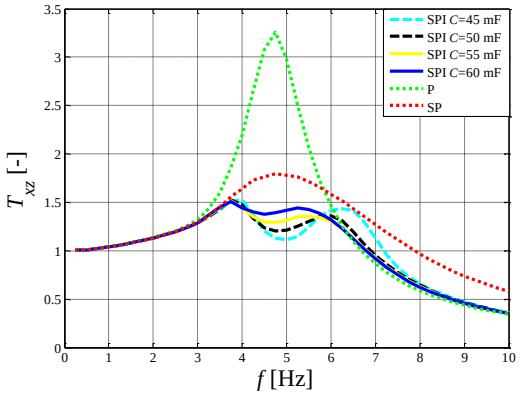

Fig. 16. Transmissibility vs frequency

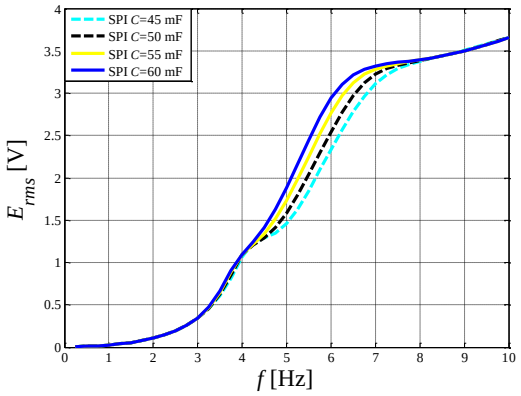

Fig. 17. Electromotive force vs frequency

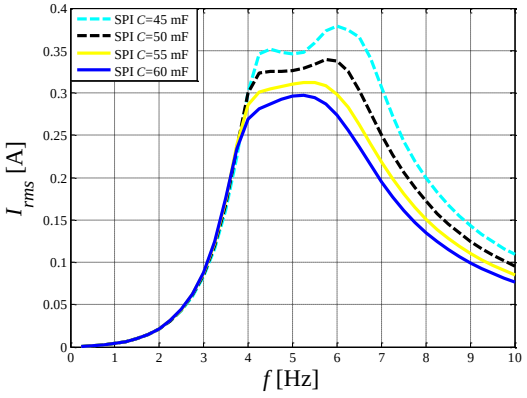

Fig. 18. Current vs frequency

DOI 10.1515/ama-2016-0025

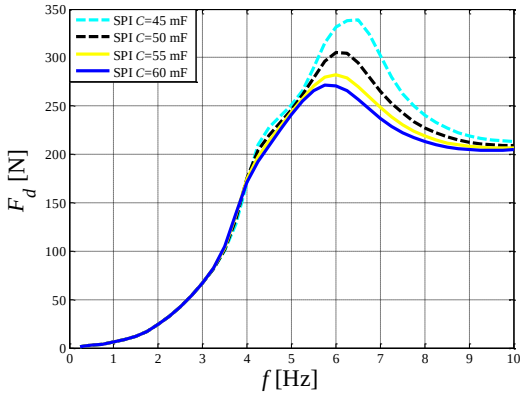

Fig. 19. Force vs frequency

For capacitor capacity C=45 mF, the value of T_{xz} registered in the frequency range (6, 8)Hz is higher than in the circuit P. The lowest value of T_{xz} in the investigated frequency range is registered in the circuit SPI for C=50 mF (Fig. 16).

The analysis of plots in Figs 20-23 reveals that reducing the inductance L will lead to:

– decrease of T_{xz} value in the frequency range (3,6) Hz (Fig. 20);
– increase of resonance frequency f_{rm} when L>45 mH and increase of anti-resonance frequency f_a when $L\leq$ 45 mH;
– lowering the value of E_{rms} in the frequency range (4,8) Hz (Fig. 21);
– increase of I_{rms} and force F_d in the frequency range (3,10) Hz (Figs 22, 23);
– increase of the frequency f at which the force F_d reaches its maximum value.

When inductance L=30 mH, the value of T_{xz} in the frequency range (6, 8) Hz is increased. The lowest values of T_{xz} in the investigated frequency range, compared to the circuits P and SP, were registered for L=45 mH. Plots in Figs 24-27 illustrate the effects of varying the resonance frequency of the electrical circuit f_r, while the quality factor Q of the circuit remains unchanged. The anti-resonance effect (Fig 24) occurs for all investigated frequencies f_r.

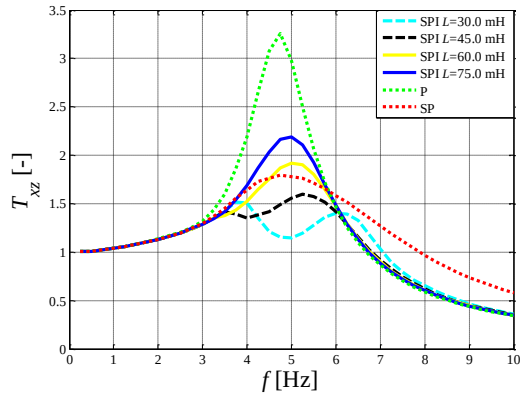

Fig. 20. Transmissibility vs frequency

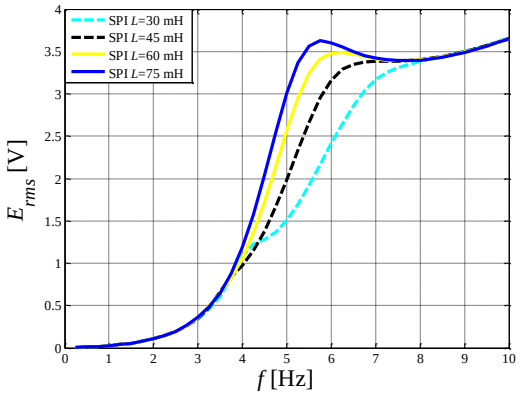

Fig. 21. Electromotive force vs frequency

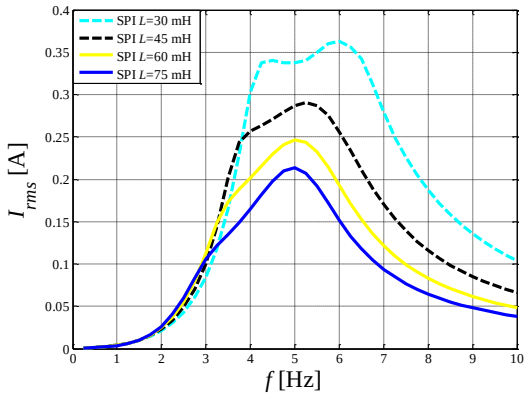

Fig. 22. Current vs frequency

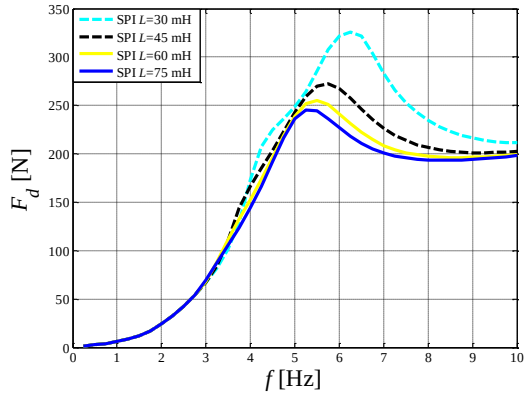

Fig. 23. Force vs frequency

The analysis of plots in Figs 24-27 reveals that increase of frequency f_r will lead to:

– increase of anti-resonance frequency f_a of the mechanical system and reduction of T_{xz} value at f_a (Fig. 24);
– reduction of the E_{rms} value in the frequency range (4, 8) Hz (Fig. 25);
– increasing the value of I_{rms} and force F_d in the frequency range (4, 10) Hz (Figs 26, 27).

DOI 10.1515/ama-2016-0025

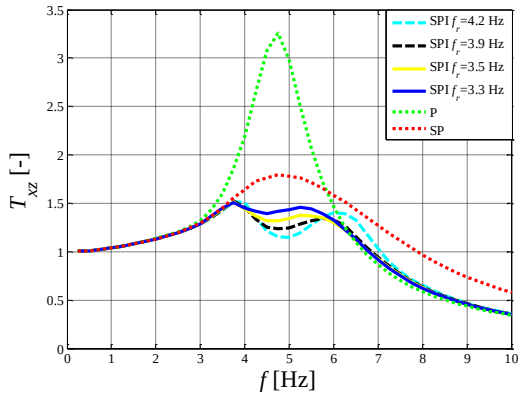

Fig. 24. Transmissibility vs frequency

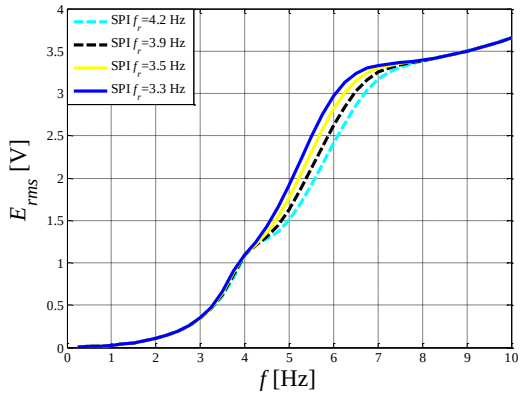

Fig. 25. Electromotive force vs frequency

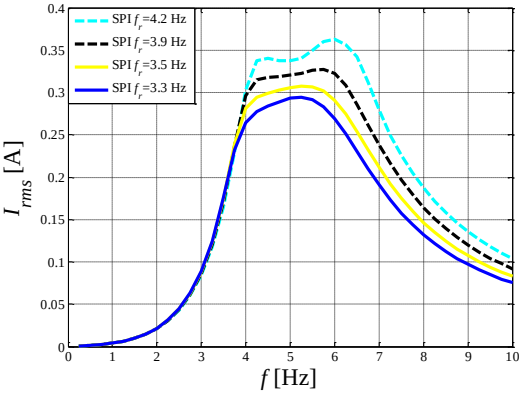

Fig. 26. Current vs frequency

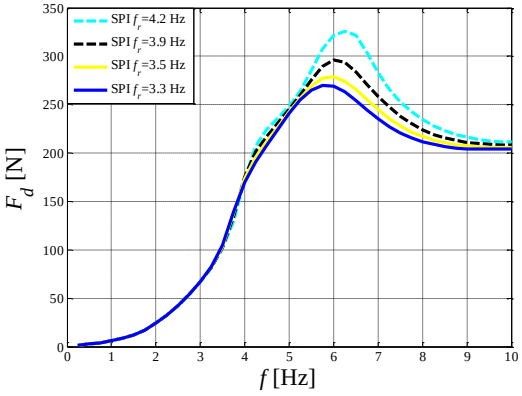

Fig. 27. Force vs frequency

It appears that the value of T_{xz} registered in the frequency range (6, 7.5) Hz is higher than in the system P when f_r=4.2 Hz. Compared to P and SP, the lowest values of T_{xz} in the investigated frequency range are registered in the system SPI, where the resonance frequency of the electric circuit is f_r=3.9 Hz.

4. SUMMARY

The study summarises the simulations of a model of a semi-active vibration reduction system comprising an MR damper, incorporating an electrical interface whose operating principle is based on voltage resonance. The interface, comprising the *R*, *L*, *C* elements, is connected between the generator coil and the MR damper control coil. The simulation procedure was performed to investigate the effect of the interface parameters on frequency characteristics of the vibration reduction system. The analysis of thus obtained frequency characteristics leads us to the following conclusions:

- the magnitude frequency response $|G_{ei}(j2\pi f)|$ reaches its maximal value at the resonance frequency of the equivalent circuit when the equivalent resistance becomes $R< 0.9\ \Omega$;
- simultaneous change of the parameters *L* and *C* allows the resonance frequency of the equivalent circuit to be tuned to resonance frequency of the vibration reduction system;
- the maximal value of the magnitude frequency response $|G_{ei}(j2\pi f)|$ at the resistance frequency is associated with the quality factor of the equivalent circuit;
- transmissibility in the system SP has lower values than in system P in the neighbourhood of resonance frequency whilst at frequencies in excess of resonance frequency its values are higher;
- in the system SPI the transmissibility values are lower when compared to P and SP in the entire frequency range;
- voltage resonance in the equivalent circuit gives rise to the anti-resonance effects in the vibration reduction system, revealed by the presence of minimum in the transmissibility vs frequency plot;
- the anti-resonance effect may occur at the same frequency at which the mechanical resonance will occur in the system P and SP.

The model of the electrical interface considered in the paper assumes linearity of *R*, *L*, *C* elements and does not take into account the influence of eddy currents. The problem of eddy currents which occur both in the magnetic circuit of the MR damper and the generator will be the subject of further authors' research.

REFERENCES

1. **Cho S. W., Jung H. J., Lee I. W.** (2005), Smart passive system based on a magnetorheological damper, *Smart Materials and Structures*, 14, 707-714.
2. **Cho S. W., Jung H. J., Lee I. W.** (2007a), Feasibility study of smart passive control system equipped with electromagnetic induction device, *Smart Materials and Structures*, 16, 2323-2329.
3. **Choi K. M., Jung H. J., Lee I. W., Cho S. W.** (2007b), Feasibility study of an MR damper-based smart passive control system employing an electromagnetic induction device, S*mart Materials and Structures*, 16, 2323¬–9.
4. **Choi Y. T., Werely N. M.** (2009), Self-powered magnetorheological dampers, *Journal of Vibration Acoustics*, 131, 44–50.

DOI 10.1515/ama-2016-0025

5. **Guo S., Yang S., Pan C.** (2006), Dynamic modeling of magnetorheological damper behaviors, *Journal of Intelligent Material Systems and Structures*, 17, 1, 3-14.
6. **Kwok N.M, Ha Q.P., Nguyen T.H., Li J., Samali B.** (2006), A novel hysteretic model for magnetorheological fluid dampers and parameter identification using particle swarm, *Sensors and Actuators A*, 132, 441-451.
7. **Rosół M., Sapiński B., Jastrzębski Ł.** (2010), Laboratory testing of signal conditioning systems in an electromagnetic generator to power-supply an MR damper, *Measurement, Automation, Monitoring*, 56(10), 1228-1233 (in Polish).
8. **Sapinski B.** (2008), An experimental electromagnetic induction device for a magnetorheological damper, *Journal of Theoretical and Applied Mechanics*, 46(4), 933-947.
9. **Sapiński B.** (2011), Experimental study of a self-powered and sensing MR-damper-based vibration control system, *Smart Materials and Structures*, 20, 105007.
10. **Sapiński B.** (2014), Energy-harvesting linear MR damper: prototyping and testing, *Smart material and Structures*, 23, 035021.
11. **Sapiński B., Jastrzębski Ł., Węgrzynowski M.** (2011), Modelling of a self-powered vibration reduction system, *Modelling in Engineering*, 10(41), 353-362 (in Polish).
12. **Sapiński B., Rosół M., Węgrzynowski M.** (2016), Evaluation of an energy harvesting mr damper-based vibration reduction systemstem, *Journal of Theoretical and Applied Mechanics*, 54(2), 333-344.
13. **Snamina J., Sapinski B.** (2011), Energy balance in self-powered MR damper-based vibration reduction system, *Bulletin of the Polish Academy of Sciences Technical Sciences*, 59(1), 75−80.
14. **Wang D. H., Bai X. X., Liao W H.** (2009), Principle, design and modeling of an integrated relative displacement magnetorheological damper based on electromagnetic induction, *Smart Materials and Structures*, 18, 095025.

This work is supported by AGH University of Science and Technology under research program No. 11.11.130.958.

DE GRUYTER
OPEN

DOI 10.1515/ama-2016-0026 acta mechanica et automatica, vol.10 no.3 (2016)

SELECTED ISSUES CONCERNING DEGRADATION OF MATERIAL IN THE PRODUCTION OF INJECTION MOLDED PLASTIC COMPONENTS

Marek JAŁBRZYKOWSKI*

*Faculty of Mechanical Engineering, Department of Materials Science and Biomedical Engineering, Bialystok University of Technology, ul. Wiejska 45C, 15-351 Białystok, Poland

m.jalbrzykowski@pb.edu.pl

received 14 July 2015, revised 14 July 2016, accepted 18 July 2016

Abstract: This paper presents the problem of thermal degradation of thermoplastic materials processed using the injection method. Attention was paid to the issue of the optimal selection of a dye for modifying the base materials. For the selected materials and dyes, derivatograph tests were performed in order to assess their thermal characteristics and breakdown kinetics. Additionally, tribological tests and microscope observations of selected samples were performed. The obtained test results suggest a diverse level of thermal processes in the analyzed materials. This is crucial for the appropriate selection of dyes for plastic materials. As it turned out, the tribological properties of materials can also influence the technological quality of the injected alloy.

Key words: Dyes For Plastic Materials, Thermal Degradation, Thermogravimetric Tests, Tribological Tests

1. INTRODUCTION

The problem of the functional quality of injection molded components is an everyday issue in all injection molding plants (Zawistowski and Zięba, 1999). The functional quality of the produced components shapes, among others, the level of effective productive work, the number of parts sold, or the amount of production scrap, both internal and external (Zawistowski and Zięba, 1999; Chun, 1999). It is a well-known fact that the functional quality mentioned above can depend on numerous factors, among which there are, for example, the processed material (Jałbrzykowski, 2012), the construction of the injection mold (Matin et al., 2012; Jałnrzykowski and Nachimowicz, 2009), or the parameters of the injection process (Zawistowski and Zięba, 1999; Chun, 1999; Chen et al., 2016; Wu and Chen, 2006) (Fig. 1). As far as the processed material is concerned, the following aspects can be mentioned, e.g. the problem of the quality of pellets, even those from the same batch; the problem of appropriate drying of material, or the problem of appropriate selection of dye and the homogeneity of components in the plasticizing system (Zawistowski and Zięba, 1999; Chun, 1999; Jałbrzykowski, 2012; Matin et al., 2012).

The data obtained from Bialystok's entrepreneurs, in addition to own experience, allow to conclude that problems concerning the quality of components in a stable process are a common occurrence, even if no quality problems have been noticed previously. To illustrate, the process has up to now been repeatable, the machine operation has been stable, and the tool underwent control twice during a production shift. The material was fed from the same batch, prepared for the process in the same way, i.e. the same temperature and drying time, on the same dryers; the same proportional content of dye, determined using agitators of the same type. Yet, despite all these precautions, quality problems of components suddenly appeared. It is probable that this situation is caused by the material, whose physical and chemical properties may not be completely uniform (even in a small volume of material). These differences, although slight, can influence the quality of the produced components. It is worth adding that in most cases these problems tended to disappear spontaneously after several minutes.

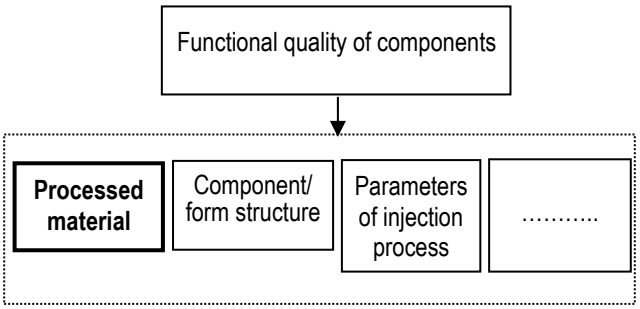

Fig. 1. Example factors influencing the functional quality of injection molded components

The issue of appropriate drying of material is obvious and no comments are in fact necessary. It can only be mentioned that the most common defect resulting from insufficient drying of material are the so-called 'silver streaks', as production nomenclature has it.

The author's interest was aroused particularly by the issue of dye selection (in the case of mixing the base material with a dye) and the homogenization of plastic. Basically, the issues concerning dye selection are connected with three aspects, i.e. the selection of a polymer matrix on the basis of which the dye is produced, the method for measuring the appropriate quantity of dye (gravimetric, volumetric, or manual, if necessary), and the homogenization of alloy in the plasticizing system. As industry practice shows, it is not enough to purchase a dye to modify

DOI 10.1515/ama-2016-0026

a specific material. This problem should be analyzed more thoroughly. It often happens that a dye purchased to modify material A was produced on the basis of material B. In such situations, manufacturers of thermoplastic components do not usually make mistakes concerning the compatibility of mixtures. However, the aspect of different ranges of processing temperatures, including the thermal degradation of the prepared ingredients, is often neglected. In extreme cases, this state may lead either to a lack of homogeneity of the plastic alloy (uneven coloring, smudges, non-plasticized pellets, etc.), or to local degradation of the mixture ingredients, despite the fact that a specific dye, dedicated specially to the modification of a specific material was used. As an example, Fig. 2 shows several samples with visible defects resulting from non-homogenous plasticizing of an alloy.

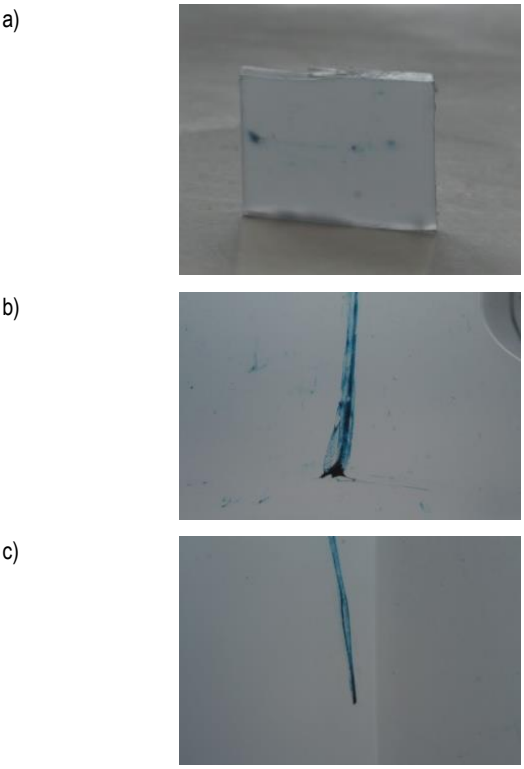

Fig. 2. Examples of defects of components (macrographic): a) section of a component b) and c) clearly visible dye smudges in the wall of the component

The issues mentioned above prompted the author to undertake a deeper analysis of situations typically encountered in the industry in the course of the production process. The aim of this paper was to assess the technological quality of selected samples made from plastic (PM- plastic materials) in the area of their thermal and tribological properties (Brachet et al., 2008; Torres et al., 2000; Badia et al., 2009; Navarro et al., 2003; Al-Salem et al., 2010).

It should be emphasized once again that the subject matter described above is still present to a smaller or greater extent in every injection moulding plant and thus is currently very much an issue of relevance (www2.dupont.com, http://www.plastech.pl, http://www.wadim.com.pl, https://www.elsevier.com, Botos et al., 2014; Bucella et al., 2015; Laurence and McKeen, 2007; Kayvon, 2015). The types of machines and raw material used, or the method of process realization is of no importance here. It can also be added that the influence of dye becomes visible not only during visual assessment, but is also reflected in other characteristics of injected parts. A common problem is, for example, cracking of mouldings despite the optimized technological process. This problem is a deeper issue that requires, above all, an in-depth analysis of mechanisms of the described phenomena. As traditional technological actions do not yield sufficient effects, a scientific explanation and solution to the described problems needs to be sought. These issues will be dealt with and analyzed if further papers. In this light, the issue becomes extremely significant. As one of the most important ones, it is the subject of studies by, among many others: DuPont (www2.dupont.com), Plastech (http://www.plastech.pl), Wadim Plast (http://www.wadim.com.pl). This subject matter has also been indicated on websites containing scientific studies (https://www.elsevier.com); however, explanation of the causes of the described phenomena is highly insufficient.

2. MATERIALS AND METHODOLOGY OF RESEARCH

2.1. Materials used for the tests

For the tests, PM samples were received in the form of pellets, directly from the production line of one of Bialystok's companies. These were four samples of materials: the base material (polycarbonate) and three kinds of dye. Respecting the company's secrets, the data concerning the materials was coded in the following way: base material – PC, dyes: blue – B, green – G, orange – O (Fig. 3). The breakdown temperature of the basic material and the dyes was adopted as the main indicator of the technological quality of the received PM's. Additionally, tests of the tribological properties of the received PM samples were performed.

The impetus to perform the tests presented in this paper were the constant problems to obtain an appropriate visual quality of the components made from PC dyed with the additives mentioned earlier.

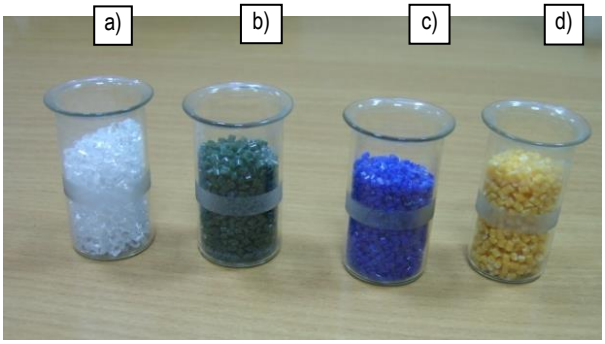

Fig. 3. Samples of materials received for the tests: a) PC, b) dye G, c) dye B, d) dye O

2.2. Methodology of tests

The aim of this paper was to assess the breakdown temperatures of the received PM's, focusing especially on the possibility of their earlier degradation. 'Earlier degradation' is understood here as breakdown of PM during the normal process of its processing (at parameters stemming from the technological process). Owing to the current, 'severe' norms of quality control, a premature ther-

DOI 10.1515/ama-2016-0026

mal breakdown of the processed materials disqualifies the produced components, e.g. in the area of visual quality, resulting in producing scrap. In order to solve this problem, thermogravimetric tests were performed as the basic tests. Supplementary to the basic tests, tribological tests whose purpose was to estimate the resistance to motion for the PM-steel system were performed. Increased values of resistance to motion can lead to the appearance of localized high temperature jumps, especially during the plasticizing process (in the slug-cylinder system), which can further intensify the process of PM breakdown. It should be mentioned that the problems connected with the visual quality of the produced components may arise due to the range of dye processing temperatures being to low in comparison with the base material.

The tests in the area of thermal properties were performed using a Paulik-Paulik-Erdey type derivatograph (Fig.4).

Fig. 4. View of the Paulik-Paulik-Erdey type apparatus (derivatograph) for thermogravimetric tests

Prior to the thermogravimetric tests, identical aliquots of materials weighing m = 250 mg were prepared. The derivatograph tests were performed at a constant velocity of heating v_t= 5 °C/min, until the maximum temperature of T = 500 °C was achieved. The parameters adopted for the tests were based, in the case of the velocity of heating, on literature data as well as standard recommendations. In the case of the maximum temperature of heating, real parameters of the injection process were used as guidelines, also taking into account the generally high temperature resistance of polycarbonate.

The subsequent analysis of the results of derivatograph tests prompted to perform additional tests, i.e. of thermal annealing in a constant temperature. These test were performed in temperatures of T_1= 280 and T_2= 300 °C. In the case of the first test, the material was annealed for t= 60 min, while the second test was being carried out for t= 30 min. The range of temperatures was adopted on the basis of the data concerning the recommended temperatures for the processing of the received PC, provided by the contractor. The time of annealing was meant to simulate the time period when the material stays in the cylinder of the injection molding machine during its down time. The aim of these tests was to check whether the time of annealing of the material in an increased temperature (even if the temperature did not exceed the breakdown temperature) has an influence on the degradation of material. The tests were performed using a furnace (Fig. 5). Prior to the tests, the furnace was annealed for 2 h, in order to achieve a stable temperature. After the temperature had stabilized, samples of materials were placed in the furnace chamber (Fig. 6).

a) b)

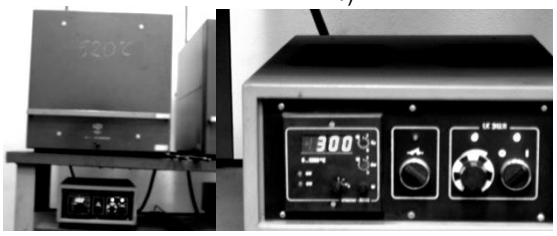

Fig. 5. The hardening furnace used for annealing tests: a) general view, b) view of the control system

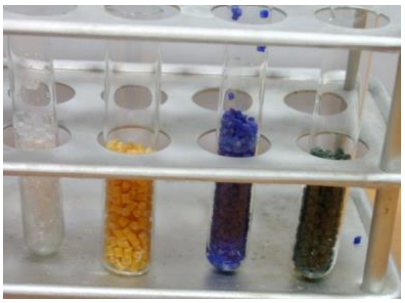

Fig. 6. An example of preparation of TS samples for the annealing tests

It should be added that before commencing the thermal tests and the tests of thermal annealing, the PM samples underwent conditioning in normal conditions for a time period of 24 h.

After the thermogravimetric tests and the annealing tests, additional tests of the tribological properties of the received materials were performed. The tribological tests were performed using a pin-on-disc tester (Fig. 7). Samples prepared for the purpose of the tests were in the form of ϕ 1.5 x 2 mm pins.

a)

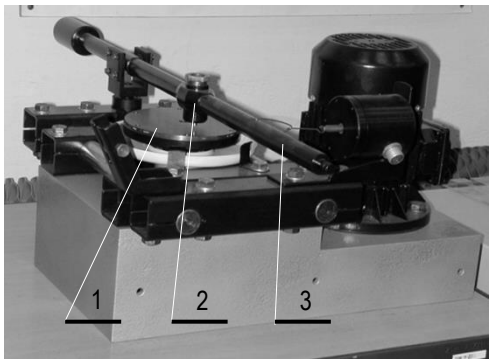

b)

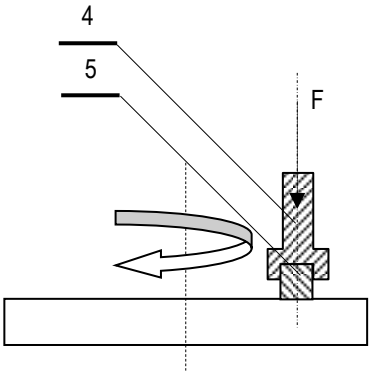

Fig. 7. Pin-on-disc tribometer: a) general view, b) scheme of the friction node; 1 – disc, 2 – pin handle, 3 – loading arm, 4 – pin fixing the sample, 5 – material sample

DOI 10.1515/ama-2016-0026

Friction tests were performed at the following constant test parameters:

- load F= 160 N,
- maximum friction time t= 3 min or until sample destruction,
- sliding velocity v_p= 0,15 m/s.

3. TEST RESULTS

The results of the thermogravimetric tests were based on the analysis of the derivatograms. Fig. 8. presents a section of an example derivatogram for PC. The derivatogram shows the mass-change curve – TG, the temperature-change curve T, the temperature-change differential curve DTA, and the mass-change differential curve – DTG. On the basis of the analysis of the functions, conclusions concerning the breakdown of chemical compounds contained in the samples that underwent the thermogravimetric analysis can be formulated. Analyzing the derivatogram for PC shown in fig. 6., it was concluded that its transition from the vitreous state to the high elasticity state occurs in a temperature of approx. 185 °C. Then, its slow gradual plasticizing can be observed. The onset of breakdown for this material occurs in a temperature of approx. 410 °C; in 420 °C the breakdown is already evident; while in a temperature of 450 °C, the breakdown process is at its most intense.

The derivatograms for the dye samples were analysed in a similar manner. It should be added that the tested dyes broke down in stages; however, due to the lack of data in the area of their chemical composition (manufacturer's secret), referenced were only the readings of temperatures corresponding to the first signs indicating the onset of breakdown of a complex chemical compound. Despite the fact that the curves were recorded in their entirety, as the chemical composition of the tested substance is not known, an in-depth, material analysis of the derivatograms is not possible. It is possible, though, to read the temperatures indicated by the DTA and DTG curves for the first signs indicating the first mass decrement and a change connected with the breakdown of material. Below, in table 1, the read characteristic temperatures for all the tested materials are summarized. It should be added that, as is commonly known, all plastics can be divided, on the basis of their structure and the physical and chemical properties, into amorphous and semicrystalline. The data provided by the contractor indicates that the received dyes were produced on the basis of polystyrene. This means that there are basically two kinds of materials being dealt with here, i.e. polycarbonate (PC), in the case of the base material, and polystyrene (PS), in the case of the dyes. In this context, it needs to be added that both materials belong to the group of amorphous materials, whose characteristic feature is that in the course of their cooling, from the plasticized to the solid state, their viscosity rapidly increases, making it difficult for the nuclei of crystallization to form and grow. This causes the lack of evident crystallization during the cooling of this type of materials, and the transition from the plasticized to the solid state is called the glass-transition point (temperature). Another name for materials of this type are 'supercooled liquids'. At the same time, during the heating of this type of materials, there is no transition through the melting point – only a transition into the state of high elasticity and the subsequent slow plasticizing**.**Regarding the data shown in table 1, it can be stated that a significant difference in the determined values of temperature between the base material and the dyes was noticed. Considering the temperature of the onset of breakdown in the case of PC and dyes G and B, the difference is approx. 100 °C, whereas in the case of PC and dye O, approx. 150 °C. It can be stated that this proves the generally high temperature resistance of PC and dyes G and B. Only in the case of dye O was a lower temperature of the onset of breakdown obtained. An important aspect, which may arouse suspicions as to the matrix of the medium of the dye, is the considerable difference between the temperature of the onset of breakdown for dye O and G and B dyes. This may mean that either other additives were used in the production process of this dye (O), which modified its general thermal properties, or that another base was used. It should be noted here that according to the technological data, the tested dyes should be characterized by thermal stability up to approx. 300 °C.

Tab 1. The read values of characteristic temperature points

Sample marking	Glass-transition temperature T_z [°C]	Temperature of the onset of breakdown [°C]
PC	175 – 185	410 - 420
O	Reading failed	255 - 260
G	75 - 85	305 –310
B	70 - 80	315 - 320

Considering, however, the value of the processing temperature of this type of PC (280 – 300 °C), then in relation to the temperature of breakdown of the dyes, the obtained values may indicate an insufficiently low margin of temperature. As is commonly known, during the plasticization process, the friction occurring between the molecules of the material, the slug and the cylinder walls leads to local high-temperature jumps, of even up to tens of degrees, which can lead to degradation of polymer structures. Assuming, thus, that the temperature on the individual cylinder and hot-channel zones (in the mold) reaches 300 °C, then during plasticizing and injection it can locally rise by tens of degrees. The result of this fact is that all the assessed dyes exceed their thermal stability. This, on the other hand, may manifest itself by the dye being charred. This means that presence of black charred inclusions, which are the result of insufficient thermal stability of dyes, in the manufactured components during injection, is possible. Keeping in mind that dyes are usually mineral compounds of metal oxides with an exceptionally high temperature resistance (e.g. titanium white TiO_2: melting point 1850 °C, boiling point 2500 °C), it can be suspected that (in this particular case) the problem is connected with the medium. In other words, it can be supposed that the issue of visual and technological quality of PC-made components dyed with a PS-based additive is most probably related to the polystyrene medium – for the particular case.

DOI 10.1515/ama-2016-0026

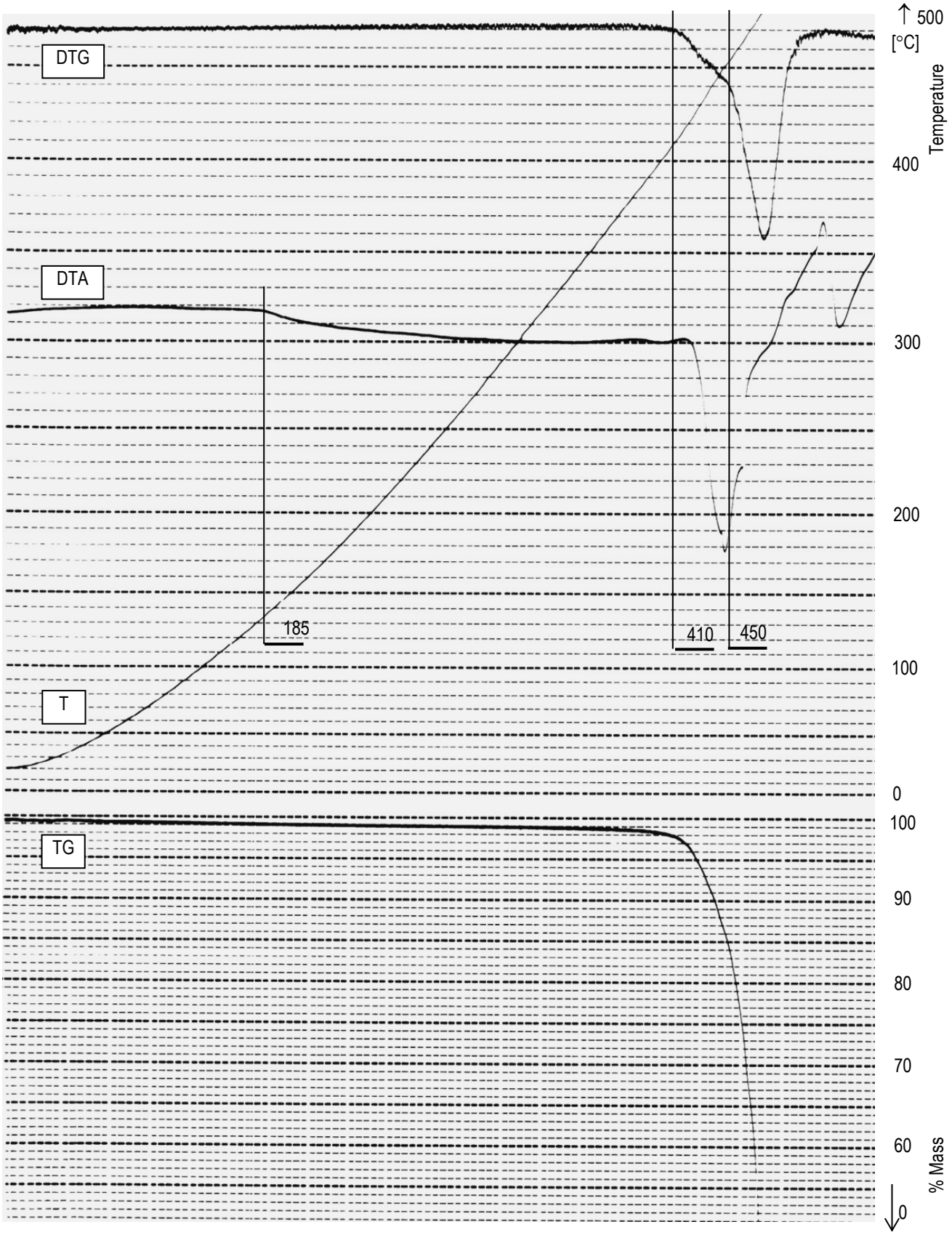

Fig. 8. An example derivatogram: TG- mass-change curve, T- temperature-rise curve, DTA- temperature-change differential curve, DTG- mass-change differential curve

Marek Jałbrzykowski
DOI 10.1515/ama-2016-0026

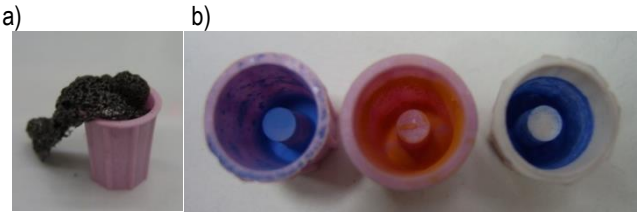

Fig. 9. View of the crucibles after derivatograph tests, remnants of: a) PC, b) B, c) O, d) G

The high temperature resistance of the pigments was confirmed in a general examination of the crucibles after the derivatograph tests. Fig. 9 shows photos of these crucibles.

As can be seen in the presented photos, PC was charred, but the maximum temperature in the derivatograph furnace (500 °C) was too high considering its temperature resistance, on the one hand; and too low to burn all the organics, on the other. This resulted in the appearance of a charred mass (Fig. 9a). In the case of the dyes, it turned out that the breakdown of these materials unfolded in such a way that no charred remnants of the process of their combustion were noticed. The matrix in which the color pigment was distributed had been burnt out earlier, due to its lower temperature resistance.

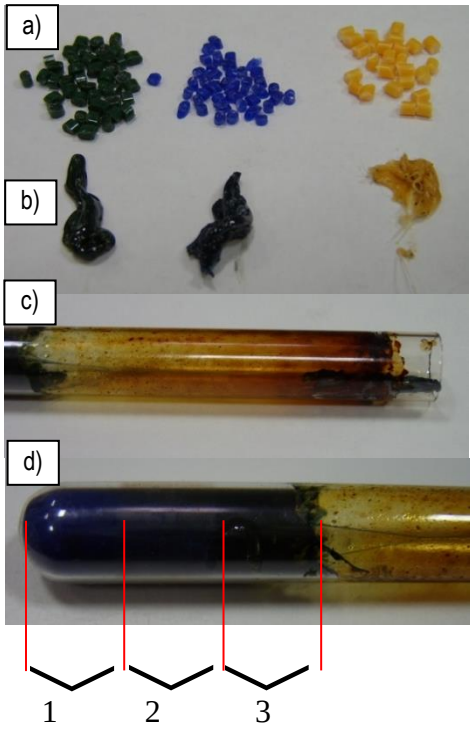

Fig. 10. Example photos of samples after the tests of thermal annealing (300 [°C], t = 30 [min]): a) dye samples before the test, b) dye samples after annealing, c) view of the charred mass (B), d) view of dye B after annealing tests; 1- the area of pigment debris, 2- intermediate zone, 3- charred medium zone

Referring back to the earlier statements concerning a faster burning of the medium used for the preparation of dyes, the following section of the research consists of tests of temperature resistance (thermal annealing) in lower temperatures (than those indicated by the temperatures of breakdown of the samples), but with the assumption that the material stays in the cylinder for a longer period of time. This state enables to simulate machine down time for the duration of, for example, short repair work. The tests in question were performed in a temperature of 280 °C for 60 min, and in a temperature of 300 °C for 30 min. Below, in fig. 10, are presented selected photos of dye samples after these tests.

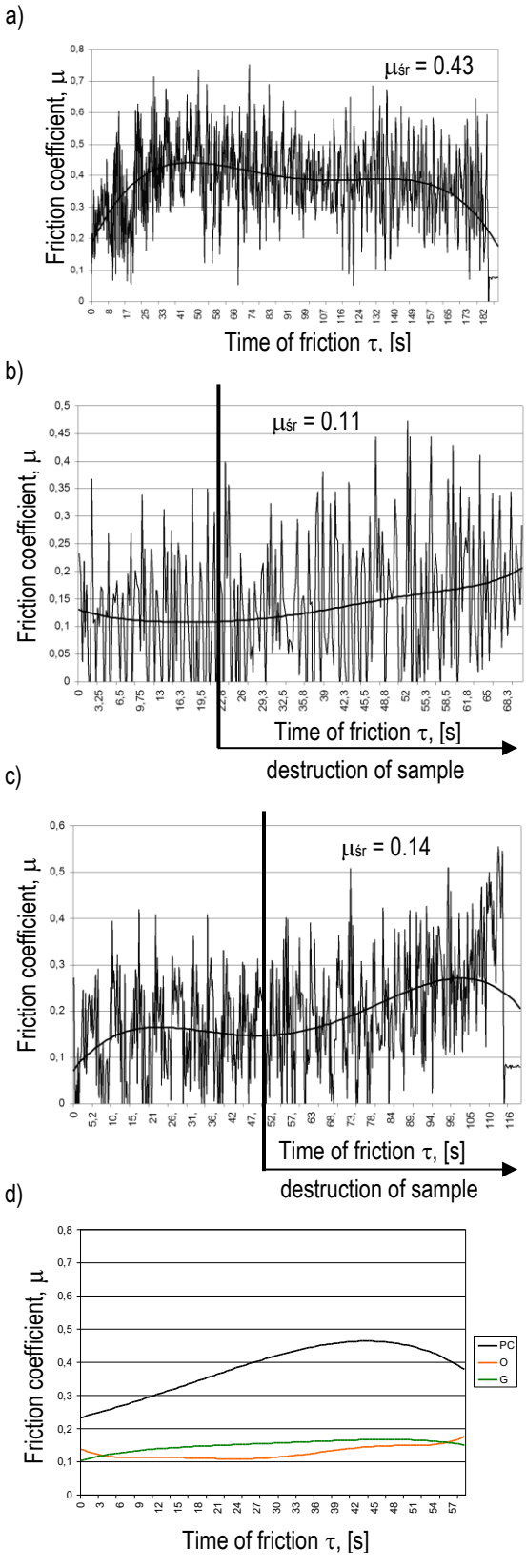

Fig. 11. Results of the tribological tests: a) for pure PC, b) for dye O, c) for dye G, d) summary graph

DOI 10.1515/ama-2016-0026

Figs. 10 a and b show samples of the dyes before the test (Fig. 10a) and after the annealing tests (fig. 10b). The presented photos show that a 'good form' was retained only by dye O, notwithstanding that this is completely unconfirmed when considering the temperature of the onset of breakdown (255 – 260 °C). In the case of dyes B and G, it can be seen that the brightness of their color, especially in the case of dye B, was affected by products of degradation. The traces of combustion of the dye medium shown in Fig. 10 c and d are even more visible. Fig. 10 c shows the walls of the test tube in which dye B was annealed. It can clearly be seen that the temperature of 300 °C and the time of annealing significantly influence the destruction of this additive. It can be added that in the case of dye B, after the annealing tests, phase borders between individual colored layers could be noticed in the test tube. The layer marked as 3 was a layer of charred material; the one marked as 1, a layer of intact dye; 2 – the layer isolated between the charred and the intact material.

There can obviously be objections concerning the conditions of the performed test; however, as mentioned earlier, friction between the molecules of the plasticized material; and between the walls of the cylinder, the slug and the material may locally lead to very high temperature jumps. With relation to this, Fig. 11 below shows the results of friction tests.

The results of these tests indicate lower values of the coefficient of friction for the dyes in comparison with PC. This means that in the conditions of the performed test, the dyes shear more easily, not causing a strong resistance to motion-related disturbance. In other words, it can be said that PC is a resistant material, not easily susceptible to shear stresses, which introduces additional disturbances (temperature rise) during the plasticization process. Keeping in mind that the value of the coefficient of friction for PC is approx. twice higher than for the dyes, a conclusion can surely be drawn that this fact is of considerable importance as far as friction heat, generated during the plasticization process, is concerned. This fact can be highly important concerning the visual quality of the manufactured components, due to the possibility of appearance of charred molecules of dye in their structure.

Describing the graphs shown in Fig. 11, it should be pointed out that in the case of PC, resistance to abrasive wear was high enough to enable to collect the test results throughout the entire duration of the performed experiment. In the case of the dyes, on the other hand (Fig. 11b and 11c), before the end of the experiment, a complete destruction of the sample collected for the tests was observed. This confirmed the low tribological resistance and easy shear of the tested dyes.

4. CONCLUSIONS

The tests carried out for the purpose of this paper and their analysis allowed to formulate the following general conclusions:

1. Lower temperatures of the onset of breakdown of the dyes in comparison with the base material were observed. It should be noted here that dye O was characterized by the lowest temperature that signified the onset of breakdown.
2. Keeping in mind the differences in the temperatures of breakdown for dyes O, G and B, it can be suspected that they were produced on different media, or the observed differences indicate dissimilarities in chemical composition between these dyes, which had a significant impact on the obtained results.
3. Keeping in mind the recommended processing temperatures of this type of PC (280 – 300 °C) and the possibility of rapid local temperature jumps during the plasticizing and injection, it is considered that the obtained levels of temperatures of breakdown for PC (410 °C) and dyes G and B (305 and 315 °C) are too low (small margin of temperature). The aforementioned local rise of temperature can cause a temperature rise by as much as tens of degrees in micro-areas of the plasticized alloy. This, in turn, may have an influence on local degradation of a, broadly understood, dye and determine the technological usability of components produced from this type of alloy. It should also be remembered that the temperature of breakdown for dye O was even lower (255 °C).
4. The performed tests of annealing in a constant temperature confirmed the misgivings (related to the dyes) concerning the kinetics of chemical reactions in the area of thermal resistance. It turned out that despite the fact that the obtained temperatures of breakdown were as high as over 300 °C, the analyzed additives broke down in lower temperatures in the case of a prolonged action of temperature. It should be noted here that the time of annealing of the dyes was 30 min. This fact may be of importance in the case of machine down time and manifest itself in the form of degradation of dyes in conditions of normal injection molding processing. It is obvious that these kinds of problems can be overcome by repeatedly injecting 'fresh material' through the cylinder. There are areas of the injection space, however, where the flow of material may be limited, and this is where the charred remnants of dyes are likely to dwell.
5. The tribological tests of the analyzed materials proved that their friction characteristics can influence temperature rise during, for example, the plasticization process. It turned out that the results of friction tests indicate twice higher values of the coefficient of friction for PC in comparison with the dyes, which has a direct impact on the increase of alloy temperature and energy losses during the plasticization of PC.
6. Summarizing all the observations, it should be emphasized that when selecting dyes for the production of injection molded TS's, the compatibility of the dye and the polymer matrix should not be the sole factor taken under consideration. The thermal properties of the composition ingredients (range of processing temperatures and thermal breakdown) should also be scrutinized, as should, in special cases, other potentially relevant properties, e.g. the tribological properties of the ingredients. Production down time, which in many cases cannot be avoided, is also not without its relevance, as despite the sufficiently high processing temperatures, it can lead to degradation of material due to a prolonged action of high temperatures in the cylinder zones.

REFERENCES

1. **Al-Salem SM, Lettieri P, Baeyens J.** (2010), Recycling and recovery routes of plastic solid waste (PSW): A review, *Waste Management*, 29, 2625-2643.
2. **Badia J.D., Francisco V., Sigbritt K., Ribes-Greus A.** (2009), Thermal analysis as a quality tool for assessing the influence of thermo-mechanical degradation on recycled poly(ethylene terephthalate), P*olymer Testing*, 28(2), 169–175.

DOI 10.1515/ama-2016-0026

3. **Botos J., Murail N., Heidemeyer P., Kretschmer K., Ulmer B., Zentgraf T., Bastian M., Hochrein T.** (2014), Color Measurement of Plastics - from Compounding via Pelletizing, up to Injection Molding and Extrusion, *Proceedings of PPS-29: The 29th International Conference of The Polymer - Conference Papers, Book Series: AIP Conference Proceedings*, V. 1593, 16-19.
4. **Brachet P., Hoydal L.T., Hinrichsen E.L., Melum F.** (2008), Modification of mechanical properties of recycled polypropylene from post-consumer containers, *Waste Management*, 28(12), 2456–2464.
5. **Buccella M., Dorigato A., Crugnola F., Caldara M., Fambri L.** (2015), Coloration Properties and Chemo-Rheological Characterization of a Dioxazine Pigment-Based Monodispersed Masterbatch, *Journal Of Applied Polymer Science*, 132(7), Article Number, 41452.
6. **Chen W.-C., Nguyen M.-H., Chiu W.-H., Chen, T.-N., Tai, P.-H.** (2016), Optimization of the plastic injection molding process using the Taguchi method, RSM, and hybrid GA-PSO, *International Journal of Advanced Manufacturing Technology*, 83(9-12), 1873-1886.
7. **Chun DH.** (1999), Cavity filling analyses of injection molding simulation: bubble and weld line formation**,** *Journal of Materials Processing Technology*, 90, 177-181.
8. **Jałbrzykowski M.** (2012), Influence of Regranulate Content on the Functional Properties of Parts Made from Thermoplastic Materials, *Mach. Dyn. Res.*, 36(1), 82-89.
9. **Jałbrzykowski M., Nachimowicz J.** (2009), The problems of reliability and durability of tools for the injection of plastic materials, *Acta Mechanica et Automatica*, 3(1), 49-53.
10. **Kayvon M.**(2014), *Sina Ebnesajjad and all: Handbook of Polymer Applications in Medicine and Medical Devices*, William Andrew Inc., Elsevier, Oxford.
11. **Laurence W. McKeen** (2007), *Effect of Temperature and other Factors on Plastics and Elastomers*, William Andrew Inc., Elsevier, NY.
12. **Matin I, Hadzistevic M, Hodolic J, Vukelic D, Lukic D** (2012): A CAD/CAE-integrated injection mold design system for plastic products, *International Journal Of Advanced Manufacturing Technology*, 63(5-8), 595-607.
13. **Navarro R., Torre L., Kenny J.M., Jiménez A.** (2003), Thermal degradation of recycled polypropylene toughened with elastomers, *Polymer Degradation and Stability*, 82(2), 279–290.
14. **Torres N., Robin J.J., Boutevin B.** (2000), Study of thermal and mechanical properties of virgin and recycled poly(ethylene terephthalate) before and after injection molding, *European Polymer Journal*, 36(10), 2075–2080.
15. **Wu C.-H., Chen W.-S.** (2006), Injection molding and injection compression molding of three-beam grating of DVD pickup lens, Sensors and Actuators, *Physical,* 125 (2), 367-375.
16. **Zawistowski H., Zięba Sz.** (1999), *Set the injection process*, Plastech, Warsaw.
17. http://www.plastech.pl/pub/downloads/zytel-poradnik-przetworstwa-tworzywa-poliamidowe-dupont.pdf
18. http://www.wadim.com.pl/pl/a/Wady-wyprasek-Srodki-zaradcze-cz-1
19. https://www.elsevier.com/__data/assets/pdf_file/0011/91649/Plastics-Used-in-Medical-Devices_link.pdf
20. www2.dupont.com/Poland_Country_Site/pl_PL/.../10_zasad.html

This research was realized from statutory activity S/WM/1/14 and financed by MSHE.

DE GRUYTER
OPEN

DOI 10.1515/ama-2016-0027 acta mechanica et automatica, vol.10 no.3 (2016)

THE MATHEMATICAL MODELING AND INVESTIGATION OF THE STRESS-STRAIN STATE OF THE THREE-LAYER THERMOSENSITIVE HOLLOW CYLINDER

Iryna RAKOCHA[*], Vasyl POPOVYCH[**]

[*]Lviv Polytechnic National University, 12 Bandera street, Lviv, Ukraine
[**]Pidstryhach Institute for Applied Problems of Mechanics and Mathematics of NASU, 3-b Naukova street, Lviv, Ukraine

irinka.rakocha@gmail.com, dept19@iapmm.lviv.ua

received 9 July 2015, revised 14 July 2016, accepted 18 July 2016

Abstract: Stationary temperature distribution in a three-layer infinite hollow cylinder based on the thermosensitive body model was determined. The cylinder is subjected to the steady temperature on the inner surface and on the outer one is present the convective heat exchange. In the second layer exist heat sources with parabolic dependence on radial coordinate. The components of the thermostressed state have been found. The influence of the temperature dependence of the thermal and mechanical components characteristics of materials on the temperature distribution has been investigated.

Key words: Three-Layered Cylinder, Thermosensitive Material, Temperature, Thermostressed State

1. INTRODUCTION

Knowledge of the components of the thermostressed state of structural elements, including hollow cylinders (Aziz, 2013; Argeso and Eraslan, 2008, Bazarenko, 2008; Fazelli et al., 2013; Shi et al., 2007; Zhu, 2002), subjected to given power and thermal loads underlie calculation on durability and reliability. The appropriate definition of temperature field and caused by it stress-strain state is based on the model of the thermosensitive body (Kushnir and Popovych, 2009; 2011), which takes into account the dependence of thermal and mechanical characteristics and parameters of heat exchange (heat transfer coefficients, degrees of surface blackness) on temperature are performed according to their application under condition of high-temperature heating.

The detailed review of studies relating to the definition of thermostressed state of thermosensitive bodies from the beginning of the investigation of the problem to its current state was provided in articles (Kushnir and Popovych, 2009; Noda, 1991). Papers (Carslaw and Jaeger, 1996; Goto and Suzuki, 1996; Grzes, 2010; Kushnir and Popovych, 2009; 2011; Kushnir and Protsiuk, 2010; Lee, 1998; Noda, 1991; Och, 2014; 2015; Popovych and Kalynyak, 2014; Shariyat, 2007, Shen, 2001; Tanigava and Akai, 1996; Yevtushenko and Kuciej, 2014; Zhu and Chao, 2002) represent mathematical models of thermostressed multilayer structures, which take into account the dependence of thermomechanical characteristics of the layer materials on the temperature as well as the new methods of their solution. In papers (Carslaw and Jaeger, 1996; Kushnir and Popovych, 2009; 2011; Kushnir and Protsiuk, 2010; Noda, 1991; Och, 2014; 2015; Popovych and Kalynyak, 2014; Zhu and Chao, 2002) the importance to take into account the thermosensitivity of structural components at investigation the temperature and stress distribution is indicated.

In the article the stationary temperature distribution in elements of microelectronics, which are modeled by three-layer hollow thermosensitive cylinder with heat sources in second layer, constant temperature on the inner surface of the cylinder and convective heat exchange with the environment on the outer one, is determined. The components of the stress-stain state have been defined. The influence of the thermosensitivity of materials on the temperature distribution and the distribution of the components of stress-strain state has been investigated.

2. THE FORMULATION OF THE PROBLEM

The three-layer infinite thermosensitive hollow cylinder is considered. Each layer was made of different material. The cylinder is heated by heat sources which are located in the middle layer and are distributed by parabolic law

$$W^{(2)}(r) = -\frac{4W_0^{(2)}}{(r_3 - r_2)^2}(r - r_2)(r - r_3).$$

The temperature is constant $\mathrm{t} = \mathrm{t}_{\mathrm{in}}$ on inner surface $\mathrm{r} = \mathrm{r}_1$ and the convective heat exchange with the environment on outer one $\mathrm{r} = \mathrm{r}_4$ is present. The coefficient of heat transfer through this surface is constant and equal to α. The conditions of ideal thermal contact between neighbour layers are satisfied. Let us determine the temperature distribution and the distribution of components of the cylinder stress-strain state at mentioned conditions.

3. THE MATHEMATICAL MODEL FOR THE DETERMINATION OF TEMPERATURE DISTRIBUTION

It includes:

– the heat conductivity equations for each layer

DOI 10.1515/ama-2016-0027

$$\frac{1}{r}\frac{d}{dr}\left(r\lambda_t^{(i)}(t_i)\frac{dt_i}{dr}\right) = W^{(i)}(r), r_i < r < r_{i+1}, i = \overline{1,3}, \quad (1)$$

– boundary conditions on the boundary surfaces

$$t_1|_{r=r_1} = t_{in}, \qquad \left[\lambda_t^{(3)}(t_3)\frac{dt_3}{dr} + \alpha(t_3 - t_{out})\right]_{r=r_4} = 0, \quad (2)$$

– contact conditions on the neighbouring surfaces of the cylinder

$$t_1|_{r=r_2} = t_2|_{r=r_2}, \qquad t_2|_{r=r_3} = t_3|_{r=r_3}, \quad (3)$$

$$\begin{aligned}\lambda_t^{(1)}(t_1)\frac{dt_1}{dr}\Big|_{r=r_2} &= \lambda_t^{(2)}(t_2)\frac{dt_2}{dr}\Big|_{r=r_2},\\ \lambda_t^{(2)}(t_2)\frac{dt_2}{dr}\Big|_{r=r_3} &= \lambda_t^{(3)}(t_3)\frac{dt_3}{dr}\Big|_{r=r_3}.\end{aligned} \quad (4)$$

Model (1)-(4) is nonlinear due to the dependence of thermal conductivity coefficients $\lambda_t^{(i)}(t_i)$ $(i = \overline{1,3})$ on temperature. Those dependencies are usually given in reference books and are represented in the form of tables.

To conduct theoretic reserch work it is convenient to present the thermal conductivity coefficients as analytical expression $\lambda_t^{(i)} = \lambda_t^{(i)}(t_i)$ with the purpose to conduct theoretic research work. To achieve such dependencies the tabular function is approximated with some functional dependence. The least squares method is an example of possible technique to be used with such approximation in order to determine the unknown parameters.

Let the thermal conductivity coefficients for each cylinder component to be in the temperature range $[t_b; t_e]$. We are going to describe them with quite common linear dependencies $\lambda_t^{(i)} = a_i t_i + b_i$. Parameters a_i and b_i are unknown. According to the method of least squares they are selected so that the sum of the differences' squares between experimental and theoretical values will bw minimal.

Let us represent the thermal conductivity coefficients of cylinder layers in the form $\lambda_t^{(i)}(t_i) = \lambda_{t0}^{(i)}\lambda_t^{(i)*}(T_i)$, where the values $\lambda_{t0}^{(i)}$ have the dimensionality of thermal conductivity coefficient and $\lambda_t^{(i)*}(T_i)$ is dimensionless function of dimensionless temperature $T_i = t_i/t_e$, (where the temperature t_e is chosen as a measuring indicator). Due to such linear dependence of the thermal conductivity coefficient on the temperature such representations will have the following form

$$\lambda_t^{(i)}(t_i) = \lambda_{t0}^{(i)}\left(1 + k_i(T_i - T_b)\right), \quad (5)$$

where $T_b = t_b/t_e$, $k_i = a_i t_e/(a_i t_b + b_i)$, a $\lambda_{t0}^{(i)} = a_i t_b + b_i$.

Let us introduce the characteristic length value l_0 and dimensionless coordinate $\rho = r/l_0$ to present the mathematical model (1)-(4) in dimensionless form:

$$\frac{d}{d\rho}\left(\rho\lambda_t^{(i)*}(T_i)\frac{dT_i}{d\rho}\right) = W^{(i)}(\rho), \rho_i < \rho < \rho_{i+1}, i = \overline{1,3}, \quad (6)$$

$$T_1|_{\rho=\rho_1} = T_{in}, \left[\lambda_t^{(3)*}(T_3)\frac{dT_3}{d\rho} + Bi(T_3 - T_{out})\right]_{\rho=\rho_4} = 0, \quad (7)$$

$$T_1|_{\rho=\rho_2} = T_2|_{\rho=\rho_2}, \qquad T_2|_{\rho=\rho_3} = T_3|_{\rho=\rho_3}, \quad (8)$$

$$\begin{aligned}\lambda_t^{(1)*}(T_1)\frac{dT_1}{d\rho}\Big|_{\rho=\rho_2} &= K_\lambda^{(2)}\lambda_t^{(2)*}(T_2)\frac{dT_2}{d\rho}\Big|_{\rho=\rho_2},\\ \lambda_t^{(2)*}(T_2)\frac{dT_2}{d\rho}\Big|_{\rho=\rho_3} &= K_\lambda^{(3)}\lambda_t^{(3)}(T_3)\frac{dT_3}{d\rho}\Big|_{\rho=\rho_3}.\end{aligned} \quad (9)$$

where: $T_{in} = t_{in}/t_e$, $T_{out} = t_{out}/t_e$, $K_\lambda^{(j)} = \lambda_{t0}^{(j)}/\lambda_{t0}^{(j-1)}$ $(j = 2,3)$, $W^{(1)}(\rho) = W^{(3)}(\rho) = 0$, $W^{(2)}(\rho) = -\frac{4\cdot Po}{(\rho_3-\rho_2)^2}\rho(\rho - \rho_2)(\rho - \rho_3)$, $Po = W_0^{(2)}l_0^2/(\lambda_{t0}^{(2)}t_e)$ is the Pomerantsev number, $Bi = \alpha l_0/\lambda_{t0}^{(3)}$ is the Biot number.

4. THE CONSTRUCTION OF THE SOLUTION OF THE MATHEMATICAL MODEL

To construct the solution of the problem (6)-(9) the Kirchhoff variables are introduced:

$$\theta_i = \int_{T_b}^{T_i}\lambda_t^{(i)*}(T_i)dT_i, \qquad i = \overline{1,3}. \quad (10)$$

The following problem relative to mentioned above variables was received

$$\frac{d}{d\rho}\left(\rho\frac{d\theta_i}{d\rho}\right) = W^{(i)}(\rho), \rho_i < \rho < \rho_{i+1}, i = \overline{1,3}, \quad (11)$$

$$\theta_1|_{\rho=\rho_1} = \theta_{in}, \left[\frac{d\theta_3}{dr} + Bi(T_3(\theta_3) - T_{out})\right]_{\rho=\rho_4} = 0, \quad (12)$$

$$T_1(\theta_1)|_{\rho=\rho_2} = T_2(\theta_2)|_{\rho=\rho_2}, T_2(\theta_2)|_{\rho=\rho_3} = T_3(\theta_3)|_{\rho=\rho_3}, \quad (13)$$

$$\frac{d\theta_1}{d\rho}\Big|_{\rho=\rho_2} = K_\lambda^{(2)}\frac{d\theta_2}{d\rho}\Big|_{\rho=\rho_2}, \frac{d\theta_2}{d\rho}\Big|_{\rho=\rho_3} = K_\lambda^{(3)}\frac{d\theta_3}{d\rho}\Big|_{\rho=\rho_3}, \quad (14)$$

where:

$$\theta_{in} = \int_{T_b}^{T_{in}}\lambda_t^{(1)*}(T_1)dT_1 = (T_{in} - T_b) + \frac{k_1}{2}(T_{in} - T_b)^2.$$

As the result of the Kirchhoff transformation we have got a simpler problem in which the nonlinearity is present in 2nd condition (12) and (13). According to the linear dependence of the coefficients of thermal conductivity on temperature (5) as the consequence of formulas (10):

$$\theta_i = (T_i - T_b) + \frac{k_i}{2}(T_i - T_b)^2 \quad (15)$$

we have

$$T_i(\theta_i) = \frac{\sqrt{1 + 2k_i\theta_i} - 1}{k_i} + T_b. \quad (16)$$

Let us note that the selected sign before the square root in temperature expressions provides the physical sense.

After integrating the equations (11) we find that:

$$\frac{d\theta_1}{d\rho} = \frac{C_{11}}{\rho}, \qquad \frac{d\theta_2}{d\rho} = \frac{C_{21}}{\rho} + \widetilde{W}^{(2)}(\rho), \qquad \frac{d\theta_3}{d\rho} = \frac{C_{31}}{\rho},$$

DOI 10.1515/ama-2016-0027

$$\theta_1 = C_{11}\ln\frac{\rho}{\rho_1} + C_{12},$$
$$\theta_2 = C_{21}\ln\frac{\rho}{\rho_2} + C_{22} + \overline{W}^{(2)}(\rho), \quad (17)$$
$$\theta_3 = C_{31}\ln\frac{\rho}{\rho_3} + C_{32},$$

where:

$$\widetilde{W}^{(2)}(\rho) = -\frac{4\cdot Po}{(\rho_3-\rho_2)^2}\left(\frac{\rho^3}{4} - \frac{\rho^2}{3}(\rho_3+\rho_2) + \frac{\rho}{2}\rho_2\rho_3 + \frac{\rho_2^3}{6\rho} \cdot\left(\rho_3 - \frac{\rho_2}{2}\right)\right),$$

$$\overline{W}^{(2)}(\rho) = -\frac{4\cdot Po}{(\rho_3-\rho_2)^2}\left(\rho^2\left(\frac{\rho^2}{16} - \rho(\rho_3+\rho_2) + \frac{\rho_2\rho_3}{4}\right) - \rho_2^3 \cdot\left(\frac{\rho_2}{16} - \frac{\rho_3+\rho_2}{9} + \frac{\rho_3}{4}\right) - \frac{\rho_2^3}{6}\cdot\ln\frac{\rho}{\rho_2}\cdot\left(\rho_3 - \frac{\rho_2}{2}\right)\right).$$

The solutions (17) contain 6 unknown constants of integration. To find them let us suppose the constants in the enpression for Kirchhoff variables to be known (the basic ones) in the first layer C_{11} and C_{12}, for example. The remaining constants are expressed through basic ones using the contact conditions on the neighbour surface in the cylinder. Herewith the equvivalent conditions (Popovych V.S. and Kalynyak B. M., 2014) instead of conditions (13) are used:

$$\theta_{i+1} - \theta_i|_{\rho=\rho_{i+1}} = \frac{k_{i+1}-k_i}{2}(T_i(\theta_i) - T_b)^2\Big|_{\rho=\rho_{i+1}}, \quad (18)$$

$i = 1,2.$

From the conditions (14) and (18) we obtain correspondingly:

$$C_{21} = C_{11}/K_\lambda^{(2)}, C_{31} = \left(C_{11}/K_\lambda^{(2)} + \rho_3\widetilde{W}^{(2)}(\rho_3)\right)/K_\lambda^{(3)},$$
$$C_{22} = C_{11}\ln\frac{\rho_2}{\rho_1} + C_{12} + \frac{k_2-k_1}{2} \cdot\left(\left(\sqrt{1+2k_1\left(C_{11}\ln\frac{\rho_2}{\rho_1} + C_{12}\right)} - 1\right)\Big/k_1\right)^2,$$
$$C_{32} = \theta_2|_{\rho=\rho_3} + \frac{k_3-k_2}{2}\left(\left(\sqrt{1+2k_2\theta_2|_{\rho=\rho_3}} - 1\right)/k_2\right)^2,$$

where:

$$\theta_2|_{\rho=\rho_3} = C_{11}\left(\ln\frac{\rho_2}{\rho_1} + \ln\frac{\rho_3}{\rho_2}/K_\lambda^{(2)}\right) + C_{12} + \overline{W}^{(2)}(\rho_3) + \frac{k_2-k_1}{2}\left(\left(\sqrt{1+2k_1\left(C_{11}\ln\frac{\rho_2}{\rho_1} + C_{12}\right)} - 1\right)\Big/k_1\right)^2.$$

The constant of integration C_{i1} and C_{i2} $(i = 2,3)$ are expressed through the basic ones C_{11} and C_{12}, which are found from boundary conditions (12). Using the first one we receive

$$C_{12} = (T_{in} - T_b) + \frac{k_1}{2}(T_{in} - T_b)^2.$$

From the second condition of (12) the algebraic equation was received

$$\frac{C_{31}}{\rho_4} + Bi\left(\frac{\sqrt{1+2k_3\theta_3|_{\rho=\rho_4}} - 1}{k_3} + T_b - T_{out}\right) = 0 \quad (19)$$

to determine the constant C_{11}.

The solution of (19) was found by software for analytical transformations. Using the obtained analytical expression for C_{11}, which is not presented because of its complexity, we find automatically expressions of others constants of integration. Knowing C_{ij} $(i = \overline{1,3}, j = 1,2)$ the temperature distributions of considered cylinder is given by formulas (16), (17).

5. THE DETERMINATION OF THE TEMPERATURE DISTRIBUTION IN THE HOLLOW NONTHERMOSENSITIVE CYLINDER

The dimensionless mathematical model for determining the temperature of a similar nonthermosensitive cylinder has the form

$$\frac{d}{d\rho}\left(\rho\frac{dT_{iN}}{d\rho}\right) = W_N^{(i)}(\rho), \quad \rho_i < \rho < \rho_{i+1}, \quad i = \overline{1,3}, \quad (20)$$

$$T_{1N}|_{\rho=\rho_1} = T_{in}, \left[\frac{dT_{3N}}{d\rho} + Bi_N(T_{3N} - T_{out})\right]_{\rho=\rho_4} = 0, \quad (21)$$

$$T_{1N}|_{\rho=\rho_2} = T_{2N}|_{\rho=\rho_2}, \quad T_{2N}|_{\rho=\rho_3} = T_{3N}|_{\rho=\rho_3}, \quad (22)$$

$$\left.\frac{dT_{1N}}{d\rho}\right|_{\rho=\rho_2} = K_{\lambda N}^{(2)}\left.\frac{dT_{2N}}{d\rho}\right|_{\rho=\rho_2},$$
$$\left.\frac{dT_{2N}}{d\rho}\right|_{\rho=\rho_3} = K_{\lambda N}^{(3)}\left.\frac{dT_{3N}}{d\rho}\right|_{\rho=\rho_3}, \quad (23)$$

where: $T_{iN} = t_{iN}/t_e$, $K_{\lambda N}^{(j)} = \lambda_{tN}^{(j)}/\lambda_{tN}^{(j-1)}$ $(j = 2,3)$, $W_N^{(1)}(\rho) = W_N^{(3)}(\rho) = 0$, $W_N^{(2)}(\rho) = -\frac{4\cdot Po_N}{(\rho_3-\rho_2)^2}\cdot\rho(\rho-\rho_2)(\rho-\rho_3)$, $Po_N = Po\cdot\lambda_{tN}^{(2)}/\lambda_{tN}^{(2)}$ is the Pomerantsev number, $Bi_N = Bi\cdot\lambda_{tN}^{(3)}/\lambda_{tN}^{(3)}$ is the Biot number.

From the problem (20)-(23) we find the following

$$\frac{dT_{1N}}{d\rho} = \frac{\bar{C}_{11}}{\rho}, \quad \frac{dT_{2N}}{d\rho} = \frac{\bar{C}_{21}}{\rho} + \widetilde{W}_N^{(2)}(\rho), \quad \frac{dT_{3N}}{d\rho} = \frac{\bar{C}_{31}}{\rho},$$

$$T_{1N} = \bar{C}_{11}\ln\frac{\rho}{\rho_1} + \bar{C}_{12},$$
$$T_{2N} = \bar{C}_{21}\ln\frac{\rho}{\rho_2} + \bar{C}_{22} + \overline{W}_N^{(2)}(\rho), \quad (24)$$
$$T_{3N} = \bar{C}_{31}\ln\frac{\rho}{\rho_3} + \bar{C}_{32},$$

where:

$$\widetilde{W}_N^{(2)}(\rho) = -\frac{4\cdot Po_N}{(\rho_3-\rho_2)^2}\left(\frac{\rho^3}{4} - \frac{\rho^2}{3}(\rho_3+\rho_2) + \frac{\rho}{2}\rho_2\rho_3 + \frac{\rho_2^3}{6\rho} \cdot\left(\rho_3 - \frac{\rho_2}{2}\right)\right),$$

$$\overline{W}_N^{(2)}(\rho) = -\frac{4\cdot Po_N}{(\rho_3-\rho_2)^2}\left(\rho^2\left(\frac{\rho^2}{16} - \rho(\rho_3+\rho_2) + \frac{\rho_2\rho_3}{4}\right) - \rho_2^3 \cdot\left(\frac{\rho_2}{16} - \frac{\rho_3+\rho_2}{9} + \frac{\rho_3}{4}\right) - \frac{\rho_2^3}{6}\ln\frac{\rho}{\rho_2}\left(\rho_3 - \frac{\rho_2}{2}\right)\right).$$

Then using the boundary conditions (21) and conditions of layer contact (22) we find constants of integration

$$\bar{C}_{11} = \left(K_{\lambda N}^{(2)}\left(\widetilde{W}_N^{(2)}(\rho_3)\rho_3 - K_{\lambda N}^{(3)}\left(\overline{W}_N^{(2)}(\rho_3) + T_{in}\right)\right)\right)/\Delta,$$

DOI 10.1515/ama-2016-0027

$$\bar{C}_{12} = T_{in},$$

$$\bar{C}_{21} = \left(\widetilde{W}_N^{(2)}(\rho_3)\rho_3 - K_{\lambda N}^{(3)}\left(\bar{W}_N^{(2)}(\rho_3) + T_{in}\right)\right)/\Delta,$$

$$\bar{C}_{22} = \frac{1}{\Delta}\left(\rho_3 \cdot \widetilde{W}_N^{(2)}(\rho_3) - K_{\lambda N}^{(3)} \cdot \left(\bar{W}_N^{(2)}(\rho_3) + T_{in}\right)\right) \cdot \left(\frac{1}{K_{\lambda N}^{(3)}} - \ln\frac{\rho_3}{\rho_2}\right),$$

$$\bar{C}_{31} = \frac{1}{\Delta}\left(\frac{\rho_3\widetilde{W}_N^{(2)}(\rho_3)}{K_{\lambda N}^{(3)}} - \bar{W}_N^{(2)}(\rho_3) - T_{in}\right) + \frac{\widetilde{W}_N^{(2)}(\rho_3)}{K_{\lambda N}^{(3)}},$$

$$\bar{C}_{32} = \left(\frac{1}{\Delta}\left(\bar{W}_N^{(2)}(\rho_3) + T_{in} - \frac{\rho_3\widetilde{W}_N^{(2)}(\rho_3)}{K_{\lambda N}^{(3)}}\right) - \frac{\widetilde{W}_N^{(2)}(\rho_3)}{K_{\lambda N}^{(3)}}\right)\left(\frac{1}{\rho_4 Bi_N} - \ln\frac{\rho_3}{\rho_2}\right) - T_{out},$$

$$\Delta = \ln\frac{\rho_2}{\rho_1}\left(1 - K_{\lambda N}^{(3)}\ln\frac{\rho_3}{\rho_2}\right).$$

6. THE DETERMINATION OF STRESS-STRAIN STATE

If the elastic modulus $\mathrm{E}^{(\mathrm{i})}(\mathrm{t_i})$, the Poisson ratio $\nu^{(\mathrm{i})}(\mathrm{t_i})$ and the temperature coefficients of the linear thermal expansions $\alpha_{\mathrm{t}}^{(\mathrm{i})}(\mathrm{t_i})$ of cylinder components are represented in the form $\chi^{(\mathrm{i})}(\mathrm{t_i}) = \chi_0^{(\mathrm{i})}\chi_{\mathrm{i}}^*(\mathrm{T_i})$, where $\chi_0^{(\mathrm{i})}$ are the dimensional quantities equal to the value of the characteristic with the temperature $\mathrm{t_b}$, and values $\chi_{\mathrm{i}}^*(\mathrm{T_i})$ are the dimensionless function of dimensionless temperature $\mathrm{T_i}$, then $E^{(i)}(t_i) = E_0^{(i)}E_i^*(T_i)$, $\nu^{(i)}(t_i) = \nu_0^{(i)}\nu_i^*(T_i)$, $\alpha_t^{(i)}(t_i) = \alpha_{t0}^{(i)}\alpha_{ti}^*(T_i)$.

Radial $\sigma_{\mathrm{r}}^{(\mathrm{i})}$ circumferential $\sigma_{\varphi}^{(\mathrm{i})}$ and axial $\sigma_{\mathrm{z}}^{(\mathrm{i})}$ stresses, radial $\mathrm{e}_{\mathrm{r}}^{(\mathrm{i})}$ and circumferential $\mathrm{e}_{\varphi}^{(\mathrm{i})}$ deformations and also radial displacements $\mathrm{u}_{\mathrm{r}}^{(\mathrm{i})}$ are calculated using expressions (Popovych Kalynyak, 2014) without mass forces:

$$\sigma_r^{(i)}(\rho) = \gamma_{1r}^{(i)}(\rho)\sigma^{(1)}(\rho_1) + \gamma_{2r}^{(i)}(\rho)e_z + \gamma_{0r}^{(i)}(\rho), \tag{25}$$

$$\sigma_\varphi^{(i)}(\rho) = \sigma^{(i)}(\rho) - \sigma_r^{(i)}(\rho), \tag{26}$$

$$\sigma_z^{(i)}(\rho) = E^{(i)}e_z + \nu^{(i)}\sigma^{(i)}(\rho) - E^{(i)}\Phi^{(i)}(T_i), \tag{27}$$

$$e_r^{(i)}(\rho) = \left(\sigma_r^{(i)}(\rho) - \nu^{(i)}\left(\sigma_\varphi^{(i)}(\rho) + \sigma_z^{(i)}(\rho)\right) + E^{(i)}\Phi^{(i)}(T_i)\right)/E^{(i)}, \tag{28}$$

$$e_\varphi^{(i)}(\rho) = \left(\sigma_\varphi^{(i)}(\rho) - \nu^{(i)}\left(\sigma_r^{(i)}(\rho) + \sigma_z^{(i)}(\rho)\right) + E^{(i)}\Phi^{(i)}(T_i)\right)/E^{(i)}, \tag{29}$$

$$u_r^{(i)}(\rho) = \rho \cdot e_\varphi^{(i)}(\rho), \tag{30}$$

where $\sigma^{(i)} = \sigma_r^{(i)} + \sigma_\varphi^{(i)}$ — are the total stresses calculated by the formula:

$$\sigma^{(i)}(\rho) = \gamma_{10}^{(i)}(\rho)\sigma^{(1)}(\rho_1) + \gamma_{20}^{(i)}(\rho)e_z + \gamma_{00}^{(i)}(\rho), \tag{31}$$

$$\gamma_{10}^{(i)}(\rho) = \frac{1}{\psi^{(i)}(\rho)} \cdot \left((1-\delta_{1i})\cdot\gamma_{1r}^{(i-1)}(\rho_i)\cdot\chi_2^{(i)}(\rho) + \left(\left(1-\left(\nu^{(1)}(\rho_1)\right)^2\right)/E^{(1)}(\rho_1) + (1-\delta_{1i}) \cdot \sum_{k=1}^{i-1}\left(\int_{\rho_k}^{\rho_{k+1}}\gamma_{1r}^{(k)}(\eta)\cdot\left(\varphi^{(k)}(\eta)\right)'d\eta + \beta^{(k)} \cdot \gamma_{1r}^{(k)}(\rho_{k+1})\right)\right)\cdot\chi_1^{(i)}(\rho)\right),$$

$$\gamma_{20}^{(i)}(\rho) = \frac{1}{\psi^{(i)}(\rho)} \cdot \left(\nu^{(i)}(\rho) - \nu^{(i)}(\rho_i) + (1-\delta_{1i})\gamma_{2r}^{(i-1)}(\rho_i)\cdot\chi_2^{(i)}(\rho) + \left(\nu^{(i)}(\rho_i) - \nu^{(1)}(\rho_1) + (1-\delta_{1i}) \cdot \sum_{k=1}^{i-1}\left(\int_{\rho_k}^{\rho_{k+1}}\gamma_{2r}^{(k)}(\eta)\cdot\left(\varphi^{(k)}(\eta)\right)'d\eta + \beta^{(k)} \cdot \gamma_{2r}^{(k)}(\rho_{k+1})\right)\right)\cdot\chi_1^{(i)}(\rho)\right),$$

$$\gamma_{00}^{(i)}(\rho) = \frac{1}{\psi^{(i)}(\rho)}\left(\left(-\delta_{1i}p_1 + (1-\delta_{1i})\cdot\gamma_{0r}^{(i-1)}(\rho_i)\right)\cdot\chi_2^{(i)}(\rho) - F^{(i)}(\rho) + F^{(i)}(\rho_i) + \left((1-\delta_{1i}) \cdot \sum_{k=1}^{i-1}\left(\int_{\rho_k}^{\rho_{k+1}}\gamma_{0r}^{(k)}(\eta)\cdot\left(\varphi^{(k)}(\eta)\right)'d\eta + \beta^{(k)} \cdot \gamma_{0r}^{(k)}(\rho_{k+1})\right) - F^{(i)}(\rho_i)\right)\chi_1^{(i)}(\rho)\right),$$

$$\gamma_{1r}^{(i)}(\rho) = \frac{1}{\rho^2}\left((1-\delta_{1i})\cdot\rho_i^2\cdot\gamma_{1r}^{(i-1)}(\rho_i) + \int_{\rho_i}^{\rho}\eta\gamma_{10}^{(i)}(\eta)d\eta\right),$$

$$\gamma_{2r}^{(i)}(\rho) = \frac{1}{\rho^2}\left((1-\delta_{1i})\cdot\rho_i^2\cdot\gamma_{2r}^{(i-1)}(\rho_i) + \int_{\rho_i}^{\rho}\eta\gamma_{20}^{(i)}(\eta)d\eta\right),$$

$$\gamma_{0r}^{(i)}(\rho) = \frac{1}{\rho^2}\left(-\rho_1^2\cdot p_1\cdot\delta_{1i} + (1-\delta_{1i})\cdot\rho_i^2\cdot\gamma_{0r}^{(i-1)}(\rho_i) + \int_{\rho_i}^{\rho}\eta\gamma_{00}^{(i)}(\eta)d\eta\right),$$

$$\chi_1^{(i)}(\rho) = 1 + \left(\frac{\rho-\rho_i}{2}\right)^2\cdot\left(\varphi^{(i)}(\rho)\right)'\cdot\frac{\rho_i}{\rho^2}\cdot\frac{E^{(i)}(\rho_i)}{1-\nu^{(i)}(\rho_i)},$$

DOI 10.1515/ama-2016-0027

$$\chi_2^{(i)}(\rho)=\frac{\rho-\rho_i}{2}\left(\frac{\rho_i^2}{\rho^2}\cdot\left(\varphi^{(i)}(\rho)\right)'+\left(\varphi^{(i)}(\rho_i)\right)'\right),$$

$$\psi^{(i)}(\rho)=\frac{1-\left(\nu^{(i)}(\rho_i)\right)^2}{E^{(i)}(\rho_i)}-\left(\frac{\rho-\rho_i}{2}\right)^2\frac{1}{\rho}\left(\varphi^{(i)}(\rho_i)\right)',$$

$$\varphi^{(i)}(\rho)=\frac{1-\nu^{(i)}(\rho)}{E^{(i)}(\rho)},\qquad\left(\varphi^{(i)}(\rho)\right)'=\frac{d}{d\rho}\left(\frac{1-\nu^{(i)}(\rho)}{E^{(i)}(\rho)}\right),$$

$$\beta_i=\varphi^{(i+1)}(\rho_{i+1})-\varphi^{(i)}(\rho_{i+1}),$$

$$F^i(\rho)=\left(1-\nu^{(i)}(\rho)\right)\cdot\Phi^{(i)}\left(T_i(\rho)\right)-\left(1-\nu^{(1)}(\rho_1)\right)\cdot\Phi^{(1)}\left(T_1(\rho_1)\right),$$

$$\Phi^{(i)}(T_i)=t_0\cdot\int_{T_p}^{T_i}\alpha_t^{(i)}(T_i)dT_i,$$

$$\sigma^{(1)}(\rho_1)=\frac{c_1d_{22}-c_2d_{12}}{d_{11}d_{22}-d_{21}d_{12}},\quad e_z=\frac{c_2d_{11}-c_1d_{21}}{d_{11}d_{22}-d_{21}d_{12}},$$

$$d_{11}=\sum_{k=1}^{n}\int_{\rho_k}^{\rho_{k+1}}\eta\cdot\gamma_{10}^{(k)}(\eta)d\eta,$$

$$d_{12}=\sum_{k=1}^{n}\int_{\rho_k}^{\rho_{k+1}}\eta\cdot\gamma_{20}^{(k)}(\eta)d\eta,$$

$$d_{21}=\sum_{k=1}^{n}\int_{\rho_k}^{\rho_{k+1}}\eta\cdot\gamma_{10}^{(k)}(\eta)\cdot\nu^{(k)}(\eta)d\eta,$$

$$d_{22}=\sum_{k=1}^{n}\int_{\rho_k}^{\rho_{k+1}}\eta\cdot\left(\gamma_{20}^{(k)}(\eta)\cdot\nu^{(k)}(\eta)+E^{(k)}(\eta)\right)d\eta,$$

$$c_1=\rho_1^2\cdot p_1-\rho_{n+1}^2\cdot p_2+\sum_{k=1}^{n}\int_{\rho_k}^{\rho_{k+1}}\eta\cdot\gamma_{00}^{(k)}(\eta)d\eta,$$

$$c_2=\frac{p}{2\pi}+\sum_{k=1}^{n}\int_{\rho_k}^{\rho_{k+1}}\eta\cdot\left(E^{(k)}(\eta)\cdot\Phi^{(k)}\left(T_k(\eta)\right)-\gamma_{00}^{(k)}(\eta)\cdot\nu^{(k)}(\eta)\right)d\eta,$$

where: $\Phi^i(T_i)$ is the purely thermal deformation, p_1, p_2 are the given constant pressures (stresses) on inner ($\rho=\rho_1$) and outer ($\rho=\rho_4$) surfaces of cylinder, p denotes known force loadings at the ends of the cylinder, $\delta_{ik}=\begin{cases}1, i=k,\\0, i\neq k,\end{cases}$ is a Kronecker symbol.

Formulas (25)-(31) to determine the stress-strain state are valid for thin layers only i.e. for which the trapezoidal formula

$$\int_{\rho_i}^{\rho}Y(\eta)d\eta=\frac{\rho-\rho_i}{2}\left(Y(\rho)+Y(\rho_i)\right)\tag{32}$$

is satisfied with the preset accuracy.

If the cylinder contains thin and thick layers, then each thick layer is segmented into few thinner ones made of the same material. To prove that cylinder has sufficiently thin layers the integral condition (Popovych and Kalynyak, 2014)

$$\rho_1^2\cdot p_1-\rho_{n+1}^2\cdot p_2=\sum_{k=1}^{n}\int_{\rho_k}^{\rho_{k+1}}\eta\cdot\sigma^{(k)}(\eta)d\eta\tag{33}$$

should be satisfied.

7. PARTICULAR CASES

Let us consider the case if the coefficients of thermal conductivity and mechanical characteristics of the non-thermosensitive cylinder (we denote them with N) are equal to the basic values of corresponding components of the thermosensitive one. The temperature distribution has the form (24), where $\lambda_{tN}^{(i)}=\lambda_{t0}^{(i)}, i=\overline{1,3}$. The Poisson ratio, the coefficient of the linear thermal expansion and the elastic modulus will have the following form $\nu_N^{(i)}=\nu_0^{(i)},\ \alpha_{tN}^{(i)}=\alpha_{t0}^{(i)},\ E_N^{(i)}=E_0^{(i)}, i=\overline{1,3}$ and formulas for the definition of components of the stress-strain state take the form:

$$\sigma_N^{(i)}(\rho)=\gamma_{10N}^{(i)}(\rho)\sigma_N^{(1)}(\rho_1)+\gamma_{20N}^{(i)}(\rho)e_z+\gamma_{00N}^{(i)}(\rho),\tag{34}$$

$$\sigma_{rN}^{(i)}(\rho)=\gamma_{1rN}^{(i)}(\rho)\sigma_N^{(1)}(\rho_1)+\gamma_{2rN}^{(i)}(\rho)e_z+\gamma_{0rN}^{(i)}(\rho),\tag{35}$$

$$\sigma_{\varphi N}^{(i)}(\rho)=\sigma_N^{(i)}(\rho)-\sigma_{rN}^{(i)}(\rho),\tag{36}$$

$$\sigma_{zN}^{(i)}(\rho)=E_0^{(i)}e_{zN}+\nu_0^{(i)}\sigma_N^{(i)}(\rho)-E_0^{(i)}\Phi_N^{(i)}(T_i),\tag{37}$$

$$e_{rN}^{(i)}(\rho)=\frac{1}{E_0^{(i)}}\left(\sigma_{rN}^{(i)}(\rho)-\nu_0^{(i)}\left(\sigma_{\varphi N}^{(i)}(\rho)+\sigma_{zN}^{(i)}(\rho)\right)+E_0^{(i)}\Phi_N^{(i)}(T_i)\right),\tag{38}$$

$$e_{\varphi N}^{(i)}(\rho)=\frac{1}{E_0^{(i)}}\left(\sigma_{\varphi N}^{(i)}(\rho)-\nu_0^{(i)}\left(\sigma_{rN}^{(i)}(\rho)+\sigma_{zN}^{(i)}(\rho)\right)+E_0^{(i)}\Phi_N^{(i)}(T_i)\right),\tag{39}$$

$$u_{rN}^{(i)}(\rho)=\rho\cdot e_{\varphi N}^{(i)}(\rho),\tag{40}$$

$$\gamma_{10N}^{(i)}(\rho)=\frac{1}{\psi_N^{(i)}}\left(\frac{1-\left(\nu_0^{(1)}\right)^2}{E_0^{(1)}}+(1-\delta_{1i})\sum_{k=1}^{i-1}\beta_N^{(k)}\cdot\gamma_{1rN}^{(k)}(\rho_{k+1})\right),$$

$$\gamma_{20N}^{(i)}(\rho)=\frac{1}{\psi_N^{(i)}}\left(\nu_0^{(i)}-\nu_0^{(1)}+(1-\delta_{1i})\sum_{k=1}^{i-1}\beta_N^{(k)}\cdot\gamma_{2rN}^{(k)}(\rho_{k+1})\right),$$

$$\gamma_{00N}^{(i)}(\rho)=\frac{1}{\psi_N^{(i)}}\left((1-\delta_{1i})\sum_{k=1}^{i-1}\beta_N^{(k)}\gamma_{0rN}^{(k)}(\rho_{k+1})-F^{(i)}(\rho)\right),$$

$$\gamma_{1rN}^{(i)}(\rho)=\frac{1}{\rho^2}\left((1-\delta_{1i})\rho_i^2\gamma_{1rN}^{(i-1)}(\rho_i)+\int_{\rho_i}^{\rho}\eta\gamma_{10N}^{(i)}(\eta)d\eta\right),$$

$$\gamma_{2rN}^{(i)}(\rho)=\frac{1}{\rho^2}\left((1-\delta_{1i})\rho_i^2\gamma_{2rN}^{(i-1)}(\rho_i)+\int_{\rho_i}^{\rho}\eta\gamma_{20N}^{(i)}(\eta)d\eta\right),$$

$$\gamma_{0rN}^{(i)}(\rho)=\frac{1}{\rho^2}\left(-\rho_1^2p_1\delta_{1i}+(1-\delta_{1i})\rho_i^2\gamma_{0rN}^{(i-1)}(\rho_i)+\int_{\rho_i}^{\rho}\eta\gamma_{00N}^{(i)}(\eta)d\eta\right),$$

$$\psi_N^{(i)}=\frac{1-\left(\nu_0^{(i)}\right)^2}{E_0^{(i)}},\varphi_N^{(i)}=\frac{1-\nu_0^{(i)}}{E^{(i)}},\beta_N^{(i)}=\varphi_N^{(i+1)}-\varphi_N^{(i)},$$

DOI 10.1515/ama-2016-0027

$$F_N^{(i)}(\rho) = \left(1-\nu_0^{(i)}\right)\cdot \Phi_N^{(i)}\left(T_{iN}(\rho)\right) - \left(1-\nu_0^{(1)}\right)\cdot \Phi_N^{(1)}\left(T_{1N}(\rho_1)\right),$$

$$\Phi_N^{(i)}(T_{iN}) = t_0\cdot \alpha_{t0}^{(i)}\left(T_{iN}-T_p\right),$$

$$\sigma_N^{(1)}(\rho_1) = \frac{c_{1N}d_{22N}-c_{2N}d_{12N}}{d_{11N}d_{22N}-d_{21N}d_{12N}},$$

$$e_{zN} = \frac{c_{2N}d_{11N}-c_{1N}d_{21N}}{d_{11N}d_{22N}-d_{21N}d_{12N}},$$

$$d_{11N} = \sum_{k=1}^{n}\int_{\rho_k}^{\rho_{k+1}} \eta\cdot\gamma_{10N}^{(k)}(\eta)d\eta,$$

$$d_{12N} = \sum_{k=1}^{n}\int_{\rho_k}^{\rho_{k+1}} \eta\cdot\gamma_{20N}^{(k)}(\eta)d\eta,$$

$$d_{21N} = \sum_{k=1}^{n}\int_{\rho_k}^{\rho_{k+1}} \eta\cdot\gamma_{10N}^{(k)}(\eta)\cdot\nu_0^{(k)}d\eta,$$

$$d_{22N} = \sum_{k=1}^{n}\int_{\rho_k}^{\rho_{k+1}} \eta\cdot\left(\gamma_{20N}^{(k)}(\eta)\cdot\nu_0^{(k)}+E_0^{(k)}\right)d\eta,$$

$$c_{1N} = \rho_1^2\cdot p_1-\rho_{n+1}^2\cdot p_2+\sum_{k=1}^{n}\int_{\rho_k}^{\rho_{k+1}}\eta\cdot\gamma_{00N}^{(k)}(\eta)d\eta,$$

$$c_{2N} = \frac{p}{2\pi}+\sum_{k=1}^{n}\int_{\rho_k}^{\rho_{k+1}}\eta\cdot\left(E_0^{(k)}\cdot\Phi_N^{(k)}\left(T_{kN}(\eta)\right)-\gamma_{00N}^{(k)}(\eta)\cdot\nu_0^{(k)}\right)d\eta.$$

In case of the average integral values of coefficients of thermal conductivity:

$$\lambda_{tn}^{(i)} = \lambda_{ts}^{(i)} = \frac{1}{T_e-T_b}\int_{T_b}^{T_e}\lambda_{t0}^{(i)}\left(1+k_i(T_i-T_b)\right)dT_i = \lambda_{t0}^{(i)}\left(1+\frac{k_i}{2}(T_e-T_b)\right),$$

$$\left\{\nu_{tn}^{(i)},\alpha_{tn}^{(i)},E_{tn}^{(i)}\right\} = \left\{\nu_{ts}^{(i)},\alpha_{ts}^{(i)},E_{ts}^{(i)}\right\} = \frac{1}{T_e-T_b}\int_{T_b}^{T_e}\left\{\nu^{(i)}(T_i),\alpha_t^{(i)}(T_i),E^{(i)}(T_i)\right\}dT_i,$$

$i=\overline{1,3}$,
we obtain the temperature distribution (24), where

$$Bi_n = Bi\frac{\lambda_{t0}^{(3)}}{\lambda_{ts}^{(3)}}, Po_n = Po\frac{\lambda_{t0}^{(2)}}{\lambda_{ts}^{(2)}}, K_{\lambda n}^{(2)} = \frac{\lambda_{ts}^{(2)}}{\lambda_{ts}^{(1)}}, K_{\lambda n}^{(3)} = \frac{\lambda_{ts}^{(3)}}{\lambda_{ts}^{(2)}}.$$

The formulas for calculating the stress-strain state will have the form (34)-(40) in which the basic values of the thermomechanical characteristics should be replaced by average integral ones.

8. NUMERICAL RESEARCH

Let us investigate the influence of temperature dependence of the thermal and mechanical characteristics of the cylinder materials on the temperature distribution and on components of stressed-strain state at different input parameters. The material in the first and in the third layers is the ceramics ZrO2, and in the second one is the titanium alloy Ti-6Al-4V (Tanigava and Akai, 1996).

Experimentally specified coefficients and thermomechanical characteristics were lineary approximated (5) in the temperature range $300\div 1100\mathrm{K}$ using the least squares method. The following values were established for ceramics:

$$\lambda_t^{(1,3)} = 1.915\cdot\left(1+0.24664\cdot\left(T_{1,3}-T_b\right)\right)\left[{}^{\mathrm{W}}/_{\mathrm{m}\cdot\mathrm{K}}\right],$$

$$\nu^{(1,3)} = 0.333,$$

$$\alpha_t^{(1,3)} = 8.783\cdot 10^{-6}\cdot\left(1-1.4128\cdot\left(T_{1,3}-T_b\right)+1.7496\cdot\left(T_{1,3}-T_b\right)^2\right)\left[{}^{1}/_{\mathrm{K}}\right],$$

$$E^{(1,3)} = 116.381\cdot\left(1-0.521357\cdot\left(T_{1,3}-T_b\right)-0.084215\cdot\left(T_{1,3}-T_b\right)^2\right)[\mathrm{GPa}],$$

and for titanium alloy

$$\lambda_t^{(2)} = 6.2\cdot\left(1+3.016\cdot\left(T_2-T_b\right)\right)\left[{}^{\mathrm{W}}/_{\mathrm{m}\cdot\mathrm{K}}\right],$$

$$\nu^{(2)} = 0.2984\cdot\left(1+0.118\cdot\left(T_2-T_b\right)\right),$$

$$\alpha_t^{(2)} = 8.8559\cdot 10^{-6}\cdot\left(1+0.49014\cdot\left(T_{1,3}-T_b\right)-0.36754\cdot\left(T_{1,3}-T_b\right)^2\right)\left[{}^{1}/_{\mathrm{K}}\right],$$

$$E^{(2)} = 105.05\cdot\left(1-0.5916\cdot\left(T_{1,3}-T_b\right)\right)[\mathrm{GPa}].$$

The coordinates of layer boundaries in the cylinder are equal $\rho_1=0.6,\rho_2=0.75,\rho_3=0.95,\rho_4=1$ with characteristic length $l_0=r_4$. The dimensionless values of temperature are $T_b=3/11$, $T_e=1, T_{in}=1/3, T_{out}=1/2$, Pomerantsev and Biot numbers are $\mathrm{Po}=-7$, $\mathrm{Bi}=2$. The constant pressures on inner and outer surfaces of cylinder and axial loadings at the ends are $p_1=p_2=p=0$.

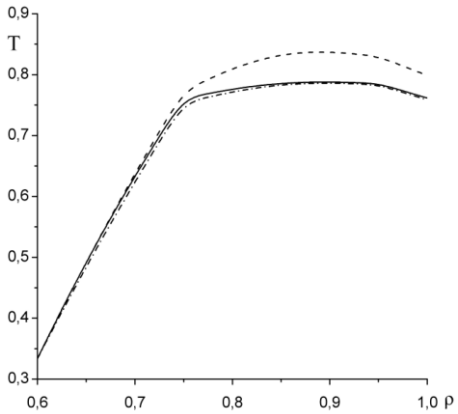

Fig. 1. The temperature distribution

The temperature distribution of the considered cylinder is presented in Fig. 1. Here and below the solid line corresponds to the thermosensitive cylinder, dashed line corresponds to the non-thermosensitive cylinder with basic values, dash-dotted line corresponds to the non-thermosensitive cylinder with the average integral values of the coefficient of thermal conductivity.

The maximal difference between temperatures in thermosen-

DOI 10.1515/ama-2016-0027

sitive and non-thermosensitive (with basic and average integral values of the coefficient of thermal conductivity) cylinders do not exceed 6%.

The algorithm for determining the components of stress-strain state because the formulas (25)-(31) are valid for thin layers only has following steps:

1. Calculating formulas (25)-(31) without segmentation of each layer in the cylinder into thin pieces.
2. Checking the satisfying of the integral condition (33).
3. If the condition (33) is not satisfied then the number of segments will be increased. Then we return to step 2. Otherwise the calculation is over.

Tab. 1 presents data obtained in finding sufficient segmentation of layers into components to achieve the accuracy $\varepsilon = 10^{-4}$.

Tab. 1. The result of segmentation of cylinder layers into thin components

The total number of layers	The number of segmentation in each layer			The satisfying of integral conditions
	I layer	II layer	III layer	
3	1	1	1	-0.004015
4	1	2	1	-0.002988
5	2	2	1	-0.000994
6	2	3	1	-0.000832

As we can see the representation of the considered cylinder as the 6 components body is enough to achieve the preset accuracy. Fig. 2-7 show distributions of stresses, deformations and displacements. The constant axes deformation is $e_z = 0.003907$.

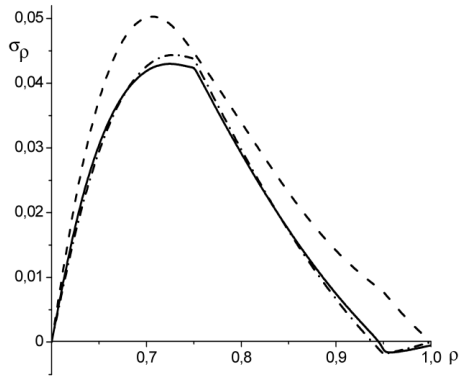

Fig. 2. The radial stresses

From Fig. 2, 3, 5-7 we can note that the stress-strain components distribution in the nonthermosensitive cylinder with average integral values of mechanical characteristics gives a better approximation to the same distribution in thermosensitive hollow cylinder in comparison to the stress-strain components distribution in the nonthermosensitive cylinder with basic values. In particular, the maximum differences of total stresses are 18%, of radial stresses are 8%, of circumferential stresses are 15%, of radial deformation are 10%, of radial displacements are 10%.

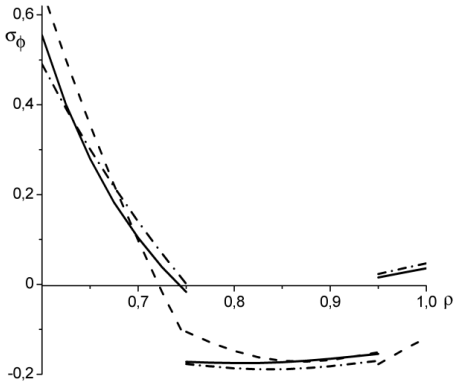

Fig. 3. The circumferential stresses

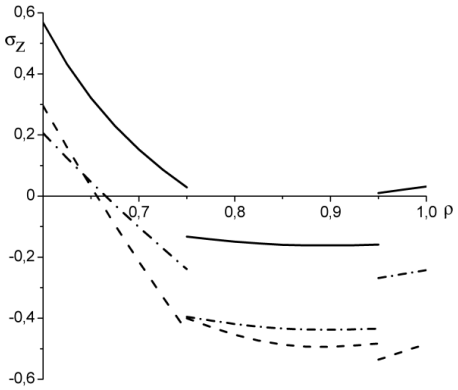

Fig. 4. The axial stresses

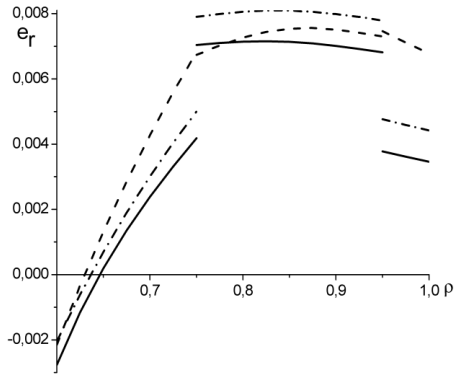

Fig. 5. The radial deformation

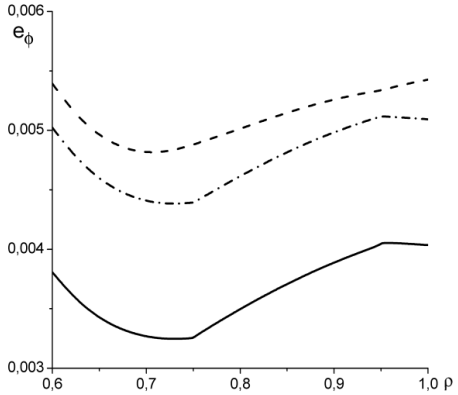

Fig. 6. The circumferential deformation

DOI 10.1515/ama-2016-0027

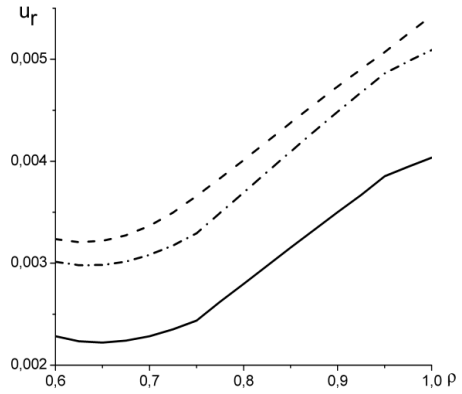

Fig. 7. The radial displacements

Use of model of nonthermosensitive body with basic values of its thermomechanical characteristics gives no correct approximation for such distribution of appropriate stress-strain components of thermosensitive cylinder but also leads to different quality results in some cases. Thus, in Fig. 2-4 we can see that stresses in the third layer of nonthermosensitive cylinder (with basic thermomechanical characteristics) are changed not only quantitatively, but also inherently (the compression in thermosensitive one and stretching in nonthermosensitive or conversely).

Let us note that for determining axial stresses it is necessary to take into account the thermosensitivity of material components because the use of basic and average integral values of thermomechanical characteristics will not give the correct distribution of σ_z.

9. SUMMARY

The nonlinear mathematical model of temperature distribution in a infinite three-layer hollow thermosensitive cylinder with heat sources distributed by parabolic law in the second layer, constant temperature and convective heat exchange on the boundary surfaces has been created. The components of the stress-strain state have been determined.

If to neglect the depemdence of thermomechanical characteristics of material components (the replacement for basic or average integral ones), then the large differences between distributions of components of stress-strain state of thermosensitive and nonthermosensitive cylinders may appear and lead to qualitatively different distributions. For the selected layer materials was shown that the distribution of the stress-strain state in nonthermosensitive cylinder with average integral values of mechanical characteristics gives a better approximation to such distribution in thermosensitive hollow cylinder. This can be useful for its rapid estimation.

REFERENCES

1. **Argeso H., Eraslan A. N.** (2008), On use of temperature-dependent physical properties in thermomechanical calculations for solid and hollow cylinders, *International journal of thermal sciences*, 47(2), 136-146.
2. **Aziz A., Torabi M.** (2013), Thermal stresses in a hollow cylinder with convective boundary conditions on the inside and outside surfaces, *Journal of thermal stresses*, 36(10), 1096-1111.
3. **Bazarenko N.** (2008), The contact problem for hollow and solid cylinders with stress-free faces, *Journal of applied mathematics and mechanics*, 72(2), 214-225.
4. **Carslaw H. S., Jaeger J. C.** (1959), *Conduction of heat in solids*, Oxford: Clarendon Press.
5. **Fazeli H., Abdous A., Karabi H., Moallemi N., Esmaeili M.** (2013), Analysis of transient heat conduction in a hollow cylinder using Duhamel theorem, *International journal of thermophysics*, 34(2), 350-365.
6. **Goto T., Suzuki M.** (1996), A boundary integral equation method for nonlinear heat conduction problems with temperature dependent material properties, *Internationla journal of heat and mass transfer*, 39(4), 823-830.
7. **Grzes P.** (2010) Influence of thermosensitivity of materials on the temperature of a PAD/DISC systems, Acta Mechanica et Automatica, 5(4), 46-53.
8. **Kushnir R. M., Popovych V. S.** (2009), *Thermoelasticity of thermosensitive solids*, Spolom, Lviv (in Ukrainian).
9. **Kushnir R. M., Popovych V. S.** (2011), *Heat Conduction Problems of Thermosensitive Solids under Complex Heat Exchange*, In Tech.
10. **Kushnir R. M., Protsiuk Yu. B.** (2010), Thermoelastic State of Layered Thermosensitive Bodies of Revolution for the Quadratic Dependence of the Heat-Conduction Coefficients, *Materials Science*, 46(1), 1-15.
11. **Lee H.-J.** (1998), The effect of temperature dependent material properties on the response of piezoelectric composite materials, *Journal of Intelligent Material Systems and Structures*, 9(7), 503-508.
12. **Noda N.** (1991), Thermal Stresses in Materials with Temperature-Dependent Properties, *Applied Mechanics Reviews*, 44(9), 383-397.
13. **Och E.** (2014), Frictional heating of sliding semi-spaces with simple thermal nonlinearities, Acta Mechanica et Automatica, 7(4), 236-240.
14. **Och E.** (2015), Frictional heating during sliding of two semi-spaces with arbitrary thermal nonlinearity, Acta Mechanica et Automatica, 8(4), 204-208.
15. **Popovych V. S., Kalynyak B. M.** (2014), Mathematical modeling and method of determining the static thermoelastic state of multilayered thermosensitive cylinders, *Math. Methods and Phys.-Mech. Fields*, 57(2), 169-186 (in Ukrainian).
16. **Shariyat M.** (2007), Thermal buckling analysis of rectangular composite plates with temperature dependent properties based on a layerwise theory, *Thin-Walled Structures*, 45(4), 439-452.
17. **Shen H.-S.** (2001), Thermal postbuckling behavior of imperfect shear deformable laminated plates with temperature-dependent properties, *Computer Methods in Applied Mechanics and Engineering*, 190(40-41), 5377-5390.
18. **Shi Zh., Zhang T., Xiang H.** (2007), Exact solutions of heterogeneous elastic hollow cylinders, *Composite structures*, 79(1), 140-147.
19. **Tanigawa Y., Akai T.** (1996) Transient heat conduction and thermal stress problems of a nonhomogeneous plate with temperature-dependent material properties, *Journal of Thermal Stresses*, 19(1), 77-102.
20. **Vigak V.** (1999), Solutions of one-dimensional problems of elasticity and thermoelasticity for cylindrical piecewise homogeneous bodies, *Journal of Mathematical Science*, 96(2), 3056-3064.
21. **Yevtuchenko A. A., Kuciej M., Och E.** (2014), Influence of thermal sensitivity of the pad and disk materials on the temperature during braking, *International Communications in Heat and Mass Transfer*, 55, 84-92.
22. **Zhu X. K., Chao Y. U** (2002), Effect of temperature-dependent material properties on welding simulation, *Computers & Structures*, 80(11), 967-976.

The work has been accomplished and partly financed under the project No. 0114U005081 of National Academy of Sciences of Ukraine.

DE GRUYTER
OPEN

DOI 10.1515/ama-2016-0028 acta mechanica et automatica, vol.10 no.3 (2016)

LASER-BEAM WELDING IMPACT ON THE DEFORMATION PROPERTIES OF STAINLESS STEELS WHEN USED FOR AUTOMOTIVE APPLICATIONS

Emil EVIN[*], Miroslav TOMÁŠ[**], Marek VÝROSTEK[*]

[*]Faculty of Mechanical Engineering, Department of Automotive Production, Technical University of Košice, Letná 9, 040 01 Košice, Slovakia
[**]Faculty of Mechanical Engineering, Department of Computer Support of Technology,
Technical University of Košice, Letná 9, 040 01 Košice, Slovakia

emil.evin@tuke.sk, miroslav.tomas@tuke.sk, marekvyrostek@gmail.com

received 2 November 2015, revised 15 July 2016, accepted 18 July 2016

Abstract: Materials other than standard and advanced high strength steels are remarkable for the thin-walled structures of the car-body in recent years in order to safety enhancement, weight and emission reduction, corrosion resistance improvement. Thus, there are presented in the paper the deformation properties of laser welded austenitic AISI 304 and ferritic AISI 430 stainless steels compared to these one measured for the high strength low alloyed steel H220PD. The properties were researched by tensile test and 3-point bending test with fixed ends on specimens made of basic material and laser welded one. The specimens were welded by solid state fiber laser YLS-5000 in longitudinal direction (the load direction). The deformation properties such as strength, stiffness and deformation work were evaluated and compared. The strength and stiffness were calculated from tensile test results and the deformation work was calculated from both, tensile test and 3-point bending test results. There has been found only minor effect of laser welding to the deformation properties for high strength low alloyed steel H220PD and austenitic stainless steel AISI 304. Otherwise, the laser welding strongly influenced the deformation work of the ferritic stainless steel AISI 430 as well as the elongation at tensile test.

Key words: Stainless Steel, Strength, Stiffness, Deformation Work, Tensile Test, 3-Point Bending

1. INTRODUCTION

Car designers are looking for ways to make vehicles lighter and safer to fulfil the emission requirements and secure the passenger's safety. As a result, several new materials such as advanced high strength steels (Baluch, 2014; Mihaliková, 2015; Evin, 2014), magnesium alloys (Solfronk, 2014), plastics and composites (Fuchs, 2008; Jacob, 2004) have been introduced to the industry. Making cars lighter helps increase fuel economy, and making them safer reduces fatalities caused by serious collisions. Stainless steel appears being remarkable as well due to its mechanical properties, energy absorption ability, strength, stiffness, corrosion resistance, formability and weldability.

It is necessary to prevent objects (car components, tree, pole, etc.) from penetrating the cabin in order to secure passengers' survival at collision with another object (Richter, 2005). Thus, the cabin space needs to be perfectly tough and strong. These depend on the strength and deformation characteristics of the carrying car-body structure components. The effectiveness of these components can be improved by design of structure and proper material selection (Bright, 2011; Burdzik, 2012). The structure of the deformation zones components may consist either of several components of different types of steel sheet or of one component consisting of high strength steel or several different high-strength steel sheets with different thickness and strength joined by laser welding – tailored blanks (Schrek, 2014; Merklein, 2014).

Materials used in car body structures have to meet wide range of criteria. The most important criterion for auto-body from the view of safety is the energy absorption ability at impact. For these cases deformation zones are applied in design of auto-body structure. These provide as much as possible energy absorption to secure minimal passenger's space deformation (Burdzik, 2012).

Absorption maximum of kinetic energy in order to reach minimum of crew organism overloading (deceleration) and preserve sufficient strength is the main role of deformable car body elements. Some components such as B-pillar, body sill, front bumper, door beams, etc. have to be strength and stiffer to preserve enough space for passengers survive at side impact. Other car body components such A-pillar, front chassis legs, front wing support, cross-beams, etc. are used to controlled deformation and kinetic energy absorption at frontal impact. Thus, they can be produced from materials with lower strength but very good formability (Burdzik, 2012; Vlk, 2000; Wallentowitz, 1996).

As mentioned, analysis of strength, stiffness and deformation work of materials used for car body components is important. Innovations of materials for car body lie on using such materials whose plastic deformation or mechanically inducted phase transformation is consumed by kinetic energy absorption at car impact. The major importance at frontal impact is on ability of material to absorb the maximum energy, while at lateral impact the main importance is on strength and stiffness due to small deformation zone in door area. (Kramer, 2009; Rediers, 1998, Evin, 2012).

The objective of the paper is to compare selected deformation properties for some stainless steels, when they are potentially used for safety elements, exhaust systems and fuel tanks. These properties have been tested for base and laser-welded material, due to wide application of laser welding when used to prepare the tailored welded blanks in automotive industry.

DOI 10.1515/ama-2016-0028

2. MATERIALS AND METHODS

The laser-beam welding impact on the deformation properties of metal plates from austenitic stainless steel AISI 304 and ferritic stainless steel AISI 430 were researched. The high strength low alloyed steel H220PD has been used as a reference material. The chemical composition shown in Tab. 1 was defined by the mobile spectrometer Belec Compact Port.

Steel strips from metal plates of micro-alloyed steel H220PD, austenitic stainless steel AISI 304 and ferritic steel AISI 430 were welded by laser-beam in continuous welding without protecting gas, using solid-state fiber laser YLS-5000 by IPG laser. Because of the importance of welding parameters (Mei, 2009; Yan, 2010), these have been optimised to reach the best quality of butt weld, based on microscopic structure evaluation in base material, heat affected zone and weld metal (the width of the butt weld and the heat affected zone, hardness HV0.5) as well as macroscopic evaluation of the butt (porosity, weld root fusion). The optimal ones parameters are shown in Tab. 2.

Tab. 2. Laser welding parameters

Material	Power of laser [kW]	Focus position [mm]	Welding speed [mm.s^{-1}]
Micro-alloyed steel H220PD	1.7	10	50
Austenitic steel AISI 304	2.1	10	70
Ferritic steel AISI 430	2.1	10	70

The mechanical properties such as yield strength, tensile strength, uniform elongation at necking, tensibility, material constant K, strain-hardening exponent of the examined basic materials and laser-welded strips were measured by standardised tests in accordance with STN EN ISO 6892-1, ISO 10113:2006 and ISO 10275:2007 with the sample stated in Fig. 1 and Fig. 2 from load diagrams of the tensile testing machine TIRAtest 2300 measured at the strain rate $\dot{\varepsilon} = d\varepsilon/dt = 0.0021\ s^{-1}$. Three specimens have been tested in 90° to the rolling direction and the average value and standard deviation have been calculated.

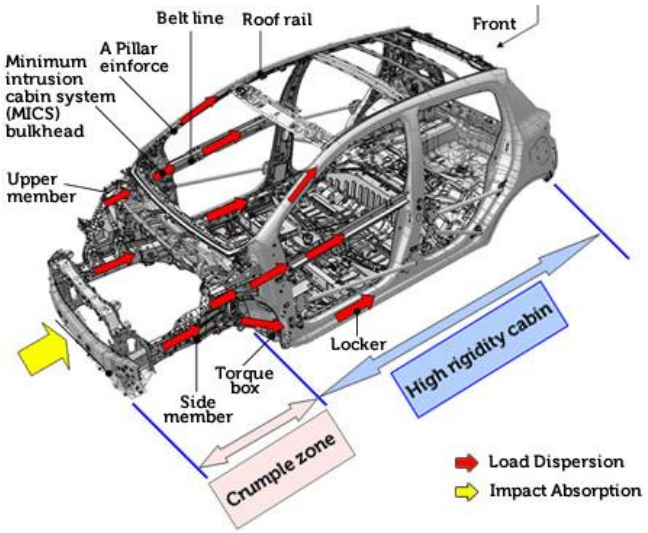

Fig. 1. Impact absorption and load dispersion at side impact (© Toyota Innovation)

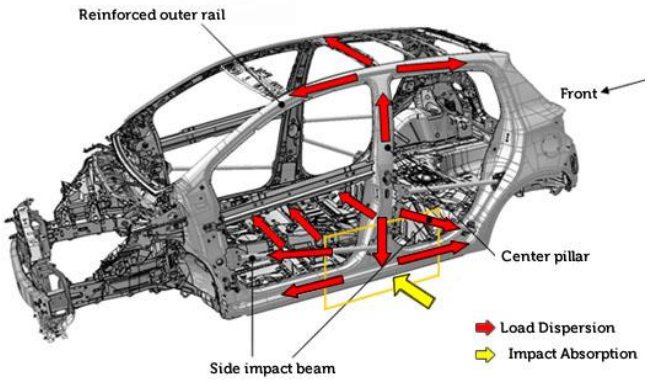

Fig. 2. Impact absorption and load dispersion at frontal impact (© Toyota Innovation)

Tab. 1. Chemical composition of materials used

Material	Chemical composition [wt %]								
H220PD	C	Si	Mn	Cu	Cr	Ni	Co	Nb	Fe
	0.077	0.019	0.358	0.017	0.009	< 0.002	0.017	0.031	99.38
AISI 304	C	Si	Mn	Cu	Cr	Ni	Co	Nb	Fe
	0.055	0.592	1.597	0.029	18.30	7.79	0.062	0.049	71.42
AISI 430	C	Si	Mn	Cu	Cr	Ni	Co	Nb	Fe
	0.038	0.374	0.502	0.071	16.45	0.19	0.045	0.015	82.22

P < 0.018; S < 0.002; Ti < 0.007; Mo < 0.026; Al < 0.026; W < 0.036; V < 0.049

The deformation work, i.e. the crashworthiness of experimental materials, has been measured by modified 3-point bending test with fixed ends on the testing machine TIRAtest 2300. Non-standardized specimens - metal steel strips 30 mm in width and 300 mm in length - have been made of base material and the laser weld one. The strips were laid at the cylinders of bending fixture and fasten by grips at the ends to prevent the strip pulling out – Fig. 5. The weld was oriented in longitudinal direction in the middle of the strip. The strip has been bent by punch until the strip fracture. The bending force - punch path dependence was recorded by PC during the test. Measured data such as maximum bending force and the punch path were used to calculate the deformation work. The distance of cylinders was 120 mm, the cylinder diameter 30 mm and the punch velocity 10 mm.min^{-1}.

DOI 10.1515/ama-2016-0028

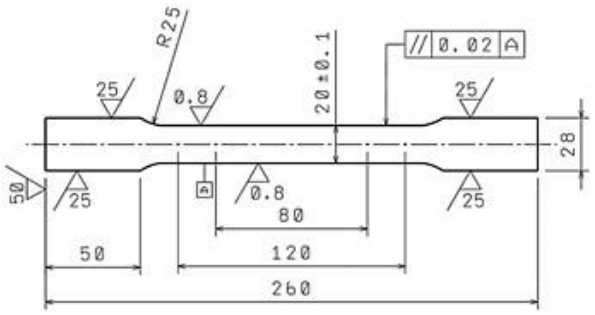

Fig. 3. Standardised specimen for tensile test

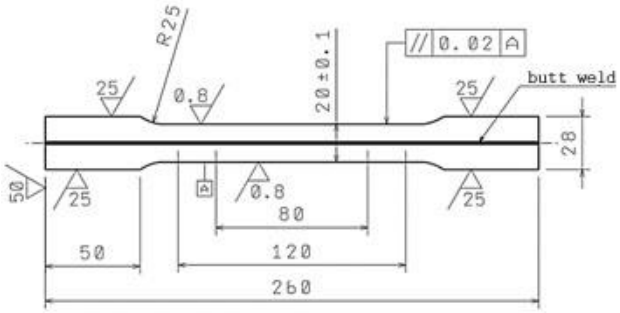

Fig. 4. Laser-welded specimen for tensile test

Fig. 5. The bending fixture on the testing machine TIRAtest 2300

3. REACHED RESULTS AND DISCUSSION

Measured values of mechanical properties for base material and laser welded ones are shown in Tab 3. These values have been used to calculate the strength, stiffness and deformation work for assessed materials. (Evin, 2012 and 2014)

The strength of a component depends on its geometry and yield stress as follows:

$$ST = \frac{R_{P0.2}}{x}. \tag{1}$$

The stiffness is affected by material properties and its geometry as well as follows:

$$STF = V_0 \frac{(R_{P0.2})^2}{x^2 \cdot E}, \tag{2}$$

where: $R_{P0.2}$ – yield stress, E – modulus of elasticity, x – degree of safety or safety constant (1.6 to 2)

The crashworthiness = absorption ability = deformation work is characteristic currently becoming increasingly important. Recent trends require for a material to absorb more energy in crash scenario. The potential absorption energy can be assessed by the area under the stress-strain curve or load-path. When assessed from the tensile test engineering diagram, the deformation work is calculated from mechanical properties as follows:

$$Wpl, necking = \frac{R_{P0.2}+Rm}{2} \cdot \frac{Ag}{100}, \tag{3}$$

where: Rm – ultimate tensile stress, Ag – uniform elongation.

When assessed from load-path curve from 3-point bending test with fixed ends, the deformation work is calculated as follows:

$$Wpl = \frac{F_{max} \cdot \Delta l}{2}, \tag{4}$$

where: F_{max} – maximum bending force, Δl – punch path to fracture.

The bending force-punch path dependence when 3-point bending with fixed end have been performed is shown in Fig. 6. The results of calculated values according to eq. (1) to eq. (4) is shown in Tab. 4 for base material and in Tab. 5 for laser-beam welded material.

The graphs for calculated properties before and after welding are shown in Fig. 7 and Fig. 8 when strength and stiffness are compared.

Tab. 3. The properties (90° to rolling dir.) of base material and laser welded one

Material			$R_{P0.2}$ [MPa]	Rm [MPa]	Ag [%]	A_{80} [%]	At [%]	K [MPa]	r [-]	n [-]
H220PD	BM	average	380	449	17	29	29	728	0.659	0.178
		stdev	2	1	1	1	1	2	0.004	0
	LW	average	366	462	17	26	26	733	0.753	0.167
		stdev	2	2	1	1	1	5	0.026	0
AISI 304	BM	average	302	765	58	62	62	1594	0.931	0.462
		stdev	1	1	3	2	2	12	0.005	0.002
	LW	average	304	753	57	62	62	1563	0.958	0.451
		stdev	3	1	2	1	1	7	0.009	0.002
AISI 430	BM	average	300	477	20	30	29	796	0.871	0.195
		stdev	3	4	2	3	3	4	0.026	0.002
	LW	average	318	437	6	6	6	802	0.870	0.194
		stdev	2	4	0	0	0	15	0.020	0.006

Emil Evin, Miroslav Tomáš, Marek Výrostek
DOI 10.1515/ama-2016-0028

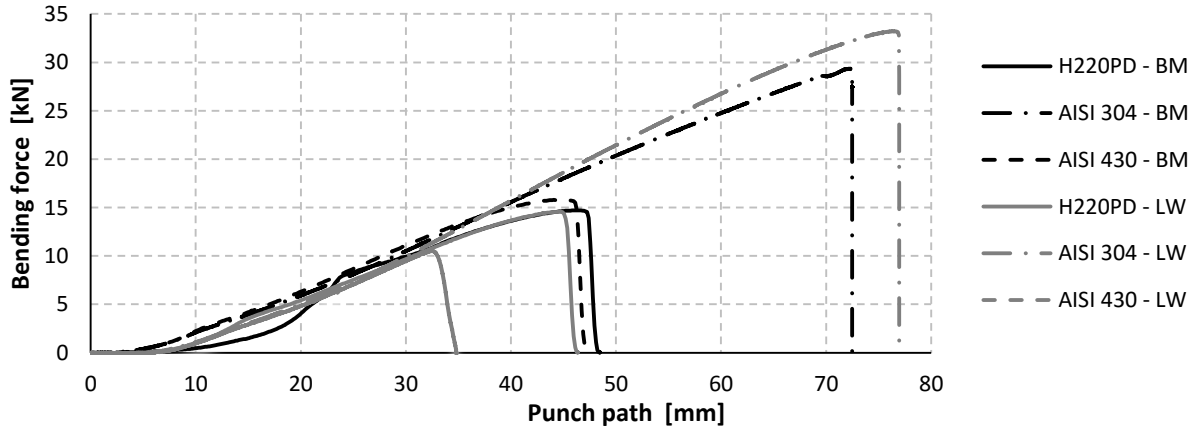

Fig. 6. Bending force – punch path dependence

Tab. 4. Calculated values of safety characteristics – base material

Material	Strength ST	Stiffness STF	Wpl eq. (3)	Wpl eq. (4)
H220PD	237.5	0.269	70.5	356.6
AISI 304	188.7	0.170	309.4	1063.5
AISI 430	187.5	0.167	77.7	374.8

Tab. 5. Calculated values of safety characteristics – laser welded material

Material	Strength ST	Stiffness STF	Wpl Eq. (3)	Wpl Eq. (4)
H220PD	228.8	0.249	70.4	337.7
AISI 304	190.0	0.172	301.3	1278.5
AISI 430	198.7	0.188	22.7	183.1

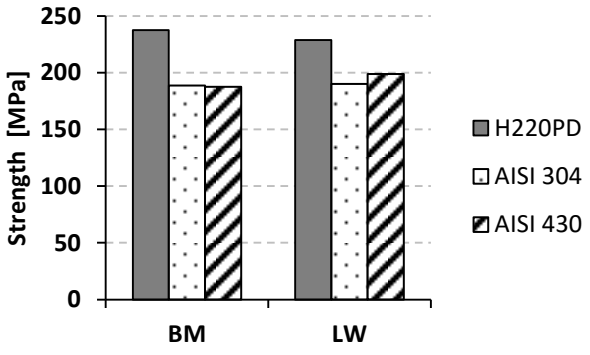

Fig. 7. Strenght comparison

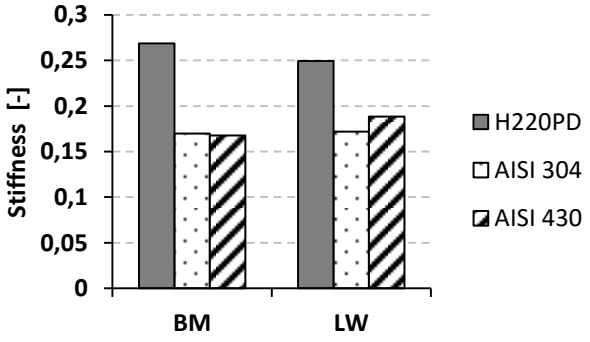

Fig. 8. Stiffness comparison

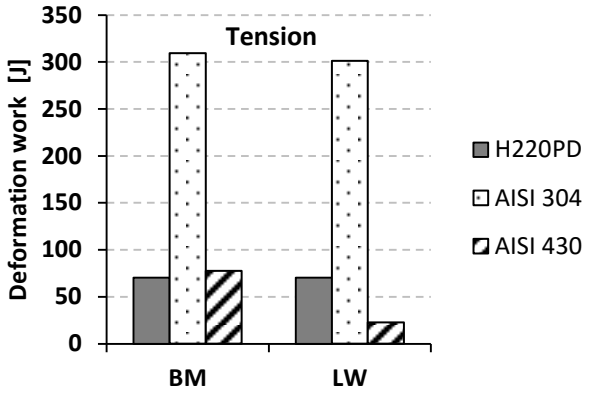

Fig. 9. Deformation work calculated from eq. (3) based on tensile test

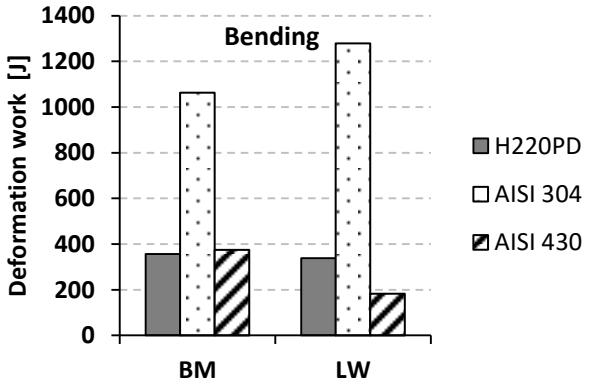

Fig. 10. Deformation work calculated from eq. (4) based on 3-point bending test with fixed ends

Laser welding of austenitic steel AISI 304 has shown only minor influence on strength and stiffness; the stiffness increased about 0.7 % (188.7 to 190) and strength 1.3 % (0.170 to 0.172) compared to the base material. The greater influence has been found for ferritic steel AISI 430 when the strength increased about 6.0 % (187.5 to198.7) and stiffness 12.4 % (0.167 to 0.188) compared to the base material. The calculated values for reference material H220PD decreased for strength about -3.7 % (237.5 to 228.8) and stiffness -7.2 % (0.269 to 0.249) compared to the base material.

DOI 10.1515/ama-2016-0028

The graphs for calculated deformation work according to eq. (3), based on tensile test properties and eq. (4), based on the bending force-punch path, are shown on Fig. 9 and Fig. 10. As it is shown in graphs, the laser welding has shown the major influence for ferritic stainless steel AISI 430 when the deformation work decreases about -70.8 % (77.7 to 22.7) as calculated from tensile test results and -51.1 % (374.8 to 183.1) as calculated from 3-point bending test results. There is only minor influence of laser welding on the deformation work for austenitic stainless steel AISI 304 (-2.6 % for tensile test and 20.2 % for 3-point bending test). The calculated deformation work for reference material H220PD decreased about 0.12 % when calculated according to eq. (3) from tensile test results or 5.3 % when calculated according to eq. (4) from 3-point bending test results.

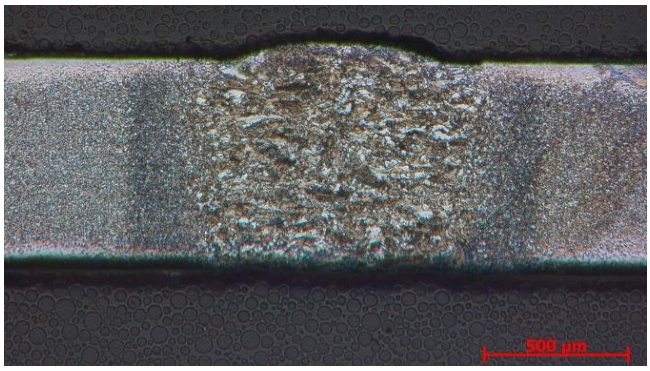

Fig. 11. Macrostructure of laser-beam welded H220PD

Fig. 12. Macrostructure of laser-beam welded AISI 304

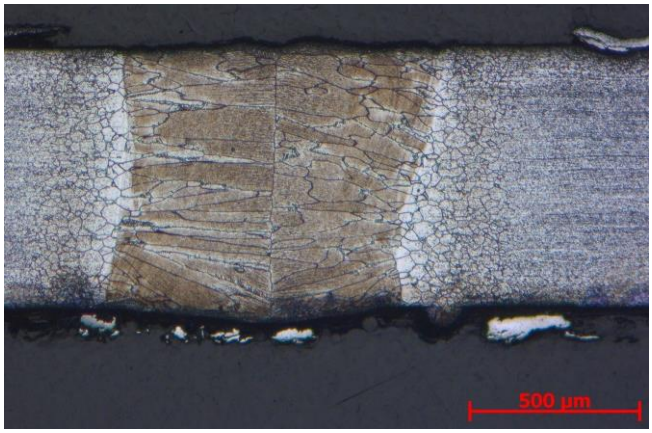

Fig. 13. Macrostructure of laser-beam welded AISI 430

The weld joint of high strength low alloyed steel H220PD when laser-beam welded is shown in Fig. 11. The base material microstructure is fine-grained ferritic with secondary additions of carbides and nitrides. In the weld material hypocutectoid ferrite is created on the grain boundaries of initial austenitic grains. The fine acicular ferrite has been found inside austenitic grains. Some islands of bainitic structure also have been found in the weld metal. The weld metal and heat affected zone is polyedric with the grain size reducing toward the base metal. The results are similar to (Wang, 2015).

The weld joint of austenitic stainless steel AISI 304 when laser-beam welded is shown in Fig. 12. Delta ferrite arranged in rows has been found in the base material microstructure as well as large amount of globulitic carbides. It complies to (Yan, 2010; Hanninen, 2001). The microstructure of weld metal and heat affected zone is austenitic with delta ferrite mainly in the grain boundaries. According to (Yan, 2010), the fast cooling in the laser-beam welding process does not offer sufficient time to complete the phase transformation delta to gamma ferrite. The microstructure is polyedric and the grain size reduces towards the heat affected zone.

Some martensite arranged in rows has been found in the ferritic stainless steel AISI 430 base material structure – Fig. 13 – and it complies with (Berretta, 2007). The weld metal microstructure is created by columnar ferrite grains growing from the boundary to the middle. Some martensite has been found in the interdendritic space. The microstructure of heat affected zone is also ferritic with martensite in the grain boundaries.

The results of calculated characteristics of strength, stiffness and deformation work for austenitic stainless steel AISI 304 are comparable to the results for H220PD considering its tendency. There is only minor influence of laser-beam welding to the strength, stiffness and deformation work calculated. It is given by their proper microstructure which is not substantially affected when they are laser-beam welded. There are any improper components in the weld metal influencing the material microstructure after welding; the fine grained ferritic microstructe of H220PD and austenitic with delta ferrite mainly in the grain boundaries for austenitic stainless steel AISI 304. But, there is a major influence of laser-beam welding to the deformation properties of ferritic stainless steel AISI 430, which creates martensite in the interdendritic space of weld metal. The strength and stiffness for ferritic stainless steel AISI 430 improves about 6.0 % and 12.4 %, but the deformation work gets worst considerably, i.e. -70.8 % when calculated from tensile test results according to eq. (3). This result has been confirmed by the deformation work when calculated from 3-point bending test with fixed ends results according to eq. (4); the deformation work gets worse about -51.1 %. Presence of brittle phase structure in the weld metal of ferritic stainless steel AISI 430 has been proven by cracking during the tensile and 3-point bending test and crack propagation from the weld metal to the base material.

4. CONCLUSSION

The stainless steel use in the automotive industry has shown the wide range of implementations in recent years, such as removable chassis components (bumper beams, frame crossmembers, suspension control arms, subframes), safety/intrusion management components (side impact beams, roof bows, roof rails, B-pillars), entire chassis frame rails, exhaust system components, etc. They present good energy absorption ability when used for safety components. The austenitic grades are applicable when

laser-beam welding is used at production of tailored welded structures due to preserving its properties, such as strength, stiffness and deformation work, as it has been presented in the paper. Otherwise, the ferritic grades applications are strongly influenced by its microstructure that create embrittling phases after welding.

REFERENCES

1. **Baluch N., Udin Z. M., Abdullah Ch. S.** (2014), Advanced High Strength Steel in Auto Industry: an Overview, *Engineering, Technology & Applied Science Research*, 4(4), 686-689.
2. **Berretta J.R., Rossi W, Neves M.D.M, Almeida, I.A., Junior, N.D.V**. (2007), Pulsed Nd:YAG laser welding of AISI 304 to AISI 420 stainless steels, *Optics and Lasers in Engineering*, 45(9), 960-966.
3. **Bright G.W., Kennedy J.I., Robinson F, Evans M. Whittaker M.T., Sullivan J., Gao Y.** (2011), Variability in the mechanical properties and processing conditions of a High Strength Low Alloy steel. *Procedia Engineering*, 10, 106-111.
4. **Burdzik R., Folęga P., Konieczny Ł., Łazarz B., Stanik Z., Warczek J.** (2012), Analysis of material deformation work measures in determination of a vehicle's collision speed, *Archives of Materials Science and Engineering*, 58-1, 13-21.
5. **Čada R.** (2003), Evaluation of strain and material flow in sheet-metal forming, *Journal of Mat. Processing Technology*,138(1-3), 170-175.
6. **Evin E., Tomáš M., Kmec J., Németh S., Katalinic B., Wessely E.** (2014), The Deformation Properties of High Strength Steel Sheets for Auto-Body Components, *Procedia Engineering,* 69, 758-767.
7. **Evin E., Tomáš M.** (2012), Comparison of deformation properties of steel sheets for car body parts. *Procedia Eng.*, 48, 115-122.
8. **Fuchs E.R.H., Field D.R., Roth, R., Kirchain, R.E.** (2008), Strategic materials selection in the automobile body. Economic opportunities for polymer composite design, *Composites science and technology*, 68, 1989-2002.
9. **Hanninen H., Romu J., Ilola R., Tervo J., Laitinen A.** (2001), Effects of processing and manufacturing of high nitrogen-containing stainless steels on their mechanical, corrosion and wear properties. *Journal of Mat. Processing Technology*, 117(3), 424-430
10. **Jacob G.C., Fellers J.F., Simunovic S., Starbuck J.M.** (2004), Energy Absorption in Polymer Composites for Automotive Crashworthiness, *Journal of Composite Materials*, 36, 813.
11. **Kramer F.** (2009), *Passive Safety of Vehicles*, Vieweg+Teubner, Weisbaden. (in German)
12. **Mei L., Chen G., Jin X., Zhang Y., Wu Q.** (2009) Research on laser welding of high-strength galvanized automobile steel sheets, *Optics and Lasers in Engineering*, 47(11), 1117-1124
13. **Merklein M., Johannes M., Lechner M., Kuppert A.** (2014), Review on tailored blanks—Production, applications and evaluation, *Journal of Materials Processing Technology*, 214(2), 151-164
14. **Mihaliková M., Német M., Girman V.** (2015), DP 600 steel research of dynamic testing, *Metalurgija,* 54(1), 211-213.
15. **Rediers B., Yang B., Juneja V.** (1998), Static and dynamic stiffness - one test both results, *Proc. of the 16th IMAC*, 30-35.
16. **Richter M., Pape H.Ch., Otte D., Krettek Ch.** (2005) Improvements in passive car safety led to decreased injury severity - a comparison between the 1970s and 1990s, *Injury*, 36(4), 484-488.
17. **Schrek A., Činák M., Švec P., Kostka P., Gajdošová V.** (2014), Influence of Stress-strain Characteristic of Laser Weld Join on the Total Formability of Tailored Welded Blanks, *Hutnícke listy*, 67(4), 41-44 (in Slovak).
18. **Solfronk P., Sobotka J., Kolnerová M., Zuzánek L.** (2014), Influence of temperature on formability of magnesium alloy AZ31B. *23rd Int. Conf. METAL 2014,* Brno, Czech Republic, 1045-1050.
19. **Vlk F.** (2000), *Auto-body of vehicles*, Editing and publishing company Vlk, Brno.
20. **Wallentowitz H., Adam H.** (1996), Predicting the crashworthiness of vehicle structures made by lightweight design materials and innovative joining methods, *International Journal of Crashworthiness*, 1(2), 163-180.
21. **Wang X.N., Chen CH.J., Wang H.S., Zhang S.H., Zhang M., Luo X.** (2015), Microstructure formation and precipitation in laser welding of microalloyed C–Mn steel, *Journal of Materials Processing Technology*, 226(12), 106-114
22. **Yan J., Gao M., Zeng X.** (2010), Study on microstructure and mechanical properties of 304 stainless steel joints by TIG, laser and laser-TIG hybrid welding, *Optics and Lasers in Engineering*, 48(4), 512-517

The work has been accomplished under the grant project VEGA 2/0113/16 "Influence of laser welding parameters on structure and properties of welded joints of advanced steels for the automotive industry" and project APVV-0273-12 "Supporting innovations of autobody components from the steel sheet blanks oriented to the safety, the ecology and the car weight reduction".

DE GRUYTER
OPEN

DOI 10.1515/ama-2016-0029

acta mechanica et automatica, vol.10 no.3 (2016)

IDENTIFYING THE ISOMORPHISM OF KINEMATIC CHAINS

Krystyna ROMANIAK*

*Faculty of Architecture, Cracow University of Technology, ul. Warszawska 24, 31-155 Kraków, Poland

krystynaromaniak@gmail.com

received 26 May 2014, revised 15 July 2016, accepted 18 July 2016

Abstract: Identification of isomorphic kinematic chains is one of the key issues in researching the structure of mechanisms. As a result the structures which duplicate are eliminated and further research is carried out on kinematic chains that do not duplicate. This dilemma has been taken up by many scholars who have come up with a variety of ideas how to solve it. The review of the methods for identifying the isomorphism of kinematic chains suggested by researchers is contained in this study, including Hamming Number Technique, eigenvalues and eigenvectors, perimeter graphs, dividing and matching vertices. The spectrum of methods applied to the issue of identifying the isomorphism of mechanisms reflects the researchers' efforts to obtain a precise result in the shortest time possible.

Key words: Isomorphism, Structure of Planar and Spatial Kinematic Chains

1. INTRODUCTION

Topological methods are applied in researching the structure of mechanism. Topology is the study of those properties of objects that do not change when homeomorphisms are applied. Homeomorphism or topological isomorphism is a continuous function that has a continuous inverse function. The word 'isomorphism' is used when describing the structure of mechanisms. Structural invariants are the following:

- number of links with their conjunctivity,
- number of kinematic pairs with their classes,
- joining of links of a specific conjunctivity through kinematic pairs of given classes (Conjunctivity of a link is a number of kinematic pairs that the link is composed of, which equivalently determines the number of links it can be joined with).

Fig. 1 presents an exemplary topological transformation that kinematic chains are subject to. Those kinematic chains are composed of seven links: three binary and four ternary links as well as nine kinematic pairs. A closer analysis of the figure indicates that individual links in all kinematic chains are joined together via identical kinematic pairs. For example, in all kinematic chains a kinematic pair A joins a binary link 1 with a ternary link 4. Other kinematic pairs are involved in similar connections. Each kinematic chain selected for this example, is made of four loops that consist of three, four, five and six links respectively. Individual contours form the following outer loops: six-link (Fig. 1a), five-link (Fig. 1b), four-link (Fig. 1c) and three-link (Fig. 1d). In terms of structure these examples are identical or in other words isomorphic because each one of them can be obtained from the remaining ones by applying isomeric transformation in which the earlier mentioned invariants have been maintained.

To identify isomorphic structures is significant because after defining the structure of mechanisms further research is carried out for non-repeating solutions. It relates to structural synthesis in particular, whereby a sets of solutions can be obtained that fulfill specific structural formulae (Ding et al., 2011; 2012; Romaniak, 2010; 2011).

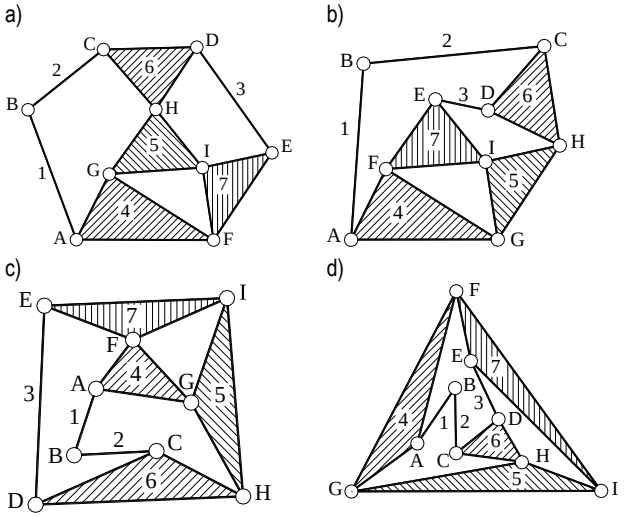

Fig. 1. Isomorphic kinematic chains

The isomorphism of kinematic chains has been taken up by many researchers who came up with a number of methods for solving this dilemma. This study discusses selected solution methods. It presents how the isomorphism of kinematic chains can be identified with the use of Hamming Number Technique (Rao and Raju, 1991), eigenvalues and eigenvectors (Chang et al., 2002; Cubillo and Wan, 2005; He et al., 2003; 2005; Uicker and Raicu, 1975), perimeter graphs (Ding and Huang, 2007; 2009), dividing and matching vertices (Zeng et al., 2014). This methods relate exclusively to the isomorphism of plane kinematic chains and do not cover spatial mechanisms. In study attempts to extend the research regarding the isomorphism of kinematic chains to the mechanisms of all groups by using new notation of spatial mechanisms.

DOI 10.1515/ama-2016-0029

2. METHODS FOR IDENTIFYING THE ISOMORPHISM OF KINEMATIC CHAINS

The isomorphism of the three seven-link kinematic chain spatial mechanisms with 1-DOM was investigated. The set of labels for those mechanisms in group 0 includes: {555555221, 555555311, 555554321, 555554411, 555554222, 555553331, 555553322, 555544421, 555544331, 555544322, 555543332, 555444431, 555444422, 555444332, 555443333, 554444441, 554444432, 554444333, 544444442, 544444433, 444444443}.

Researching isomorphism required that the mechanisms were presented in a form of diagrams and structural graphs, and the adjacency matrices were determined of which elements took the value of 1 when links were adjacent and 0 when links were not adjacent. The kinematic chains were marked C_1, C_2, C_3 and structural graphs G_1, G_2, G_3 respectively.

The kinematic chains as shown were used to illustrate a few isomorphism identification methods. The first method selected is the one in which the Hamming Number Technique is applied (Rao and Raju, 1991). This method defines a specific equivalence whereby number s_k= 0 is ascribed to two elements a_{ik}, a_{jk} in rows i, j and a column k when these elements are the same ($a_{ik} = a_{jk}$), or the number $s_k = a_{ik} + a_{jk}$, which is the sum of the numbers when the elements are different ($a_{ik} \neq a_{jk}$). For example, the number $s_1 = a_{11} + a_{21} = 1$ was calculated for an adjacency matrix M_{p1} where $a_{11} \neq a_{21}$. Then the Hamming number matrix has been generated with Hamming numbers as elements obtained from the following formula:

$$h_{ij} = \sum_{k=1}^{n} s_k \,. \tag{1}$$

The h_{12} element of the H_1 matrix is the sum of s_k numbers with k = 1,..., 7 ascribed to the elements a_{1k}, a_{2k} of the adjacency matrix M_{p1} (h_{12} = 1 + 1 + 1 + 1 + 0 + 1 + 1 = 6).

For adjacency matrices M_{p1}, M_{p2}, M_{p3} the three Hamming matrices H_1, H_2, H_3 were determined respectively.

When identifying the isomorphism of kinematic chains the following definitions are in use:

- the Hamming link which corresponds to the i – th link of a kinematic chain and is the sum of all elements in the i – th row of the Hamming matrix H. For example the Hamming link for the first link of a kinematic chain (see Fig.2a) is the number 28 obtained by summing up all elements from the first row of the Hamming matrix H_1,
- the Hamming chain for any kinematic chain is a sum of all Hamming links. The Hamming chain for H_1, H_2, H_3 matrixes equals the number 152,
- the string of the Hamming link for any i – th link of a kinematic chain is a string of numbers made up of the Hamming link and all the integers from *0* to n in the i – th row of the Hamming matrix (n is the dimension of the adjacency matrix and the Hamming matrix). For example, for the first row of the Hamming matrix H_1 a corresponding string of the Hamming link are the numbers: 28 and 13000111, where the Hamming link is 28 implying that the first row of the Hamming matrix H_1 comprises of one 7, three 6s, no 5s, no 4s, no 3s, one 2, one 1 and one 0,
- the Hamming chain string contains a Hamming chain and the Hamming chain strings in diminishing order.

$$H_1 = \begin{bmatrix} 0 & 6 & 1 & 7 & 2 & 6 & 6 \\ 6 & 0 & 5 & 1 & 4 & 2 & 0 \\ 1 & 5 & 0 & 6 & 3 & 5 & 5 \\ 7 & 1 & 6 & 0 & 5 & 1 & 1 \\ 2 & 4 & 3 & 5 & 0 & 4 & 4 \\ 6 & 2 & 5 & 1 & 4 & 0 & 2 \\ 6 & 0 & 5 & 1 & 4 & 2 & 0 \end{bmatrix}, \quad H_2 = \begin{bmatrix} 0 & 6 & 4 & 3 & 5 & 4 & 6 \\ 6 & 0 & 4 & 3 & 3 & 2 & 2 \\ 4 & 4 & 0 & 5 & 3 & 4 & 2 \\ 3 & 3 & 5 & 0 & 6 & 3 & 5 \\ 5 & 3 & 3 & 6 & 0 & 3 & 1 \\ 4 & 2 & 4 & 3 & 3 & 0 & 2 \\ 6 & 2 & 2 & 5 & 1 & 2 & 0 \end{bmatrix},$$

$$H_3 = \begin{bmatrix} 0 & 6 & 4 & 3 & 6 & 5 & 4 \\ 6 & 0 & 4 & 3 & 2 & 3 & 2 \\ 4 & 4 & 0 & 5 & 2 & 3 & 4 \\ 3 & 3 & 5 & 0 & 5 & 6 & 3 \\ 6 & 2 & 2 & 5 & 0 & 1 & 2 \\ 5 & 3 & 3 & 6 & 1 & 0 & 3 \\ 4 & 2 & 4 & 3 & 2 & 3 & 0 \end{bmatrix}.$$

The following sequences of Hamming chains have been obtained:

- matrix H_1 152, 28, 13000111, 18, 01110112, 25, 01301011, 21, 11100031, 22, 00131101, 20, 01110211, 18, 01110112,
- matrix H_2 152, 28, 02121001, 20, 01012201, 22, 00131101, 25,01203001, 21, 01103011, 18, 00022201, 18,01100311,
- matrix H_3 152, 28, 02121001, 20, 01012201, 22, 00131101, 25,01203001, 18, 01100311, 21, 01103011, 18, 00022201.

The ultimate criteria when identifying isomorphism is a comparison of the sequences of Hamming chains. In the case of the example discussed, the sequences of Hamming chains for H_2 and H_3 matrices are identical, hence the kinematic chains C_2, C_3 are identical in terms of structure.

Another method identifies the isomorphism of kinematic chains by applying eigensystem i.e. those kinematic chains are not isomorphic for which the eigenvalues of adjacency matrix are different (Chang et al., 2002; Cubillo and Wan, 2005; He et al., 2003; 2005; Uicker at al., 1975).

The following sequences of Hamming chains have been obtained:

- matrix H_1 152, 28, 13000111, 18, 01110112, 25, 01301011, 21, 11100031, 22, 00131101, 20, 01110211, 18, 01110112,
- matrix H_2 152, 28, 02121001, 20, 01012201, 22, 00131101, 25,01203001, 21, 01103011, 18, 00022201, 18,01100311,
- matrix H_3 152, 28, 02121001, 20, 01012201, 22, 00131101, 25,01203001, 18, 01100311, 21, 01103011, 18, 00022201.

The ultimate criteria when identifying isomorphism is a comparison of the sequences of Hamming chains. In the case of the example discussed, the sequences of Hamming chains for H_2 and H_3 matrices are identical, hence the kinematic chains C_2, C_3 are identical in terms of structure.

DOI 10.1515/ama-2016-0029

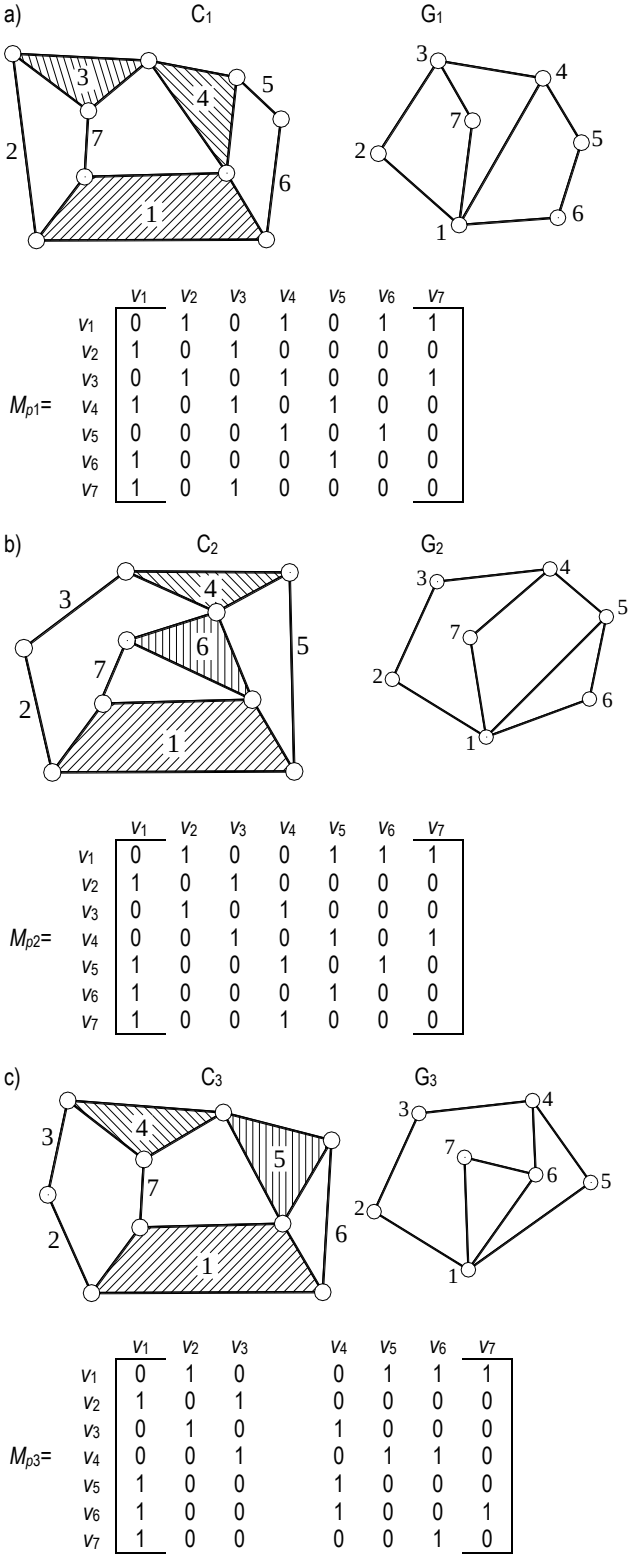

M_{p1}=

	v_1	v_2	v_3	v_4	v_5	v_6	v_7
v_1	0	1	0	1	0	1	1
v_2	1	0	1	0	0	0	0
v_3	0	1	0	1	0	0	1
v_4	1	0	1	0	1	0	0
v_5	0	0	0	1	0	1	0
v_6	1	0	0	0	1	0	0
v_7	1	0	1	0	0	0	0

M_{p2}=

	v_1	v_2	v_3	v_4	v_5	v_6	v_7
v_1	0	1	0	0	1	1	1
v_2	1	0	1	0	0	0	0
v_3	0	1	0	1	0	0	0
v_4	0	0	1	0	1	0	1
v_5	1	0	0	1	0	1	0
v_6	1	0	0	0	1	0	0
v_7	1	0	0	1	0	0	0

M_{p3}=

	v_1	v_2	v_3	v_4	v_5	v_6	v_7
v_1	0	1	0	0	1	1	1
v_2	1	0	1	0	0	0	0
v_3	0	1	0	1	0	0	0
v_4	0	0	1	0	1	1	0
v_5	1	0	0	1	0	0	0
v_6	1	0	0	1	0	0	1
v_7	1	0	0	0	0	1	0

Fig. 2. Seven-link kinematic chains of mechanisms presented in a form of structural diagrams, adjacency matrices and structural graphs

The following sequences of Hamming chains have been obtained:

- matrix H_1 152, 28, 13000111, 18, 01110112, 25, 01301011, 21, 11100031, 22, 00131101, 20, 01110211, 18, 01110112,
- matrix H_2 152, 28, 02121001, 20, 01012201, 22, 00131101, 25,01203001, 21, 01103011, 18, 00022201, 18,01100311,
- matrix H_3 152, 28, 02121001, 20, 01012201, 22, 00131101, 25,01203001, 18, 01100311, 21, 01103011, 18, 00022201.

The ultimate criteria when identifying isomorphism is a comparison of the sequences of Hamming chains. In the case of the example discussed, the sequences of Hamming chains for H_2 and H_3 matrices are identical, hence the kinematic chains C_2, C_3 are identical in terms of structure.

Another method identifies the isomorphism of kinematic chains by applying eigensystem i.e. those kinematic chains are not isomorphic for which the eigenvalues of adjacency matrix are different (Chang et al., 2002; Cubillo and Wan, 2005; He et al., 2003; 2005; Uicker at al., 1975).

For the adjacency matrix discussed (Fig.2) the following eigenvalues were obtained: M_{p1}: 0.441, -0.441, 0, -1.178, 1.178, -2.724, 2.724, M_{p2}: -1.751, -0.934, -2.165, 0.252, 0.708, 1.157, 2.733, M_{p3}: 0.708, 0.252, 1.157, -0.034, -1.751, -2.165, 2.733. As the eigenvalues for C_1 are different from those obtained for C_2 and C_3 , the kinematic chain C_1 is not isomorphic with the C_2 and C_3 chains. To identify the isomorphism of C_2 and C_3 it is necessary to determine the eigenvectors. If the eigenvectors are not equivalent, the chains are structurally different. The eigenvalues and eigenvectors for C_2 and C_3 are presented in Tab. 1. The kinematic chains C_2 and C_3 have the same eigenvalues and corresponding eigenvectors, hence they are isomorphic.

Tab. 1. Eigenvalues and eigenvectors for kinematic chains C_2 and C_3

C_2	Eigenvalues						
	-1.751	-0.934	-2.165	0.252	0.708	1.157	2.733
	Eigenvectors						
	0.421	-0.121	0.52	0.346	0.28	-0.259	0.523
	-0.535	-0.268	-0.17	0.088	0.659	0.307	0.279
	0.516	-0.371	-0.151	-0.324	0.186	0.614	0.24
	-0.368	-0.079	0.498	-0.17	-0.527	0.403	0.377
	0.159	-0.512	-0.456	-0.417	-0.21	-0.272	0.461
	-0.331	0.679	-0.029	-0.281	0.098	-0.459	0.36
	-0.03	0.215	-0.47	-0.697	-0.349	0.125	0.329
C_3	Eigenvalues						
	0.708	0.252	1.157	-0.034	-1.751	-2.165	2.733
	Eigenvectors						
	0.28	0.346	0.259	0.121	0.421	0.52	-0.523
	0.659	0.088	-0.307	0.268	-0.535	-0.17	-0.279
	0.186	-0.324	-0.614	-0.371	0.516	-0.151	-0.24
	-0.529	-0.17	-0.403	0.079	-0.368	0.498	-0.377
	-0.349	0.697	-0.125	-0.215	-0.03	-0.47	-0.329
	-0.21	-0.417	0.272	0.512	0.159	-0.456	-0.461
	0.098	-0.281	0.459	-0.697	-0.331	-0.029	-0.36

Graphs such as: perimeter, canonical perimeter, characteristic perimeter, together with adjacency matrices obtained for each individual graph are used by the authors of yet another kinematic chain isomorphism identifying method (Ding and Huang, 2007; 2009). The loops that form a given kinematic chain constitute the base for research. Tab. 2 presents six loops which were obtained for each kinematic chain. In further discussions the key elements are the loops with the highest number of links i.e. the longest. The kinematic chain C_1 takes two loops i.e. K_3 and K_5, whereas kinematic chains C_2 and C_3 take the K_3 loop.

DOI 10.1515/ama-2016-0029

Tab. 2. Loops forming kinematic chains in Fig. 3

Loops	Kinematic chain C_1	Kinematic chain C_2	Kinematic chain C_3
K_1	1 2 3 7 1	1 2 3 4 7 1	1 2 3 4 5 1
K_2	1 2 3 4 1	1 2 3 4 5 1	1 2 3 4 6 1
K_3	1 2 3 4 5 6 1	1 2 3 4 5 6 1	1 2 3 4 6 7 1
K_4	1 7 3 4 1	1 7 4 5 1	1 7 6 1
K_5	1 7 3 4 5 6 1	1 7 4 5 6 1	1 7 6 4 5 1
K_6	1 4 5 6 1	1 5 6 1	1 6 4 5 1

Perimeter graphs were formed adopting the longest loop as external. The K_3 loop was selected for all kinematic chains (Fig.3).

a) 1234561

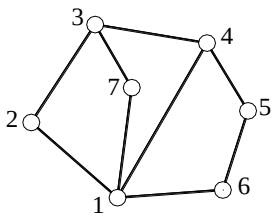

$$M_{p1} = \begin{bmatrix} 0 & 1 & 0 & 1 & 0 & 1 & 1 \\ 1 & 0 & 1 & 0 & 0 & 0 & 0 \\ 0 & 1 & 0 & 1 & 0 & 0 & 1 \\ 1 & 0 & 1 & 0 & 1 & 0 & 0 \\ 0 & 0 & 0 & 1 & 0 & 1 & 0 \\ 1 & 0 & 0 & 0 & 1 & 0 & 0 \\ 1 & 0 & 1 & 0 & 0 & 0 & 0 \end{bmatrix}$$

b) 1234561

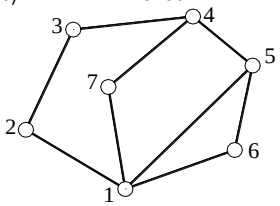

$$M_{p2} = \begin{bmatrix} 0 & 1 & 0 & 0 & 1 & 1 & 1 \\ 1 & 0 & 1 & 0 & 0 & 0 & 0 \\ 0 & 1 & 0 & 1 & 0 & 0 & 0 \\ 0 & 0 & 1 & 0 & 1 & 0 & 1 \\ 1 & 0 & 0 & 1 & 0 & 1 & 0 \\ 1 & 0 & 0 & 0 & 1 & 0 & 0 \\ 1 & 0 & 0 & 1 & 0 & 0 & 0 \end{bmatrix}$$

c) 1234671 1234561

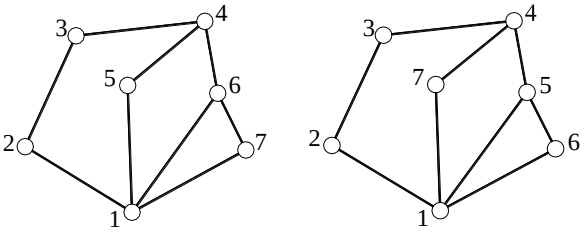

$$M_{p3} = \begin{bmatrix} 0 & 1 & 0 & 0 & 1 & 1 & 1 \\ 1 & 0 & 1 & 0 & 0 & 0 & 0 \\ 0 & 1 & 0 & 1 & 0 & 0 & 0 \\ 0 & 0 & 1 & 0 & 1 & 0 & 1 \\ 1 & 0 & 0 & 1 & 0 & 1 & 0 \\ 1 & 0 & 0 & 0 & 1 & 0 & 0 \\ 1 & 0 & 0 & 1 & 0 & 0 & 0 \end{bmatrix}$$

Fig. 3. Structural graphs: perimeter = canonical perimeter and adjacency matrix for the C_1 chain (a), perimeter = canonical perimeter and adjacency matrix for the C_2 chain (b),perimeter, canonical perimeter and adjacency matrix for the C_3 chain (c)

The structural graphs in Figs. 2a and 2b are simultaneously perimeter graphs in Figs. 3a and 3b. Renumbering the vertices so that each external vertex takes a consecutive integer transforms a perimeter graph into a canonical perimeter graph. By analogy, for consecutive longest loops two graphs are formed. In the example for both loops K_2 and K_3 the same canonical perimeter graph was obtained. For a graph with several elements in the canonical adjacency matrix set, the matrix with the highest number of the binary string contained in the upper-right triangle of the matrix in the canonical adjacency matrix is defined as characteristic adjacency matrix, and the corresponding canonical perimeter graph is defined as characteristic perimeter graph. If for any two given graphs their characteristic perimeter graphs are identical, then the graphs are regarded as isomorphic. In the example the canonical perimeter matrices are identical for C_2 and C_3 hence these kinematic chains are isomorphic.

In another method for detecting the isomorphism of kinematic chains, the authors applied structural graphs and adjacency matrices (Zeng, 2014). Within an adjacency matrix the sub-blocks were selected which are defined as square sub-matrices of the adjacency matrix along the principal diagonal (Fig 4). The degrees of vertices of a graph are organised in a descending sequence making up lists denoted as List (d). If lists are different, the graphs are not isomorphic. In the case in question the degree lists for graphs G_1, G_2, G_3 are identical and form a list {4, 3, 3, 2, 2, 2, 2}. Each list of the List (d) constitutes the base for an adjacency matrix and the lists' vertices follow the order set up by the lists. Within those matrices, sub-blocks made by vertices of the same degree are selected (Fig. 5a,b,c). Then in the sub-blocks for individual vertices a sum of squares of degrees of the vertices adjacent to them is calculated, which is called the expanded square degree of the vertex and denoted by S. For example, in the sub-block made up by vertices {v_2, v_3, v_4} in Fig. 4 the vertex v_2 has one adjacent vertex v_3; vertex v_3 has two adjacent vertices v_2 and v_4; vertex v_4 has one adjacent vertex v_3. Thus the sum S of the vertex v_2 is the square of degree of v_3 and equal to four, S of v_3 is the sum of squares of the degrees of v_2 and v_4 and equal to five; S of v_4 is the square of the degree of v_3 and equal to four.

In the next step a list of expanded square degrees is created, which contains the descending sequence of S sums of all vertices in a sub-block and is denoted as List (S). For the sub-block {v_2,v_3,v_4} in Fig.4 the list(S) is {5,4,4} and corresponds to vertices {v_3,v_4,v_2}.

M_{p1}=

	v_1	v_2	v_3	v_4	v_5	v_6	v_7
v_1	0	1	0	1	0	1	1
v_2	1	0	1	0	0	0	0
v_3	0	1	0	1	0	0	1
v_4	1	0	1	0	1	0	0
v_5	0	0	0	1	0	1	0
v_6	1	0	0	0	1	0	0
v_7	1	0	1	0	0	0	0

Fig. 4. Exemplary sub-blocks obtained for graph G_1

The equivalence of the expanded square degree lists is a necessary condition for isomorphism. For individual graphs (Fig. 5 a,b,c), the expanded square degree lists were established for three sub-blocks. The following was obtained:

- G_1: List(S) sub-block {v_1} – {0}; List(S) sub-block {v_3,v_4} – {4,4}; List(S) sub-block {v_2,v_5,v_6,v_7} – {1,1,0,0} corresponding to vertices {v_5,v_6,v_2,v_7},
- G_2: List(S) sub-block {v_1} – {0}; List(S) sub-block {v_4,v_5} – {4,4}; List(S) sub-block {v_2,v_3,v_6,v_7} – {1,1,0,0},
- G_3: List(S) sub-block {v_1} – {0}; List(S) sub-block {v_4,v_6} – {4,4}; List(S) sub-block {v_2,v_3,v_5,v_7} – {1,1,0,0}.

DOI 10.1515/ama-2016-0029

a)

M_{p1}=	v_1	v_3	v_4	v_2	v_5	v_6	v_7
v_1	0	0	1	1	0	1	1
v_3	0	0	1	1	0	0	1
v_4	1	1	0	0	1	0	0
v_2	1	1	0	0	0	0	0
v_5	0	0	1	0	0	1	0
v_6	1	0	0	0	1	0	0
v_7	1	1	0	0	0	0	0

b)

M_{p2}=	v_1	v_4	v_5	v_2	v_3	v_6	v_7
v_1	0	0	1	1	0	1	1
v_4	0	0	1	0	1	0	1
v_5	1	1	0	0	0	1	0
v_2	1	0	0	0	1	0	0
v_3	0	1	0	1	0	0	0
v_6	1	0	1	0	0	0	0
v_7	1	1	0	0	0	0	0

c)

M_{p3}=	v_1	v_3	v_4	v_2	v_5	v_6	v_7
v_1	0	0	1	1	0	1	1
v_3	0	0	1	0	1	1	0
v_4	1	1	0	0	0	0	1
v_2	1	0	0	0	1	0	0
v_5	0	1	0	1	0	0	0
v_6	1	1	0	0	0	0	0
v_7	1	0	1	0	0	0	0

d)

M_{p1}=	v_1	v_3	v_4	v_5	v_6	v_2	v_7
v_1	0	0	1	0	1	1	1
v_3	0	0	1	0	0	1	1
v_4	1	1	0	1	1	0	0
v_5	0	0	1	0	1	0	0
v_6	1	0	0	1	0	0	0
v_2	1	1	0	0	0	0	0
v_7	1	1	0	0	0	0	0

e)

M_{p2}=	v_1	v_3	v_4	v_2	v_5	v_6	v_7
v_1	0	0	1	1	0	1	1
v_3	0	0	1	0	1	0	1
v_4	1	1	0	0	0	1	0
v_2	1	0	0	0	1	0	0
v_5	0	1	0	1	0	0	0
v_6	1	0	1	0	0	0	0
v_7	1	1	0	0	0	0	0

f)

M_{p3}=	v_1	v_3	v_4	v_5	v_6	v_2	v_7
v_1	0	0	1	1	0	1	1
v_3	0	0	1	0	1	1	0
v_4	1	1	0	0	0	0	1
v_5	1	0	0	0	1	0	0
v_6	0	1	0	1	0	0	0
v_2	1	1	0	0	0	0	0
v_7	1	0	1	0	0	0	0

Fig. 5. Adjacency matrices with sub-blocks: according to List(d) for graphs G_1 (a), G_2 (b), G_3 (c), according to List(S) for graphs G_1 (d), G_2 (e), G_3 (f)

According to the lists the vertices of the same expanded square degree make a sub-block (Fig. 5d,e,f). For example, after obtaining List (S), the vertices in sub-blocks in Fig.5a form sub-blocks in Fig.5d. Then the correlations between individual sub-blocks within an adjacency matrix is investigated. For this purpose the correlation degree is defined and denoted as $v_i(g_m)$. It specifies the number of vertices from the g_m sub-block which the v_i vertex from the g_n sub-block is adjacent to. In the adjacency matrix in Fig.5d, for example, there are four sub-blocks denoted as g_1, g_2, g_3, g_4. The vertex v_4 in g_2 has one adjacent vertex v_5 in g_3, hence $v_4(g_3) = 1$. Another correlation degree list from g_n to g_m is made and denoted as List($g_n(g_m)$) with correlation degrees $v_i(g_m)$ in descending sequence of vertices in the g_n sub-block. The following correlation lists have been obtained for sub-blocks shown in Fig.5d, e, f:

- graph G_1: List($g_1(g_2)$) - {1}, List($g_1(g_3)$) - {1}, List($g_1(g_4)$) - {2}, List($g_2(g_3)$) - {1,0} corresponding to vertices {v_4,v_3}, List($g_2(g_4)$) - {2,0} corresponding to vertices v_3, v_4, List($g_3(g_4)$) - {0,0},
- graph G_2: List($g_1(g_2)$) - {1}, List($g_1(g_3)$) - {1}, List($g_1(g_4)$) - {2}, List($g_2(g_3)$) - {1,0} corresponding to vertices v_4, v_6, (List($g_2(g_4)$) - {1,1}, List($g_3(g_4)$) - {0,0},
- graph G_3: List($g_1(g_2)$) - {1}, List($g_1(g_3)$) - {1}, List($g_1(g_4)$) - {2}, List($g_2(g_3)$) - {1,0} corresponding to vertices v_4, v_5, List($g_2(g_4)$) - {1,1}, List($g_3(g_4)$) - {0,0}.

The equivalence of the correlation degree lists of graphs is a necessary condition for isomorphism. The correlation degree list for the G_1 graph is not equivalent with the lists for G_2 and G_3 , hence the G_1 graph is not isomorphic with the G_2 and G_3.

Each vertex of the adjacency matrix of the G_2 and G_3 graphs belongs to the same sub-block made via the expanded square degree division and via the correlation degree division in both matrices, which means that both matrices are equal and that the G_2 and G_3 graphs are isomorphic.

3. RESEARCHING THE ISOMORPHISM OF SPATIAL CHAINS

Methods presented in Chapter II relate exclusively to the isomorphism of plane kinematic chains and do not cover spatial mechanisms. It is mainly because the base in these methods are diagrams in which kinematic pairs are noted by one symbol i.e. a circle. This is possible only for plane mechanisms whereby both the revolute and prismatic kinematic pairs are noted with such a symbol.

For spatial mechanisms the class of kinematic pairs has to be considered in their structural diagrams. As an example in the parallel mechanism presented in Fig.6 there are four kinematic pairs of class III (The class of kinematic pairs depends on the number of parameters of kinematic bonds which a given pair imposes on the motion that one link can make in relation to the other. A link's free motion can be described by six parameters such as three revolutions and three translations along the orthogonal axis of the coordinate system. Each independent move which one link is able to make in relation to the other is called a degree of freedom W. Any constraints imposed on that movement is called a parameter of a kinematic bond H with values ranging from 1 to 5. Thus W=6-H. Hence a kinematic pair that enables one revolution or one translation is a pair of class V, as five out of its six degrees of freedom have been restricted. The pair of class IV means that four parameters of a kinematic bond have been imposed, the remaining two determine two degrees such as, for example, a revolution and a translation.) (three spherical pairs at the platform which make three revolutions around a coordinate axis possible and one at the base enabling two translations and one revolution), one kinematic pair of class IV (the pair at the base enabling a translation and a revolution) and one pair of class V (at the base enabling one revolution). Hence a structural diagram of these mechanisms contains information about the class of kinematic pairs (Fig. 6b).

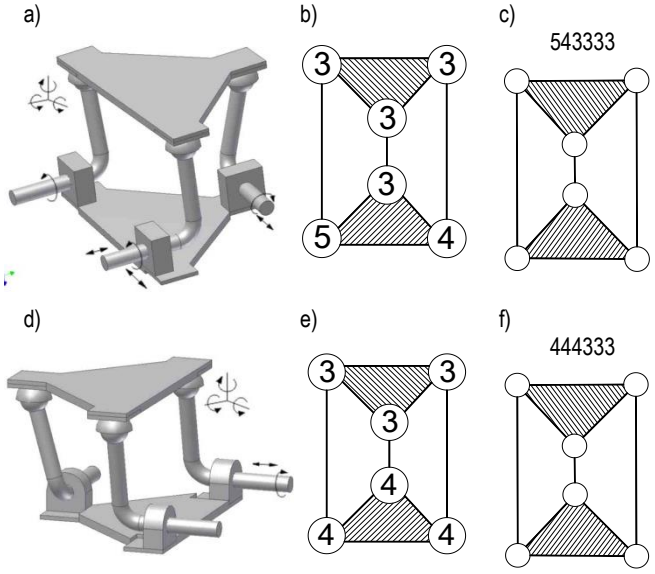

Fig. 6. Parallel mechanisms (a, d) in the traditional (b, e) and in the generalised structural notation (c, f)

DOI 10.1515/ama-2016-0029

Structural analysis of spatial mechanisms indicates that the mechanisms can be grouped according to the same graphic notation in which individual mechanisms differ in the classes of kinematic pairs (Romaniak, 2010; 2011; Uicker and Raicu, 1975). For example, the parallel mechanism in Fig. 6d can have a graphic representation corresponding to the parallel mechanism in Fig.6a having provided appropriate classes of kinematic pairs. A new generalised notation for spatial mechanisms has been proposed whereby classes of kinematic pairs are noted in a form of labels next to a graphic diagram (Fig. 6c, f).

Splitting the structural notation of spatial mechanisms into two parts i.e. graphic representation and a label enables the structural research used for plane mechanisms to be applied to spatial chains whose graphic diagram is identical to that of plane mechanisms. Therefore the methods of structural synthesis as well as methods for researching the chains' isomorphism, presented in Chapter II, can be used in here. Closely linked with the graphic diagram and determined following current structural formula, the labels are the sequences of numbers whose isomorphism is easy enough to check.

The proposed notation of spatial mechanisms attempts to extend the research regarding the isomorphism of kinematic chains to the mechanisms of all groups. However, it is not an ideal method as the notation in a form of a graphic diagram and a label provides a certain set of solutions restricted to various locations of kinematic pairs in a given diagram (Fig. 7).

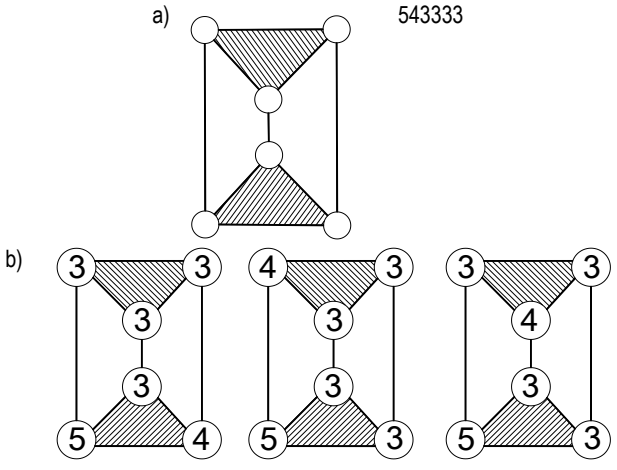

Fig. 7. A parallel mechanism with the three non-isomorphic solutions (b) obtained from the generalized notation (a)

After linking the graphic notation with labels the solutions obtained need to be checked again in order to eliminate isomorphic chains.

4. CONCLUSIONS

A rapidly increasing number of new methods applied to the issue of identifying the isomorphism of mechanisms reflects the researchers' efforts to obtain a precise result in the shortest time possible. In the examples presented in this paper an attempt has been made to expand the area of research to include spatial mechanisms. It has been made possible by applying a special notation for spatial chains, in which the classes of kinematic pairs are noted next to their graphic representations. Thus the research for diagrams and the labels is carried out separately, and then any method developed for flat chains can successfully be used when graphic representation is concerned. Every method discussed herein leads to an equally correct solution in terms of the isomorphism of the chains presented. Although eliminating chains of the same graphic representation, those methods do not fully sort out the problem of duplicating spatial kinematic chains. What remains to be checked is the isomorphism of chains after graphic representation has been joined with labels. Then structurally identical solutions need to be selected and eliminated.

REFERENCES

1. **Chang Z. Zhang C., Yang Y., Wang Y.** (2002), A New Method to Mechanism Kinematic Chain Isomorphism Identification, *Mechanism and Machine Theory,* 37, 411-417.
2. **Cubillo J. P., Wan J**. (2005), Comments on Mechanism Kinematic Chain Isomorphism Identification Using Adjacent Matrices, *Mechanism and Machine Theory,* 40, 131-139.
3. **Ding H., Hou F., Kecskemethy A., Huang Z.** (2011), Synthesis of a complete set of contracted graphs for planar non-fractionated simple-jointed kinematic chains with all possible DOFs, *Mechanism and Machine Theory,* 46(11), 1588-1600.
4. **Ding H., Hou F., Kecskemethy A., Huang Z.** (2012) Synthesis of the Whole Family of planar 1-DOF kinematic chains and Creation of Their Atlas Databases, *Mechanism and Machine Theory*, 47(1), 1-15.
5. **Ding H., Huang Z.** (2007), The Establishment of the Canonical Perimeter Topological Graph of Kinematic Chains and Isomorphism Identification, *Journal of Mechanical Design*, 129, 915-923.
6. **Ding H., Huang Z.** (2009), Isomorphism Identification of Graphs: Especially for the Graphs of Kinematic Chains, *Mechanism and Machine Theory*, 44, 122-139.
7. **He P. R., Zhang W. J., Li Q.** (2005), Some Further Development on the Eigensystem Approach for Graph Detection, *Journal of the Franklin Institute*, 342, 657-673.
8. **He P. R., Zhang W. J., Li Q., Wu F. X.** (2003) A New Method for Detection of Graph Isomorphism Based on the Quadratic Form, *Journal of Mechanical Design*, 125, 640-642.
9. **Rao A. C, Raju D**. (1991), Application of the Hamming Number Technique to Detect Isomorphism Among Kinematic Chains and Inversions, *Mechanism and Machine Theory*,26, 55-75.
10. **Romaniak K**. (2010), Generalized Methods of Kinematic Chains Structural Synthesis, *International Journal of Applied Mechanics and Engineering*, 15(3), 821-829.
11. **Romaniak K.** (2011), *Methods of Structural Synthesis of Mechanisms* (in Polish), Wydawnictwo ATH w Bielsku-Białej, Bielsko-Biała.
12. **Romaniak K.** (2011), Structural Synthesis of Parallel Mechanisms (in Polish), *Modelowanie Inżynierskie*, 11(42), 359-367.
13. **Uicker J. J., Raicu A.** (1975), A Method for the Identification Recognition of Equivalence of Kinematic Chains, *Mechanism and Machine Theory*, 10, 375-383.
14. **Zeng K., Fan X., Dong M., Yang P.** (2014), A fast algorithm for kinematic chain isomorphism identification based on dividing and matching vertices, *Mechanism and Machine Theory*, 72, 25-38.

DE GRUYTER
OPEN

DOI 10.1515/ama-2016-0030

acta mechanica et automatica, vol.10 no.3 (2016)

THE FEM ANALYSIS OF STRESS DISTRIBUTION IN FRONT OF THE CRACK TIP AND FRACTURE PROCESS IN THE ELEMENTS OF MODIFIED AND UNMODIFIED CAST STEEL G17CrMo5-5

Robert PAŁA*, Ihor DZIOBA*

*Department of Machine Design Fundamentals, Faculty of Mechatronics and Machine Design, Kielce University of Technology, Al. 1000-lecia PP 7, 25-314 Kielce, Poland

rpala@tu.kielce.pl, pkmid@tu.kielce.pl

received 4 May 2015, revised 15 July 2016, accepted 18 July 2016

Abstract: The article presents influence of modification of the low-alloy cast steel G17CrMo5-5 by rare earth metals on stress distribution in front of the crack at the initial moment of the crack extension. Experimental studies include determination of strength and fracture toughness characteristics for unmodified (UM) and modified (M) cast steel. In the numerical computations, experimentally tested specimens SEN(B) were modelled. The true stress–strain curves for the UM and M cast steel are used in the calculation. The stress distributions in front of the crack were calculated at the initial moment of the crack extension. On the basis of data on the particle size inclusions in the UM and M cast steel, and the calculated stress distributions was performed an assessment of the possibility of the occurrence of cleavage fracture. The analysis results indicate that at room temperature for the UM cast steel, there is a possibility of cleavage fracture, while for the M cast steel occurrence of cleavage fracture is negligible.

Keywords: Fracture Toughness, Stress Distributions in Front of the Crack, Cast Steel, Fracture Mechanisms

1. INTRODUCTION

Elements made of low-alloy cast steel are widely used in different branches of industry, especially in power industry. One main problem observed during utilization of these elements was occurence of a sudden destruction. In the studies (Bolanowski, 2005; Gajewski and Kasińska, 2009; Heon et al., 2006; Luniov, 2002) were received wide scatter intervals of the impact energy data. The modification of cast steels by rare earth metals (REM) leads to an increase of mechanical properties (Gajewski and Kasińska, 2009; Kasińska, 2014). These changes were caused by microstructure transformations, which were occurred because of adding the REM. For low-alloy cast steel G17CrMo5-5, especially a significant increase was obtained for the fracture toughness characteristics (Dzioba et al., 2015).

According to the local approach to fracture, the fracture process begins if the level of stresses (or strains) in front of the crack, exceeds the critical value on the critical distance (Beremin, 1983; McClintok, 1968; Ritchie et al., 1973; Seweryn, 1994). By Ritchie-Knott-Rice's modified criterion, the fracture process occurs if the tensile (opening) stresses in front of the crack exceed the critical value at the critical distance (Dzioba et al., 2010; Neimitz et al., 2010).

In the present study, the authors focused on the analysis of the process of cast steel cracking G17CrMo5-5 in an original condition (UM) and after modification of the REM (M). Main objective of the analysis is to evaluate the possibility of the occurrence of cleavage fracture in the tested types of steel. The analysis was based on the approach taking into account stress values, that arised in front of the crack tip, and microstructural constituents of the material - particle sizes, the particle size of the inclusions (Dzioba, 2011; 2012).

2. TEST METHODS AND MECHANICAL PROPERTIES OF G17CrMo5-5 CAST STEEL

Experimental studies including determination of strength and fracture toughness characteristics were carried out on two melts of the low-alloy cast steel G17CrMo5-5 (Tab. 1) (EN–10213–2:1999). The difference between the two melts based on a modification of one of them with the addition of rare earth metals (REM), introduced in the form of mischmetals, having the following composition: 49.8% Ce, 21.8% La, 17.1% Nd, 5.5% Pr, 5.35% the remainder of REM. Heat treatment after casting included normalizing (940 ^{0}C) for 1 hour and tempering (710 ^{0}C) for 2 hours (Gajewski and Kasińska, 2009; Kasińska, 2014).

Tab. 1. Chemical composition of the low-alloy cast steel G17CrMo5-5

C	Si	Mn	Cr	Mo	Ni	Al	S	P
0.17	0.4	0.6	1.2	0.53	0.1	0.034	0.012	0.018

Modified and unmodified cast steel after a heat treatment has a ferritic-pearlitic-bainitic microstructure. An addition of REM to alloy caused a reduction of an average grain size. The modification also caused changes in the morphology of nonmetallic inclusions. Irregular shape of nonmetallic inclusions of the UM cast steel changed to spherical (Fig. 1) (Gajewski and Kasińska, 2009; Kasińska, 2014).The sizes of the spherical particles are smaller (about twice) and they are uniformly dispersed in the metal matrix for the M cast steel (Fig. 2) (Gajewski and Kasińska, 2009; Kasińska, 2014).

DOI 10.1515/ama-2016-0030

a) b)

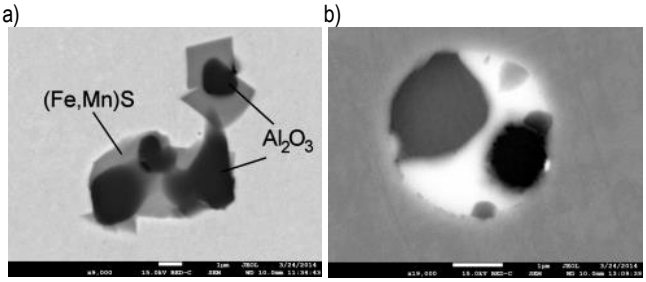

Fig. 1. Shape of nonmetallic inclusions in cast steel G17CrMo5-5: a) irregular – for UM; b) spheroidal – for M (Gajewski and Kasińska, 2009)

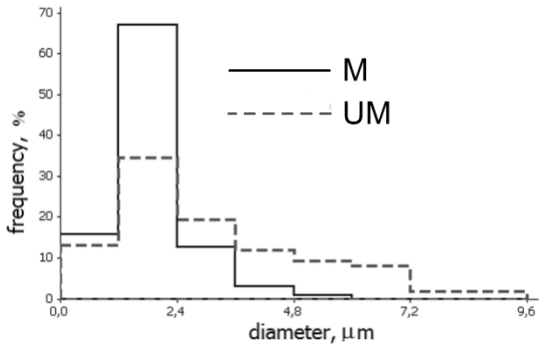

Fig. 2. The size distributions of the inclusions, d_i, in UM and M cast steel

All tests were performed at temperature T_{test}=+20 ^{0}C. Strength characteristics were determined in the uniaxial tensile test on the standard, 5-times round specimens on the testing machine UTS/Zwick-100, which is equipped with an automated control and data recording system. The tensile specimens were cut-out directly from the tested SEN(B) specimens. The results are shown in Tab. 2, where σ_0 is a yield strength, σ_u is an ultimate strength, n is a power exponent in the Ramberg-Osgood law, A_5 is an elongation, Z is an area reduction. We can observe that modification by REM of the cast steel caused an increase of strength characteristics and plasticity.

Tab. 2. Strength characteristics of the UM and M cast steel G17CrMo5-5

Specimens	σ_0 MPa	σ_u MPa	n	A_5 %	Z %
UM_1	444	587	12.08	19	52
UM_2	442	595	11.47	19	62
UM_3	441	596	11.47	20	59
Average	**442**	**593**	**11.67**	**19.7**	**58**
M_2	468	620	12.45	22	69
M_3	457	618	11	22	56
Average	**463**	**619**	**11.73**	**22**	**63**

Fracture toughness was determined on the SEN(B) specimens: B=12 mm, W=24 mm, S=96 mm. Fatigue cracks were derived from the notches. During derivation of the fatigue cracks, loading was performed on the testing machine MTS-250 under conditions of controlled force and at a frequency of 20 Hz. In accordance with the requirements of the standard (ASTM E1820-09), the length of the fatigue crack was about 1.5 mm, and the total dimension of the notch and the fatigue crack was about a_0/W≈0.5. The method of a potential drop changing was used to measure the growth of the crack length during the test (ASTM E1737-96). In case of the specimens made of the UM cast steel after ductile crack growth, occurred a brittle fracture. However a ductile extension of the crack was large (Fig. 3), so that it enabled to determine the J_R curve (Fig. 4). For the M cast steel was observed a fully ductile increment of the crack extension, in the whole range of loading (Fig. 3). The J_R resistance curves for the M cast steel are placed higher than the J_R resistance curves for the UM (Fig. 4). The critical values of J integral, J_C, and values at the initial moment of the crack extension, J_i, for the tested specimens are presented in Tab. 3.

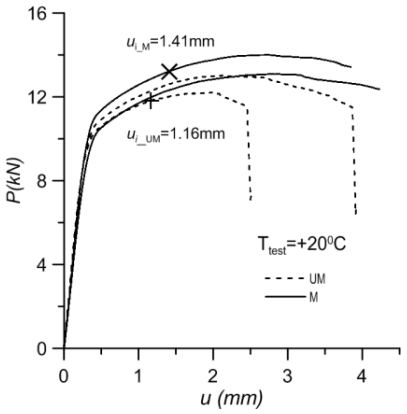

Fig. 3. Load-displacement curves of the M and UM cast steel and points coresponding to the J_i values

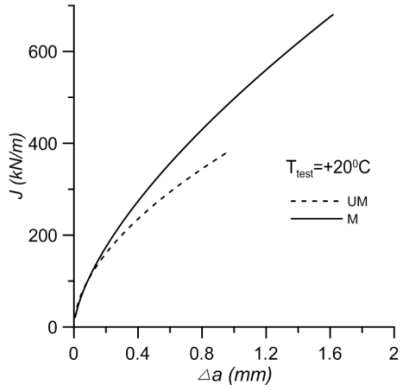

Fig. 4. J_R curves for the M and UM cast steel for the specimens analyzed in FEM

Tab. 3. J_i and J_C values for the M and UM cast steel (* - the spesimen analyzed in FEM)

Specimens	J_i kN/m	J_C kN/m	Type of crack extension, length of crack extantion
UM_17	194	299	Ductile-Brittle; Δa_D=1.80mm
UM_18*	160	246	Ductile-Brittle; Δa_D=0.87mm
Average UM	**177**	**273**	
M_16	210	317	Fully Ductile
M_18*	207	312	Fully Ductile
Average M	**209**	**315**	

DOI 10.1515/ama-2016-0030

3. NUMERICAL ANALYSIS OF STRESS DISTRIBUTIONS IN FRONT OF THE CRACK

Numerical analysis was performed on SEN(B) specimens. Computations were carried out in Adina 8.9. The ¼ part of the three-dimensional specimen was modeled, because two symmetry planes exist. The specimen in thickness direction was divided into ten layers. The layers became thinner in the direction of the free surface. This was caused by a greater gradient of the component stress changes near the side surface of the specimen. Tip of the crack was modeled as a quarter of an arc of a radius 10 μm. The finite element mesh size was reduced in the radial direction to the crack tip. In the computations there were used 20-nodal three-dimensional finite elements. The load in calculation was defined by a displacement of the loading roll of the testing machine at the moment, which corresponded to the J-integral value, at the initiation of crack extension. Those moments are points on the load-displacement curves for the UM (u_{i_UM}) and M (u_{i_M}) cast steel (Fig. 3). In computation the load increased linearly to reach a certain value. The real σ-ε curves derived on the basis of the plots obtained during uniaxial tensile tests for the UM and M cast steel (Fig. 5), which were used in FEM calculation. The model of a large strain was adopted.

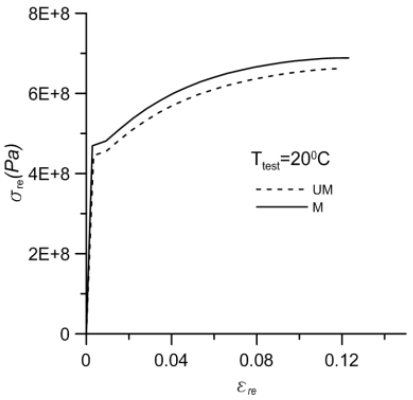

Fig. 5. Plot of modeled materials used in numerical computations – true σ-ε curves

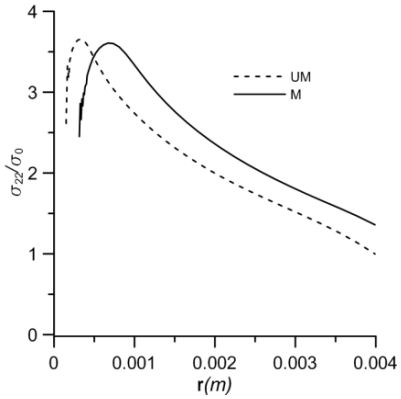

Fig. 6. Normalized opening stresses distribution in the specimen axis

The stress distributions in front of the crack tip σ_{11}, σ_{22}, σ_{33} in the particular layers were obtained. The value of the maximum opening stresses, σ_{22}, for the UM and M cast steel reaches the highest level ~3.6σ_0 in the axis of the specimen (Fig. 6). The maximum opening stresses decrease with a distance in a direction to a free surface of the specimens (Figs. 6-9). However, a lower max levels of the opening stresses in the thickness direction obtained for the SEN(B) specimens made of the M cast steel (Figs. 6-9).

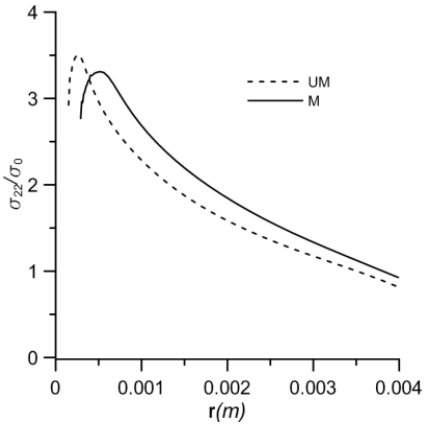

Fig. 7. Normalized opening stresses distribution in the 5th layer

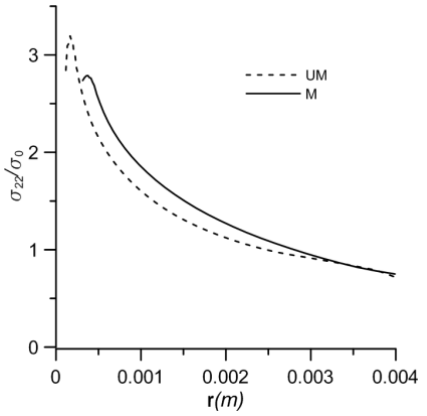

Fig. 8. Normalized opening stresses distribution in the 8th layer

Parameters of the triaxiality stress state in front of the crack at the critical moment for the UM and M cast steel were calculated. The parameters T_z (Guo, 1993) and *3R* (Rice and Tracey, 1969) are used in fracture mechanics to evaluate the triaxiality stress state level. The weighted average value of T_z – $T_{m,}$ and the weighted average value of *3R* – $3R_m$ were proposed to evaluate the triaxiality stress state in the paper (Neimitz et al., 2015). These parameters take into account the specimen thickness.

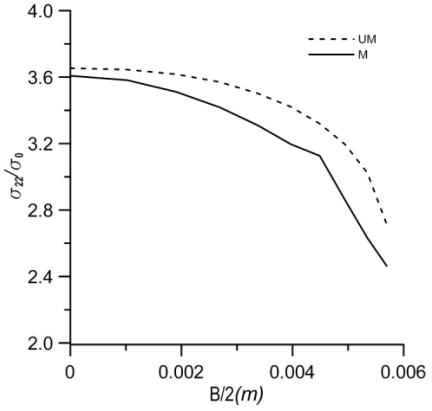

Fig. 9. Distribution of the maximum values of the normalized opening stresses in thickness direction

DOI 10.1515/ama-2016-0030

$$T_{\mathrm{z}} = \frac{\sigma_{33}}{\sigma_{11}+\sigma_{22}}, \quad (1)$$

$$T_{\mathrm{m}} = \frac{2}{B}\sum_{i=1}^{10} T_{\mathrm{z}i}B_i\,, \quad (2)$$

$$3R = \frac{(\sigma_{11}+\sigma_{22}+\sigma_{33})/3}{\sigma_0}\,, \quad (3)$$

$$3R_{\mathrm{m}} = \frac{2}{B}\sum_{i=1}^{10} 3R_iB_i, \quad (4)$$

where: σ_{11}, σ_{22}, σ_{33} are stress components in the stress plane, opening and in the thickness direction, respectively; σ_0 is a yield stress; *i* is a layer number; *B* is a layer thickness.

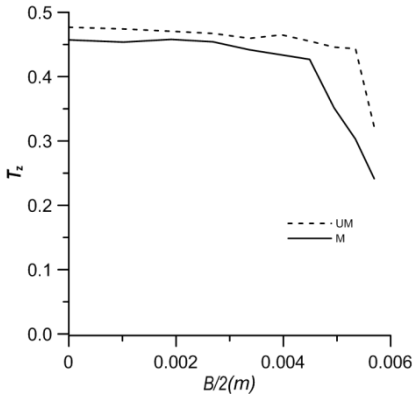

Fig. 10. Distributions of the T_z parameter in a direction of the specimen thickness

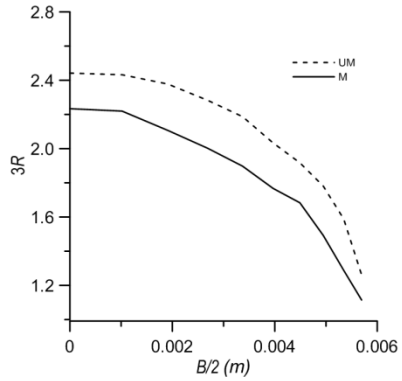

Fig. 11. Distributions of the 3*R* parameter in a direction of the specimen thickness

The parameters T_m and $3R_m$ were calculated for specimens made of the UM and M cast steel. A higher level of these parameters was obtained for the UM cast steel G17CrMo5-5 (Tab. 4).The higher level of stress triaxiality indicates higher restrictions on the growth of a plastic zone in front of the crack, reducing the amount of energy stored, and, as a result, decreasing the fracture toughness characteristics. The derived experimental results confirmed that increase of the triaxiality stress state in the specimen indicates a reduction of fracture toughness (Tab. 4).

Tab. 4. The weighted average parameters T_m and $3R_m$ for UM and M cast steel

	T_m	$3R_m$	J_i (kN/m)
UM	0.46	2.16	160
M	0.42	1.91	207

4. EFFECT OF MICROSTRUCTURE ON FRACTURE PROCESS OF G17CrMo5-5 CAST STEEL

The results of numerical calculations indicate more favourable conditions for the implementation of cleavage fracture in the unmodified cast steel, which quantitatively expressed at higher values of the triaxiality parameters, especially *3R* parameter. Detailed studies of microstructure revealed some differences in the microstructure of the UM and M cast steel. In both variants of steel, there is a similar microstructure of ferrite with large areas of perlite-bainite (Figs. 12a, 12b). But for the UM cast steel a characteristic feature is a larger quota of a ferritic component in the microstructure and larger size of ferrite grains (D_z =8-25 μm for UM; D_z =3-15 μm for M).

a)

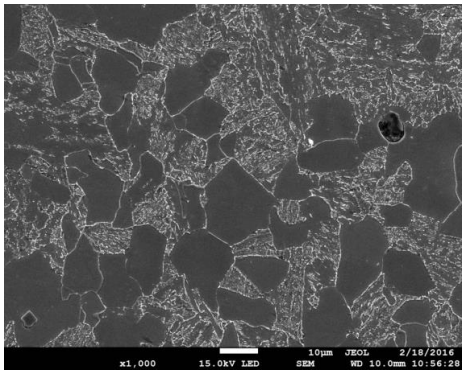

b)

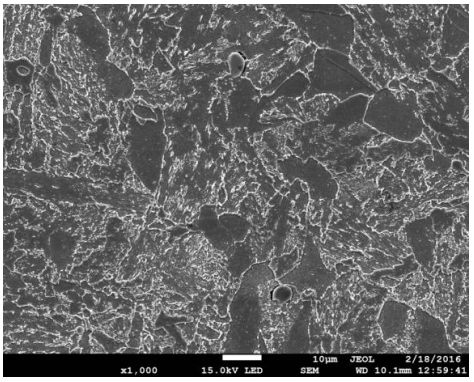

Fig. 12. Cast steel G17CrMo5-5 microstructure: a) for UM; b) for M

According to the concept of a local approach to the process of fracture, cleavage fracture will be made if the level of stress exceeds the critical levels, necessary for the development of micro-cracks inside the grain, and to overcome the grain boundary and the development of cracks in the adjacent grains (Pineau, 2006). In order to evaluate these critical levels, we may use the formulas proposed in the works of Knott et al. (Curry and Knott, 1978; Dolby and Knott, 1972; Knott, 1977). Critical level of stresses of the microcrack initiation from micro-defect can be assessed using the formula:

$$\sigma_{\mathrm{Ci}} = \frac{\pi}{2}\left(\frac{4E\gamma_{\mathrm{p}}}{\pi(1-\nu^2)d_{\mathrm{i}}}\right)^{1/2}. \quad (5)$$

While the stress level required for the development of microcrack from the grain into neighbouring one by the formula:

DOI 10.1515/ama-2016-0030

$$\sigma_{Cg} = \left(\frac{\pi E \gamma_{gl}}{(1-\nu^2)D_g}\right)^{1/2}. \quad (6)$$

In the formulas (5) and (6): E is Young's modulus; ν is the Poisson's ratio; γ_p is a unit surface energy of cracks that propagates in ferrite; γ_{gl} is a unit surface energy of the crack propagating through the grain boundaries; d_i is a diameter of the inclusion particle; D_g is a diameter of the ferrite grain.

The results of the analysis of the cracking process in the UM and M cast steel G17CrMo5-5 are shown in Fig. 13. A solid line $\sigma = f(d)$ shows the dependence of critical stresses of the microcrack initiation from the micro-defect (by the formula 5). A dash line $\sigma = f(D)$ shows the dependence of the critical stresses of the microcrack growth through the grain boundary (by the formula 6). The lower horizontal dash and point line indicates the stress level, at which in the UM cast steel cleavage fracture may initiate from the particles of the largest size d_i =10 μm, (by the formula 5 and data from the Fig. 2). The upper horizontal dash and point line indicates the maximum level of the opening stresses for the UM, which were calculated numerically in the axis of the specimen (σ_C =1580 MPa). Respectively, for the M cast steel horizontal lower solid line indicates the level of the microcrack growth initiation from the particles of the maximum size, d_i =6 μm. The upper horizontal solid line corresponds to the maximum level of the opening stresses for the M cast steel (σ_C =1650 MPa). The analysis shows that in the M cast steel, cleavage fracture at the possibly highest level of loading (σ_C =1650 MPa) is likely because of microdefects nucleations and growth on the particles of inclusions d_i >3.7 μm. Also the microcrack growth through grain boundary is possible, because of the boundaries in grains of values D_g >12 μm. From the distribution of particles size presented in the Fig. 2, follows that there is about 5% inclusions of the appropriate size in the cast steel, simultaneously with a small part of ferrite grains of the appropriate size (~15%), which means that probability of the cleavage fracture occurrence is very low, less than 1%. Given that the part of the pearlite-bainite component of the microstructure construction of the M cast steel is dominant, and the growth of cleavage fracture in the microstructures of this type is difficult (Lewandowski and Thompson, 1987), the probability of realization of material cleavage fracture is negligible. Thus, the fracture process in the M cast steel will be realized by ductile mechanism. However, the probability of the cleavage fracture occurrence exists, it can be rarely realized locally in the individual ferrite grains.

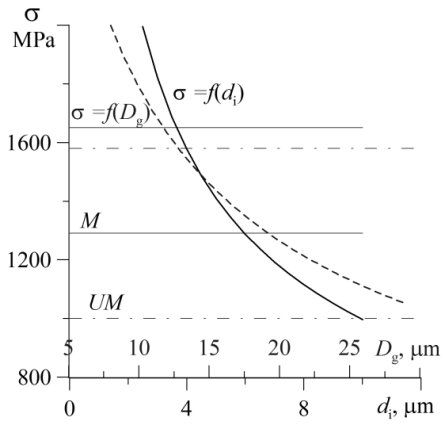

Fig. 13. Plots of the critical stresses for the M and UM cast steel

In the UM cast steel at the highest level of stresses (σ_C =1580 MPa) the initiation of cleavage fracture is possible beacuse the microcracks growths in the ferrite grain from inclusions d_i >4.0 μm. The growth of microcracks by a grain boundary is possible if D_g >13 μm. There is ~30% of the particles of the right sizes and ~40% of the ferrite grains of the right size. Taking into consideration that the ferrite grains occupy ~35% in the microstructure of the UM cast steel, the possibility of the occurrence of the global cleavage fracture is 4.2%. It is an assessment for the maximum value of stress loading. However, if we take into account the demand criteria of fracture, according to which for the realization of the cleavage fracture, stresses should reach the critical level in a material in a critical length, the probability of the occurrence of the global cleavage fracture in the UM cast steel will decrease. However, the probability of the occurrence of the cleavage fracture in the local limited areas is higher (~10%). On the basis of the conducted analysis, it can be stated that in the UM cast steel, the fracture process will be realized at the dominance of ductile mechanism. In the local areas, the occurrence of cleavage fracture is possible. In this material, there is also a low probability of the global occurrence of cleavage fracture.

In the Figures 14a and 14b are shown the photos the specimens of the M and UM cast steel. In the specimen of the M cast steel was observed only ductile fracture mechanism, realized through the nucleation and growth of voids around large particles (Fig. 14a), which is confirmed by the results of the assessment presented above. Fracture mechanism in the UM cast steel is also consistent with the presented above the results of the analysis. Generally dominates ductile fracture mechanism, however we can also observe scarce local areas, where cleavage fracture occurs. It is also worth mentioning, that in the specimens of the UM cast steel after increase of the subcritical fracture (Δa > 0.8 mm), the fracture mechanism changed into cleavage type. The change may be explained that for the moving fracture, the level of stresses increases in front of the crack tip (Neimitz at al., 2010), which leads to the increase of the probability of cleavage fracture.

a)

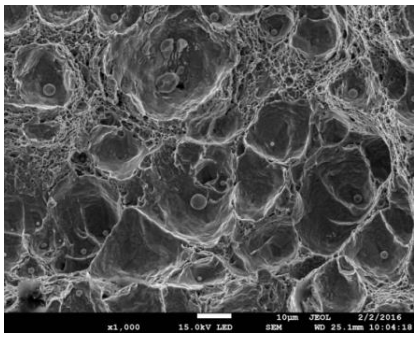

b)

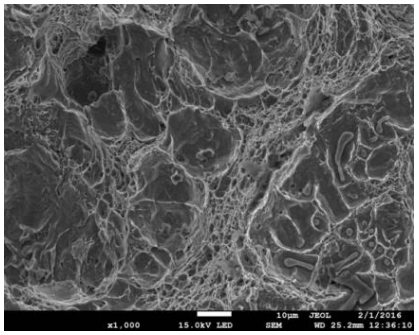

Fig. 14. The fracture surface of sub-critical crack for the cast steel G17CrMo5-5: (a) M; (b) UM

5. CONCLUSIONS

Addition of rare earth metals to melting of the low-alloy cast steel G17CrMo5-5 increases the strength, plasticity and fracture toughness characteristics. The FEM analysis results indicate that for the initial moment of the crack extension in the modified (M) and unmodified (UM) material is required to obtain a similar level of the opening stresses in the specimen axis, $\sigma_{22} \approx 3.6\sigma_0$. However, in the M cast steel the length of the critical interval is about twice greater than in the UM cast steel. Increasing of the critical interval indicates a higher fracture toughness of a material (Luniov, 2003; Seweryn, 1994). Distributions of the main stresses and parameters of the triaxiality stresses state T_z and $3R$ in the thickness direction were presented. The weighted average values T_m and $3R_m$ were calculated. For the M cast steel, the level of triaxiality stresses state parameters are lower, that indicates lower constraint on plasticity growth and higher fracture toughness in the specimens.

Assessment of the probability of cleavage fracture was carried out, based on the numerically calculated stress distributions in front of the crack tip and the data distributions the size of non-metallic inclusions and ferrite grains. The results of assessment allowed to predicted the mechanisms of crack propagation in the UM and M cast steel, that is consistent with the results observed during specimens tests.

These results confirm the beneficial effect of the cast steel modifying by the REM, thus leading to preferred microstructure changes - to reduce the particle size of the inclusions, the reduction of grain sizes, increasing the part of the pearlite-bainite component. These changes will decrease the maximum value of the stress levels in front of the cracks, which leads to increased fracture toughness and crack growth by only safe ductile mechanism. Then, in the unmodified cast steel there is a real possibility of the brittle fracture occurrence.

REFERENCES

1. ASTM E1737-96, *Standard Test Method for J-integral Characterization of Fracture Toughness*.
2. ASTM E1820-09, *Standard Test Method for Measurement of Fracture Toughness*, Annual book of ASTM standards. V.03.01, 1070-1118 (2011).
3. **Beremin F.A.** (1983), A local criterion for cleavage fracture of a nuclear pressure vessel steel, *Metallurgical Transaction*, A, 14A, 2277-2287.
4. **Bolanowski K.** (2005), Structure and properties of MA-steel with rare earth elements addition, *Archives of Metallurgy and Materials*, 50, 327-332.
5. **Curry D.A., Knott J.F.** (1978), Effect of microstructure of cleavage fracture stress in steel, *Metallurgical Science*, 511-514.
6. **Dolby R.E. Knott J.F.** (1972), Toughness of martensitic and martensitic-bainitic microstructures with particular reference to heat affect zones, *Journal of the Iron and Steel Institute*, 210, 857-865.
7. **Dzioba I.** (2011), The influence of the microstructural components on fracture toughness of 13HMF steel, *Materials Science*, 47 (5), 357-364.
8. **Dzioba I.** (2012), *Modelling and anslysis of fracture process in ferritic steels*, Politechnika Świętokrzyska, Kielce, (in Polish).
9. **Dzioba I., Gajewski M., Neimitz A.** (2010), Studies of fracture processes in Cr-Mo-V ferritic steel with various types of microstructure, *International Journal Pressure Vessel and Piping*, 87, 575-586.
10. **Dzioba I., Kasińska J., Pała R.** (2015), The influence of the rare earth metals modification on the fracture toughness of G17CrMo5-5 cast steel at low temperatures, *Archives of Metallurgy and Materials*, 60, 773-777.
11. EN–10213–2:1999. *Cast steel G17CrMo5-5*.
12. **Gajewski M., Kasińska J.** (2009), Rare earth metals influence on mechanical properties and crack resistance of GP240GH and G17CrMo5-5 cast steels, *Archives of Foundry Engineering*, 9, 37-44.
13. **Guo W.** (1993), Elastoplastic three dimensional crack border field - I. Singular structure of the field, *Engineering Fracture Mechanics*, 46, 93-104.
14. **Heon Y.H, ChanJin P., HyukSang K.**(2006), Effect of misch metal on the formation of non – metallic inclusions in 25% Cr duplex stainless steels, *Scripta Materialia*, 55, 991-994.
15. **Kasińska J.** (2014), Influence of rare earth metals on microstructure and inclusions morphology G17CrMo5-5 cast steel, *Archives of Metallurgy and Materials*, 59, 993-996.
16. **Knott J.F.** (1977), Micromechanisms of fracture and fracture toughness of engineering alloys, *ICF-4 Fracture*, 1, 61-91.
17. **Lewandowski J.J., Thompson A.W.** (1987), Micromechanisms of cleavage fracture in fully pearlitic microstructures, *Acta Metallurgica*, 35, 1453-1462.
18. **Luniov V.V.** (2003), Non metallic inclusions and properties of cast steels, *Przegląd Odlewnictwa*, 53(9). 299-304.
19. **McClintok F.A.** (1968), A criterion for ductile fracture by growth of holes, *Journal of Applied Mechanics*, 35 (4), 353-371.
20. **Neimitz A., Dzioba I., Pała R., Janus U.** (2015), The influence of the out-of-plane constraint on fracture toughness of high strength steel at low temperatures, *Solid State Phenomena*, 224, 157-166.
21. **Neimitz A., Gałkiewicz J., Dzioba I.** (2010),The ductile to cleavage transition in ferritic Cr-Mo-V steel: A detailed microscopic and numerical analysis, *Engineering Fracture Mechanics*, 77, 2504-2526.
22. **Pineau A.** (2006), Development of the local approach to fracture over the past 25 year: theory and applications, *International Journal of Fracture*,138, 139-166.
23. **Rice J.R., Tracey D.M**. (1969), On the ductile enlargement of voids in triaxial stress fields, *Journal of the Mechanics and Physics of Solids*, 17, 201-217.
24. **Ritchie R.O., Knott J.F., Rice J.R.** (1973), On the relationship between critical tensile stress and fracture toughness in mild steel, *Journal of the Mechanics and Physics of Solids*, 21, 395-410.
25. **Seweryn A**. (1994), Brittle Fracture criterion for structures with sharp notches, *Engineering Fracture Mechanics*, 45 (5), 673-681.

Acknowledgments: Financial support from the Polish Ministry of Science and Higher Education under contract 01.0.08.00/2.01.01.01.0008 and National Centrum of Testing and Development contract PBS1/B5/13/2012 are gratefully acknowledged.

DE GRUYTER
OPEN

DOI 10.1515/ama-2016-0031

acta mechanica et automatica, vol.10 no.3 (2016)

WEAR RESISTANCE OF PISTON SLEEVE MADE OF LAYERED MATERIAL STRUCTURE: MMC A356R, ANTI-ABRASION LAYER AND FGM INTERFACE

Szymon HERNIK*

*Institute of Applied Mechanics, Faculty of Mechanical Engineering, Cracow University of Technology,
Al. Jana Pawła II 37, 31-864 Kraków, Poland

hernik@mech.pk.edu.pl

received 25 July 2015, revised 15 July 2016, accepted 18 July 2016

Abstract: The aim of this paper is the numerical analysis of the one of main part of car engine – piston sleeve. The first example is for piston sleeve made of metal matrix composite (MMC) A356R. The second improved material structure is layered. Both of them are comparison to the classical structure of piston sleeve made of Cr-Ni stainless steel. The layered material structure contains the anti-abrasion layer at the inner surface of piston sleeve, where the contact and friction is highest, FGM (functionally graded material) interface and the layer of virgin material on the outer surface made of A356R. The complex thermo-elastic model with Archard's condition as a wear law is proposed. The piston sleeve is modelling as a thin walled cylindrical axisymmetric shell. The coupled between the formulation of thermo-elasticity of cylindrical axisymmetric shell and the Archard's law with functionally changes of local hardness is proposed.

Key words: Piston Sleeve, Wear, Thermo-Elasticity, Archard's Law, Metal Matrix Composite MMC, Functionally Graded Material FGM

1. INTRODUCTION

The aim of this paper is the numerical analysis of wear of the one of main part of car engine – piston sleeve. The wear process can be described as a removing a thin layer from the surface of the material (Sarkar, 1976). Wear process depends of various types of mechanisms responsible for removal of material from surfaces. At the instant of wear, the rate of volume removed per unit sliding distance must be a function of the volume of material available at the junctions. In general, this definition can be describe as:

$$\frac{\mathrm{d}V}{\mathrm{d}S} = -\beta_1 V, \tag{1}$$

where: term V denotes volume, S is the sliding distance and β_1 is a constant which depends, possibly, on the applied loads. The constant β_1 usually has negative sign describes a situation, where the original volume at the junctions diminishes with sliding distance (Sarkar, 1976).

In alternative model proposed by Archard (1953) two nominally flat surfaces contact each to other at the high asperities which flow plastically, because of the concentrated localised stresses there. As this happens, the compliance between the couple improves, that is the gap between the two surfaces diminishes resulting in further protuberances making contacts elsewhere.

For a large distance *S*, the total volume of wear per unit sliding distance can be represented as:

$$V = \beta \frac{F}{3\sigma_y} S, \tag{2}$$

where: F denotes applied load, β – wear coefficient, σ_y – yield surface limit. Denominator in (2) can be represented by local hardness H of the material, where $H = 3\sigma_y$.

Constitutive relation, contains the thermo-elasticity formulation combined with Archard's law, is described by the decrease of the thickness due to wear at the inner layer of the piston sleeve (Wajand and Wajand, 2005).

2. TEMPERATURE FIELD IN CYLINDRICAL SHELL

The axisymmetric distribution of temperature and its change through the longitudinal direction x is assumed. Moreover, a linear distribution of temperature through the thickness is considered as a loading:

$$T(x,y) = T_x(x) + \frac{\bar{T}(x)}{h} y, \tag{3}$$

where: T_x is a mean value of temperature of the shell wall, $\bar{T}$ stands for temperature gradient inner and outer layer, *x* is the axial coordinate, *h* stands for thickness of cylindrical shell.

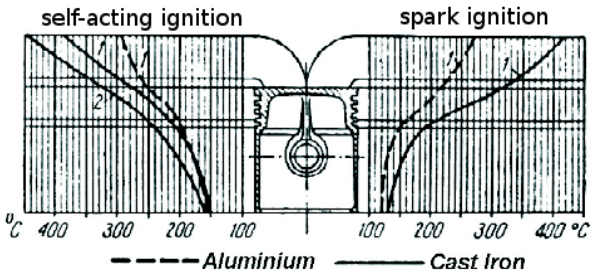

Fig. 1. Temperature distribution of piston: 1-four phase engine (Otto engine), 2-two phase engine (Diesel engine), after Leśniak (1964)

Experiments confirm that almost whole heat flux which enters the upper piston surface goes towards rings and cylindrical part

DOI 10.1515/ama-2016-0031

of the piston, whereas the lower surface subjects to adiabatic conditions. On the other hand, the temperature distribution at upper piston surface is not uniform (Leśniak, 1964). Above observation is confirmed by Fig. 1, where it is shown the distribution of the temperature in Otto and Diesel engines. In this case, the temperature distribution of piston sleeve may be well approximated by square function as follows:

$$\bar{T}(x) = 150x^2 - 300x + 250, \tag{4}$$

$$T_x(x) = 75x^2 - 150x + 175, \tag{5}$$

It is assumed that the value of temperature is equal to $\mathrm{T_w} = 100\ ^\circ\mathrm{C}$ – approximately the temperature of boiling of the cooling liquid in pressure at the inner layer, whereas the value of the temperature at the outer layer is equal to $\mathrm{T_z} = 250\ ^\circ\mathrm{C}$.

3. MECHANICAL MODEL

3.1. Bending of shell

The Piston sleeve is a thin structure of cylindrical shape, where the thickness is smaller in comparison with convenient its length. According to that properties, the simplest mechanical model is based on cylindrical axisymmetric thin walled shell. It is assumed:

- Body forces and pressure on circumference surface are constant, hence the assumption of axisymmetric is true. Above variables can change allow the axial direction. All forces are moved to middle layer, where the radius of cylindrical surface is equal *R* (see Fig. 2*)*.
- Radial displacement is very small in comparison to thickness *h*.
- The temperature is changed trough the thickness *h* and axial coordinate *x*.
- Influence of axial force on bending moments are small and it is omitted.
- Young modulus *E*, Poisson ratio υ and coefficient of thermal expansion α are not depend on temperature.

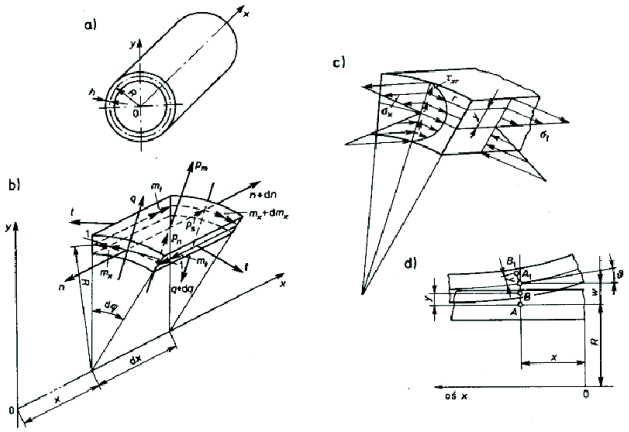

Fig. 2. Bending cylindrical shell: a) geometry, b) internal forces, c) distribution of stresses, d) deformation of middle layer; after Życzkowski (1988)

When the axial forces *n* are omitted, the internal equilibrium equation in displacement form coupled with Eq. (3) is following as:

$$\frac{\mathrm{d}^2}{\mathrm{d}x^2}\left[\mathcal{D}\left(\frac{\mathrm{d}^2 w}{\mathrm{d}x^2} - \alpha(1+\upsilon)\frac{\bar{T}}{h}\right)\right] + \frac{Eh}{R^2}w == p + \frac{Eh\alpha T_x}{R}, \tag{6}$$

where: $w(x)$ – unknown radial displacement function, x – axial coordinate, $\mathcal{D}(x,N) = \frac{Eh^3(x,N)}{12(1-\upsilon^2)}$ – bending stiffness, α – coefficient of thermal expansion, h – thickness of shell, R – radius of shell, E – Young modulus, p – pressure, υ – Poisson's ratio.

The bending stiffness $\mathcal{D}$ cannot be shifted before the differential operator, like in classical form, because the thickness of piston sleeve is not constant. There is a function of axial coordinate x and number of cycles in wear process N.

3.2. Boundary condition

Uniqueness of the solution of the boundary value problem described by equation (6) requires formulation of an appropriate set of boundary conditions. Classical formulation is not favourable because its incompatibility between thermal and mechanical boundary conditions. This effect can be solved by adding two axisymmetric elastic ribs. The first one is located at the upper part of piston sleeve $(x = 0)$ and the other one in the below part $(x = l)$, both modelling as disks, where l denotes the length of piston sleeve.

Differences of the temperature distribution in ribs are not taken into account because the dimension of ribs is small in comparison to dimension of the structure. A radial displacement of ribs is a function of temperature θ and transverse force q is given by formula:

$$u(\theta) = \alpha\theta r_1 - \frac{qr_1}{Eh}\frac{(1-\upsilon)\bar{r}^2+(1+\upsilon)}{1-\bar{r}^2} = f_b(\theta, q, \mathrm{r}), \tag{7}$$

where: $\bar{r} = r_1/r_2$, $r_1 = R$ – outer radius of piston sleeve, $r_2 = R + l_1$, l_1 – height of rib.

The boundary conditions are as follows:

$$\begin{aligned} &w(0) = f_b(\theta, q, \mathrm{r} = r_1), \\ &w(l) = f_b(\theta, q, r = r_1), \\ &m_x(0) = 0, \\ &w'(0) = 0, \end{aligned} \tag{8}$$

where: the $\mathrm{m_x}$ is a radial moment and w' is an angle of deflection.

4. FORMULATION OF WEAR FOR PISTON SLEEVE

The inner surface of piston sleeve is degraded by rings and the thickness of piston sleeve is decreasing. Some experiments lead to special kind of wear in this type of structure – wedge shape wear (see Fig. 3).

All facts above considered the formulation of the thickness function can be described as follows:

$$\begin{cases} h(x,N) = h_0 & \text{for } x < x_0 \\ h(x,N) = h_0 + \delta h(x,N) & \text{for } x \geq x_0, \end{cases} \tag{9}$$

where: N – number of cycles, $\delta h(x,N)$ is an infinitesimal change of the thickness at one cycle depends on variable x, x_0 is the point where the wedge's shape wear starts. Application of Eq. (1) in the problem of thin shell, where the sliding distance is collinear to coordinate x and total volume is reduced to the problem of change of thickness, previous equation can be rewritten as follows:

$$\frac{\mathrm{d}\delta h}{\mathrm{d}x} = -a\,\delta h, \tag{10}$$

where: constant a stands for a certain material parameter [1/m] having essential role in modelling of wedge's shape wear, see Eqs. (10)-(15). Other words, Eq. (10) can be read as: the rate of thickness removed per unit sliding distance is a function of the thickness of material available at the junction, see Sarkar (1976). After solve very simple differential equation (10), we can introduced:

$$\delta h(x,N) = C(N)e^{-ax}, \tag{11}$$

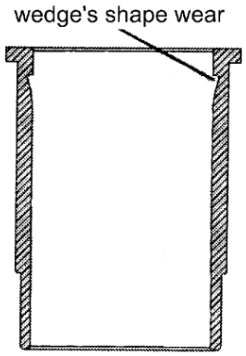

Fig. 3. Wedge's shape wear of piston sleeve

On the other hand the total volume of removed material can be described as:

$$\Delta V = \int_{x_0}^{x_1} 2\pi R\delta h(x,N)\,\mathrm{d}x, \tag{12}$$

where: the $x_1 - x_0$ is a sliding distance in one cycle. Comparison Archard's law and result of integration from Eq. (12), we can describe the following equation:

$$\beta\frac{F}{H}S = 2\pi R\,C(N)\frac{e^{-ax_0}-e^{-ax_1}}{a}. \tag{13}$$

Next it is assumed $\mathrm{e}^{-\mathrm{ax}_1} \approx 0$, $\mathrm{e}^{-\mathrm{ax}_0} \approx 1$ and summarise sliding distance $S = \mathrm{N}(\mathrm{x}_1 - \mathrm{x}_0)$, we can easily find that:

$$C(N) = -\frac{a}{2\pi R}\,\beta\frac{F}{H}\,N(x_1 - x_0). \tag{14}$$

Substituting (14) to (11) and after that introduced both of them into equation (9) we have finally relation describing change of thickness in the following form:

$$\begin{cases} h(x,N) = h_0 & \text{for } x < x_0 \\ h(x,N) = h_0 - \dfrac{a}{2\pi R}\,\beta\dfrac{FS}{H}\,e^{-ax} & \text{for } x \geq x_0. \end{cases} \tag{15}$$

The constant wear parameter $\beta = 2\cdot 10^{-6}$ is experimentally determined and substituting to all numerical examples after Natarajan et al. (2006). The load F is calculated as follow:

$$F = 2\pi R h_r p_g\,, \tag{16}$$

where: $\mathrm{p_g}$ denotes the constant gas pressure in the cylinder in the one cycle of sliding and $\mathrm{h_r}$ is a medium height of the cylinder rings (Leśniak, 1964). Obviously the original problem is not axisymmetric since wedge's shape wear occurs in the plane perpendicular to the axis of piston pin. However, for simplicity the axially symmetry of the problem is assumed.

5. RESULTS

Numerical integration of the problem takes advantage of step-by-step procedure and the shooting method presented in Press et al., 1983 and Skrzypek et al., 2008.

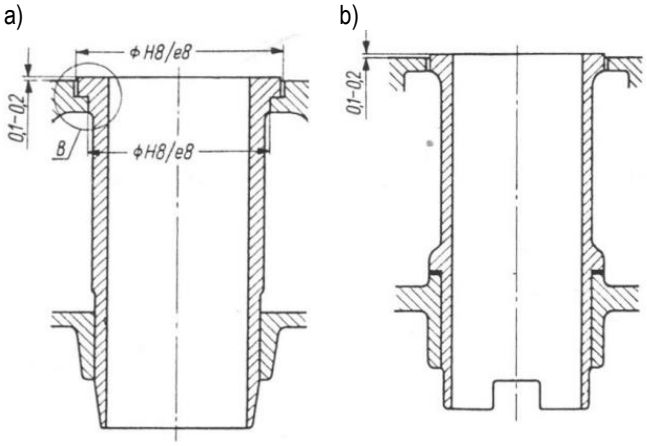

Fig. 4. Wet piston sleeves: a) piston sleeve with upper flange, b) piston sleeve with bottom flange (Wajand and Wajand, 2005)

From the technological point of view there are two types of wet piston sleeve. One of them has got flange on the upper surface (see Fig. 4a). The bottom part of the piston can extend after heating up. In another type of piston a flange is in the bottom part (see Fig. 4b), where the flange rest on ring-shaped sprue (Wajand and Wajand, 2005). Aforementioned it is assumed mechanical model presented with all geometrical parameters in Fig. 5 and it is used in all numerical examples in this paper.

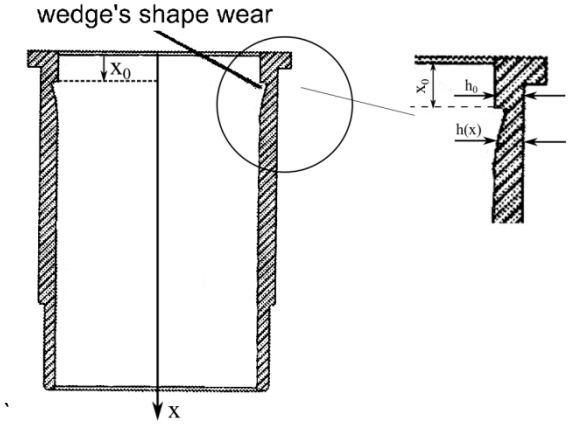

Fig. 5. Mechanical model and geometrical data of piston sleeve.

DOI 10.1515/ama-2016-0031

First numerical example is the reference problem necessary to calibrate material data. The sampling piston sleeve is made of Cr-Ni steel and detailed material data is shown in Tab. 2 and another parameter of analysis is presented in Tab. 1.

Tab. 1. Geometrical and material parameters

Wear coefficient [3] β [-]	Gas pressure in cylinder [5] p_g [MPa]	Medium height of the cylinder rings [5] h_r [mm]	Constant geometric parameter a [1/mm]
$2 \cdot 10^{-6}$	5.0	3.0	$5 \cdot 10^{-2}$
Outer radius shell R [mm]	Length of shell l [mm]	thickness of rib h_b [mm]	Height of rib l_1 [mm]
90.0	140.0	5.0	5.0
Initial thickness of shell h_0 [mm]			
5.0			

Tab. 2. Material data of Cr-Ni steel; after http://www.matweb.com

Young modulus E [GPa]	Poisson's ratio υ [-]	Thermal expansion coefficient α [1/K]	Hardness H [MPa]
170.0	0.33	18.5 x 10^{-4}	66.9

From the experimental point of view, maximum wear (drop of the thickness) is 0.1 mm. If the length of the wedge is equal as below, the piston sleeve will absolutely be unserviceable. Fig. 6 clearly shows wedge-shaped wear, coordinate is equal x/l, where *l* is the length of piston sleeve. It is where the dimensionless worth to notice that the number of cycles leading to destructive wear is equal $N = 2.2 \cdot 10^7$ in the first, reference example.

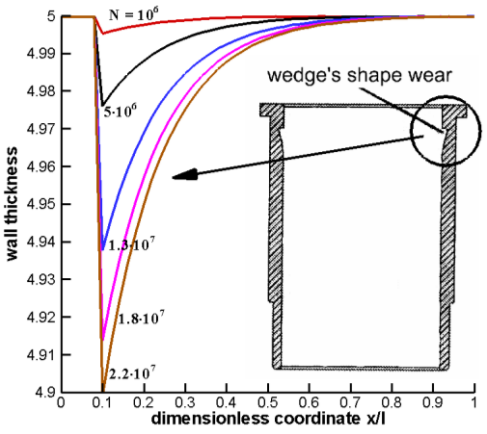

Fig. 6. Distribution of thickness function for piston sleeve made of Cr-Ni steel

5.1. Piston sleeve made of metal matrix composite MMC A356R

In the next numerical example piston sleeve is made of special kind of aluminium-based composite. The chemical formula of this material, called A356R, is Al-$Si_7Mg_{0.3}$ + 6% TiB_2. Material data of this material is shown in Tab. 3.

Tab. 3. Material data of MMC A356R; after Egizabal [2].

Young modulus E [GPa]	Poisson's ratio υ [-]	Thermal expansion coefficient α [1/K]	Hardness H[MPa]
79.0	0.33	22.4 x 10^{-6}	338.0

Thickness drop is presented in Fig. 7. Character of the plot is the same like in previous example (see Fig. 6). It is well visible that similar wedge-shaped wear appears, however the number of cycles leading to destruction increases ($N = 1.06 \cdot 10^8$). This is the advantage of application of A356R composite.

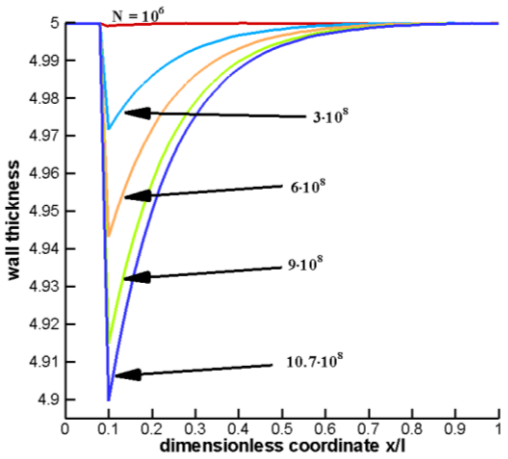

Fig. 7. Distribution of thickness function for piston sleeve made of aluminium composite A356R

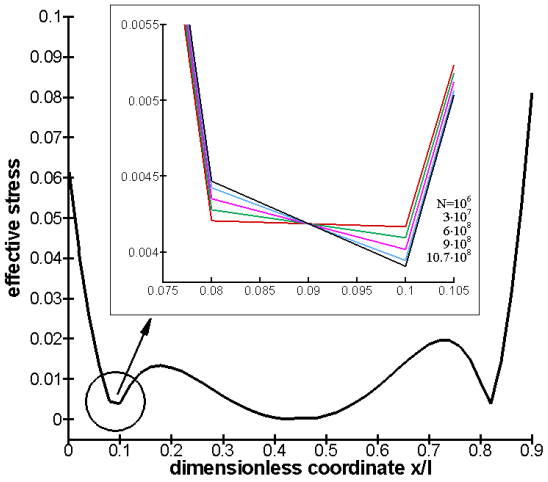

Fig. 8. Distribution of von Mises stress using the shell theory in piston sleeve made of A356R.

Next plot shows von Misses effective stress (see Fig. 8). Detailed analysis reveals existence of smoothness of effective stress near the point where wedge appears. It is a very dangerous effect, because it can lead to fracture in micro level. This is a consequence of stress concentrate at this point. Solution for this prob-

lem is applying the anti-abrasion thin layer. However combination of two material of huge differences of material hardness can be provided to huge concentration of stress at this point. Remedy for this problem is introduced the functionally graded materials (FGM) as an interface between the anti-abrasion layer with huge local hardness and virgin material.

5.2. Piston sleeve made of A356R composite material with abrasion resistant thin layer

There was presented the comparison between pistons sleeve made of classical Ni-Cr steel and composite material A356R in the previous sections. Material A356R is very sophisticated, however its wear properties is not perfect. The solution for this problem is introduced the abrasion resistant thin layer.

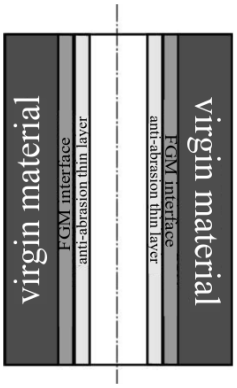

Fig. 9. Material model of piston sleeve with anti-abrasion thin layer

On the other hands connection of two materials with huge difference of properties can lead to micro fracture on interface. In this case application of middle layer from FGM (functionally graded material) is necessary. FGM is special kind of structural concept with spatial varying thermomechanical properties. Varying volume fraction of both constituents ceramic and metal determines the local macroscopic (effective) properties of a composites at the given point of structure. This structures was developed by Japanese engineering and scientists in 1980 (Suresh and Mortensen, 1998).

In the presented example it is introduced layer material of piston sleeve. In the inner side, where the rings contact with piston sleeve, it is applied thin layer of ductile iron as an anti-abrasion layer, because the hardness of ductile iron is huge (see the material data presented in Tab. 4). On the opposite side it is introduced composite material A356R (virgin material) and between them, it is applied the FGM interface with functionally changes of local hardness (see Fig. 9).

Tab. 4. Material data of ductile iron; after http://www.matweb.com

Young modulus E [GPa]	Poisson's ratio υ [-]	Thermal expansion coefficient α [1/K]	Hardness H[MPa]
172.0	0.29	12.0 x 10^{-6}	583.8

In this example it is applied that the failure wedge is 0.1 mm. This is the same value like in previous examples. From engineering practise point of view, the maximum wear of piston sleeve should not be greater than thickness of thin anti-abrasion layer. However, from the cognitive point of view, the value of thickness of anti-abrasion thin layer is applied as $\mathrm{h_{wear}} = 0.09$ mm, which is smaller than maximum wear. The thickness of FGM layer is applied as $\mathrm{h_{FGM}} = 0.03$ mm.

The main parameter, which is determined the velocity of wear process, is local hardness, hence this material property is introduced in form presented in Eq. (17) in the FGM interface layer.

$$H(y) = H_c - \widetilde{H}[1 + \mathrm{tgh}(y - y_0)] \tag{17}$$

where it is substituted:

$$\widetilde{H} = 0.5(H_c - H_{VM})$$
$$y_0 = h_{wear} + \frac{1}{2}h_{FGM} \tag{18}$$

Symbol $\mathrm{H_c}$ means the local hardness of anti-abrasion layer and $\mathrm{H_{VM}}$ is a local hardness of virgin material. Distribution of hardness function through the FGM interface is presented in Fig. 10.

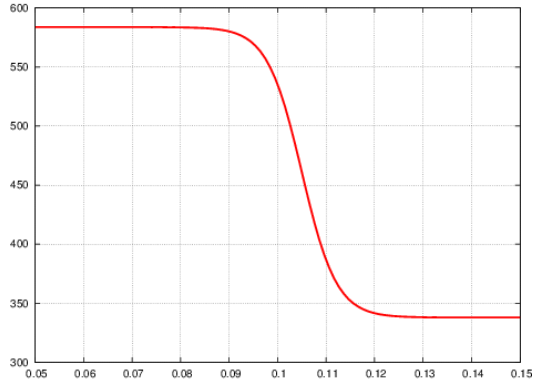

Fig. 10. Distribution of local hardness function $\boldsymbol{H(y)}$

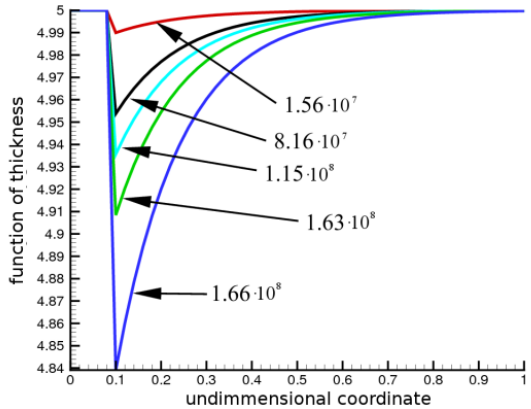

Fig. 11. Thickness function of piston sleeve with anti-abrasion layer and FGM interface

The first layer from $\mathrm{y} = 0.05$ to $\mathrm{y} = 0.09$ is made of ductile iron with huge value of local hardness. The next layer of thickness 0.03 is FGM interface, where the local hardness varying spatial to the value of local hardness of virgin material – A356R.

Applying an anti-abrasion layer in the piston sleeve leads to more effective resistant of wear (see Fig. 11). The number of cycles, after that the wear reaches the critical value

DOI 10.1515/ama-2016-0031

is $N = 1.66 \cdot 10^8$. It is worth to noticed that the velocity of wear process progresses rapidly, when the value of wear is greater than the thickness of anti-abrasion layer.

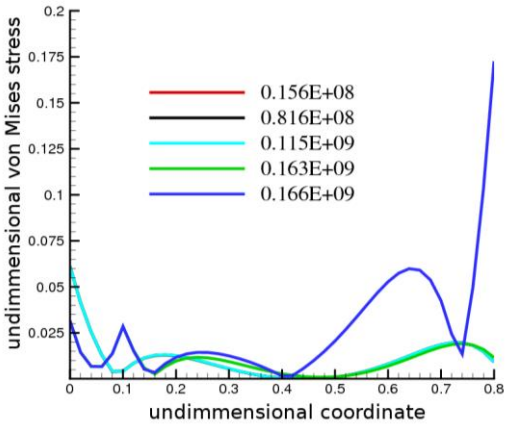

Fig. 12. Von Mises stress of piston sleeve with anti-abrasion layer and FGM interface

The next figure is presented the distribution of equivalent H-M-H stress. When the degradation of surface is grater then anti-abrasion layer, the distribution of stresses are changed. It is a consequence of modification of material. It is going to change from the ductile iron to the composite material A356R, hence the material coefficients change too.

6. CONCLUSIONS

- Numerical model presented in this paper with complex thermo-elastic phenomena and linear wear law (Archard's law) is proposed to describe wear process in piston sleeve.
- Wear resistance of piston sleeve made of composite material A356R is higher in comparison to the wear of the sampling piston sleeve made of Cr-Ni steel.
- The layered structure of material with FGM interface between the anti-abrasion layer and virgin composite material A356R improves the strength of piston sleeve, because the graded interface eliminates the concentration of stresses.

List of symbols: V – total volume of material, S – sliding distance, n – material constant in wear law, F – applied load, β – wear coefficient, σ_y – yield surface limit, H – local hardness of the material, $T = T(x, y)$ – function of temperature, x – axial coordinate, y – radial coordinate, $T_x(x)$ – mean value of temperature of the shell wall, $\bar{T}(x)$ – temperature gradient inner and outer layer, h_0 – initial thickness of shell, δh - infinitesimal change of thickness, $h = h(x, N)$ – function of thickness of cylindrical shell, T_w – approximately the temperature of boiling of the cooling liquid, T_z - temperature at the outer layer of shell, R – radius of shell, E – Young modulus, ν – Poisson's ratio, α – coefficient of thermal expansion, $w(x)$ – radial displacement function, $D = D(x, N)$ – bending stiffness, p – pressure, N – number of cycles in wear process, l- length of piston sleeve, $\theta = \theta(r)$ – function of temperature in ribs, q – transverse force in ribs, l_1 – height of rib, x_0 – coordinate of points where the wear process is start, a – material constant, h_r – medium height of cylinder rings, p_g – constant gas pressure in the cylinder in the one cycle of sliding, H_c – local hardness of anti-abrasion layer, H_{VM} – local hardness of virgin material, h_{wear} – thickness of anti-abrasion layer, h_{FGM} – thickness of FGM layer.

REFERENCES

1. **Archard J.F.** (1953), Contact and rubbing of flat surfaces, *Journal of Applied Physics*, 24, 981-988.
2. **Egizabal P.** (2007), Influence of Titanium Diboride (TiB2) particles on the microstructure and properties of reinforced AlSi7Mg0.3 and Al-Cu5MgTi alloys for plaster casting applications, *PhD thesis, Institut de Chimie de la Matiére Condensée de Bordeaux*, Bordeaux, in French.
3. **Leśniak Z. [eds]** (1964), *Cars from A to Z*, Wydawnictwo Komunikacji i Łączności (in Polish).
4. **Natarajan N., Vijayarangan S., Rajendran I.** (2006), Wear behaviour of A356/25SiCp aluminium matrix composites sliding against automobile friction material, *Wear*, 261(7-8), 812-822.
5. **Press W.H., Teukolsky S.A., Vetterling W.T., Flannery B.P.** (1983), *Numerical Recipes in Fortran*, Cambridge University Press, Cambridge.
6. **Sarkar A.D.** (1976), *Wear of metals*, Pergamon Press Ltd, Oxford.
7. **Skrzypek J.J., Ganczarski A.W., Rustichelli F., Egner H.** (2008), *Advanced materials and structures for extreme operating conditions*, Springer-Verlag, Berlin-Heidelberg.
8. **Suresh S., Mortensen A.** (1998), *Fundamentals of Functionally Graded Materials: Processing and Thermomechanical Behaviour of Graded Metals and Metal-Ceramic Composites*, Cambridge University Press, Cambridge.
9. **Wajand J.A., Wajand J.T.** (2005), *Middle- and high-speed combustion engines*, WNT, Warszawa, (in Polish).
10. **Życzkowski M.** (1988), Strength of structural elements, PWN Warszawa (in Polish).
11. Material data Library: http://www.matweb.com

DE GRUYTER
OPEN

DOI 10.1515/ama-2016-0032

acta mechanica et automatica, vol.10 no.3 (2016)

THE EFFECT OF TECHNOLOGICAL PARAMETERS ON INTENSITY OF SHOT PEENING PROCESS OF 51CrV4 STEEL

Magdalena BUCIOR[*], Lidia GAŁDA[*], Feliks STACHOWICZ[**], Władysław ZIELECKI[*]

[*]Faculty of Mechanical Engineering and Aeronautics, Department of Manufacturing Processes and Production Engineering, Rzeszow University of Technology, Powstańców Warszawy 8, 35-959 Rzeszów, Poland
[**]Faculty of Mechanical Engineering and Aeronautics, Department of Materials Forming and Processing, Rzeszow University of Technology, Powstańców Warszawy 8, 35-959 Rzeszów, Poland

magdabucior@prz.edu.pl, lgktmiop@prz.edu.pl, stafel@prz.edu.pl, wzktmiop@prz.edu.pl

received 12 May 2015, revised 18 July 2016, accepted 20 July 2016

Abstract: In the paper the effect of selected technological parameters of shot peening on process intensity of 51CrV4 steel was presented. The experiments were conducted according to statistical 3-level completed plan PS/DC 32. Technological parameters were changed in the range: shot peening time t = 1-3 min and pressure p = 0.2-0.4 MPa. In the article the analysis of experiment reproducibility, impact parameters significance and adequacy of equation were done. As the result of investigations the adequate equation was obtained describing the effect of technological parameters. Significant influence on process intensity was found in case of pressure and interaction of both analyzed technological parameters. The biggest energy of stream shots was gained at the maximum pressure of 0.4 MPa and the shot peening time of 3 minutes. As the result of analysis according to design of experiment (DOE) the adequate equation describing the dependencies between technological parameters and process intensity was found.

Keywords: Almen Intensity, Shot Peening, Plan PS/DC 3^2

1. INTRODUCTION

Machines parts operating under cyclic loading are particularly exposed to cracking. Prevention of this harmful phenomenon could be realized by the appropriate materials and suitable treatment application.

The vibrating screener used for the separation of the fine-grained and wet materials worked on the basis of parametric resonance. During exploitation of separating screener the large deformation and cracks occurred near the edges of sieve plate (Śledź et al., 2014). The traditional steel is usually used in such type of the screeners. The comparative examinations (Śledź et al., 2013; 2014; 2015) allowed to choose the most appropriate material for the sieve plate. The spring steel 51CrV4 was selected and the shot peening technology was proposed to improve the fatigue strength. This method is widely used to increase the fatigue strength of materials by compressive residual stress creation in their surface layers (Llaneza and Belzunce, 2015; Tekeli, 2002; Torres and Voorwald, 2002; Zielecki, 1987). The reasons for compressive residual stresses arising during shot peening are plastic deformation, temperature and structural transformations (Nakonieczny, 2002). Because plastic deformations after the strengthening process form the homogenous layer with compressive stresses in metal surface the increase in durability of processed parts occures.

The new peening methods are also discovered that could be more effective than classical shot peening. Soyama and Takeo (2016) found that cavitation peening led to the fatigue life enhancement of duralumin plate with a hole. Shot peening was succesfully implemented in chromium coated elements processing to restore the fatigue strength that was impaired by chromium electroplating (Korzynski et al., 2009). Application of the shot peening to process the AZ91 alloy surface allowed to enhance up to 87% greater fatigue strength compared to turned surface (Korzynski, 2011). Shot peening was also combined with other processes to get better fatigue performance. Lv et al. (2016) combined the shot peening with laser surface melting treatments and found that the shot peening intensity strongly affected the microhardnes, residual stresses and fatigue life of processed 20CrMnTi steel gears. Shot peening is commonly used for surface cleaning after previous treatment to obtain premium quality (Zyzak, 2010) or to assure the high adhesion of the coating.

Shot peening intensity is the measure of the shot stream energy. The process intensity is also one of the basic measure ensuring the process repeatability. The energy of the shot stream is directly related to the compressive stresses that are imparted in the machined parts (http://www.metalimprovement.com). The intensity can be increased by the large shots application, the velocity enhancement of shot stream, the impact angle modification and also by the extension of process time.

Taking into account the high cost and experiments duration the suitable planning, realization and analysis seem to be very important task (Jebahi et al., 2016; Skowronek, 2007). Experimental design and optimization are tools often used to examine different type of problems in research, development and production (Lundstedt et al., 1988). The main aim of planning of experiments is to obtain the answer for the question: how to plan the experiment regarding possible low costs and a lot of useable information at the same time (Pietraszek, 2004). There are a number of technical limitations in machines technology so the DOE enables the test realization and obtaining results that could

be impossible to get in any other way or could determine high costs. It is possible to find the appropriate design of the experiment allowing the rational application (Korzyński, 2013). The mathematical basis and methodology of results elaboration is well described in technical literature. The main classification of experimental plans is for dynamic and static type (Polański, 1984). Also numerical simulation of shot peening process could be provided as the suplementation of experiment but the matter of simplification assumption of the model always remain. Developed robust simulation is promising technique that enables to get properly simulated shot peening models (Jebahi et al., 2016).

For the assessment of the influence of technological parameters the full 2-factorial design of 3-levels (PS/DC 32) was used. This plan enables the optimum achievement if it appears in examined area. The determined experiment designs are characterized by values of input factors in precisely described way that excludes the accidental choice. Such DOE is formulated to gain the possibly fast results with minimal costs. Great advantage of DOE is the facility of the mathematical results calculation (Korzyński, 2013).

2. METHODS

The effect of selected technological parameters of shot peening on process intensity was examined with 51CrV4 usage. Chemical composition of 51CrV4 steel is presented in Tab. 1. The experiments were conducted according to the static 2-factorial 3-level completed plan PS/DC 3^2. All experiments were realized with triple repetition. The significance level of α = 0.05 was assumed. The process intensity was assessed by value of the Almen strip deflection f_A measured with the usage of Almen Gage TSP-3 (Fig. 1a) in compliance with SAE standard J442_201302 (2013). According to SAE standard J443_201006 it is recommended that the test strip of A type should be applied for intensities that produce arc heights of 0.10 mm to 0.60 mm (SAE standard J443_201006, 2010). Because of the thickness of the peened sample and the medium process intensity the control samples A-2 with hardness of 44-50 HRC were used. The Almen strips were peened on one side only. The residual compressive stresses brought by shot peening caused the Almen strip bend in arc convex towards processed side (Fig. 1b). Almen strip arc height f_A is the function of the shot stream energy and it is the quantity measure of intensity. Steel and control samples were processed in device shown in Fig. 2.

Tab. 1. Chemical composition of 51CrV4 steel

Chemical composition %								
Steel 51CrV4	C	Mn	Si	S	P	Cr	Ni	V
	0.46-0.54	0.5-0.8	0.15-0.4	0.03 max	0.03 max	0.8-1.1	0.4 max	0.1-0.2

The plan of the experiment implies the adoption of three levels of controlling factors coded as x:

- the minimum (–),
- the central (0),
- the maximum (+),

and their normalization is described by the following relations:

$$x_k = \frac{\hat{x}_k - \hat{x}_{k0}}{\Delta\hat{x}_k}, \quad (1)$$

$$\hat{x}_{k0} = \frac{\hat{x}_{k\,max} + \hat{x}_{k\,min}}{2}, \quad (2)$$

$$\Delta\hat{x}_k = \frac{\hat{x}_{k\,max} - \hat{x}_{k\,min}}{2}, \quad (3)$$

where: x_k - coded form of input factor, $\hat{x}_k$ - real value of input factor, $\hat{x}_{k0}$ - the central value of the factor in real scale, $\Delta\hat{x}_k$ - step change of controlled factor.

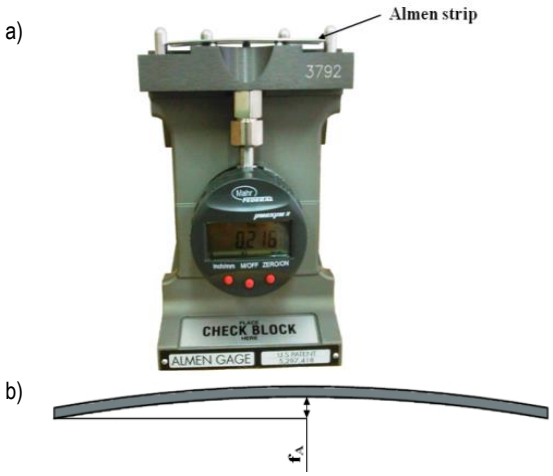

Fig. 1. Photo of Almen gage TSP-3 (a) and scheme of Almen strip after shot peening (b)

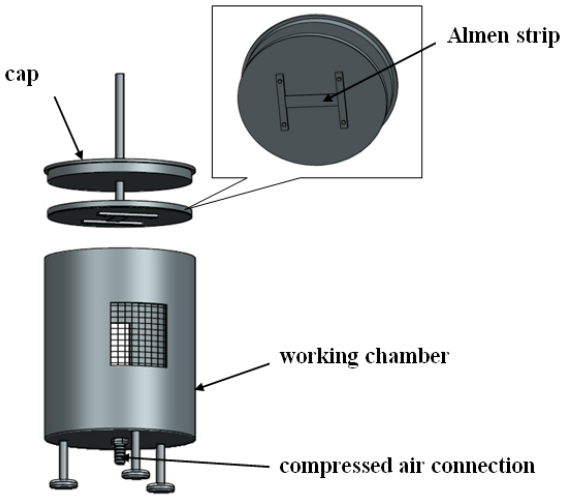

Fig. 2. Device for shot peening process

Technological parameters were changed in the range: shot peening time t = 1-3 min and pressure p = 0.2-0.4 MPa. The values of these parameters are presented in Tab. 2. In the experiment the constant parameters were: the ball diameter d_b = 2 mm and the distance from the strip to the nozzle l = 250 mm. In the preliminary test the biggest degree of surface coverage was obtained with the ball diameter equal to 2 mm.

Tab. 2. Values of technological parameters set in the experiment

Input factors	t, min	p, MPa
the minimum (–)	1	0.2
the central (0)	2	0.3
the maximum (+)	3	0.4
Output factor	f_A	

DOI 10.1515/ama-2016-0032

3. RESULTS AND DISCUSSION

The matrix of the 3-level completed plan PS/DC 3^2 with two input factors x_1, x_2, their interactions and average process intensity is presented in Tab. 3.

Tab. 3. Matrix of plan PS/DC 3^2 and results

Nr	x_0	x_1	x_2	x_1^2	x_2^2	x_1x_2	$\overline{f_{Ai}}$	σ
1	+	+	+	+	+	+	0.474	0.024
2	+	+	0	+	0	0	0.330	0.020
3	+	+	–	+	+	–	0.162	0.020
4	+	0	+	0	+	0	0.358	0.005
5	+	0	0	0	0	0	0.274	0.026
6	+	0	–	0	+	0	0.143	0.019
7	+	–	+	+	+	–	0.274	0.014
8	+	–	0	+	0	0	0.162	0.024
9	+	–	–	+	+	+	0.089	0.003

where: x_1 - coded value of time t, x_2 - coded value of pressure p, $\overline{f_{Ai}}$ - average of three measurement results of Almen strip in the i-th experiment, σ - standard deviation.

Methodology of 3-level plan requires to perform a few steps. The central values of time *t* and pressure *p* were calculated by the following relations:

$$\hat{x}_{10} = \frac{t_{max} + t_{min}}{2} = 2\ min, \tag{4}$$

$$\hat{x}_{20} = \frac{p_{max} + p_{min}}{2} = 0.3\ MPa. \tag{5}$$

Variability units of time *t* and pressure *p* were calculated by the following relations:

$$\Delta\hat{x}_1 = \frac{t_{max} - t_{min}}{2} = 1\ min, \tag{6}$$

$$\Delta\hat{x}_2 = \frac{p_{max} - p_{min}}{2} = 0.1\ MPa. \tag{7}$$

Coding factors of time *t*, pressure *p* and Almen intensity f_A were got by the following relation:

$$x_1 = \frac{\hat{x}_1 - \hat{x}_{10}}{\Delta\hat{x}_1} = \frac{t-2}{1}\ min, \tag{8}$$

$$x_2 = \frac{\hat{x}_2 - \hat{x}_{20}}{\Delta\hat{x}_2} = \frac{p-0.3}{0{,}1}\ MPa, \tag{9}$$

$$y = f_A. \tag{10}$$

As the result of experiments conducted according to the plan PS/DC 3^2 and matematical analyses the function was obtained:

$$y = f(x). \tag{11}$$

The function f(x) is approximated by a polynomial function and represents a good description of the relationship between the experimental variables and gives the response in a limited experimental domain (Lundsted, 1998). To determine the function optimum the quadratic terms should stay in the model. It is possible to determine non-linear relationships between the experimental variables and responses by introducing these terms in the model. The polynomial function below describes a quadratic model with two variables x_1 and x_2:

$$y = b_0 + b_1x_1 + b_2x_2 + b_{11}x_1^2 + b_{22}x_2^2 + b_{12}x_1x_2\ , \tag{12}$$

where: b_0 , ... , b_{12} - regression factors.

The regression factors were calculated according to formulas:

$$b_0 = \frac{1}{9}(-\bar{y}_1 + 2\bar{y}_2 - \bar{y}_3 + 2\bar{y}_4 + 5\bar{y}_5 + 2\bar{y}_6 - \bar{y}_7 + 2\bar{y}_8 - \bar{y}_9) = 0.262, \tag{13}$$

$$b_1 = \frac{1}{6}(\bar{y}_1 + \bar{y}_2 + \bar{y}_3 - \bar{y}_7 - \bar{y}_8 - \bar{y}_9) = 0.074, \tag{14}$$

$$b_2 = \frac{1}{6}(\bar{y}_1 - \bar{y}_3 + \bar{y}_4 - \bar{y}_6 + \bar{y}_7 - \bar{y}_9) = 0.119, \tag{15}$$

$$b_{11} = \frac{1}{6}(\bar{y}_1 + \bar{y}_2 + \bar{y}_3 - 2\bar{y}_4 - 2\bar{y}_5 - 2\bar{y}_6 + \bar{y}_7 + \bar{y}_8 + \bar{y}_9) = -0.010, \tag{16}$$

$$b_{22} = \frac{1}{6}(\bar{y}_1 - 2\bar{y}_2 + \bar{y}_3 + \bar{y}_4 - 2\bar{y}_5 + \bar{y}_6 + \bar{y}_7 - 2\bar{y}_8 + \bar{y}_9) = -0.005, \tag{17}$$

$$b_{12} = \frac{1}{4}(\bar{y}_1 - \bar{y}_3 - \bar{y}_7 + \bar{y}_9) = 0.032. \tag{18}$$

In order to assess the relevance of regression factors the following values were calculated - eqs. (19-25).

G – empirical value was calculated by the relation:

$$G = \frac{S^2(y)_{i\,max}}{\sum_{i=1}^{N} S^2(y)_i} = 0.2039, \tag{19}$$

where: $S^2(y)_i$ – variation of measured values, N – total number of experiments according to planned matrix.

The numbers of freedom degrees were calculated according to formulas:

$$f_1 = N = 9, \tag{20}$$

$$f_2 = r - 1 = 2, \tag{21}$$

where: G_{kr}- critical value specified by Cochran's statistic:

$$G_{kr} = G_{(\alpha;f_1;f_2)} = 0.4775. \tag{22}$$

In case of $G < G_{kr}$ (0.2039 < 0.4775) the experiment was realised in sufficient reproducibility.

To evaluate the relevance of regression factor some necessary values were caltulated. The number of freedom degrees f, the value of the coefficient form Student's t statistics t_{kr} and critical value b_{kr} were calculated by the relations:

$$f = N(r-1) = 18, \tag{23}$$

$$t_{kr} = t_{(\alpha;f)} = 2.1009, \tag{24}$$

$$b_{kr} = t_{(\alpha;f)}\sqrt{\frac{S^2(y)}{Nr}} = 0.0076. \tag{25}$$

In case of $|b_k| > b_{kkr}$ the regression coefficient has significant influence otherwise the factor was rejected.

As the effect of calculation the assesment of regression coefficient relevance was done and the results are presented in Tab. 4.

Tab. 4. Results of significance assesment

Regression factors	Relevance
b_0	significant
b_1	significant
b_2	significant
b_{11}	significant
b_{22}	insignificant
b_{12}	significant

After the reduction of insignificant regression factors the func-

DOI 10.1515/ama-2016-0032

tion is as follow:

$$y = 0.262 + 0.074\,x_1 + 0.119\,x_2 - 0.010\,x_1^2 + 0.032\,x_1x_2. \quad (26)$$

After decoding and calculation the searching equation representing the theoretical model is presented below:

$$f_A = -0.091 - 0.010t^2 + 0.018t + 0.55p + 0.32tp. \quad (27)$$

The adequatness of obtained equation was examined with application of the Fischer-Snedecor statistics. Firstly, the variance adequatness was calculated with formula:

$$S_{ad}^2(y) = \frac{r\sum_{i=1}^{N}(\hat{y}_i - \bar{y}_i)^2}{N-k-1} = 0.0009, \quad (28)$$

where: r – number of replication, $\hat{y}_i$ – values calculated from the regression equation for all levels of input factors, $\bar{y}_i$ – average of measured values in i-th experiment, N – total number of experiments, k – number of regression equation expressions (without free expresssion) after rejection the insignificant expressions.

Next the empirical value of the F coefficient was calculated and compared to critical value Fkr got from the statistics $F_{kr} = F_{(\alpha;f_1;f_2)} = F_{(0.05;4;18)} = 2.9277$.

$$F = \frac{S_{ad}^2(y)}{S^2(y)} = 2.5381. \quad (29)$$

The obtained regression equation was adequate because $F < F_{kr}$ $(2.5381 < 2.9277)$ at the assumed significance level α = 0.05. Graphically the obtained relations are presented in Fig. 3.

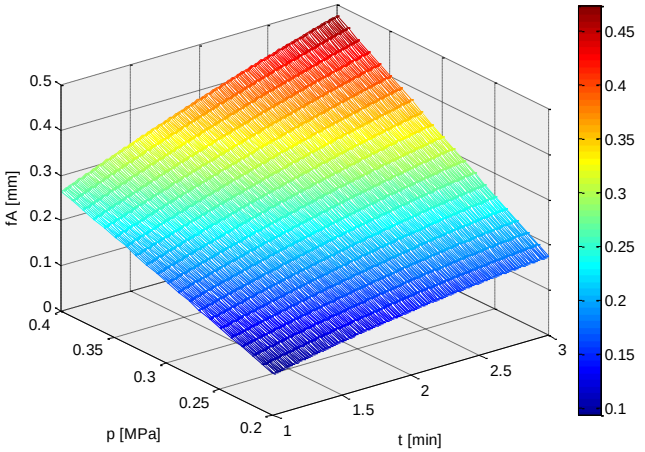

Fig. 3. The effect of technological parameters of shot peening on process intensity of 51CrV4 steel

Duration of the shot peening in the analysed range influenced the process intensity but not as much as the pressure. The maximum value of f_A = 0.474 mm was obtained at the highest settings of both technological parameters while the minimum f_A = 0.089 mm was at the lowest values of shot peening technological parameters. For the implementation in production companies the most interesting are technologies which are economically explained so taking into account the process time the best variant could be at minimum t = 1 min but maximum p = 0.4 MPa. Then the process intensity is equal to 0.274 mm and is the same as at t = 2 min and p = 0.3 MPa and also close to the value obtained at t = 3 min and p = 0.3 MPa (f_A = 0.33 mm). But if there is greater intensity needed the time duration should be longer at least 3 min and pressure higher. The maximum pressure of 0.4 MPa gives the highest energy of the shot stream but the time of exposition is important too.

The values of shot peening intensity f_A obtained in the experiment and calculated from the model are presented in Fig. 4.

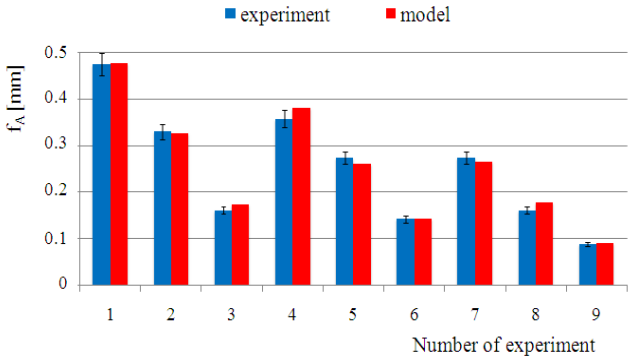

Fig. 4. The theoretical and experimental values of shot peening intensity f_A according to PS/DC 3^2

Comparing the theoretical and experimental values the good agreement is observed. Almost all values calculated from the model are in the limits of 5% error amount of measured values obtained in the experiments.

4. CONCLUSION

The most significant effect on process intensity was found in case of pressure and interaction of both analyzed technological parameters. The maximum value of shot peening intensity was obtained at maximum technological parameters values p = 0.4 MPa and t = 3 min. The time duration of the process is important factor as well. The analysis of experiment repeatability, impact significance and adequacy of equation were made according to statistical 3-level completed plan PS/DC 3^2. As the result of investigations the adequate equation was obtained describing the effect of technological parameters. The theoretical model was in accordance with experimental data.

REFERENCES

1. **Jebahi M., Gakwaya A., Leveskue J., Mechri O., Ba K.** (2016), Robust methodology to simulate real shot peening process using discrete-continuum coupling method, *International Journal of Mechanical Sciences*, 107, 21-33.
2. **Korzyński M.** (2013), *Experiment methodology*, WNT, Warszawa (in Polish).
3. **Korzynski M., Dzierwa A., Pacana A., Cwanek J.** (2009), Fatigue strenght of chromium coated elements and possibility of its improvement with ball peening, *Surface & Coatings Technology*, 204, 615-620.
4. **Korzynski M., Zarski T., Korzynska K.** (2011), Surface layer condition and the fatigue strenght of an AZ91 alloy after ball peening, *Journal of Materials Processing Technology*, 211, 1982-1988.
5. **Llaneza V., Belzunce F.J.** (2015), Study of the effect produced by shot peening on the surface of quenched and tempered steels: roughness, residual stresses and work hardening, *Applied Surface Science*, 356, 475-485.

DOI 10.1515/ama-2016-0032

7. **Lundstedt T., Seifert E., Abramo L., Thelin B., Nyström A., Pettersen J., Bergman R.** (1998), Experimental design and optimization. *Chemometrics and Intelligent Laboratory Systems*, 42, 3-40.
8. **Lv Y., Lei L., Sun L.** (2016), Influence of different combined severe shot peening and laser surface melting treatments on the fatigue performance of 20CrMnTi steel gear, *Materials Science & Engineering A*, 658, 77-85.
9. **Metal Improvement Company,** (2005), *Shot peening applications*. http://www.metalimprovement.com//premium/PDF/greenbook_v9/english/Chapter%2011.pdf (dostęp: 03 marzec 2015).
10. **Nakonieczny A.** (2002), Surface treatment by dynamic plastic deformation. Shot peening. Instytut Mechaniki Precyzyjnej, Warszawa (in Polish).
11. **Pietraszek J.** (2004), *Experiment planning. Opportunity or necessity.* http://www.statsoft.pl/Portals/0/Downloads/doe.pdf (in Polish), (dostęp 05 marzec 2015).
12. **Polański Z.** (1984), *Experiment planning in technique*, PWN, Warszawa (in Polish).
13. **Skowronek A.** (2007), Optimization of elastic experiment plan generativity. *Czasopismo Techniczne. Informatyka*, Wydawnictwo Politechniki Krakowskiej, 63-74 (in Polish).
14. **Śledź M., Bąk Ł., Zielecki W.** (2014), The effect of shot peening on fatigue strength of selected steel sheets*,* Publishing House of Rzeszow University of Technology, *Monograph: Selected issues and problems in mechanical engineering*, Rzeszów, 69-83 (in Polish).
15. **Śledź M., Stachowicz F., Zielecki W.** (2015), The effect of shot peening on the fatigue strength of steel sheets, *Metallic Materials,* 53, 91-95.
16. **Śledź, M., Bąk, Ł., Stachowicz, F., Zielecki, W.** (2013), Analysis of the effect of shot peening on mechanical properties of steel sheets used as screener sieve materials, *Journal of Physics: Conerence Series*, 451, 012029.
17. **Soyama H., Takeo F.** (2016), Comparison between cavitation peening and shot peening for extending the fatigue life of a duralumin plate with a hole, *Journal of Materials Processing Technology*, 227, 80-87.
18. **Tekeli S.** (2002), Enhancement of fatigue strength of SAE 9245 steel by shot peening*, Materials Letters*, 57, 604-608.
19. **Torres M. A. S., Voorwald H. J. C.** (2002), An evaluation of shot peening, residual stress and stress relaxation on the fatigue life of AISI 4340 steel, *International Journal of Fatigue*, 24, 877-886.
20. **Zielecki W.** (1987), The effect of shot peening intensity on fatigue strength and surface layer properties of 50HF steel, Zeszyty Naukowe Politechniki Rzeszowskiej, *Mechanika,* 14, 35-40 (in Polish).
21. **Zyzak P.** (2010), Characteristic of a shot stream in a rotor cleaning machine, *Archives of Metallurgy and Materials*, 55 (3), 977-984.
22. SAE standard J442_201302 (2013) Test Strip, Holder, and Gage for Shot Peening, SAE International.
23. SAE standard J443_201006 (2010) Procedures for Using Standard Shot Peening Almen Strip, SAE International.

Acknowledgement: This work was supported by the European Research Agency - FP7-PEOPLE-2011-IAPP - Marie Curie Industry - Academia Partnerships and Pathways, grant agreement No. 284544.

DOI 10.1515/ama-2016-0033

LOCAL AND DISTORTIONAL BUCKLING OF AXIALLY LOADED COLD ROLLED SIGMA PROFILES

Katarzyna CIESIELCZYK*, Katarzyna RZESZUT*

*Faculty of Civil and Environmental Engineering, Poznan University of Technology, Piotrowo 5, 60-965 Poznan, Poland

katarzyna.ciesielczyk@put.poznan.pl, katarzyna.rzeszut@put.poznan.pl

received 6 September 2015, revised 19 July 2016, accepted 20 July 2016

Abstract: In this paper the local and distortional buckling analyses of axially loaded cold-rolled channel and sigma profiles were performed. The critical buckling load was computed by solving the linear eigenvalue problem for different numerical models using Finite Element Method and simplified formulas implemented in Eurocode and proposed by Hancock and Schafer. The buckling analyses were conducted to prove that the sigma cross-section can be successfully replaced by channel cross-section with additional elastic supports placed in folds of the web. It was demonstrated that the folds in the web of the sigma cross-section (additional elastic supports) reduce the slenderness of the web. So, the critical distortional stress can be calculated based on analytical formulas derived for the channel cross-section taking into account the web height between the folds.

Key words: Cold Rolled Sigma Profiles, Local And Distortional Buckling, Eurocode 3, Finite Element Method

1. INTRODUCTION

Application of thin-walled cold–formed sections increased the importance of local and distortional buckling phenomena which may appear at a similar or lower load level as global instability. In engineering approach buckling modes presented in the Tab. 1 are investigated separately. Global buckling is analysed based on Vlasov theory, which do not takes into account a local instability. Whereas the local buckling is considered based on the concept of effective cross-section. While the distortional buckling is analysed using the simplified analytical formulas derived for equivalent cross-sections including flange with an edge stiffener. An alternative design procedure for cold-formed steel member is the Direct Strength Method widely discussed in (Schafer, 2008). This method employs gross cross-section properties, but requires an accurate calculation of member elastic buckling behaviour. It equals or betters the traditional Effective Width Method implemented in Eurocodes (Eurocode 3). The efficiency of Direct Strength Method is analysed in (Yua and Schafer, 2007) for cold-formed steel C- and Z-section beams through the comparing study of experimental data and results obtained from nonlinear finite element model. It was found that the moment gradient effect on distortional buckling failures can be conservatively accounted for in the Direct Strength Method by using an elastic buckling moment that accounts for the moment gradient. On the other hand in (He et al., 2014) based on experimental data of fixed-ended web-stiffened lipped channel columns eroded by mode interaction behaviour combined with distortional and local deformations authors concludes that the Current Direct Strength Method (DSM) provides very unsafe predictions. Therefore the they proposed two DSM-based design approaches, namely, the nominal strength against local-distortional (NLD) and distortional-local (NDL) procedures. Similar conclusions were drawn in (Wang and Young, 2014) for cold-formed steel channels with stiffened webs subjected to bending. This studies have demonstrated that the local and distortional buckling still a need for of scientific research.

It is worth to mention that distortional buckling of compression members is associated with the deformation of the contour in a form of symmetrical or asymmetrical closing or opening of the section and change of the angle between adjacent walls. Distortional buckling of compression members has been widely discussed in literature. In Lau and Hancock (1990) the authors proposed distortional buckling formulas for columns made of cold-rolled channel cross-sections. The distortional buckling analysis was also carried out by (Schafer, 2000). The Schafer's report data was used by Pala (2006) for training and testing a new neural network (NN) to determine of the elastic distortional buckling stress (EDBS) of cold-formed steel C-sections with both end sections pinned. It was found that the proposed NN based-formula can be used for the explicit formulation of various analyses of EDBS, especially when an analytic expression could not be obtained from the results of experimental and numerical studies. The effectiveness of new NN based-formula was tested by parametric study for distortional buckling stress on cold-formed steel presented in Pala and Caglarb (2007). The comparative analysis conducted by Szymczak and Werochowski (2005) showed that the critical distortional stresses calculated according the designing code are overestimated in relation to the formulas proposed by Hancock and Schafer.

An analytical model for predicting the critical stress of distortional buckling of zed and sigma cold-formed steel sections was proposed by Long-yuan and Jian-kang (2008). They derived and validated closed-form formulas providing a good prediction of the distortional buckling stress, despite its simplicity. Next, analyses of distortional buckling of cold-formed sigma purlins using EN1993-1-3 was performed by Long-yuan (2009). He analysed the influence of different support conditions at both the tension and compression ends of the web on the critical stress

DOI 10.1515/ama-2016-0033

of distortional buckling of sigma purlins. Moreover he performed the comparison with finite strip analysis. The general explicit analytical formulae to provide distortional critical stress for cold-formed steel C-section columns subjected to uniform compression was derived in Zhou et al. (2015) by employing the Lau and Hancock model and by introducing a new factor for considering the web rotational restraint reduced by web bending.

Tab. 1. The buckling modes of axially loaded thin-walled sigma profile

Buckling modes		
local buckling	distortional buckling	
	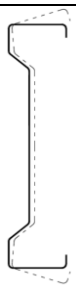	
Global buckling		
vertical translation	horizontal translation	rotation
		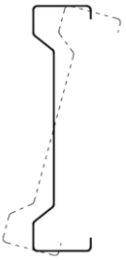

In this paper the local and distortional buckling analyses of cold-rolled sigma profiles were performed. In the first part of the study three numerical models were created using Finite Element Method. The buckling analyses were conducted to prove that the sigma cross-section can be successfully replaced by channel cross-section with additional elastic supports placed in folds of the web. Then, based on the assumption that the folds of the web (additional elastic supports) reduce the slenderness of the web the critical distortional stress was calculated basing on Eurocode recommendations and Hancock and Schafer formulas. In the second part, the FEM numerical model corresponding to Eurocode recommendation was created in order to verify the assumptions introduced in the analytical analysis and to investigate the interactive buckling, which is not taken into account in analytical formulas.

2. BUCKLING FEM ANALYSIS

2.1. Linear eigenvalue problem

In the numerical computations the values of critical buckling load for axially loaded channel and sigma bars were computed by solving the linear eigenvalue problem:

$$(\mathbf{K}^O + \lambda \mathbf{K}^G)\mathbf{U} = 0, \tag{1}$$

where: $\mathbf{K}^O$ – is the small-displacement stiffness matrix, $\mathbf{K}^G$ – is the initial stress matrix, λ – is the load multiplier and $\mathbf{U}$ – is eigenvector represents the buckling mode shapes. In Eq. (1) the proportional loading and linearization of the pre-buckling state was assumed. The critical buckling loads are given by the following formula:

$$P^{cr} = \lambda^{cr} P, \tag{2}$$

where: P – is the reference load (the base state).

2.2. Numerical model 1

The real and simplified numerical model was created using Abaqus CEA software (Abaqus 6.13 Documentation). In the simplified model the sigma cross-section was replaced by channel cross-section with supports as shown in Fig. 1. The main aim of this part of the study was to verify the influence of supports on the value of critical stress.

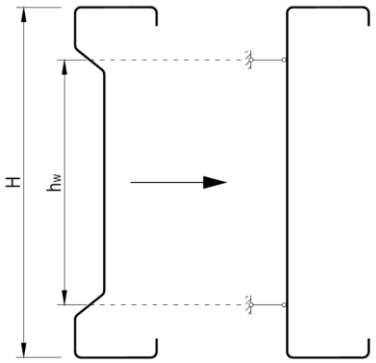

Fig. 1. Geometry of numerical model 1: a) real cross-section, b) simplified model: channel with additional supports

The element was meshed by four nodes shell finite elements S4R with dimension 4 x 4 mm. R means that the reduced integration was used. The axially compressive forces were applied to the special defined reference points. The reference points were created in the gravity centre of the cross section on he both side of the beam as shown in Fig. 2. The reference points were connected with the cross-section by coupling constraints. The boundary conditions were created to imitate a static shame of simply supported beam and then were also applied to the reference points. The computation were performed in Abaqus CEA program using Buckling Type of analysis in order to calculate the load proportionality factor.

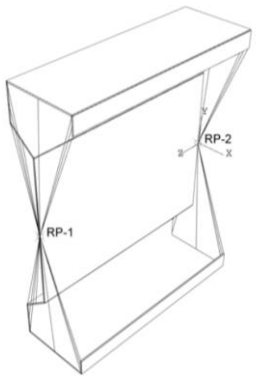

Fig. 2. The reference points in one of the created models

DOI 10.1515/ama-2016-0033

The analysis was performed for several cold-formed symmetrical channel and sigma profiles with dimensions shown in Fig. 3 (flange width b = 70 mm, wall thickness t = 1.5 mm and the lip width c = 16 mm). The six different values of height of the cross section (H= 140, 200, 230, 260, 300 and 350 mm) and different slenderness ratio of the bar (L/i_{min}= 10, 25, 50, 75, 100, 125, 150, 200 and 250) were analysed.

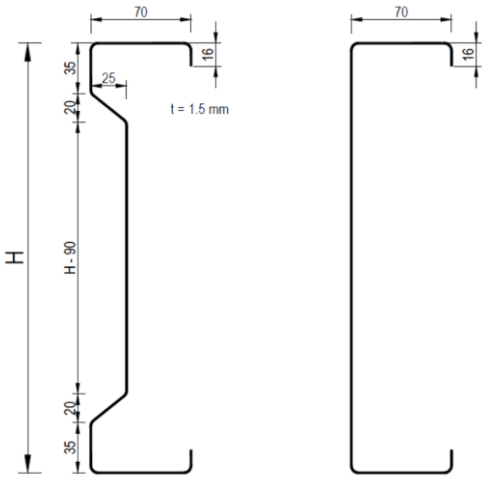

Fig. 3. Dimensions of the analysed models

2.3. Results – numerical model 1

The values of critical stress were calculated for several values of slenderness ratio (the beam length vs radius of gyration). In majority of the analysed cases the local and global interactive buckling phenomena was observed.

Exemplary results obtained in buckling analysis for the cross-section of the height of 230 mm and different slenderness ratio were presented in the Fig. 4.

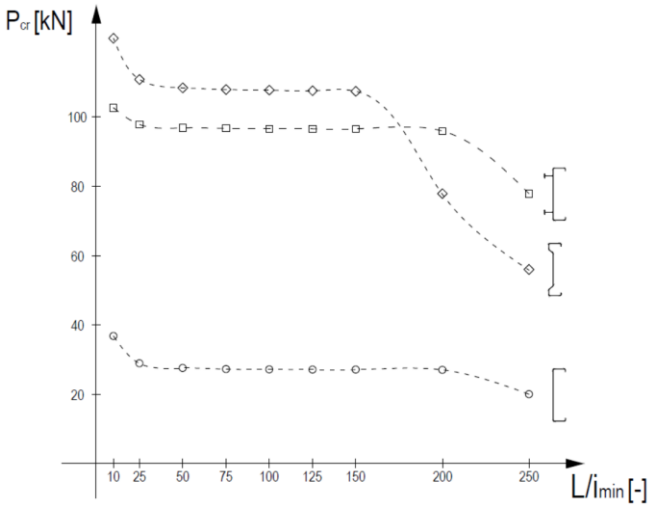

Fig. 4. The values of the critical load (P_{cr}) as a function of concentric axially loaded thin-walled bar slenderness radio (L/i_{min})

It was found that for the large values of the slenderness ratio (200 ÷ 250) the dominant buckling mode was the global one. This buckling mode was successfully described by Vlasov theory. As it was mentioned before, for the lower slenderness ratio the local and global interactive buckling occur. The same phenomena was observed as well in the case of the channel, sigma and simplified model.

It is worth to mention that obtained results for the sigma and simplified model (Fig. 1) remained in the compliance for the slender ratio (10 – 150). The slightly different behaviour was observed for the higher slenderness ratio when the global buckling occurred.

For slenderness ratio equal less than or equal to 100 the pure local buckling mode was extracted. The obtained results for this case were presented in Tab. 2. The local forms of buckling for the cross-section for the height of 230 mm were presented in the Fig. 5.

Tab. 2. The values of critical stress for different height of the cross-section

The critical stress σ_{cr} [MPa]			
H [mm]			
$L/i_{min} \leq 100$ – local buckling			
140	134.30	445.49	455.60
200	79.90	293.79	322.91
230	45.66	162.60	170.62
260	52.19	120.62	145.11
300	44.06	84.98	97.03
350	40.60	67.87	74.14

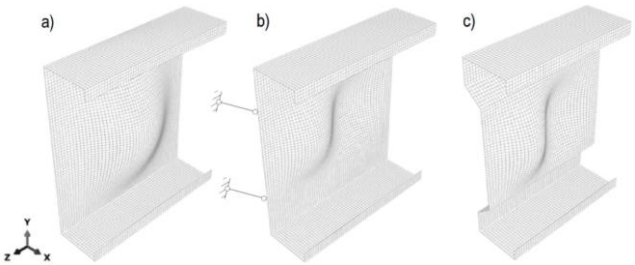

Fig. 5. The local forms of buckling for: channel (a), channel with additional supports (b) and sigma (c) cross-section

One can noticed that applying the simplified model (Fig. 5 b) provides the similar results comparing to the real sigma cross-section both in the shape of the buckling mode and the value of critical buckling stresses (Tab. 2).

3. DISTORTIONAL BUCKLING

3.1. Theoretical background

The critical distortional buckling stress for edge or intermediate stiffener according to (Eurocode 3, 2006) is evaluated from:

$$\sigma_{cr,s} = \frac{2\sqrt{KEI_s}}{A_s}, \tag{3}$$

where: K – is the spring stiffness per unit length according to

DOI 10.1515/ama-2016-0033

the formula (4), A_s – is the area of the effective cross-section, I_s – is the moment of inertia of the effective cross-section.

$$K = \frac{Et^3}{4(1-\nu^2)} \cdot \frac{1}{b_1^2 h_w + b_1^3 + 0{,}5 b_1 b_2 h_w k_f}, \quad (4)$$

where: t – is flange thickness, h_w – is the web depth, b_1, b_2 – is the distance between the web-to-flange junction and the gravity centre of the effective area of the edge stiffener of flange respectively 1 or 2, k_f – is the ratio which is equal to 1 for a symmetric section in compression.

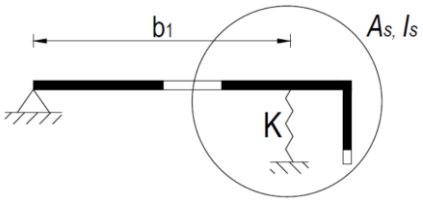

Fig. 6. The model used to analyse distortional buckling according to EN-1993-1-3 (Eurocode 3, 2006)

Alternatively, the critical distortional buckling stress can be calculated from the equations formulated by Lau and Hancock (5) or from formula proposed by Schafer (8).

$$\sigma_{cr} = \frac{E}{2A_f}\left[(\alpha_1 + \alpha_2) - \sqrt{(\alpha_1 + \alpha_2)^2 - 4\alpha_3}\right], \quad (5)$$

where: $\mathrm{A_f}$ – is the cross-sectional area of the flange and lip, $\alpha_1, \alpha_2, \alpha_3$ – are coefficients dependent on the geometrical characteristics and the value of elastic rotation spring stiffness $\mathrm{k_\phi}$ (Fig. 7).

The main idea of the Lau and Hancock method is to determine the flexural – torsional buckling critical stress of the model shown in the Fig. 7, where $\mathrm{h_y}$ and $\mathrm{h_z}$ are the coordinates of the centroid of flange and lip and $\mathrm{k_2}$ is the translational spring stiffness.

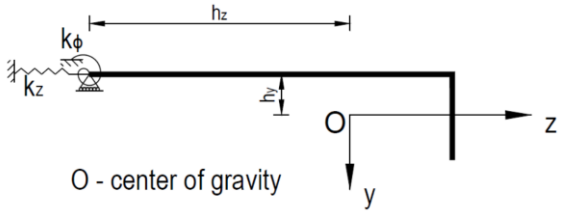

Fig. 7. The Lau and Hancock model

This method can be used only in the case when the value of rotation spring stiffness is greater than 0. The modification of Lau and Hancock method for the case when the value of rotation spring stiffness is less than 0 was proposed by Davies and Jiang (1996). Two additional variables were introduced: $\sigma`_{\mathrm{cr}}$ – stress determined by the formula (5) assuming $\mathrm{k_\phi} = 0$ and σ_{w} – the web critical buckling stress (6).

$$\sigma_w = \frac{\pi^2 D}{t h_w^4}\left(\frac{h_w^2 + \lambda^2}{\lambda}\right)^2, \quad (6)$$

where: D – is plate stiffness, λ – is the half – wavelength.

Finally the distortional critical buckling stress (when $\mathrm{k_\phi} < 0$) can be determined using following formula:

$$\sigma_{cr} = \frac{2\sigma`_{cr} A_f + \sigma_w t h_w}{A}, \quad (7)$$

where: A – is the total area of the cross-section.

However, the critical stress proposed by Schafer is given as a function of rotational stiffness of the support at the point of the flange-web junction.

$$\sigma_{cr} = \frac{k_{\varphi fe} + k_{\varphi we}}{k_{\varphi fg} + k_{\varphi wg}}, \quad (8)$$

where: $k_{\varphi fe}, k_{\varphi we}$ – are elastic rotational spring stiffness of the flange and web and $k_{\varphi fg}, k_{\varphi wg}$ – are geometric rotational spring stiffness of the flange and web.

3.2. Numerical model 2

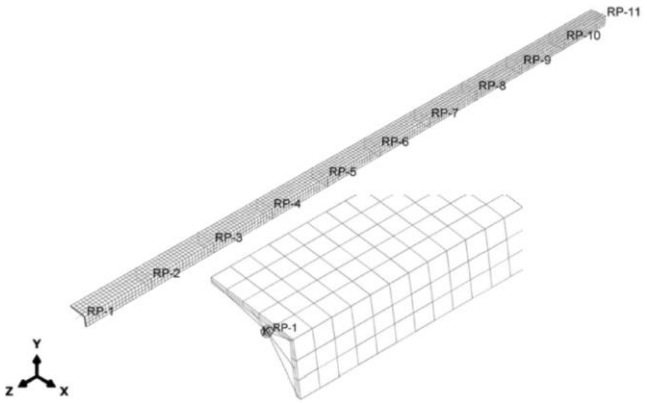

Fig. 8. The numerical model 2

To verify the analytical models presented in the paragraph 3.1 the numerical model 2 using finite element method and shell elements S4R was created. In numerical model 2 (Fig. 8) the boundary conditions and geometry were applied according to the Eurocode 3 recommendations (Fig. 6). The elastic spring supports were modelled with the stiffness equal to the value determined from the formula 4.

The numerical examples were carried out for the simplified model which corresponded to the sigma cross-section with the high H= 140, 200, 230, 260, 300 and 350 mm. Based on the conclusions drawn from analysis conducted in paragraph 2.3, during the calculations of critical distortional stress using Eurocode, Hancock and Schafer formulas the reduce value of the web height (hw) was applied (distance between two additional elastic supports Fig. 1). The obtained results was compared with the FEM numerical model corresponding to Eurocode equivalent cross-section. The results of the calculations were presented in Tab. 3.

Tab. 3. The critical distortional buckling stress

H [mm]	hw [mm]	Shafer [MPa]	Lau-Hancock [MPa]	EN 1993-1-3 [MPa]	FEM [MPa]
140	50	423.01	341.56	323.61	308.49
200	110	266.90	245.75	250.69	262.83
230	140	216.18	211.25	228.85	242.66
260	170	172.60	177.27	211.89	220.76
300	210	124.87	129.06	194.19	213.57
350	260	81.65	102.43	117.28	129.21

DOI 10.1515/ama-2016-0033

4. CONCLUDING REMARKS

In this paper the local and distortional buckling analyses of axially loaded cold-rolled channel and sigma profiles were performed. The special attention was focused on creating the simplified models of sigma cross-sections which allowed for applying the analytical formulas for calculation of distortional buckling derived for the channel cross-section. For this purpose the finite element models were created in order to verify simplified formulas implemented in Eurocode and proposed by Hancock and Schafer. The performed buckling analyses proved that the sigma cross-section can be successfully replaced by channel cross-section with additional elastic supports placed in folds of the web. It was demonstrated that the folds in the web of the sigma cross-section (additional elastic supports) reduce the web slenderness. So, the critical distortional stress can be calculated based on analytical formulas derived for the channel cross-section taking into account the web height between the folds (h_w).

REFERENCES

1. **Abaqus Documentation** – version 6.13, http://www.abaqus.com
2. **Davies J.M., Jiang C.** (1996), Design of thin walled columns for distortional buckling, *Proceedings of the Second International Conference on Coupled Instability in Metal Structures CIMS'96*, Liege, Belgium.
3. **EN 1993-1-3, Eurocode 3** (2006), *Design of steel structures – Part 1-3: General rules – Supplementary rules for cold-formed members and sheeting.*
4. **He Z., Zhou X., Liu Z., Chen M.** (2014), Post-buckling behaviour and DSM design of web-stiffened lipped channel columns with distortional and local mode interaction, *Thin-Walled Structures*, 84, 189–203.
5. **Lau, S.C.W., Hancock, G.J.** (1990), Inelastic buckling of channel columns in the distortional mode, *Thin – Walled Structures*, 10, 59-84.
6. **Long-yuan Li** (2009), Analyses of distortional buckling of cold-formed sigma purlins using EN 1993-1-3, *Journal of Constructional Steel Research*, 65, 2099-2102.
7. **Long-yuan Li, Jian-kang Ch.** (2008), An analytical model for analysing distortional buckling of cold-formed steel sections, *Thin – Walled Structures*, 46, 1430-1436.
8. **Pala M.** (2006) A new formulation for distortional buckling stress in cold-formed steel members, *Journal of Constructional Steel Research*, 62, 716–722.
9. **Pala M.**, Caglarb N. (2007), A parametric study for distortional buckling stress on cold-formed steel using a neural network, *Journal of Constructional Steel Research*, 63, 686–691.
10. **Schafer B.W.** (2000), *Distortional buckling of cold-formed steel columns*, Final Report of AISI.
11. **Schafer B.W.** (2008), Review: The Direct Strength Method of cold-formed steel member design, *Journal of Constructional Steel Research*, 64 766–778.
12. **Szymczak C., Werochowski W.** (2005), Distortional instability of axially loaded cold-formed elements with stiffened flanges (in Polish), *Inżynieria i Budownictwo*, R. 61, 2, 85-88.
13. **Wang L., Young B.** (2014), Design of cold-formed steel channels with stiffened webs subjected to bending, *Thin-Walled Structures*, 85, 81–92.
14. **Yua C., Schafer B.W.** (2007),Simulation of cold-formed steel beams in local and distortional buckling with applications to the direct strength method, *Journal of Constructional Steel Research*, 63, 581–590.
15. **Zhou X., Liu Z., , He Z.** (2015), General distortional buckling formulae for both fixed-ended and pinned-ended C-section columns, *Thin-Walled Structures*, 94, 603–611.

Financial support by the grant 01/11/DSPB/0605/2016 DSPB is kindly acknowledged.

DE GRUYTER
OPEN

DOI 10.1515/ama-2016-0034

acta mechanica et automatica, vol.10 no.3 (2016)

SUGGESTED RESEARCH METHOD FOR TESTING SELECTED TRIBOLOGICAL PROPERTIES OF FRICTION COMPONENTS IN VEHICLE BRAKING SYSTEMS

Andrzej BORAWSKI*

*Faculty of Mechanics and Construction of Machinery, Mechanical Department, Białystok University of Technology, ul. Wiejska 45 C, 15-351 Białystok, Poland

a.borawski@pb.edu.pl

received 11 June 2015, revised 20 July 2016, accepted 22 July 2016

Abstract: The braking system is one of the most important systems in any vehicle. Its proper functioning may determine the health and life the people inside the vehicle as well as other road users. Therefore, it is important that the parameters which characterise the functioning of brakes changed as little as possible throughout their lifespan. Multiple instances of heating and cooling of the working components of the brake system as well as the environment they work in may impact their tribological properties. This article describes a method of evaluating the coefficient of friction and the wear speed of abrasive wear of friction working components of brakes. The methodology was developed on the basis of Taguchi's method of process optimization.

Key words: Brakes, Taguchi's Method, Friction

1. INTRODUCTION

Brakes are one of the most important components of any vehicle. Their proper and effective work determines the life and health of drivers, passengers, and other road users. That is why a lot of research is conducted in order to identify the problems connected with the construction and work of brakes, and making them more effective.

The most common types of brakes in today's vehicles are friction brakes. This type of brake uses friction in order to transform mechanical energy into thermal energy. The amount of heat produced during braking, as well as the speed of its distribution depends, among other things, on the material that was used to manufacture the brake system components. Results of simulations (performed using MES) show, that the elements that get heated the most during braking are brake discs and pads (Yevtushenko et al, 2014, 2015, 2016). Thermal energy is then released into the atmosphere and to other parts of the brake system, as well as the vehicle's suspension.

Multiple instances of heating (to temperatures of up to several hundreds degrees Celsius) and cooling may change the tribological properties of brake pads and discs. Consequently, this may reduce the braking force (Śnieżka, 1998). The corrosive environment brake systems work in (salt and water, especially during winter) are also significant. Increasing the braking distance has a direct influence on the level of danger in traffic. Therefore it is important to determine if and how the tribological properties of brake friction components change.

2. METHODOLOGY

Proper planning of the test is not an easy task. However, it allows obtaining the best results with minimum work (Polański, 1984), which contributes to limiting the time and costs generated by the research. Among numerous possibilities used by researchers (Kamiński, 2013; Borawski, 2015; Szpica, 2015a, 2015b), Taguchi's method of process optimisation was used to plan the experiment. The experiment itself will be conducted using the ball cratering test which allows examination of abrasive wear resistance (Osuch-Słomka et al, 2013).

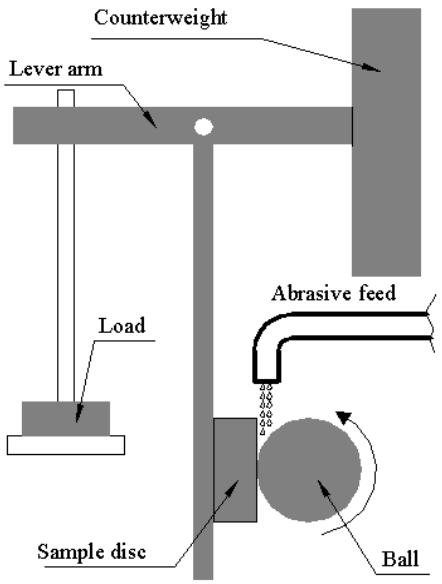

Fig. 1. Abrasive wear testing set

In this method, the friction pair is composed by the studied material's sample and a counter sample, a 1" (25.4 mm) ball. When the ball is moving it grinds against the sample causing it to wear (Fig. 1). Its smooth, polished surface may influence the tests

results (Allsopp et al, 1998). In extreme cases it may turn out that no results were obtained (no abrasive wear occurred). That is why in order to enhance the effect of abrasive damage it is suggested to use hard abrasives suspended in water and fed onto the friction surface (Fildes et al, 2012).

As a result of the test, a crater is formed in sample. The diameter of the crater depends on, among other things, the working parameters of the friction pair (load, rotational speed and sliding distance). Proper adjustment of these elements determines obtaining accurate test results (Cozza, 2014).

2.1. Test object

In accordance with the applicable standard (PN-EN 1071-6:2008) the test objects are samples which are 1" (25.4 mm) in diameter and 10 mm thick. It is recommended to cut 2 samples from each studied component of the braking system (from each disc and each pad). The samples should be prepared using a method that prevents the material from heating, such as water-jet cutting. This prevents further changes in the structure of the material. Next, the sample should be sanded, remembering about minimizing the temperature of the sample during sanding. Otherwise, the obtained results will not correspond with the actual value of the K_C factor. Fig. 2 shows samples that were first cut from a brake disc and then sanded.

Fig. 2. Examples of samples prepared for ball-cratering tests

2.2. Planning the experiment

The first step of planning the experiment should involve conducting preliminary research. The obtained results will allow to evaluate what ranges of input parameters produce satisfying craters. Recommended input parameters (based on the norm and results of preliminary research) that produce reliable results in most cases are presented in Tab. 1. Experience shows, however, that setting these parameters does not produce satisfactory results for some materials. In such cases, the parameters should be adjusted, for example by increasing the load or the sliding distance (resulting in extending the time of the experiment) (Cozza, 2014). Increasing the ball's speed of rotation is not recommended, as it tends to result in increased relative error of the measurements. The preliminary parameters of the experiment will be set properly if the relative error of the crater diameters created in the preliminary tests do not exceed 0.01.

Tab. 1. Recommended input parameters based on the norm (PN-EN 1071-6:2008) and own preliminary research

Load [N]	Distance [m]	Speed of rotation [rpm]
0.2	50	38
0.4	100	80
0.6	150	150

In the example presented in Fig. 3, the relative error for all friction distances obtained in 5 tests fits into the assumed value. If the relative error exceeded 0.01 for any distance, this value should be rejected and replaced with the arithmetic mean of the other two values.

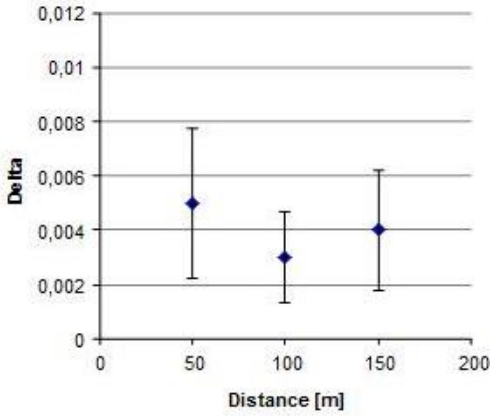

Fig. 3. Example diagram showing the relative errors of measured crater diameters (results of five tests, minimum, maximum and mean values).

After finding the preliminary ranges for input parameters of the experiments, the next step is to find their optimal values. This is done with an orthogonal array. In the discussed case there are three entry parameters, and each of theses has three values. Therefore, the orthogonal array will have the form presented in Tab. 2.

Tab. 2. Example orthogonal array of the experiment

Experiment no.	Load [N]	Distance [m]	Speed of rotation [rpm]
1	0.2	50	38
2	0.2	100	80
3	0.2	150	150
4	0.4	50	80
5	0.4	100	150
6	0.4	150	38
7	0.6	50	50
8	0.6	100	150
9	0.6	150	80

Each of the nine tests should be conducted at least three times. In accordance with the "less is best" criterion and using the results obtained previously, the next step is finding the ETA function following the relation:

DOI 10.1515/ama-2016-0034

$$\eta = -10\log_{10}\left[\left(\frac{1}{n}\right)\right]\sum {y_i}^2 \quad (1)$$

where: n – number of measurements, y_i – value of analysed parameter.

Example graphs of ETA functions for particular parameters are presented in Fig. 4.

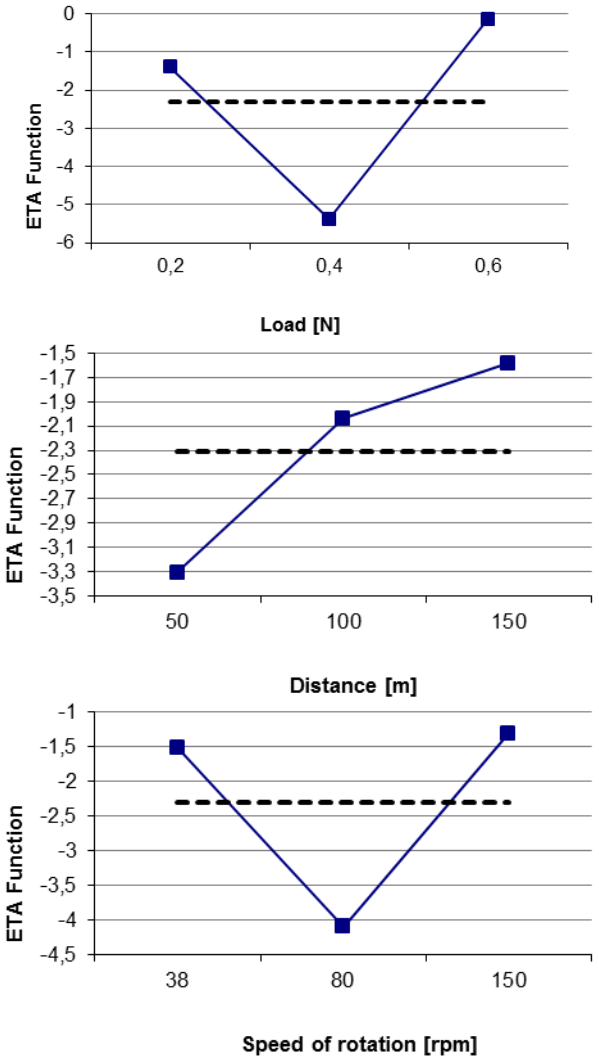

Fig. 4. Example ETA function graph based on preliminary research

After analysing the value of ETA functions, the optimal parameters for the experiment are:

- load: 0.6N;
- distance: 150 m;
- speed of rotation: 150 rpm.

2.3. Course of the experiment

Using the optimal input parameters for the experiment that were determined using Taguchi's methodology, it is possible to plan the proper experiment (Tab. 3). Its results will make it possible to determine the abrasive wear factor (K_C). In order to avoid random errors, it is recommended to repeat every test at least three times (for each sample, 1÷i). It is also necessary to calculate the relative error of the crater diameters which, as mentioned earlier, should not exceed 0.01.

Tab. 3. Example plan of the proper experiment, aiming at determining the K_C factor

Sample no	Parameters		Number of repetitions
1	Load:	0.6 N	≥3
	Distance:	150 m	
	Speed of rotation:	150 rpm	
2	Load:	0.6 N	≥3
	Distance:	150 m	
	Speed of rotation:	150 rpm	
...	Load:	0.6 N	≥3
	Distance:	150 m	
	Speed of rotation:	150 rpm	
i	Load:	0.6 N	≥3
	Distance:	150 m	
	Speed of rotation:	150 rpm	

For the purpose of this article, the tests were carried out using a T-20 slurry abrasive testing machine, which allows testing friction pairs with abrasive suspensions (Fig. 5). The recommend abrasive is a silicon carbide water suspension.

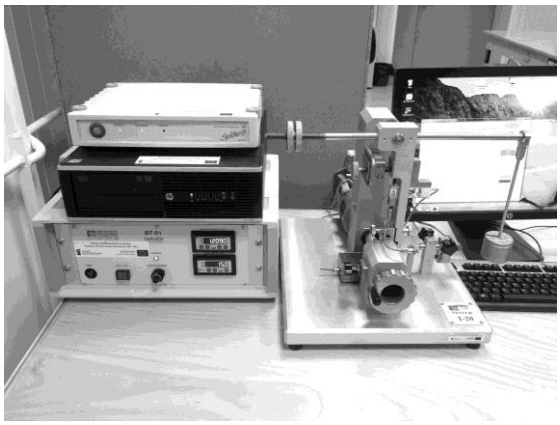

Fig. 5. T-20 Workstation

The machine is capable of recording the coefficient of friction during the test. In order to keep the measured value as close as possible to the actual value (unlike in tests aimed at determining K_C) it is recommended to perform a "dry" run, without feeding the abrasive suspension to the friction pair. This is because the slurry may underestimate the results of the test.

3. COMPILING THE RESULTS

The direct results of the tests are craters created in the samples. Examples of grooves created by ball friction are presented in Fig. 6.

The diameter of the crater should be measured in two planes (Fig. 7) to calculate the arithmetical mean:

$$b = \frac{b1+b2}{2}. \quad (2)$$

The volume of the crated can be calculated using the relation:

$$V = \pi\frac{b^4}{64R}, \quad (3)$$

where: R – Ball radius.

$$V = K_C S N \,, \tag{4}$$

where: K_C – Abrasive wear factor, S – distance, N – load.

Transformation of Archard's equation (4) produces the formula for the rate of abrasive wear:

$$K_C = \pi \frac{b^4}{64RSN} \,. \tag{5}$$

The K_C factors and the coefficients of friction should be calculated and measured for each sample cut from the brake system component and then compared.

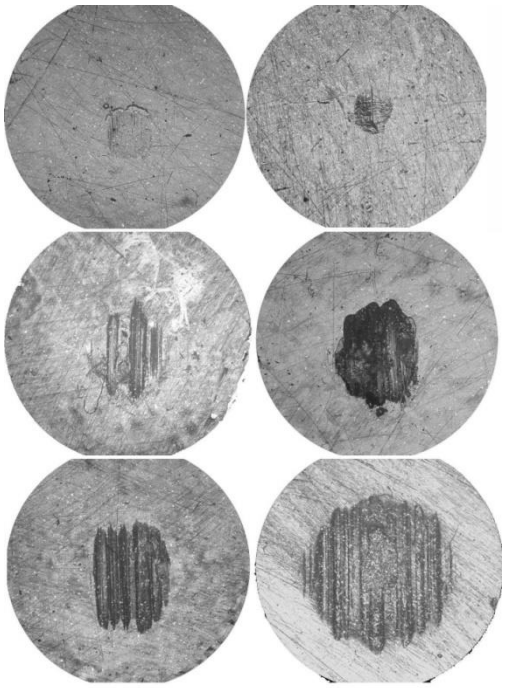

Fig. 6. Examples of craters created in the samples as a result of ball-cratering tests, photographs taken with an OLYMPUS BX51M microscope, 10x zoom.

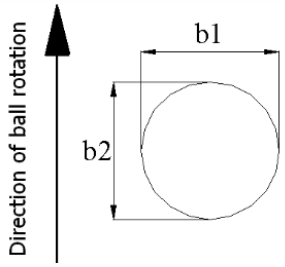

Fig. 7. Crater diameter measurement diagram

4. SUMMARY

1. The developed method is a quick, economical and effective way of measuring abrasive wear.
2. The method is characterised by repeatability and reproducibility, and it requires significantly less testing time than other methods, such as ball-on-disc.
3. Proper planning of the experiment requires conducting preliminary research in order to determine input parameters (ball rotation speed, load and sliding distance).
4. Precision in preparing the sample determines the quality of the results. Specialised equipment, such as water-jet cutting, is helpful at this stage.
5. The results of K_C factor calculations and the results of the coefficient of fraction measurements enable the comparison of tribological properties of the samples taken from the components of the brake system.

REFERENCES

1. **Allsopp D.N.; Trezona R.I.; Hutchings I.M.** (1998), The effects of ball surface condition in the micro-scale abrasive wear test, *Tribology Letters*, 5(4), 259-264.
2. **Borawski A.** (2015), Modification of a fourth generation LPG installation improving the power supply to a spark ignition engine, *Eksploatacja i Niezawodnosc – Maintenance and Reliability*, 17(1), 1-6.
3. **Cozza R.C.** (2014), Influence of the normal force, abrasive slurry concentration and abrasive wear modes on the coefficient of friction in ball-cratering wear tests, *Tribology International,* 70, 52-62.
4. **Fildes J.M.; Mayers S.J.; Kilaparti R.; Schlepp E.** (2012), Improved ball crater micro-abrasion test based on a ball on three disc configuration, *Wear*, 274-275, 414-422.
5. **Kamiński Z.** (2013), Experimental and numerical studies of mechanical subsystem for simulation of agricultural trailer air braking systems, *International Journal of Heavy Vehicle Systems*, 20(4), 289-311.
6. **Osuch-Słomka E.; Ruta R.; Słomka Z.** (2013), The use of a modern method of designing experiments in ball-cratering abrasive wear testing, *Journal of Engineering Tribology*, 227, 1177-1187.
7. **PN-EN 1071-6:2008** Advanced technical ceramics - Methods of test for ceramic coatings - Part 6: Determination of the abrasion resistance of coatings by a micro-abrasion wear test
8. **Polański Z.** (1984), *Experiment planning in technology*, PWN Warszawa (in Polish).
9. **Ścieszka S. F.** (1998), *Friction brakes – material, structural and tribological problems*, ITE, Radom.
10. **Szpica D.** (2015), Fuel dosage irregularity of LPG pulse vapor injectors at different stages of wear, *Mechanika*, 22(1), 44-50.
11. **Szpica D.** (2015), Simplified numerical simulation as the base for throttle flow characteristics designation, *Mechanika*, 21(2), 129-133.
12. **Yevtushenko A.A., Grzes P.** (2014), Mutual influence of the velocity and temperature in the axisymmetric FE model of a disc brake. *International Communications in Heat and Mass Transfer*, 57, 341-346.
13. **Yevtushenko A.A., Grzes P.** (2015), 3D FE model of frictional heating and wear with a mutual influence of the sliding velocity and temperature in a disc brake, *Int. Comm. Heat Mass Transf*., 62, 37-44.
14. **Yevtushenko A.A., Grzes P.** (2016), Mutual influence of the sliding velocity and temperature in frictional heating of the thermally nonlinear disc brake, *International Journal of Thermal Science*, 102, 254-262.

The study was conducted within the University's research project no. MB/WM/1/2015, financed from funds used for the development of young scientists and doctoral students.

DE GRUYTER
OPEN

DOI 10.1515/ama-2016-0035 acta mechanica et automatica, vol.10 no.3 (2016)

DYNAMICS OF THE NON-CONTACT ROUNDNESS MEASUREMENT WITH AIR GAGES

Czesław Janusz JERMAK*, Mirosław RUCKI*

*Poznan University of Technology, Institute of Mechanical Technology, Division of Metrology and Measurement Systems, ul. Piotrowo 3, 60-965 Poznań, Poland

czeslaw.jermak@put.poznan.pl, miroslaw.rucki@gmail.com

received 11 December 2015, revised 20 July 2016, accepted 22 July 2016

Abstract: The paper presents the results of investigations on the air gages dynamic characteristics in the measurement of the round profiles of motor cylinders. The principle of the measuring device is explained, and the analysis of the air gages dynamics is described. The results of dynamic calibration enabled to eliminate those configurations of air gages that may not meet the requirements of the measurement they were designed for. After the proper air gages were chosen, the entire system underwent the accuracy test and passed it successfully revealing the method accuracy better than 10% compared to the reference measurement.

Key words: Air Gage, Back-Pressure, Out-of-Roundness

1. INTRODUCTION

The quality management in 25 years has shifted researches away from TQM to focus on the tools and techniques and improving measurement systems (O'Neil, 2016). Especially valuable in that context are non-contact measuring techniques (Valicek et al., 2007), among others air gages (Shiraishi, 2002). Despite the air gages are unable to perform a measurement with nanoscale accuracy, they still find their application in the industrial precise measuring tasks like in-process inspection (Vacharanukul and Mekid, 2005) both passive and active type (Wang et al., 2005; Menzies and Koshy 2009) or automatic control (Wieczorkowski, 1995).

Even though the investigations on the dynamic properties of the air gages had been performed since the middle of the 20th century both in Western countries and in the Soviet Union (Yribarren, 1955; Dmitriev and Chernyshev, 1958), the long response time of the devices seemed to be the main obstacle for their development (Tsidulko, 1965). Nowadays, however, application of the piezoresistive pressure transducers and reduction of the measuring chamber volume (Jermak and Rucki, 2012) allowed to apply the air gage in the fast non-contact measurement of complicated geometrical features like roundness and cylindricity. The goal of the present study was to analyze dynamic properties of the air gauges and to choose the ones with proper dynamic characteristics to be implemented in the Geoform device dedicated for the roundness assessment. The device with chosen air gauges underwent overall accuracy test through a comparative analysis with the reference measurement data.

2. OUT-OF-ROUNDNESS MEASUREMENT WITH THE AIR GAGES

The team of the Division of Metrology and Measurement Systems (Poznan University of Technology) has proposed the innovative device Geoform designed for the complex measurement of the cylinders for the motor industry. The series of investigations proved the capability of the air gages to measure within assumed tolerances (Derezynski and Jakubowicz, 2016). In order to achieve non-contact measurement with high dynamics, the small chamber air gages (back-pressure type) had been proposed.

A simple one-cascade back-pressure gage consists of two nozzles (inlet d_w and measuring one d_p), as it is shown in the Fig. 1. The pressured air of pressure p_z enters the measuring chamber of certain volume V_k through the inlet nozzle, and leaves through the measuring one. Here, the surface of the measured detail serves as a flapper which restricts the air outflow, so the pressure p_k in the chamber in some extend is proportional to the displacement s. The volume V_k of the chamber depends on its length l_k and inner diameter d_k.

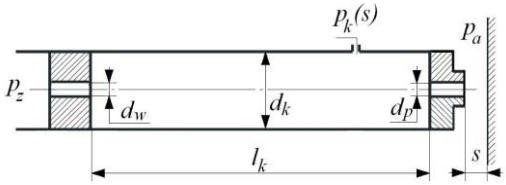

Fig. 1. Scheme of the back-pressure air gage

Typically, engineers do not calculate the exact response time or amplitude characteristics of the air gages. For instance, Jun Liu et al. (2012) consider the velocity of the gage head during the form measurement relatively low so that the dynamic error can be ignored, or Grandy et al. (2009) use the simplified dynamic models with reference to the geometric parameters of an air gage. It was proved that the dynamics of the air gages with small volumes (ca. 0.5 to 4.0 cm^3) combined with a piezoresistive pressure transducer could be modelled as a first-order dynamic system, but some additional knowledge is required in order to avoid unexpected dynamic errors (Rucki and Jermak, 2012). Hence, after exact analysis of their dynamic characteristics, the devices could be applied for the measurement in dynamic conditions, like

DOI 10.1515/ama-2016-0035

a cylindricity measurement.

Traditionally, quality control is performed offline, after a part is produced (Gao et al., 2014), and the Geoform device was designed for this kind of measurement. It is based on the complete automatic set, where the detail is placed manually (Fig. 2, left). The measuring head goes up from lower part of the set, and perform the measurement in three intersections (bottom, middle and top) turning around 360º (Fig. 2, right). The novelty of the method consists of following: the measuring head contains three independent air gages (Fig. 3), it is placed on the flexible rod (a floating head), and it is based on the original algorithm designed for analysis of three independent signals to determine the roundness of the measured detail.

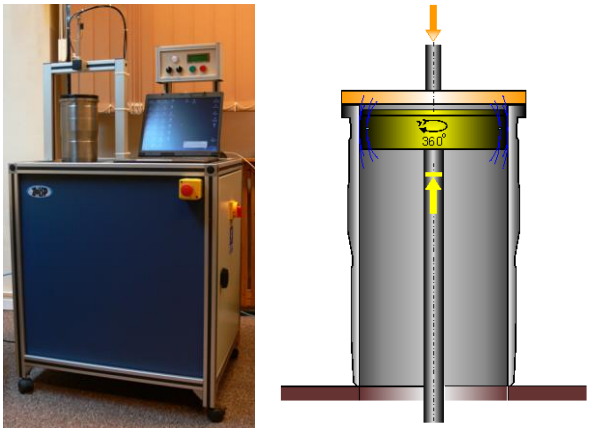

Fig. 2. The Geoform equipment (left) and the scheme of measurement (right) (Jermak et al., 2010)

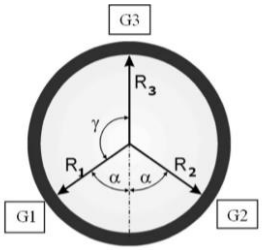

Fig. 3. Position of three air gages in the Geoform measuring head

The algorithm consists of the following operations:

- data collection which is performed from three air gages independently, when the gage head turns 370° (there are up to 1000 points recorded),
- smoothening of the obtained data in order to eliminate the excessive errors,
- profile closure which is necessary because of flexible type of the gage head (the coordinates of the points corresponding with 0° and 360° are different and need to be adjusted to each other),
- interpolation according to the Bessel's formula (Pollard, 1977) performed in order to reduce the number of analyzed points down to 720,
- calculation of the profile and its out-of-roundness.

The calculations are performed as if the typical V-block measurement is done (Stepien, 2010), only instead of fixed two points of the V-block, the collected data from two air gages (G2 and G1 shown in the Fig. 3) are used. To obtain the would-be value ΔW of V-block measurement from the collected points G1, G2 and G3, the following formula is applied (Cellary and Jermak, 2009):

$$\Delta W = \Delta R_3 + \frac{\Delta R_1 + \Delta R_2}{2\cos\alpha}, \tag{1}$$

where: ΔR_1, ΔR_2 and ΔR_3 – indication changes for the gages G1, G2 and G3 respectively, 2α – the angle between gages G1 and G2.

The measuring task was defined by the initial laboratory measurement of the cylinders for motor industry with the reference device Talyrond 365. The assumed tolerance was 15 µm near the upper and lower edges, and 10 µm in the middle part of the cylinder. The highest amplitudes revealed 2nd and 3rd harmonics: 2.6 µm and 0.98 µm respectively. Amplitudes of 4th, 5th and 7th harmonics were of similar distribution type and did not exceed 0.56 µm (mean values lower than 0.08 µm).

In order to enable the reliable harmonic analysis up to 15th harmonics, and to reduce the measurement time down to 10 s, it was needed to evaluate the dynamic characteristics of the applied air gages, and to shape them to ensure the acceptable error level.

3. SINE INPUT ANALYSIS

Dynamic variables are time or space dependent in both their magnitude and frequency content. A dynamic calibration determines the relationship between an input of known dynamic behaviour and the measurement system output. Usually, such calibrations involve applying either a sinusoidal signal or a step change as the known input signal (Figliola and Beasley, 2006). When the input signal forms a simple periodic function, $F(t) = A\cdot\sin\omega t$, and the initial conditions are $y(0) = y_0$, then the function could be written as following:

$$T\dot{y} + y = KA\sin\omega t, \tag{2}$$

where: T – time constant, K – static sensitivity (multiplication), A – amplitude, $\omega=2\pi f$ – rotational speed, f – frequency.

The amplitude of the steady response depends on the value of the applied frequency f.

In order to generate a sine input signal, the dedicated laboratory equipment has been developed (Fig. 4). It consists of replaceable model of the air gage (1) with the pressure transducer (3), eccentric shaft of highly smooth surface and eccentricity e = 20 µm (2) which rotary speed can be changed from ω = 0.1 rad/s up to 20 rad/s, and the electronic devices for conditioning and acquisition of the measurement signals (4). Fig. 5 presents the block diagram of the sine input analysis system.

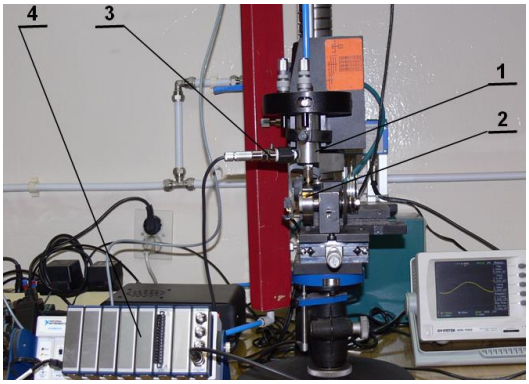

Fig. 4. Laboratory equipment for the sine input analysis of the air gages

DOI 10.1515/ama-2016-0035

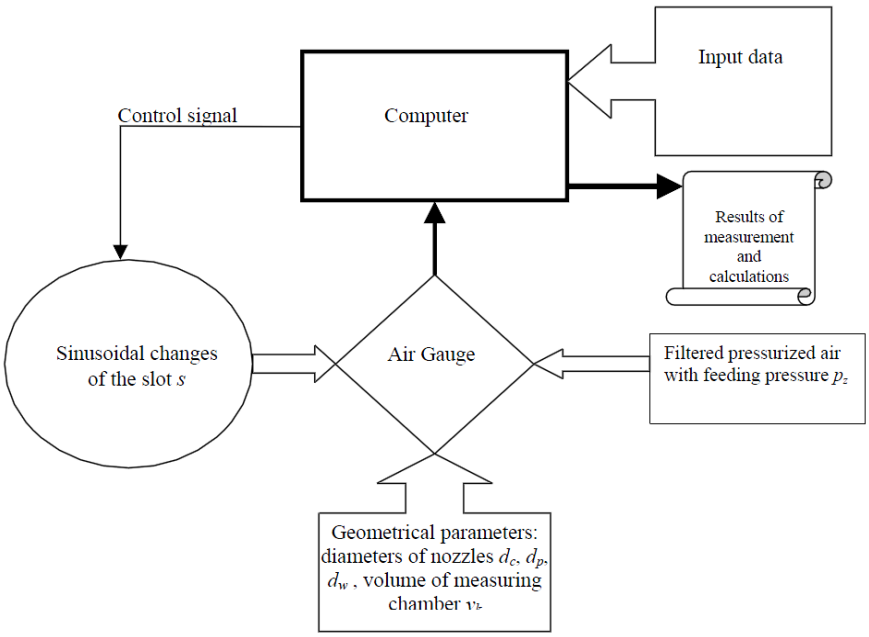

Fig. 5. Block diagram of the dynamic calibration setup (Rucki and Barisic, 2009)

The system presented in the Figs. 4 and 5 enables to analyse the air gages of various geometrical parameters (nozzles diameters and dimensions of the measuring chambers explained in the Fig. 1). The data of the examined air gauge is input into the computer, as well as the conditions of experiment. The computer controls the measurement process generating the sinusoidal changes of slot *s* and processes the collected measurement data.

The measurement system collected 20 periods of the alternating pressure for each assumed rotational speed with sampling time 0.001 of the examined period. Then, the corrected (true) value of the sine input was calculated, as well as the amplitude of the air gage response. The calculation algorithm was based on the spline functions of the 2nd order and the least square method. The obtained results are the amplitude—frequency characteristics as well as the time constant and frequency. The value $f_{0.05}$ means a frequency when the dynamic error $\delta(\omega)$ is smaller than 5%.

During the roundness measurement, the measured cylinder typically rotates with a speed of ca. 6 rpm. Therefore, to perform the registration of at least 15 harmonics of the profile with the acceptable amplitude error below 5%, the upper frequency bound $f_{0.95}$ could not be lower than 1.5 Hz. From the metrological perspective, it should be even higher to reduce the dynamic error as well as the measurement time. Hence, the following criteria were set to evaluate the dynamic quality of examined air gages:

- upper frequency bound should be $f_{0.95} > 1.5$ Hz,
- time constant T should not exceed 30 ms.

Because of strong evidence that the outer diameter of the measuring nozzle d_c have some impact on the dynamical characteristics (for larger d_c/d_p ratio the time constant T appeared to be longer) (Rucki, 2011), that parameter was taken into consideration. Thus, the following geometry of the air gages underwent examinations:

- the measuring nozzles of inner diameters d_p = 1.211, 1.405 and 1.610 mm, of the ratios $D_c = d_c/d_p$ = 1.5, 2 and 3,
- the volumes of the measuring chambers V_{k1} = 0.25, V_{k2} =1.22 and V_{k3} =3.90 cm^3,
- the inlet nozzles of the diameters d_w = 0.570, 0.625, 0.720, 0.830 and 1.020 mm.

4. MEASUREMENT RESULTS

From the experimental amplitude–frequency characteristics obtained with the experimental setup described above, the values of upper frequency bound $f_{0.95}$ and time constant T was calculated for each examined air gage proposed to be applied in the Geoform device. The results are presented in the Tables 1 to 6. The same results for the smallest measuring nozzle d_p = 1.211 mm and the smallest chamber volume V_{k1} = 0.25 cm^3 are presented graphically in the Fig. 6.

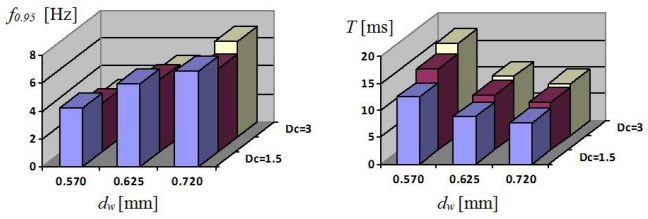

Fig. 6. Graphs of frequency $f_{0.95}$ (left) and time constant T (right) for the air gage with d_p = 1.211 mm and V_{k1} = 0.25 cm^3

Using the time constant values (Tabs. 4-6), the amplitude–frequency characteristics were calculated. Fig. 7 presents the graph showing the influence of the measuring chamber volume on the obtained characteristics.

DOI 10.1515/ama-2016-0035

Tab. 1. Values of the upper frequency bound $f_{0.95}$ [Hz] for the chamber V_{k1} = 0.25 cm^3

d_p[mm]	1.211			1.405			1.610		
d_w[mm]	0.570	0.625	0.720	0.625	0.720	0.830	0.720	0.830	1.020
$d=d_w/d_p$	0.471	0.516	0.603	0.444	0.520	0.591	0.447	0.516	0.633
D_c=1.5	4.18	5.91	6.85	5.62	8.80	9.67	6.41	9.89	12.45
D_c=2	3.50	5.21	5.94	5.12	6.86	9.04	6.01	9.46	9.74
D_c=3	3.08	4.79	6.85	4.88	5.95	8.37	6.04	8.52	9.12

Tab. 2. Values of the upper frequency bound $f_{0.95}$ [Hz] for the chamber V_{k2} =1.22 cm^3

d_p[mm]	1.211			1.405			1.610		
d_w[mm]	0.570	0.625	0.720	0.625	0.720	0.830	0.720	0.830	1.020
$d=d_w/d_p$	0.471	0.516	0.603	0.444	0.520	0.591	0.447	0.516	0.633
D_c=1.5	3.82	4.02	4.52	4.31	4.84	5.01	4.17	7.31	8.32
D_c=2	3.11	3.38	3.98	3.89	3.98	5.12	5.02	6.80	7.02
D_c=3	2.62	2.84	3.01	3.42	4.02	5.46	5.77	6.45	6.85

Tab. 3. Values of the upper frequency bound $f_{0.95}$ [Hz] for the chamber V_{k3} =3.90 cm^3

d_p[mm]	1.211			1.405			1.610		
d_w[mm]	0.570	0.625	0.720	0.625	0.720	0.830	0.720	0.830	1.020
$d=d_w/d_p$	0.471	0.516	0.603	0.444	0.520	0.591	0.447	0.516	0.633
D_c=1.5	1.53	1.81	2.27	2.02	2.86	3.10	2.46	4.12	4.96
D_c=2	1.48	1.88	2.37	1.95	2.01	3.11	3.32	3.43	4.08
D_c=3	1.25	1.68	2.19	1.68	2.83	3.08	2.06	3.04	3.66

Tab. 4. Values of the time constant T [ms] for the chamber V_{k1} = 0.25 cm^3

d_p[mm]	1.211			1.405			1.610		
d_w[mm]	0.570	0.625	0.720	0.625	0.720	0.830	0.720	0.830	1.020
$d=d_w/d_p$	0.471	0.516	0.603	0.444	0.520	0.591	0.447	0.516	0.633
D_c=1.5	12.51	8.85	7.64	9.03	5.94	5.41	8.16	5.29	4.20
D_c=2	14.95	10.06	8.81	10.21	7.62	5.78	8.01	5.53	5.37
D_c=3	16.96	10.92	9.61	10.72	8.79	6.25	8.66	6.14	5.74

Tab. 5. Values of the time constant T [ms] for the chamber V_{k2} =1.22 cm^3

d_p[mm]	1.211			1.405			1.610		
d_w[mm]	0.570	0.625	0.720	0.625	0.720	0.830	0.720	0.830	1.020
$d=d_w/d_p$	0.471	0.516	0.603	0.444	0.520	0.591	0.447	0.516	0.633
D_c=1.5	13.70	13.01	11.57	12.13	10.84	10.43	12.54	7.16	6.29
D_c=2	16.82	15.48	13.14	13.45	13.14	10.21	10.42	7.69	7.45
D_c=3	20.00	18.41	17.38	15.30	13.02	9.58	9.07	8.11	7.64

Tab. 6. Values of the time constant T [ms] for the chamber V_{k3} =3.90 cm^3

d_p[mm]	1.211			1.405			1.610		
d_w[mm]	0.570	0.625	0.720	0.625	0.720	0.830	0.720	0.830	1.020
$d=d_w/d_p$	0.471	0.516	0.603	0.444	0.520	0.591	0.447	0.516	0.633
D_c=1.5	34.12	28.90	23.04	25.89	18.29	16.87	21.30	12.70	10.54
D_c=2	35.35	27.83	22.07	26.82	26.02	16.82	22.55	15.25	12.82
D_c=3	41.88	31.14	23.93	31.14	18.48	16.98	25.39	17.21	14.29

DOI 10.1515/ama-2016-0035

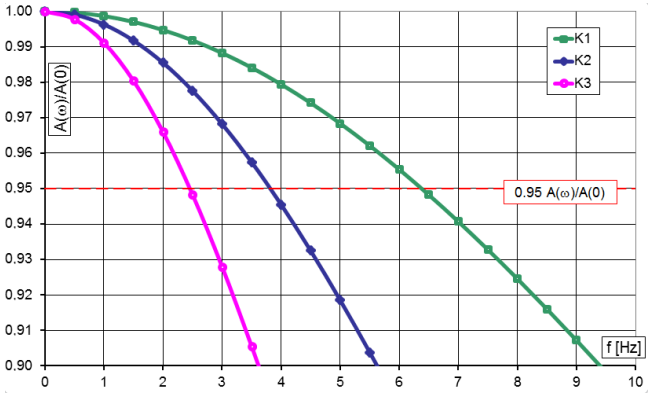

Fig. 7. Amplitude–frequency characteristics for the air gages with d_p = 1.211 mm and different measuring chambers (K1 to K3)

For the measuring chambers K1 and K2, all the examined combinations revealed the normalized amplitudes to lay between 0.987 and 1, which meant the dynamic error smaller than 1.5% for the input frequencies below 1.5 Hz. It proved that those air gages could be applied even for faster measurements than assumed. However, some configurations combined with the measuring chamber V_{k3} =3.90 cm³ did not meet this requirement. Considering the fact that the value of the time constant T could differ 100% between the initial and final values of the measuring range (Rucki and Jermak, 2012), the measuring chamber V_{k3} =3.90 cm³ is not recommended for the discussed measuring task. It provides values of $f_{0.95}$ mostly lower than 3 Hz, which may led to the dynamic error larger than estimated one.

It should be noted that the inlet nozzles apart of the determination of the static sensitivity (multiplication) K and the measuring range have impact on the dynamic characteristics. In any configuration, time constant grows longer for smaller inlet nozzles. On the other hand, the values of the upper frequency bound $f_{0.95}$ are larger for larger inlet nozzles, and they are more sensitive to d_w when the measuring chamber volume is smaller and measuring nozzle is larger.

From the perspective of the roundness measurement with the air gages, the dynamic characteristics are better if the upper frequency $f_{0.95}$ is larger (ability to measure faster with the acceptable dynamic error). Thus, among the examined combinations of geometrical parameters of the air gages, the best dynamics revealed those of the smaller measuring chamber volume, smaller outer diameters of the measuring nozzles, and bigger inlet nozzle diameters. It can be seen in the diagram (Fig. 8) showing frequencies $f_{0.95}$ for various inlet and measuring nozzles combined with the measuring chamber of volume V_{k1} = 0.25 cm³.

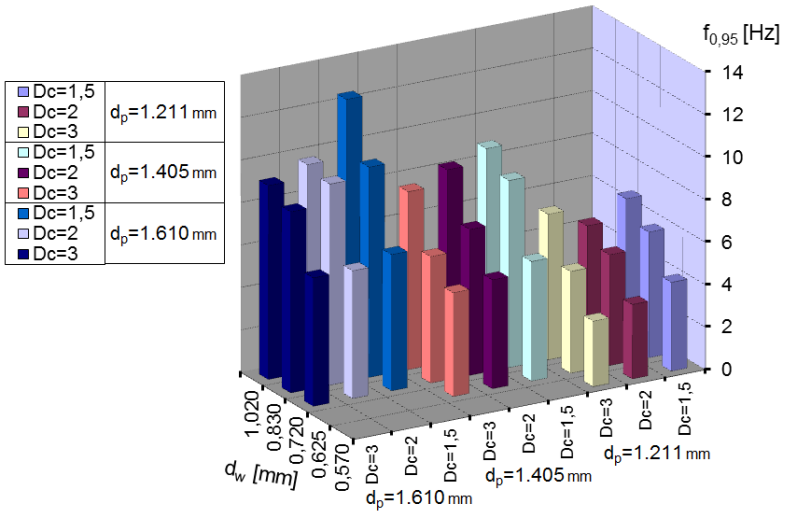

Fig. 8. Upper frequency bound $f_{0.95}$ values for the air gages with the measuring chamber volume V_{k1} = 0.25 cm³

5. FINALLY APPROVED AIR GAGES AND METHOD EVALUATION

The above analysis enabled to evaluate the dynamic characteristics of the air gages of different geometrical parameters proposed to perform the measuring task in the Geoform device with required accuracy. Those configurations that met static requirements on the multiplication and measuring range, underwent dynamic calibration and analysis to eliminate the ones of too large dynamic error. As a result, the following air gages were chosen:

- measuring nozzle d_p = 1.610 mm,
- the normalized parameter of outer diameter D_c = 3,
- inlet nozzle d_p = 1.020 mm,
- the measuring chamber volume $V_k \approx$ 1.2 cm³.

This configuration had the following static characteristics: multiplication |K| = 0.505 kPa/µm and the measuring range z_p = 106 µm. The exact values of the multiplication are shown in the Fig. 9 for each air gage installed in the gage head of the Geoform device.

The proposed out-of-roundness measurement method underwent the overall test through a comparative analysis with the reference data obtained from Talyrond 365 device made by Taylor-Hobson. According to Adamczak et al. (2010), the relative error Δ_{MP} could be calculated as following:

$$\Delta_{MP} = \frac{\Delta R_{m_i} - \Delta R_{a_i}}{\Delta R_{a_i}}, \tag{3}$$

where: ΔR_{m_i} – out-of-roundness value obtained by the tested method from the i-th point, ΔR_{a_i} – respective value obtained by the reference method.

DOI 10.1515/ama-2016-0035

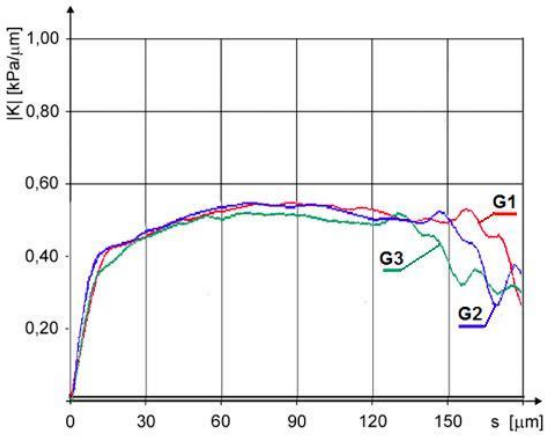

Fig. 9. Experimental graphs of multiplications of the air gages G1, G2 and G3

After the mean value of all measuring points $\overline{\Delta}_{MP}$ is calculated, the following formula is used for the tested method accuracy *MA*:

$$MA = \left|\overline{\Delta}_{MP} \pm u_p s\right| \cdot 100\% \ , \tag{4}$$

where: u_p – a coefficient of normal distribution for P=0.95, *s* – standard deviation.

The accuracy of a measuring device to be used for measurement of the geometrical surface structure during the product quality control should lay in the range of 10-25% (Adamczak et al. 2010). After 100 repetitions with different cylinders, the *MA* factor for Geoform was calculated as 9.40%, which was highly satisfactory, especially when considering incomparably lower price and faster work of the tested device Geoform.

6. CONCLUSIONS

Automated quality control is an important aspect of modern manufacturing process (Milo et al., 2015). The proposed method based on air gages provides quick, relatively cheap and reasonably accurate device for non-contact measurement of inner cylinders with out-of-roundness tolerances of 10-15 μm. The air gauges had been found fully capable to measure with the required accuracy, but the problem of dynamic errors was to solve. It was achieved by thorough analysis of the work conditions and dynamic characteristics of the applied air gages, and by the sine input analysis. The configurations of air gages, which appeared to generate too large dynamic errors, were eliminated and replaced by the ones able to work in even faster dynamic conditions than assumed. The methodology of dynamic analysis of the air gages proved to be effective, which resulted in the highly accurate roundness measurement. The Geoform device successfully passed the accuracy test with the reference method.

REFERENCES

1. **Adamczak S., Janecki D., Stępień K.** (2010), Qualitative and quantitative evaluation of the accuracy of the V-block method of cylindricity measurements, *Precision Engineering*, 34, 619–626.
2. **Cellary A., Jermak Cz. J.** (2009), Pneumatic Method for Reference Out-Of-Roundness Measurement, *Proceedings of the 4th International Conference Metrology in Production Engineering,* Poznan – Zerkow, 59–64.
3. **Derezynski J., Jakubowicz M.** (2016), Verification tests of the air gauges metrological characteristics, *Mechanik*, 3, 196–199.
4. **Dmitriev V.N., Chernyshev V.I.** (1958), Calculation of the time domain characteristics of the pneumatic flow-through chambers, *Avtomatika i telemehanika*, 12, 1118–1125 (in Russian).
5. **Figliola R.S., Beasley D.E.** (2006), *Theory and Design for Mechanical Measurements*, 4th ed., John Wiley& Sons Inc., Clemson.
6. **Gao R.D., Tang X., Gordon G., Kazmer D.O.** (2014), Online product qualty monitoring through in-process measurement, *CIRP Annals – Manufacturing Technology*, 63(1), 493–496.
7. **Grandy D., Koshy P., Klocke F.** (2009), Pneumatic non-contact roughness assessment of moving surfaces, *CIRP Annals – Manufacturing Technology*, 58(1), 515–518.
8. **Jermak Cz. J., Rucki M.** (2012), *Air Gauging: Static and Dynamic Characteristics*, IFSA, Barcelona.
9. **Jermak Cz.J., Cellary A., Rucki M.** (2010), Novel method of non-contact out-of-roundness measurement with air gauges, *Proceedings of the eu**spen** 10th International Conference*, Delft, 71–74.
10. **Jun Liu** et al. (2012), Design and accuracy analysis of pneumatic gauging for form error of spool valve inner hole, *Flow Measurement and Instrumentation*, 23, 26–32.
11. **Menzies I., Koshy P.** (2009), In-process detection of surface porosity in machined castings, *International Journal of Machine Tools & Manufacture*, 49(6), 530–535.
12. **Milo M.W., Roan M., Harris B.** (2015), A new statistical approach to automated quality control in manufacturing processes, *Journal of Manufacturing Systems*, 36, 159–167.
13. **O'Neill P., Sohal A., Teng Ch.W.** (2016), Quality management approaches and their impact on firms' financial performance – An Australian study, *International Journal of Production Economics*, 171, 381–393.
14. **Pollard J.H.** (1977), *A Handbook of Numerical and Statistical Techniques*, Cambridge University Press, Cambridge.
15. **Rucki M.** (2011), *Dynamic properties of the back-pressure air gauges with small measuring chambers,* Poznan University of Technology, Poznan (in Polish).
16. **Rucki M., Barisic B.** (2009), Response Time of Air Gauges With Different Volumes of the Measuring Chambers, *Metrology and Measurement Systems*, 16(2), 289–298.
17. **Rucki M., Jermak Cz. J.** (2012), Dynamic Properties of Small Chamber Air Gages, *Journal of Dynamic Systems, Measurement, and Control*, 134(1), p. 011001 (6 pages).
18. **Shiraishi M., Yamagiwa T., Ito A.** (2002), Practical dimensional error control and surface roughness inspection in turning, *Proceedings of ASME-2002 Mechanical Engineering Congress and Exposition,* New Orleans, 45–51.
19. **Stępień K.** (2010), In situ measurement of cylindricity – Problems and solutions, *Precision Engineering*, 38, 697–701.
20. **Tsidulko F.V.** (1965), *Dynamics of the pneumatic devices for the dimensional measurement*, Mashinostroyeniye, Moskva (in Russian).
21. **Vacharanukul K., Mekid S.** (2005), In-Process Dimensional Inspection Sensors, *Measurement*, 38, 204–218.
22. **Valicek J.** et al. (2007), An investigation of surfaces generated by abrasive waterjets using optical detection, *Journal of Mechanical Engineering*, 53(4), 224–232.
23. **Wang Y. H.** et al. (2005), An Automatic Sorting System Based on Pneumatic Measurement, *Key Engineering Materials*, 295-296, 563–568.
24. **Wieczorkowski S.** (1995), *Automatic regulation of the rotational speed of the pneumatic misroturbines,* Research Publication Series of Lodz University of Technology, No. 703, Lodz (in Polish).
25. **Yribarren R.** (1955), The pneumatic method applied to dynamic measurement, *Proceedings of the Symposium on Engineering dimensional metrology,* London, 225–240.

This work was supported by the Ministry of Science and Higher Education, Poland, project N505 010 32/1555.

DE GRUYTER
OPEN

DOI 10.1515/ama-2016-0036 acta mechanica et automatica, vol.10 no.3 (2016)

COMPARATIVE EVALUATION OF THE DIFFERENT DATA MINING TECHNIQUES USED FOR THE MEDICAL DATABASE

Anna KASPERCZUK[*], Agnieszka DARDZIŃSKA[**]

[*]Department of Mechanics and Computer Science, Bialystok University of Technology, ul. Wiejska 45c, 15-351 Bialystok, Poland

a.kasperczuk@doktoranci.pb.edu.pl, a.dardzinska@pb.edu.pl

received 2 February 2016, revised 22 July 2016, accepted 25 July 2016

Abstract: Data mining is the upcoming research area to solve various problems. Classification and finding association are two main steps in the field of data mining. In this paper, we use three classification algorithms: J48 (an open source Java implementation of C4.5 algorithm), Multilayer Perceptron - MLP (a modification of the standard linear perceptron) and Naïve Bayes (based on Bayes rule and a set of conditional independence assumptions) of the Weka interface. These classifiers have been used to choose the best algorithm based on the conditions of the voice disorders database. To find association rules over transactional medical database first we use apriori algorithm for frequent item set mining. These two initial steps of analysis will help to create the medical knowledgebase. The ultimate goal is to build a model, which can improve the way to read and interpret the existing data in medical database and future data as well.

Key words: Data Mining, Classification, WEKA, J48, MLP, Apriori, Association Rules

1. INTRODUCTION

The past 20 years show dynamic growth in the amount of information in electronic formats. The accumulation of this data has taken place at an explosive rate and it has been estimated that the amount of information in the world doubles every two years (Dardzinska, 2013; Dardzinska and Romaniuk, 2015a). Collected data often hold valuable and interesting information.

Intensive rise of the field of knowledge discovery in databases (KDD) and data mining (DM) is a response to a sharp increase in the amount of information collected in databases and data warehouses. Data mining techniques allow us to find new, previously unknown relationships and patterns in databases that can be used later to build support decision-making information system (Dardzinska and Romaniuk, 2015b). This phenomenon is largely reflected in medicine, where the progress of information technology has contributed to the sudden increase in the amount of data. Using these technologies, we are able to bring unprecedented knowledge that can be useful in the treatment of various diseases (Yoo et al., 2012).

In this paper we present how to choose the best classifier, verify it, and then extract interesting association rules in medical database. For the purpose of this paper we use voice disorders database, which data was collected among academic staff. The occupational voice diseases are chronic diseases that are directly related to the profession and working conditions. In the case of vocal organ teacher, the diseases are the results of continuous voice strain. Increasingly, it takes into account also the psychophysical load occurring in their professional teacher as a risk factor increasing the likelihood of disease burden and vocal organ (Sliwinska-Kowalska et al., 2006). Therefore, it becomes extremely important to find such traits among patients which have the greatest impact on their recovery.

2. MATERIAL AND METHODS

Based on the survey of 240 people we built a database consisting of 240 objects and 68 attributes. Data refers to issues related to fonoaudiology, speech therapy and voice diseases. This database has been prepared in the extension .arff, which is accepted by Weka 3.6.11. There are 68 original classification attributes including age, place of residence, workplace, frequency of voice work, frequency of clinical control, surgical treatments, smoking and other features important from the point of view of fonoaudiology.

In this work (for testing and verification) we use Weka interface (Wakaito Environment for Knowledge Analysis), developed at University of Wakaito, New Zealand. It is a collection of machine learning algorithms for data mining tasks. Weka supports several standard data mining tasks, more specifically, data preprocessing, clustering, classification, regression, visualization, and feature selection. All techniques of Weka software are predicated on the assumption that the data is available as a single flat file or relation, where each data point is described by a fixed number of attributes (numeric, normally, or nominal attributes, but some other types of attributes are also supported by this software).

This software has many important advantages, so that we use it in our work:

- it is fully implemented in the Java programming language, therefore runs on almost any architecture;
- it is easy to use due to its graphical user interface;
- it is a huge collection of data preprocessing and modeling techniques.

2.1. Classification

First we focus on finding the best classification algorithm for given database. The classifier is an algorithm that implements

DOI 10.1515/ama-2016-0036

classification, especially in a concrete implementation. We use for this classification – model finding process that is used for portitioning data into different classes according to some initial assumptions. In other words, we can say that classification is the process of generalizing the data according to different instances. There are many different classifiers and many different types of dataset resulting in difficulty in knowing which will perform most effectively in any given case. It is already widely known that some classifiers perform better than others on different datasets. It is always possible that another classifier may work better. To decide which classifier will work the best for a given dataset there are two options. First is to put all the trust in an expert's opinion based on knowledge and experience. Second is to run through every possible classifier that could work on the dataset, identifying rationally the one which presents the best results (Cheng, Greiner, 2001; Dardzinska, 2013).

Classification is a data mining algorithm that creates a step-by-step guide for how to determine the output of a new data instance. It is the process of finding a set of models that differentiate data classes and concepts. We used it to predict group memberships for data instances. In first step we describe a set of predetermined classes. Each tuple is assumed to belong to a predefined class as determined by class label attribute, the set of tuples are used for model construction, called training sets. The model is represented as classification rules, decision trees or mathematical formulas. Model usage that is used for classifying future data trends and unknown objects. It estimates the accuracy of the constructed model by using certain test cases. Test sets are always independent of the training sets (Dardzinska, 2013; Frawley et al., 1991).

In Weka we have three basic steps for classification:

- preparing the data;
- choose classify and apply algorithm;
- analyze the result or output.

Tab.1. Classification attributes

Attribute	Value
Smoke	{0-never, 1-no, but I used, 2-yes}
Allergy	{no, yes}
Thyroid_disease	{no, yes}
Reflux	{no, yes}
Horm_disorders (hormonal dosorders)	{no, yes}
Reflux_treat (reflux tratment)	{no, yes}
Cons_therapy (conservative therapy)	{no, yes}
Voice_rehabilitation	{0 -never, 1-once, 2-few times}
Laring_surgery (larynx surgery)	{no, yes}
Infection_resp (upper respiratory tract infections)	{no, yes}

In the following subsections we discussed various classification algorithms, which we used in our work (Thair, 2009).

J48 is a popular machine learning algorithm based upon J.R. Quilan C4.5 algorithm. All data are of the categorical type and therefore continuous data will not be examined at this stage. The algorithm will however leave room for adaption to include this capability. The algorithm was tested against C4.5 for verification purposes (Freund, 1999; Ras and Dardzinska, 2011).

Multilayer Perception (MLP) is a network, which can be built step by step by user, created by an algorithm or both. The network can also be monitored and modified during the whole training time. The nodes in this network are all sigmoid (except for when the class is numeric, when the output nodes become threshold linear units).

Naive Bayes is a numeric estimator, where precision values are chosen based on analysis of the training set. This classifier will use a default precision of 0.1 for numeric attributes when built classifier is called with zero training instances (Bouckaert, 2004).

Based on the knowledge of voice hygiene and factors affecting the occurrence of voice diseases, we chose the class attributes of classification (Tab.1).

2.2. Association rules

Let us assume that $S = (X, A, V)$ is an information system, where (Agrawal and Srikant, 1993; Dardzinska, 2013):

- X is a nonempty, finite set of objects;
- A is a nonempty, finite set of attributes;
- V is a set of all attributes values.

Then, $a : X \rightarrow V_a$ is a function for any $a \in A$, that returns the value of the attribute of a given object. The attributes are divided into three different categories: set of stable attributes A_1 (the values of such attributes cannot be changed in time), set of flexible attributes A_2 and set od decision attributes D (in both of them the values of attributes can change), such that $A = A_1 \cup A_2 \cup D$ (Han et al., 2000; Pauk and Dardzinska, 2012).

Tab.2. Information System

Object	Stable attributes A_1	Flexible attributes A_2	
	Attribute a	Attribute b	Attribute c
x_1	$a1$	$b1$	L
x_2	$a1$	$b2$	L
x_3	$a1$	$b3$	H
x_4	$a2$	$b3$	H
x_5	$a2$	$b2$	L
x_6	$a2$	$b3$	L

Example of the information system $S = (X, A, V)$ is presented in Tab.2. The set of objects consists of six elements $X = \{x_1, x_2, x_3, x_4, x_5, x_6\}$. The set of attributes consists of two subsets A_1, A_2, where A_1 includes stable attributes $\{a\}$, and A_2 is a set with only flexible attributes $\{b, c\}$. The domain of attribute a consists of two values $\{a1, a2\}$, attribute b can reach three values $\{b1, b2, b3\}$, while the attribute c has two different values $\{L, H\}$ (Agrawal and Srikant, 1993; Dardzinska and Ras, 2003).

Information systems can be also seen as decision tables. In Tab. 3 we have decision System $S = (X, A, V \cup \{d\})$, with one stable attribute a, two flexible attributes b and c and the decision attribute d. "Place of birth" is an example of a stable attribute. "Blood pressure" or "Glucose level" of diagnosed patient is an example of a flexible attribute. "Operation", "Hospitalization", "Medical Treatement" are the examples of decision attributes values.

DOI 10.1515/ama-2016-0036

Tab.3. Decision System

Object	Atribute a	Attribute b	Attribute c	Decision d
x_1	$a1$	$b1$	L	+
x_2	$a1$	$b2$	L	+
x_3	$a1$	$b3$	H	-
x_4	$a2$	$b3$	H	+
x_5	$a2$	$b2$	L	-
x_6	$a2$	$b3$	L	+

Extracting association is one of the most important data mining tasks, which works on the principle of association rules between items that are significant in the database. Obtained results form the basis for decision-making and forecasting, which is undoubtedly a great advantage of the described method (Dardzinska and Romaniuk, 2015a; Ras et al., 2008). First, each set of items is called an itemset, if the support for the set is higher than a minimum threshold of support (Bouckaert, 2004; Ras and Joshi, 1997). Next we generate rules. To confirm the rule, for example $X \rightarrow Y$, where X and Y are itemsets, the support and the confidence of the rule are calculated in a standard way, i.e. by the support of the rule we mean the number of objects in information system S satisfying $X \cap Y$ (number of transactions that contain both X and Y) $\sup(r) = \mathrm{card}(X \cap Y)$, while the confidence is the ratio between the number of objects satisfying $X \cap Y$ and the number of objects saisfying X: $\mathrm{conf}(r) = \frac{\mathrm{card}(X \cap Y)}{\mathrm{card}X)}$ (Dardzinska and Romaniuk, 2015b; Deogun, et al., 1994; Han and Kamber, 2006). The rule with support and confidence above the minimum thresholds (given at the begining by the user) is the rule which should be added to the knowledge base (Dardzinska and Romaniuk, 2015b).

3. RESULTS AND DISCUSSION

We adapted the data prepared in the form of surveys and prepared them in the form of a database. Further, the data is saved with extension ARFF (Attribute Relation File Format) format to process in WEKA.

Then we start with the Weka tool use the explorer application and select the preprocess button followed by this open the result analysis data set. After that we can choose filter, which can be used to transform the data from one format to other e.g. numeric attributes into discrete ones. It is also possible to delete instances and attributes according to specific criteria on the preprocess screen.

3.1. Mining classification rules

To find the best classifier we should pay attention to the following parameters we receive in output (Bouckaert, 2004; Han et al., 2000):

- TP Rate - rate of true positives (instances correctly classified as a given class);
- FP Rate - rate of false positives (instances falsely classified as a given class);
- Precision - proportion of instances that are truly of a class divided by the total instances classified as that clases;
- Recall - proportion of instances classified as a given class divided by the actual total in that class (equivalent to TP rate);
- F-Measure - general indicator of quality of the model;
- ROC Curve (ROC Area) - a graphical plot that illustrates the performance of a binary classifier system as its discrimination threshold is varied. The accuracy of the test depends on how well the test separates the group being tested into those with and without the disease in question. Accuracy is measured by the area under the ROC curve;
- Kappa Statistic - it is a measure of conformity between the proposed allocation instance of the class and the actual, which is about the overall accuracy of the model;
- Number of correctly classified instances.

As part of the development of data we compared the individual parameters for each classifier. The results are presented in Tab. 4, Tab. 3, Fig. 1 and Fig. 2.

Tab.4. WEKA results for Recall, F-Measure, Precison

	Recall			F-Measure			Precision		
	J48	NaiveBayes	MLP	J48	NaiveBayes	MLP	J48	NaiveBayes	MLP
Smoke	0.987	0.992	1	0.987	0.991	1	0.988	0.992	1
Allergy	0.983	0.936	1	0.983	0.937	1	0.983	0.939	1
Thyroid_disease	0.992	0.949	1	0.992	0.97	1	0.992	0.97	1
Reflux	0.966	0.97	1	0.963	0.951	1	0.967	0.954	1
HORM_DISORDES	0.987	1	1	0.987	1	1	0.987	1	1
REFLUX_TREAT	1	1	1	1	1	1	1	1	1
CONS_THERAPY	0.966	0.905	1	0.965	0.906	1	0.965	0.908	1
INFECTION_RESP	0.97	0.894	1	0.97	0.896	1	0.971	0.901	1
VOICE_REHABILITATION	0.992	0.907	1	0.991	0.912	1	0.992	0.935	1
THYROID_SURGERY	0.979	0.967	1	0.977	0.97	1	0.98	0.978	1
LARING_SURGERY	0.996	0.983	1	0.996	0.984	1	0.996	0.986	1

DOI 10.1515/ama-2016-0036

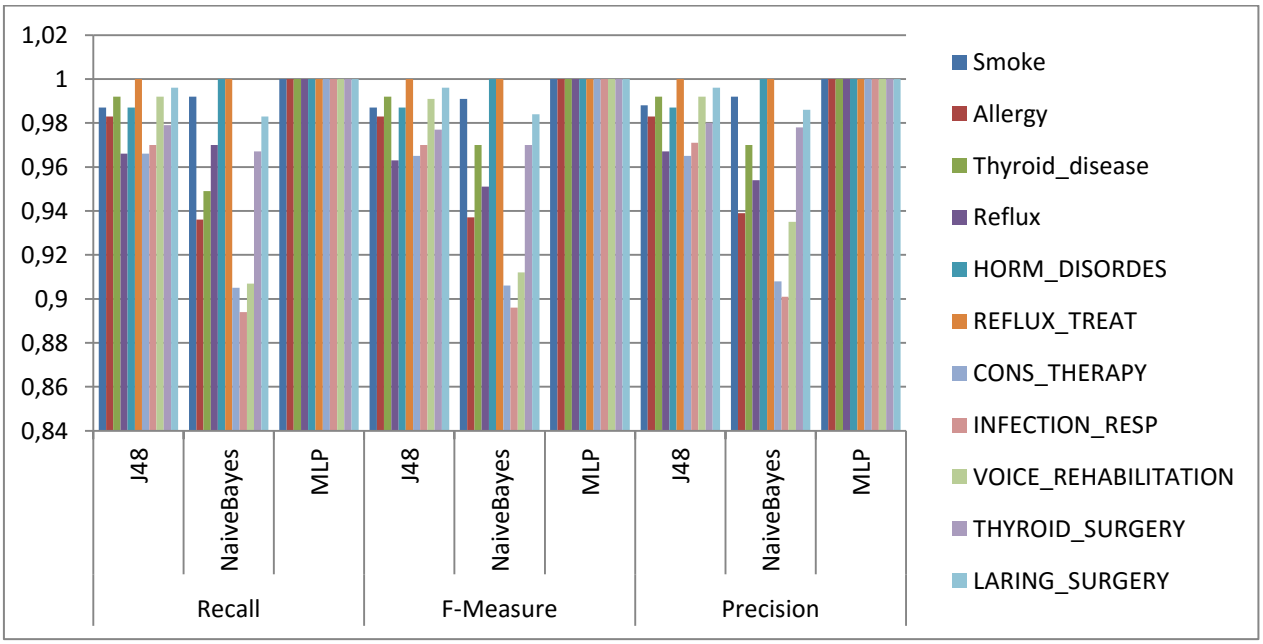

Fig.1. WEKA results for Recall, F-Measure, Precision

If we compare the Precision parameter, it can be noticed that in most cases the values are also the highest for the algorithm MLP (Fig. 1). The highest value (close to 1) indicate a good classifier. However, it should be noted that for some attributes, such us: Smoke, Allergy, Reflux, we have similar value for all examined classifiers (Tab. 4).

The chart for Recall (Fig. 1) shows that the highest values, close to 1, we calculated for Multilayer Perception algorithm. For every choosen attribute this value is equal to 1 (Tab. 4). In this case we calculated, that the worse algorithm is Naïve Bayes, because of low values of the proportion of instances classified.

The same situation we have for value of F-Measure. For every classification attribute the value is close to 1 (Tab. 4). It proves the high quality of the generated model.

When we describe the quality of the generated model of a classification, it is important to turn attention into two parameters: Kappa Statistic and number of correctly classified instances. For J48 algorithm we received the average score 0.92, which is a satisfying result. The Multilayer Perception algorithm give us the value of Kappa Statistic equal to 1. It indicates very high quality. For Naïve Bayes we got the lowest values among the considered classifiers. For properly classified instances distribution is similar. The value of Kappa Statistic for MLP is equal to 1 and the number of correctly classified instances was 100%.

We got high dispersion of results for the ROC Area (Fig. 2). We note that values for J48 and MLP are similar and ranges from 0.883 to 1 (Tab. 5). The largest value equal to 1 has occurred for Multilayer Perception, which is why it can be expected as the best classifier.

Tab.5. WEKA results for TP Rate, FP Rate, ROC Area

	TP Rate			FP Rate			ROC Area		
	J48	**NaiveBayes**	**MLP**	**J48**	**NaiveBayes**	**MLP**	**J48**	**NaiveBayes**	**MLP**
Smoke	0.987	0.992	1	0.031	0.021	0	0.996	0.994	1
Allergy	0.983	0.936	1	0.046	0.073	0	0.987	0.97	0.974
Thyroid_disease	0.992	0.97	1	0.047	0.119	0	0.952	0.925	0.965
Reflux	0.966	0.949	1	0.299	0.154	0	0.863	0.993	0.989
HORM_DISORDES	0.987	1	1	0.137	0	0	0.882	0.953	0.916
REFLUX_TREAT	1	1	1	0	0	0	0.96	0.981	0.876
CONS_THERAPY	0.966	0.905	1	0.054	0.104	0	0.948	0.953	1
INFECTION_RESP	0.97	0.894	1	0.105	0.154	0	0.984	0.94	0.995
VOICE_REHABILITATION	0.992	0.907	1	0.027	0.015	0	0.996	0.983	1
THYROID_SURGERY	0.979	0.967	1	0.292	0.002	0	0.932	0.996	1
LARING_SURGERY	0.996	0.983	1	0.046	0.002	0	1	1	1

DOI 10.1515/ama-2016-0036

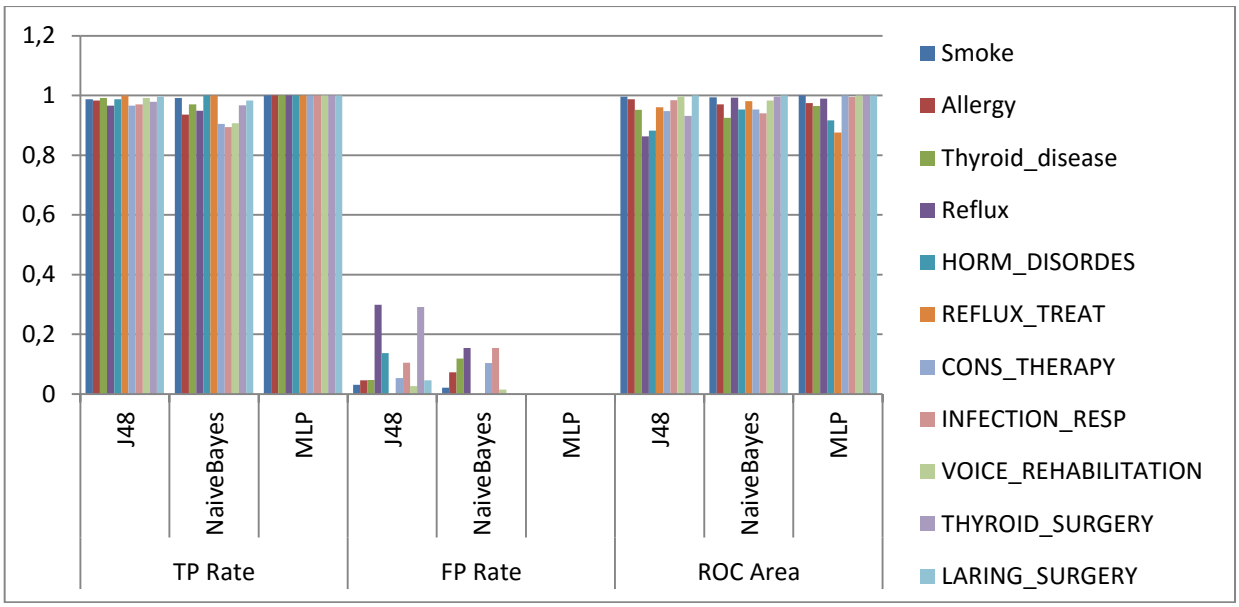

Fig.2. WEKA results for TP Rate, FP Rate, ROC Area

It can be seen that the value of TP Rate is the best for Multiplayer Perception (Fig. 2). For every attribute this value is close to 1, which is a very good result. Not so impressive results we received for Naïve Bayes classifier (Tab. 5).

For the best classification algorithm value of FP Rate is close to 0. In this case the best results we calculated also for Multilayer Perception (Fig. 2). For the majority of selected attributes classifying this value amounted to 0, which indicates a very good operating algorithm.

The results indicate, that the MLP is the best performing classifier for considered voice disorders database.

3.2. Association rules

Based on the survey of 60 people we built a database consisting of 60 objects and 68 attributes. The data refer to issues related to fonoaudiology. speech therapy and voice diseases. This database has been prepared in the extension .arff. which is accepted by the installation program. Weka. We use the Apriori Algorithm and we want to find the association rules in our database.

For the purposes of analysis the following values:

- minimum support: 0.9 (54 instances);
- minimum metric <confidence>: 0.9.

are taking into consideration.

During the analysis several interesting association rules were obtained. Some ot them are given below:

1. REFLUX_TREAT=no, 57==>ASTHMA=no, 57 conf:(1)
2. VOICE_PER=2,REFLUX_TREAT=no,55==>ASTHMA=no,55 conf:(1)
3. HORM_DISORDES=no,54==>ASTHMA=no,54 conf:(1)
4. EDU=2,REFLUX_TREAT=no,54==>ASTHMA=no,54 conf:(1)
5. EDU=2,57==>ASTHMA=no,56 conf:(0.98)
6. VOICE_PER=2,57==>ASTHMA=no,56 conf:(0.98)
7. THYROID_SURGERY=no,56==>ASTHMA=no,55 conf:(0.98)
8. VOICE_PER=2,ASTHMA=no,56 ==>REFLUX_TREAT=no,55 conf:(0.98)
9. GENDER=K,55==>ASTHMA=no,54 conf:(0.98)
10. LARYNG_SURGERY=no,55==>ASTHMA=no,54 conf:(0.98)

These are the best rules extracted from given data. All of them have the support and the confidence above given minimal thresholds. The attributes forming these rules are described below. Others, with the support below the minimal value (given by the user and consulted with the expert) are passed over.

@attribute	'REFLUX_TREAT'	{'no', 'yes'}
@attribute	'ASTHMA'	{'no', 'yes'}
@attribute	'VOICE_PER'	{'0','1','2'}
	0-(0-2y), 1-(2-10 y), 2-(> 10 y)	
@attribute	'HORM_DISORDES'	{'no', 'yes'}
@attribute	'EDU'	{'0','1','2'}
	0-primary, 1-secondary, 2-higher	
@attribute	'THYROID_SURGERY'	{'no', 'yes'}
@attribute	'GENDER'	{'K', 'M'}
@attribute	'LARYNG_SURGERY'	{'no', 'yes'}
@attribute	'EDU'	{'0','1','2'}
	0-primary, 1-secondary, 2-higher	
@attribute	'THYROID_SURGERY'	{'no', 'yes'}
@attribute	'GENDER'	{'K', 'M'}
@attribute	'LARYNG_SURGERY'	{'no', 'yes'}

4. CONCLUSION

In this paper we propose method to find the best classifier and association rules in voice disorders database using WEKA methods. The voice disorders database was collected among academic professionals. The occupational diseases are chronic diseases that are directly related to the profession and working conditions. In the case of vocal organ teacher, these diseases are the result of continuous voice strain. It becomes important to find such traits among patients have the greatest impact on their recovery. The obtained results are interesting, however we will wish on finding new algorithm which will be more useful in people with voice disorders treatment.

DOI 10.1515/ama-2016-0036

REFERENCES

1. **Agrawal R., Srikant R.** (1993), Fast algorithm for mining assocation rules, *International Conference on Very Large Databases*, 487-499.
2. **Bouckaert R** (2004), Naive Bayes Classifiers That Perform Well with Continuous Variables*, Lecture Notes in Computer Science Volume*, 3339, 1089-1094.
3. **Cheng J, Greiner R** (2001), Learning Bayesian Belief Network Classifiers, *Algorithms and System In Stroulia & Matwin LNAI 2056*, 141-151.
4. **Dardzinska A, Romaniuk A** (2015a), Incomplete distributed information systems optimization based on queries*, Advances in Swarm and Computational Intelligence*, Volume 9142 of LNCS Springer, 265-274.
5. **Dardzinska A.** (2013), *Action Rules Mining*. Springer, pp.90.
6. **Dardzinska A., Ras Z.** (2003), On Rules Discovery from Incomplete Information Systems, *Proceedings of ICDM'03 Workshop on Foundations and New Directions of Data Mining*, Melbourne, Florida, IEEE Computer Society.
7. **Dardzinska A., Romaniuk A.** (2015b) Queries for detailed information system selection, *Position Papers of the 2015 Federated Conference on Computer Science and Information Systems, Annals of Computer Science and Information Systems vol. 6*, Computer Science and Information Systems: FedCSIS, 11-15.
8. **Deogun J., Raghavan V., Sever H.** (1994), Rough set based classification methods and extended decision tables*, International Workshop on Rough Sets and Soft Computing*, 302-309.
9. **Frawley W., Piatetsky-Shapiro G., Matheus C.** (1991), Knowledge discovery in databases, *An overview. Knowledge Discovery in Databases*, 1–27.
10. **Freund Y, Mason L.** (1999), The alternating decision tree algorithm, *In Proceedings of the 16th International Conference on Machine Learning,* 124-133.
11. **Han J., Kamber M.** (2006), Data Mining: Concepts and Techniques, *Morgan Kaufmann Publishers*, Second Edition, 21-27.
12. **Han J., Pei J., Yin Y.** (2000), Mining frequent patterns without candidate generation, *ACM SIGMOD International Conference on Management of Data*, 1–12.
13. **Pauk J., Dardzinska A.** (2012), New method for finding rules in incomplete information systems controlled by reducts in flat feet treatment, *Image Proc. and Communications Challenges. Advances in Intelligent and Soft Computing*, 184, 209-214.
14. **Ras Z., Dardzinska A.** (2011), From Data to Classification Rules and Action*,. International Journal of Intelligent Systems*, Wiley, 26(6), 572-590.
15. **Ras Z., Dardzinska. A.,Tsay. L., Wasyluk H.** (2008), Association Action Rules, *IEEE Interna-tional Conference on Data Mining Workshops*, 283-290.
16. **Ras Z., Joshi S.** (1997), Query approximate answering system for an incomplete DKBS*, Fundamenta Informaticae Journal*, 20(3/4), 313-324.
17. **Sliwinska-Kowalska M., Niebudek-Bogusz E., Fiszer M., et al**. (2006), The prevaence and risk factors for occupational voice disorders in teachers, *Folia Phoniatr. Logop*, 58(2), 85-101.
18. **Thair Nu Phyu** (2009), Survey of Classification Techniques in Data Mining, *Proceedings of the International MultiConference of Engineers and Computer Scientists*, Vol I IMECS.
19. **Yoo I, Alafaireet P, Marinov M, et al.** (2012), Data mining in healthcare and biomedicine, *A survey of the literature. Journal of medical systems*, 36(4), 2431-2448.

Research was performed as a part of projects MB/WM/8/2016 and financed with use of funds for science of MNiSW

DE GRUYTER
OPEN

DOI 10.1515/ama-2016-0037

acta mechanica et automatica, vol.10 no.3 (2016)

OBSERVATIONS OF MR FLUID CLUMPING BEHAVIOUR IN A SQUEEZE-MODE DAMPER

Bogdan SAPIŃSKI*

*Department of Process Control, AGH University of Science and Technology, Al. Mickiewicza 30, 30-059 Kraków, Poland

deep@agh.edu.pl

received 25 February 2016, revised 25 July 2016, accepted 27 July 2016

Abstract: The study summarises the results of quasi-static experimental tests of an MR squeeze-mode damper prototype (MRSQD) performed at the MTS testing machine. Of particular interests was the influence of MR fluid clumping behaviour in the MRSQD working gap on the force output of the device. The MRSQD tests were assessed by measuring the damping force output at prescribed sinusoidal displacement inputs and at various (fixed) voltage levels resulting in the respective average current levels in the control coil. The influence of piston position offset on the damping force was also investigated. The collected data were shown in the form of damping force time histories and damping force-piston displacements loops and discussed with respect to MR fluid clumping behaviour.

Key words: MR Fluid, Squeeze Mode, Damper, Clumping Behaviour

1. INTRODUCTION

In consideration of the manner in which the material is utilized in a controllable device, MR fluid-based hardware is separated into following categories: flow (valve) mode, direct shear (clutch) mode, squeeze mode and gradient pinch mode. To date only the flow mode- and shear mode devices have been commercialized. No squeeze mode-hardware has been reported beyond the academia so far with the exception given in (Kim, 2014).

In squeeze mode-devices the flow channel height varies in the direction parallel to that of the magnetic field. As the distance between the opposing surfaces changes, the MR fluid is squeezed out and into the flow channel (Fig.1). In this mode, MR fluids can generate a large range of controllable force in envelopes that can only accommodate small strokes – stresses approach 100-150kPa with displacements of the order of several millimeters. This fact indicates the potential applications of MR fluids.

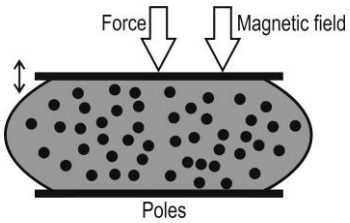

Fig. 1. MR fluid in squeeze mode

A very interesting aspect of the squeeze mode is the clumping phenomenon. How to minimise the effect of clumping behaviour is still a challenging problem. Research data reported so far reveal that if the same test is repeated without mixing the MR fluid, a progressively increasing force will be developed in consecutive test runs. This behaviour is suspected to be due to particle aggregation in MR fluid during squeeze process. As the MR fluid is to be squeezed, iron particles are trapped in the magnetic field in the gap while the carrier fluid is radially flowing outward. This causes iron particles to form aggregates in the gap and separate from the carrier fluid, and this effect is intensified after each test repeat (see Fig. 2).

Farjud et al. (2011a) proposed the definition to quantify clumping behaviour and revealed that the effect of clumping can be greatly reduced by a magnetic dither during piston return that can help the clumped particles re-disperse in the MR fluid. The reduction of clumping effect is because during piston return the dither can cause the iron particles to escape aggregates and for new chains.

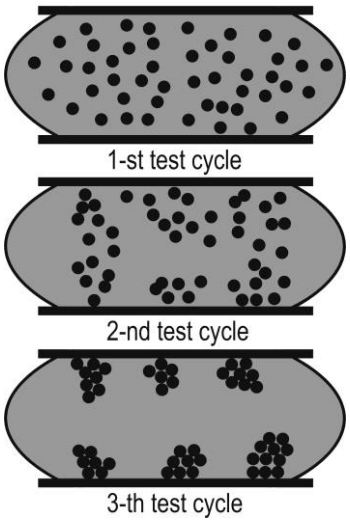

Fig. 2. Illustration of MR fluid clumping behaviour

The flow and direct shear modes abound in reports in the literature whilst there is little published data relating to the squeeze

DOI 10.1515/ama-2016-0037

mode. As regards the pinch mode, there are reports of few studies. Because many properties of MR fluids in the squeeze mode are still unknown, this mode has recently received recently a great deal of attention and still poses a major challenge to researchers. The studies exploring MR fluids in the squeeze mode and the involved phenomena are but a few. For example, (Mazlan et al., 2007; Farjoud at al., 2009a, b) revealed that MR fluids can provide a much larger range of controllable force in small operational envelopes compared to flow and direct shear modes. Systematic investigation of MR fluids reported in squeeze mode research described in (Mazlan et al., 2012) showed that the fluids experienced rheological changes in three stages during compression and tension and that fluid-particles separation phenomenon was the main cause of the unique behaviour of MR fluids. (Horak, 2013) showed that in the presence of a magnetic field, iron particles are arranged in column-like chain structures which get deformed due to compression and the MR fluid provides increased resistance to compressive loading and its yield stress tends to increase. Guo et al., (2013) studied compression behaviour of MR fluids under nonuniform magnetic field and showed that there exists a magnetic-field gradient-induced normal force when compared to the uniform field.

As regards the MR squeeze-mode dampers, one of the first major contribution was an MR semi-active damper (Jolly et al., 1996). Another attempt was a dual-coil mixed-mode damper which utilized shear and squeeze mode (Manecke et al., 2006). (Mazlan, 2008) examined the behavior of water-based MR fluids and hydrocarbon oil based MR fluids under compressive and tensile loads. (Farjoud et al., 2009) tested a squeeze-mode rheometer and provided a non-dimensional model which was validated experimentally. The same author(s) revealed a squeeze-mode damper prototype and developed a mathematical model of the damper suitable for design and engineering studies (Farjoud et al., 2011a; Farjoud, 2011b; Zhang et al., 2011). Gołdasz and Sapiński (2011) provided a numerical study in which a squeeze-mode mount was subjected to sweep-sine displacement inputs and characterized the mount model in terms of dynamic stiffness and damping vs. frequency. Gong et al. (2014) tested a dual-cavity high-force damper subjected to sinusoidal displacement inputs and fixed coil currents. The most recent study (Sapiński and Gołdasz, 2015) summarises the results of an MR damper prototype development and performance evaluation study.

The objective of the study was to analyse MR fluid clumping behaviour in the MRSQD in quasi-static states. For this purpose the device was tested in the MTS testing machine under predetermined sinusoidal displacement inputs and at various (fixed) voltage levels resulting in the respective average current levels in the control coil. Influence of piston position offset on the damping force was also investigated. The MR fluid clumping behaviour was discussed basing on the determined performance figures of the MRSQD (force time histories and force-piston displacement loops).

The paper is organized as follows. Section 1 outlines state-of-the art. solutions in the field of squeeze mode of MR fluids, MR fluid-based hardware and clumping phenomenon of MR fluids. Section 2 summarises the structure and operation principle of the MRSQD. Section 3 discusses experimental results of the device in the context of MR fluid clumping behaviour. The final conclusions are given in Section 4.

2. MR SQUEEZE-MODE DAMPER

A schematic diagram of the MRSQD is shown Fig. 3. The numeric symbols in the figure indicate all key components of the MRSQD (1-8) and the key highlights materials used for manufacturing of the device. The hardware features two concentric cylinders (1, 2). The inner non-magnetic cylinder (2) houses the piston (3), the core assembly (4), and the floating piston (5). The core assembly incorporates the coil (6). The outer cylinder (1) is made of a ferromagnetic material. The distance between the lower surface of the piston and the upper surface of the core is referred to as the working gap of time-varying height. The distance between the piston and the core varies according to the prescribed displacement (force) input (along the vertical z-axis). The floating piston below the core assembly separates the MR fluid from the coil spring located in the compensating chamber below the floating piston (5). The chamber incorporates a preloaded spring system (not shown in Fig. 2) for fluid volume compensation. Alternatively, the compensating chamber could be filled in with pressurized gas. The choice of the coil spring was due to convenience. The current in the control coil induces a magnetic field of the strength *H*. The magnetic flux generated by the current in the control coil (6) travels through the core and into the control gap, the outer cylinder, and back into the core through radially projected arms in the core base. The inner cylinder (2) of sufficient wall thickness is used to reduce the amount of magnetic flux bypassing the control gap, i.e. magnetic short circuit. All of the components ensure an efficient magnetic flux return path.

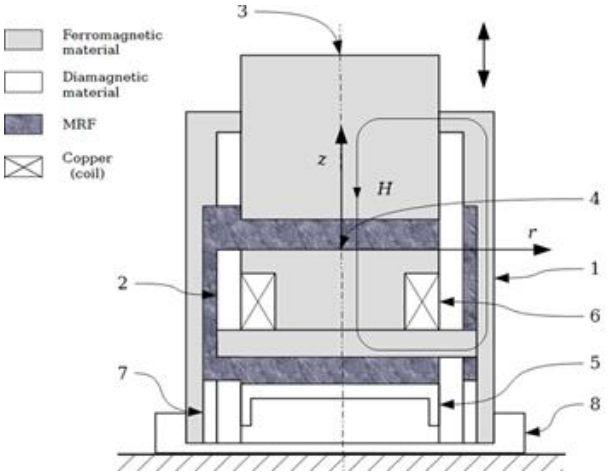

Fig. 3. Schematic diagram of the MRSQD

The flux induced in the working gap upon the application of the coil current effectively modifies the yield stress of the fluid, and its resistance to flow. As the piston moves downward, the distance between the core and the piston decreases. The excess of MR fluid is squeezed out of the working gap into the fluid volume between the inner cylinder and the outer housing of the MRSQD, and then into the compensating chamber. The additional fluid volume that enters the compensating chamber pushes the floating piston against the coil spring. The structure incorporates a non-magnetic ring (7), whereas the base cap (8) is used for fixing the assembly against the ground. The outer cylinder length is 133 mm and the diameter is 102 mm. The MR fluid type employed in the MRSQD is BASF Basonetic 4035 (Kieburg, 2010) with the volume of 110 ml.

DOI 10.1515/ama-2016-0037

3. EXPERIMENTS

The MRSQD was tested in a MTS 810 machine driven by a FlexTest SE type controller (Fig. 4). The displacement of the piston was measured using a LVDT type sensor, whereas the force output of was read out by the force sensor).

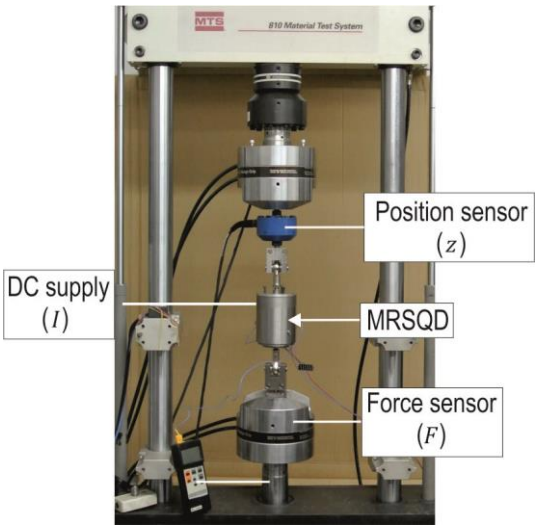

Fig. 4. MRSQD ready for tests

Experimental tests were performed to investigate the influence of the parameters of the sine piston displacement input (amplitude A and frequency f), the current level in the control coil I and piston offset x_0 on the force generated by the device and to obtain the force vs time and force vs force displacement plots. The experiment involved two stages. In the first stage the piston was displaced with respect to its midpoint position x_0=0 mm, and in the stage – with respect to the piston position shifted downwards x_0=1.44 mm (Fig. 5).

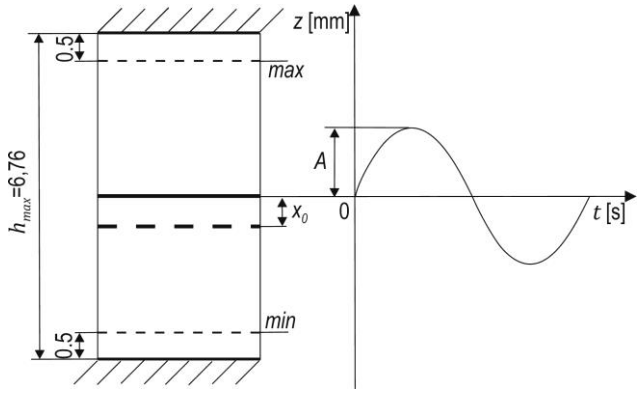

Fig. 5. Illustration of sinusoidal displacement of the piston in the gap

The device testing was assessed by measuring the force output at prescribed sinusoidal displacement inputs $x(t)= x_0 + A \cdot sin(2\pi ft)$ at various (fixed) voltage levels resulting in the average coil current level I: 0, 1, 2 and 3 A, respectively. For the purpose of experiments the data were collected within the range of frequency f(1, 10) Hz with the step 1 Hz and for the following displacement amplitude A: 0.72, 1.44 and 2.88 mm, respectively. The effect of piston position offset on the damping force waveform was investigated, too. In the tested MRSQD the maximum gap height h_{max} was equal to 6.76 mm, and displacement input amplitude range was limited up to A=2.88 mm in order to preserve a minimum gap of 0.5 mm on either side of the piston, i.e. between the lower surface of the piston and the upper surface of the core on one side and between the piston and the stop position on the other. Throughout the tests at room temperature of 25°C the signal sampling frequency was 1 kHz.

Selected tests results are depicted in Fig. 6-11, plotting force time histories in the range (1, 10) s and force-displacement loops registered in 2-nd test cycle, and 8-th test cycle of the piston motion. In Figs 6-9 x_0=0 mm while in Fig. 10 and 11, x_0=1.44 mm. Plots in Fig. 6 and 7 compare force time histories and force-displacement loops for current level 1 A and 3 A, and displacement input with amplitude A=2.88 mm, and frequency 1 Hz and 4 Hz. It is apparent that the when the current is higher, the damping force gets higher, too. It should be noted that critical value of force measured by the force sensor was adjusted to be 5000 N. Since the damping force reaches this value in the 4-th test cycle, the force-displacement loop in this case is represented by a "point" with force value of about 3900 N and position of z=2.88 mm. In this case the minimal height of the squeezed layer of MR fluid is 0.5 mm. A similar tendency is revealed in plots shown in Fig. 8 and 9, though in these case the damping force value 5000 N is not exceeded. This is so because the amplitude is A=1.44 mm, i.e. two times smaller. In this case the minimal height of the squeezed layer of MR fluid is 1.94 mm. It appears that for such piston displacement amplitude and current levels in the control coils, the influence of frequency on the damping force is rather minor. Plots in Fig. 10 and 11 present force time histories and force-displacement loops at piston position offset x_0=1.44 mm for current level 1 A and 3 A, displacement inputs with amplitude A=1.44 mm, frequency 1 Hz and 4 Hz. Note that in this case, the amplitude of displacement is the same as in case shown in Fig. 8 and 9. Comparing the plots in those figures, it is apparent that the influence of the piston position offset on the damper force is rather minor. Of particular importance are force-displacement loops in Fig. 10b. The actual shape of these plots is associated with the restriction of the damping force measured by the force sensor (similar case to that depicted in Fig. 6b, see the plot of the 8-th test cycle).

The presented plots clearly reveal a lack of symmetry - the force values are lower when the piston moves upwards than during its downward movement. When analysing force time histories in each test an increase of the damping force is observed with each cycle of the piston movement. This is caused by the clumping behavior of MR fluid in the working gap. When comparing the plots through Fig 6a, 8a to 10a, it is apparent that at the assumed current level in the control coil (I=1 A), the lower height of MR fluid squeezed, the higher damping force. Moreover, in the assumed time range the damping force does not reach steady state value. Similar situation refers to the plots in Fig. 6b and 8b (then I=3 A) but then the damping force reaches higher values due to the higher level of the current in the control coil. The plots in Fig. 7a and 9a show that at the assumed frequency displacement input (f =4 Hz), the damping force achieves steady state value the contrary to the situation presented in Fig. 6a and 8a (then f=1 Hz).

DOI 10.1515/ama-2016-0037

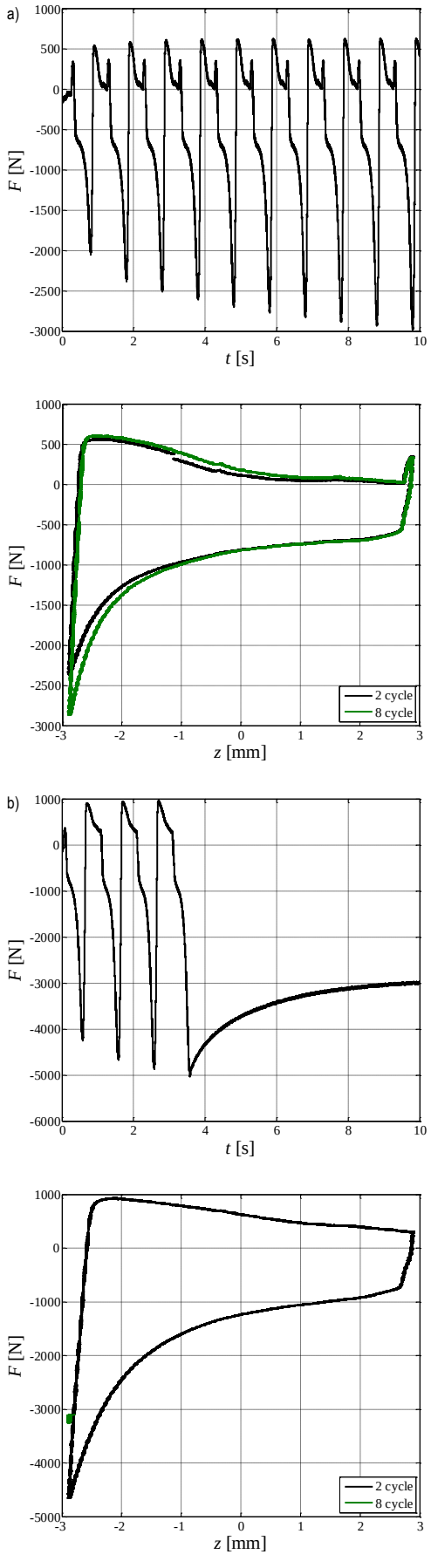

Fig. 6. Force vs. time and force vs. piston displacement; A=2.88 mm, f=1 Hz: a) I=1.0 A, b) I=3.0 A

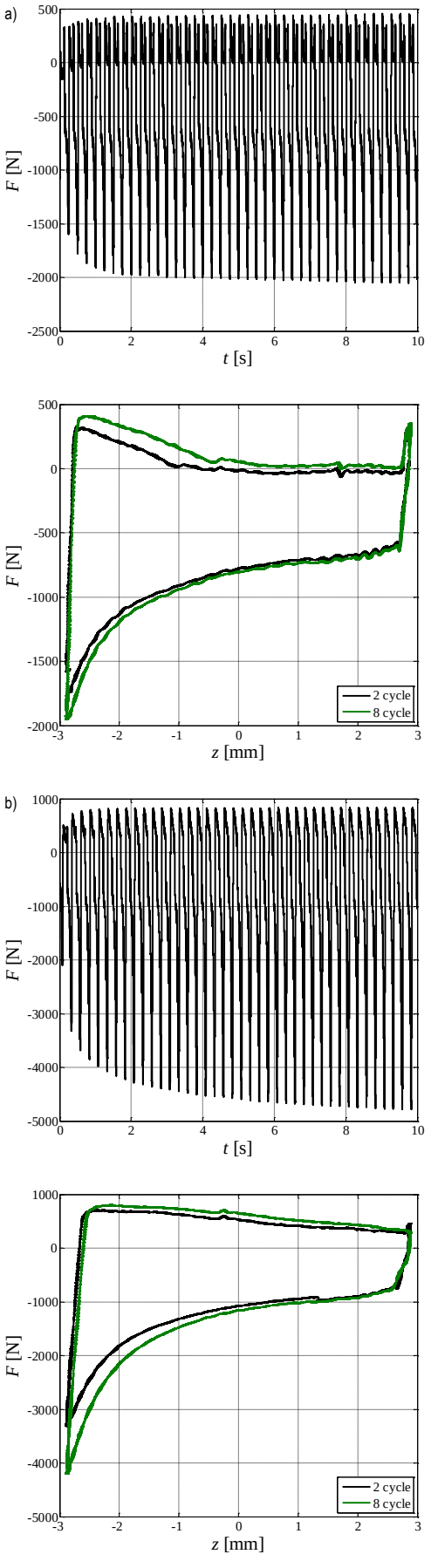

Fig. 7. Force vs. time and force vs. piston displacement; A=2.88 mm, f=4 Hz: a) I=1.0 A, b) I=3.0 A

DOI 10.1515/ama-2016-0037

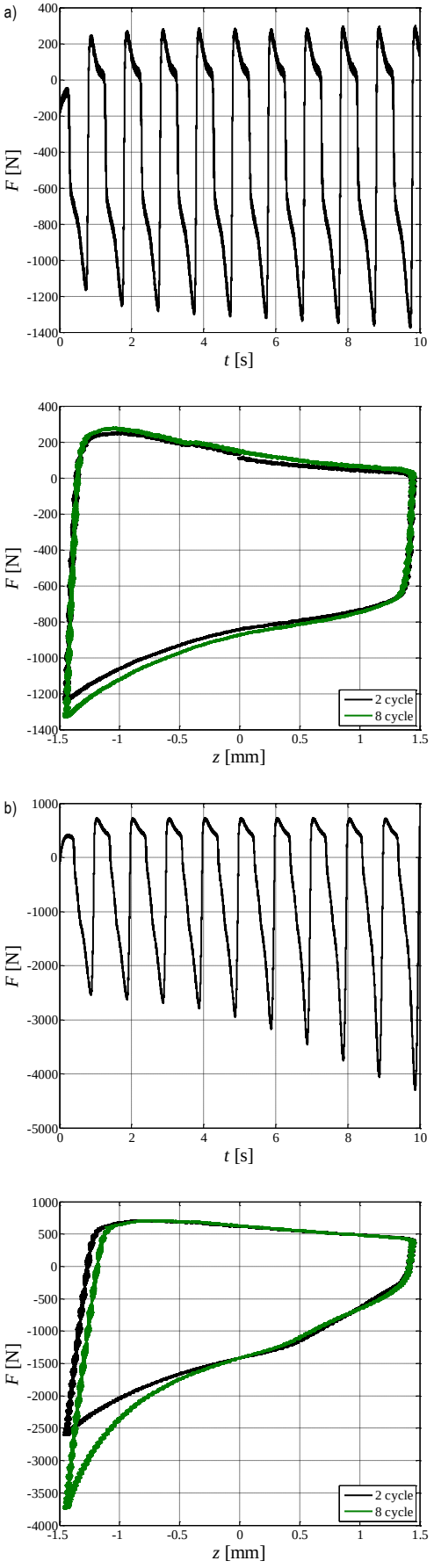

Fig. 8. Force vs. time and force vs. piston displacement; A=1.44 mm, f=1 Hz: a) I=1.0 A, b) I=3 .0 A

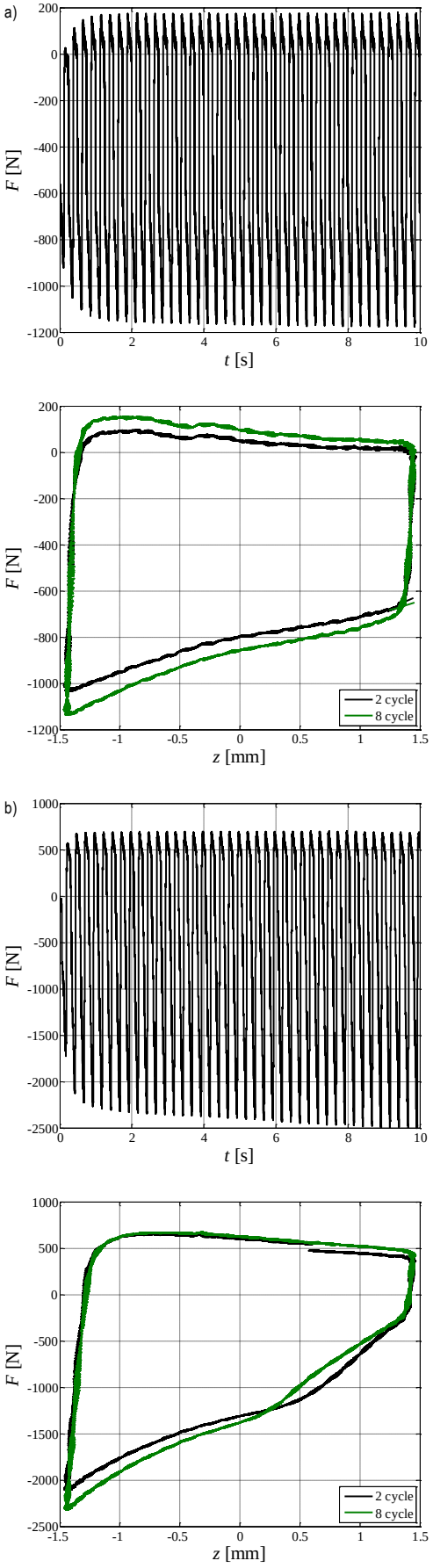

Fig. 9. Force vs. time and force vs. piston displacement; A=1.44 mm, f=4 Hz: a) I=1.0 A, b) I=3.0 A

DOI 10.1515/ama-2016-0037

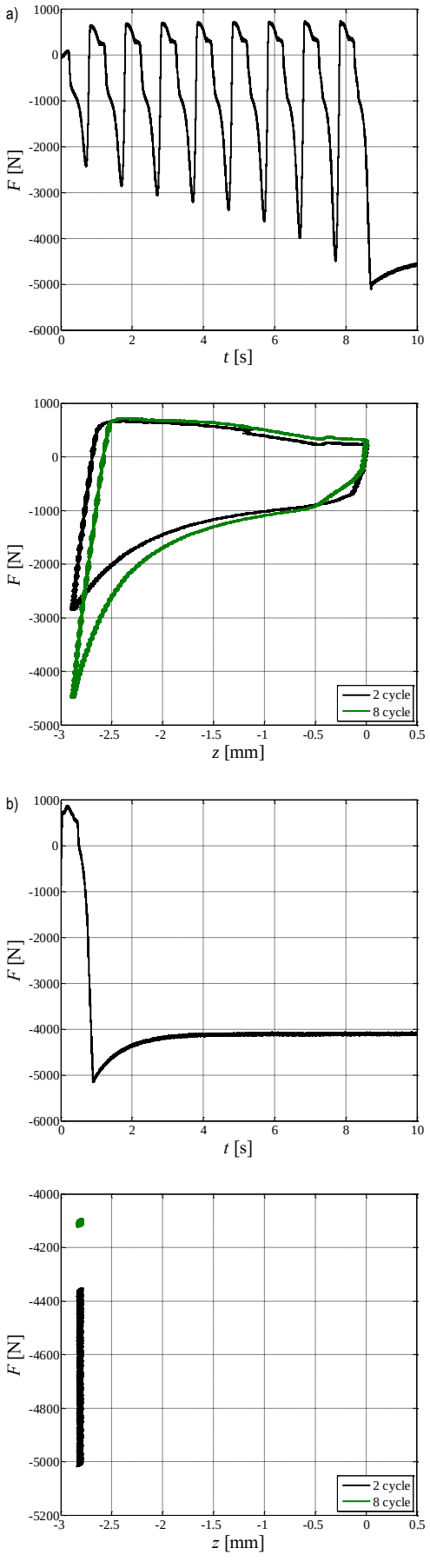

Fig. 10. Force time history and force vs. piston displacements; A=1.44 mm, f=1 Hz, x_0=1.44 mm: a) I=1.0 A, b) I=3.0 A

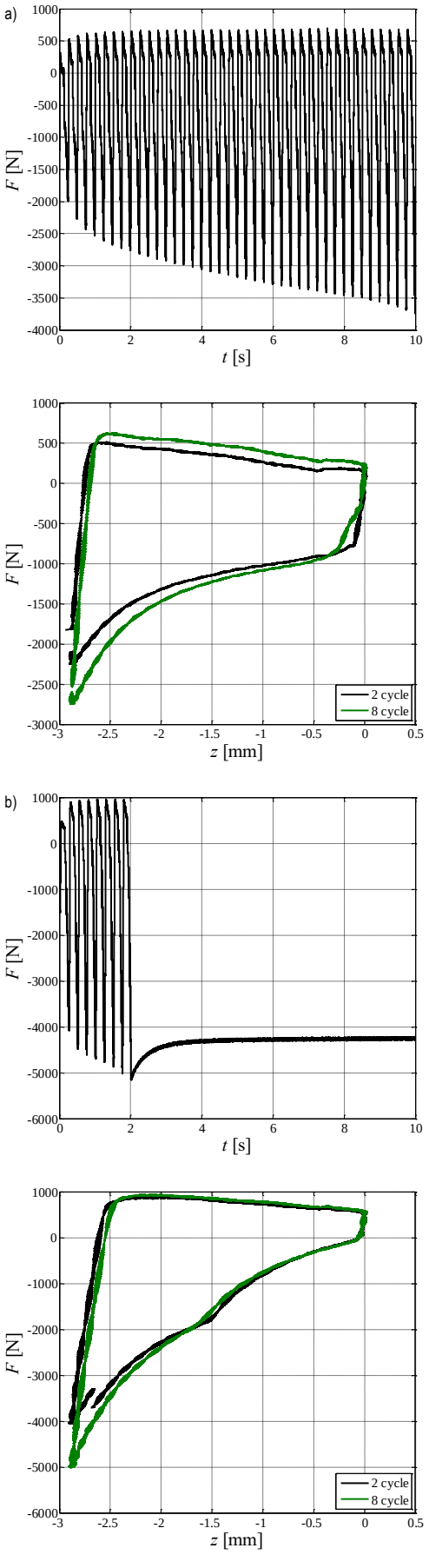

Fig. 11. Force time history and force vs. piston displacements; A=1.44 mm, f=4 Hz, x_0=1.44 mm: a) I=1.0 A, b) I=3 A

DOI 10.1515/ama-2016-0037

4. SUMMARY

The paper summarises the results of quasi-static experimental testing of an MRSQD, with the focus on MR fluid clumping behaviour in the working gap. The influence of displacement inputs' parameters (amplitude and frequency), current level in the control coil and piston position offset on the damping force output of the device was also investigated. The acquired data are presented in the form of damping force time histories and damping force-piston displacements loops.

The discussion of the results lead us to the following conclusions:

- plots of damping force time histories and damping force-piston displacement loops are not symmetrical,
- the influence of current in the control coil is signifficant, the higher the current level, the higher the damping force,
- the influence of piston velocity (amplitude and/or frequency of displacement input) and similarly piston position offset on the damping force is rather small,
- in each test a significant increase of the damping force is observed with each cycle of the piston movement, which is associated with the clumping behavior of MR fluid in the gap,

Further research efforts will be focused on investigation the influence of magnetic signal dither to reducing the clumping effect in the device.

REFERENCES

1. **Farjoud A., Ahmadian M., Cavey R.** (2009a), Rheometer characterization of MR fluids in squeeze mode, *Proc. SPIE 7288, Active and Passive Smart Structures and Integrated Systems*, 72880R.
2. **Farjoud A., Cavey R., Mehdi A., Craft M.,** (2009b), Magnetorheological fluid behavior in squeeze mode, *Smart Materials and Structures*, 18, 095001.
3. **Farjoud A., Craft M., Burke W., Ahmadian M.** (2011a), Experimental investigation of MR squeeze mounts. *Journal of Intelligent Material Systems and Structures*, 22, 1645–1652.
4. **Farjoud A., Ahmadian M., Mahmoodi N., Zhang X., Craft M**. (2011b), Non-linear modeling and testing of magneto-rheological fluids in low shear rate squeezing flows, *Journal of Smart Materials and Structures*, 20, 085013.
5. **Gołdasz J., Sapiński B.** (2011), Model of a squeeze mode magnetorheological mount. *Solid State Phenomena*,177, 116–124.
6. **Gong X., Ruan X., Shouhu X., Yan, Q., Deng H.** (2014), Magnetorheological Damper Working in Squeeze Mode, Hindawi Publishing Corporation, *Advances in Mechanical Engineering*, 410158..
7. **Guo Ch., Xinglong Gong X., Xuan S., Qin L., Yan Q.** (2013), Compression behaviors of magnetorheological fluids under nonuniform magnetic field, *Rheol. Acta*, 52, 165-176.
8. **Horak W.** (2013), *Theoretical and experimental analysis of magnetorheological fluid squeeze flow mode*, PhD Thesis, AGH University of Science and Technology, Krakow.
9. **Jolly M., R., Carlson J. D.** (1996), Controllable squeeze film damping using magnetorheological fluids, *Proc. of the 5th International Conference on New Actuators, Bremen*, 333–336.
10. **Kieburg Ch.** (2010), MR Fluid Basonetic 4035, *BASF Technical Information*.
11. **Kim J.-H.** (2014), *Damping force control filled with magneto-rheological fluids and engine mount having the same*, US Patent No. US 8,672,105 B2.
12. **Manecke P, Winkler B., Manhartsgruber B.** (2006), *Magneto-rheological damper*, US Patent 7070027.
13. **Mazlan S.A., Ekreem N. B., Olabi A.G**. (2007, The performance of magnetorheological fluid in squeeze mode, *Smart Materials and Structures*, 16, 1678-1682.
14. **Mazlan S.A** (2008), *The behaviour of magnetorheological fluids in squeeze mode*, Ph.D. Dissertation, University of Dublin.
15. **Sapiński B., Gołdasz J.** (2015), Development and performance evaluation of an MR damper in squeeze mode, *Smart Materials and Structures*, 24, 115007.
16. **Zhang X. J., Farjud A., Ahmadian M., Guo K. H., Craft M.** (2011), Dynamic Testing and Modelling of an MR Squezee Mount, *Journal of Intelligent Material Systems and Structures*, 22, 1717–1728.

This work is supported by AGH University of Science and Technology under research program No. 11.11.130.958.

ABSTRACTS

Łukasz Jastrzębski, Bogdan Sapiński
Electrical Interface for a Self-Powered MR Damper-Based Vibration Reduction System

The study investigates the behaviour of an electrical interface incorporated in a MR damper-based vibration reduction system powered with energy recovered from vibration. The interface, comprising the R, L and C elements, is connected in between the coil in an electromagnetic electric generator and the control coil in the MR damper and its function is to convert the output voltage from the generator. The interface model was formulated and computer simulations were performed to find out how the parameters of the interface should influence the frequency responses of the vibration reduction system.

Marek Jałbrzykowski
Selected Issues Concerning Degradation of Material in the Production of Injection Molded Plastic Components

This paper presents the problem of thermal degradation of thermoplastic materials processed using the injection method. Attention was paid to the issue of the optimal selection of a dye for modifying the base materials. For the selected materials and dyes, derivatograph tests were performed in order to assess their thermal characteristics and breakdown kinetics. Additionally, tribological tests and microscope observations of selected samples were performed. The obtained test results suggest a diverse level of thermal processes in the analyzed materials. This is crucial for the appropriate selection of dyes for plastic materials. As it turned out, the tribological properties of materials can also influence the technological quality of the injected alloy.

Iryna Rakocha, Vasyl Popovych
The Mathematical Modelling and Investigation of the Thermoelastic State of the Three-Ply Thermosensitive Hollow Cylinder

Stationary temperature distribution in a three-layer infinite hollow cylinder based on the thermosensitive body model was determined. The cylinder is subjected to the steady temperature on the inner surface and on the outer one is present the convective heat exchange. In the second layer exist heat sources with parabolic dependence on radial coordinate. The components of the thermostressed state have been found. The influence of the temperature dependence of the thermal and mechanical components characteristics of materials on the temperature distribution has been investigated.

Emil Evin, Miroslav Tomáš, Marek Výrostek
Laser-Beam Welding Impact on the Deformation Properties of Stainless Steels When Used for Automotive Applications

Materials other than standard and advanced high strength steels are remarkable for the thin-walled structures of the car-body in recent years in order to safety enhancement, weight and emission reduction, corrosion resistance improvement. Thus, there are presented in the paper the deformation properties of laser welded austenitic AISI 304 and ferritic AISI 430 stainless steels compared to these one measured for the high strength low alloyed steel H220PD. The properties were researched by tensile test and 3-point bending test with fixed ends on specimens made of basic material and laser welded one. The specimens were welded by solid state fiber laser YLS-5000 in longitudinal direction (the load direction). The deformation properties such as strength, stiffness and deformation work were evaluated and compared. The strength and stiffness were calculated from tensile test results and the deformation work was calculated from both, tensile test and 3-point bending test results. There has been found only minor effect of laser welding to the deformation properties for high strength low alloyed steel H220PD and austenitic stainless steel AISI 304. Otherwise, the laser welding strongly influenced the deformation work of the ferritic stainless steel AISI 430 as well as the elongation at tensile test.

Krystyna Romaniak
Identifying the Isomorphism of Kinematic Chains

Identification of isomorphic kinematic chains is one of the key issues in researching the structure of mechanisms. As a result the structures which duplicate are eliminated and further research is carried out on kinematic chains that do not duplicate. This dilemma has been taken up by many scholars who have come up with a variety of ideas how to solve it. The review of the methods for identifying the isomorphism of kinematic chains suggested by researchers is contained in this study, including Hamming Number Technique, eigenvalues and eigenvectors, perimeter graphs, dividing and matching vertices. The spectrum of methods applied to the issue of identifying the isomorphism of mechanisms reflects the researchers' efforts to obtain a precise result in the shortest time possible.

Robert Pała, Ihor Dzioba
Analysis of Stress Distribution in front of the Crack Tip in the Elements of Modified and Unmodified Cast Steel G17CrMo5-5

The article presents influence of modification of the low-alloy cast steel G17CrMo5-5 by rare earth metals on stress distribution in front of the crack at the initial moment of the crack extension. Experimental studies include determination of strength and fracture toughness characteristics for unmodified (UM) and modified (M) cast steel. In the numerical computations, experimentally tested specimens SEN(B) were modelled. The true stress–strain curves for the UM and M cast steel are used in the calculation. The stress distributions in front of the crack were calculated at the initial moment of the crack extension. On the basis of data on the particle size inclusions in the UM and M cast steel, and the calculated stress distributions was performed an assessment of the possibility of the occurrence of cleavage fracture. The analysis results indicate that at room temperature for the UM cast steel, there is a possibility of cleavage fracture, while for the M cast steel occurrence of cleavage fracture is negligible.

Szymon Hernik
Wear Resistance of Piston Sleeve Made of Layered Material Structure: MMC A356R, Anti-Abrasion Layer and FGM Interface

The aim of this paper is the numerical analysis of the one of main part of car engine – piston sleeve. The first example is for piston sleeve made of metal matrix composite (MMC) A356R. The second improved material structure is layered. Both of them are comparison to the classical structure of piston sleeve made of Cr-Ni stainless steel. The layered material structure contains the anti-abrasion layer at the inner surface of piston sleeve, where the contact and friction is highest, FGM (functionally graded material) interface and the layer of virgin material on the outer surface made of A356R. The complex thermo-elastic model with Archard's condition as a wear law is proposed. The piston sleeve is modelling as a thin walled cylindrical axisymmetric shell. The coupled between the formulation of thermo-elasticity of cylindrical axisymmetric shell and the Archard's law with functionally changes of local hardness is proposed.

Magdalena Bucior, Lidia Gałda, Feliks Stachowicz, Władysław Zielecki
The Effect of Technological Parameters on Intensity of Shot Peening Process of 51CrV4 Steel

In the paper the effect of selected technological parameters of shot peening on process intensity of 51CrV4 steel was presented. The experiments were conducted according to statistical 3-level completed plan PS/DC 32. Technological parameters were changed in the range: shot peening time t = 1-3 min and pressure p = 0.2-0.4 MPa. In the article the analysis of experiment reproducibility, impact parameters significance and adequacy of equation were done. As the result of investigations the adequate equation was obtained describing the effect of technological parameters. Significant influence on process intensity was found in case of pressure and interaction of both analyzed technological parameters. The biggest energy of stream shots was gained at the maximum pressure of 0.4 MPa and the shot peening time of 3 minutes. As the result of analysis according to design of experiment (DOE) the adequate equation describing the dependencies between technological parameters and process intensity was found.

Katarzyna Ciesielczyk, Katarzyna Rzeszut
Local and Distortional Buckling of Axially Loaded Cold Rolled Sigma Profiles

In this paper the local and distortional buckling analyses of axially loaded cold-rolled channel and sigma profiles were performed. The critical buckling load was computed by solving the linear eigenvalue problem for different numerical models using Finite Element Method and simplified formulas implemented in Eurocode and proposed by Hancock and Schafer. The buckling analyses were conducted to prove that the sigma cross-section can be successfully replaced by channel cross-section with additional elastic supports placed in folds of the web. It was demonstrated that the folds in the web of the sigma cross-section (additional elastic supports) reduce the slenderness of the web. So, the critical distortional stress can be calculated based on analytical formulas derived for the channel cross-section taking into account the web height between the folds.

Andrzej Borawski
Suggested Research Method for Testing Selected Tribological Properties of Friction Components in Vehicle Braking Systems

The braking system is one of the most important systems in any vehicle. Its proper functioning may determine the health and life the people inside the vehicle as well as other road users. Therefore, it is important that the parameters which characterise the functioning of brakes changed as little as possible throughout their lifespan. Multiple instances of heating and cooling of the working components of the brake system as well as the environment they work in may impact their tribological properties. This article describes a method of evaluating the coefficient of friction and the wear speed of abrasive wear of friction working components of brakes. The methodology was developed on the basis of Taguchi's method of process optimization.

Czesław Janusz Jermak, Mirosław Rucki
Dynamics of the Non-Contact Roundness Measurement with Air Gages

The paper presents the results of investigations on the air gages dynamic characteristics in the measurement of the round profiles of motor cylinders. The principle of the measuring device is explained, and the analysis of the air gages dynamics is described. The results of dynamic calibration enabled to eliminate those configurations of air gages that may not meet the requirements of the measurement they were designed for. After the proper air gages were chosen, the entire system underwent the accuracy test and passed it successfully revealing the method accuracy better than 10% compared to the reference measurement.

Anna Kasperczuk, Agnieszka Dardzińska
Comparative Evaluation of the Different Data Mining Techniques Used for the Medical Database

Data mining is the upcoming research area to solve various problems. Classification and finding association are two main steps in the field of data mining. In this paper, we use three classification algorithms: J48 (an open source Java implementation of C4.5 algorithm), Multilayer Perceptron - MLP (a modification of the standard linear perceptron) and Naïve Bayes (based on Bayes rule and a set of conditional independence assumptions) of the Weka interface. These classifiers have been used to choose the best algorithm based on the conditions of the voice disorders database. To find association rules over transactional medical database first we use apriori algorithm for frequent item set mining. These two initial steps of analysis will help to create the medical knowledgebase. The ultimate goal is to build a model, which can improve the way to read and interpret the existing data in medical database and future data as well.

Bogdan Sapiński
Observations of MR Fluid Clumping Behaviour in a Squeeze-Mode Damper

The study summarises the results of quasi-static experimental tests of an MR squeeze-mode damper prototype (MRSQD) performed at the MTS testing machine. Of particular interests was the influence of MR fluid clumping behaviour in the MRSQD working gap on the force output of the device. The MRSQD tests were assessed by measuring the damping force output at prescribed sinusoidal displacement inputs and at various (fixed) voltage levels resulting in the respective average current levels in the control coil. The influence of piston position offset on the damping force was also investigated. The collected data were shown in the form of damping force time histories and damping force-piston displacements loops and discussed with respect to MR fluid clumping behaviour.